UNIVERSITY OF CALIFORNIA,
IRVINE

Fast-ion studies in the National Spherical Torus Experiment: Transport by instabilities and acceleration by high harmonic fast waves

DISSERTATION

submitted in partial satisfaction of the requirements
for the degree of

DOCTOR OF PHILOSOPHY

in Physics

by

Deyong Liu

Dissertation Committee:
Professor William W. Heidbrink, Chair
Professor Liu Chen
Professor Roger D. McWilliams

2009

TABLE OF CONTENTS

Page

LIST OF FIGURES **vi**

LIST OF TABLES **xii**

ACKNOWLEDGMENTS **xiii**

CURRICULUM VITAE **xvi**

ABSTRACT OF THE DISSERTATION **xix**

1 Introduction **1**

1.1 Fusion Energy 1

1.2 Tokamaks 7

1.3 Spherical Torus 10

1.4 National Spherical Torus Experiment 11

1.5 Fast Ions 14

1.6 Thesis Objective and Organization 15

2 Plasma Heating Systems and Diagnostics in the National Spherical Torus Experiment **18**

2.1 Plasma Heating Systems 18

2.1.1 Ohmic Heating System 19

2.1.2 Neutral Beam Injection System 19
2.1.3 High Harmonic Fast Wave Heating System 21
2.2 Major Diagnostics 22
2.2.1 Thomson Scattering Diagnostic 23
2.2.2 Charge Exchange Recombination Spectroscopy 25
2.2.3 Motional Stark Effect Diagnostic 26
2.2.4 Mirnov Coil Arrays 27
2.2.5 Soft X-Ray Arrays 27
2.2.6 Neutron Detectors 29
2.2.7 Fast Ion Loss Probe 29
2.2.8 E||B Type Neutral Particle Analyzer 30
2.2.9 Fast-Ion D-Alpha Diagnostic 31

3 Solid State Neutral Particle Analyzer 34

3.1 Working Principles 35
3.2 Hardware Description 36
3.2.1 Setup 36
3.2.2 Noise Reduction Techniques 38
3.2.3 Fast Digitization of Raw Signals 40
3.3 Data analysis 42
3.3.1 Software-based Pulse Height Analysis 42
3.3.2 Energy Calibration 43
3.3.3 Noise Analysis 46
3.4 Characteristics of the NPA Diagnostics 51
3.5 SSNPA Measurements in Quiescent Plasmas 54

4 Simulation Codes **59**

4.1 TRANSP Code 59

4.2 CQL3D Code 60

4.3 FIDA Simulation Code 60

4.4 NPA Simulation Codes 61

4.4.1 TRANSP-based NPA Simulation 63

4.4.2 FIDA_NPA Simulation 64

5 Profiles of Fast Ions that are Accelerated by High Harmonic Fast Wave Heating **78**

5.1 Introduction and Motivation 78

5.2 Experimental Conditions and Results 80

5.2.1 Experimental Conditions 80

5.2.2 Neutron Measurements 84

5.2.3 NPA and SSNPA Measurements 86

5.2.4 FIDA Measurements 90

5.3 Discussion and Comparison with Theory 94

5.4 Conclusion 109

6 Redistribution and Loss of Fast Ions during Instability Bursts **110**

6.1 Introduction 110

6.2 Overview of Fishbone and Sawtooth 112

6.2.1 Fishbone Instability 112

6.2.2 Sawtooth Instability 113

6.3 Measurements and Data Analysis 115

6.3.1 Experimental Measurements during Fishbone Events 116

6.3.2 Experimental Measurements during Sawtooth Events 128

6.3.3 TAE Avalanches 133
6.4 Modelling of Fishbones and Sawteeth 136
6.5 Summary 138

7 Conclusions and Future Work **139**

7.1 Summary of Results 139
7.2 Suggestions for Future Research 142

Bibliography **145**

Appendices **155**

A Data Acquisition of the SSNPA Array 155
B Pulse Height Analysis Routines 157

LIST OF FIGURES

Page

1.1 Fusion cross-sections vs deuteron kinetic energy for fusion reactions D-T, D-D and D-He^3. 3

1.2 Compilation of tokamak $nT\tau_E$ progress. 5

1.3 Progress towards ignition in inertial confinement fusion 6

1.4 (a) Schematic of Tokamak; (b) cross section of toroidal plasma. . . . 9

1.5 The shape and magnetic topology for a conventional Tokamak and a spherical torus. 11

1.6 A cutaway view of the NSTX device. 12

2.1 Layout of injection lines of three neutral beam sources in NSTX with solid state neutral particle analyzer array and E||B type neutral particle analyzer. 20

2.2 Schematic diagram of the rf distribution system showing the twelve antenna elements, the six RF inputs (T1– T6) and the splitting decoupling network (D1–D6). 21

2.3 Laser systems of the MPTS system. 24

2.4 Collecting optics of the MPTS system. 24

2.5 CHERS viewing geometry. 25

2.6 Plan view of the MSE-CIF diagnostic layout on NSTX. 26

2.7 Layout of the Ultrasoft X-ray (USXR) system on NSTX. 28

2.8 Illustration of the E||B spectrometer concept. 30

2.9 Three types of atomic processes are involved in the emission of a photon by a fast ion. 32

2.10 Layout of the FIDA system on NSTX. 33

3.1 Silicon photodiodes used in the SSNPA diagnostic. 36

3.2 Schematic view of collimating tube, aperture, Al foil, and detector. . 37

3.3 Schematic diagram of the SSNPA electronics. 38

3.4 A photo of the SSNPA diagnostic, which shows the flight tubes and preamps in copper shielding boxes. 39

3.5 Software-based pulse height analysis for the SSNPA diagnostic. 41

3.6 Layout of the energy calibration of SSNPA detectors. 43

3.7 The energy calibration with a mono-energetic source for the SSNPA diagnostic. 44

3.8 The energy calibration of the SSNPA diagnostic with gas-filled-torus shots. 45

3.9 The fraction of pulses above the injection energy increases monotonically with (a) incident energy and (b) count rate in the gas-filled-torus shots. 47

3.10 The linear relation between the neutron rate and SSNPA noise. . . . 48

3.11 The noise of the SSNPA diagnostic comes from the combination of pulse pile-up and neutron/gamma ray radiation 49

3.12 Three type of neutrals can contribute to the NPA/SSNPA signals. . . 51

3.13 The SSNPA signal is localized to a significant extent by beam neutrals in real space and a small pitch range in velocity space. 52

3.14 The pitch of fast ions that can be sampled by the NPA and SSNPA diagnostics as a function of the viewing tangency radius. 53

3.15 Temporal evolution of plasma current, NB power, neutron yield, counts in Chord 1 of the SSNPA, and the E||B NPA signal in shot 119598 . . 56

3.16 Temporal evolution of plasma parameters and SSNPA signals, which shows the fast ion slowing down process during the beam off period. . 57

3.17 Comparison of fast-ion slowing down time from experimental data fitting and classical Coulomb collision theory. 58

4.1 Flow diagram of the FIDA_NPA simulation code. 66

4.2 Coordinates used in TRANSP and FIDA_NPA simulations and general North-South-East-West coordinates. 67

4.3 Comparison of beam neutral density profiles predicted from the TRANSP and FIDA_NPA simulations. 69

4.4 Comparison of halo neutral densities calculated from a 1-D diffusion model and the Monte-Carlo halo simulation code. 72

4.5 Comparison of neutral density, attenuation factor, and differential CX efflux from the FIDA_NPA and TRANSP simulations for shot 122631 and t=0.1s 73

4.6 Energy spectra from the FIDA_NPA and TRANSP simulations at three time slices. 75

4.7 Temporal evolution of the measured plasma parameters and the NPA flux from the FIDA_NPA simulation. 76

4.8 Primary beam neutral and halo neutral density along the NPA sightline at six time slices from the FIDA_NPA simulations for shot 122631. . 77

5.1 Elevation of the NSTX vacuum vessel, showing the flux surfaces, the locations of resonance layers, the midplane locations of the FIDA channels and elevation minor radii of the E||B type NPA during the four-shot vertical scan. The hashed region represents the approximate extent of the neutral beam that produces the FIDA and NPA signals. The rectangles indicate the approximate locations of the FIDA lenses. 81

5.2 Temporal evolution of plasma parameters, spectrum of Mirnov coils and neutron emission rate in the no-RF reference shot and three nominally identical RF shots. 82

5.3 Spectra of Mirnov coil signals in the frequency range of [1000, 2000] kHz in the discharges with and without RF. Note that color indicates FFT mode amplitude. The FFT mode amplitude in our experiment is relative weak (less than 1/4 of that in typical NSTX plasmas). . . . 83

5.4 Details of a neutron pulse in the measurements and TRANSP simulations. 86

5.5 (a) Rise rate and (b) decay time of neutron emission rate versus time in the discharges with and without HHFW heating. The symbols represent experimentally measured values. The solid lines are TRANSP predictions 87

5.6 Energy spectra of active CX signals from the E||B type NPA at a sightline tangency radius of 70 cm for NSTX shots 128739 (with RF) and 128742 (without RF). 89

5.7 Energy spectra of total CX signals of chord 1 of SSNPA with tangency radius of 60 cm in shots 128739 (with RF) and 128742 (without RF). 89

5.8 Energy spectra of channel 11 ($R_{maj} = 108$ cm) of the FIDA diagnostic in the no-RF reference shot and three nominally identical RF shots. . 91

5.9 Integrated FIDA density ($E_\lambda = 10 - 65$ keV) vs major radius in the shots with and without RF. 92

5.10 Relative change in integrated FIDA density in the discharges with and without HHFW heating for energy integration range of (a) $E_\lambda = 10-65$ keV and (b) $E_\lambda = 35 - 65$ keV during the time window $0.29 - 0.35$ s. 93

5.11 Fast ion orbits during successive passes through a resonance layer. The ICRF wave gives perpendicular energy to fast ions and thus pushes them into the trapped particle region. The particle's banana tips eventually end up close to the resonance layer. 95

5.12 Velocity space of fast ions. 96

5.13 Trajectories of fast ions that can contribute the NPA active or passive signals. 98

5.14 The pitches of the E||B NPA at different tangency radii vs vertical angle. Generally the pitch goes down when the E||B NPA scans vertically from zero vertical angle. 99

5.15 Energy spectra of active signals from the E||B type NPA during four nominally identical discharges, in which the NPA scanned vertically. . 100

5.16 Averaged energy spectra of total CX signals of four chords of SSNPA in four nominally identical discharges with HHFW heating 101

5.17 Comparison of the measured NPA energy spectra and NPA simulations using CQL3D predicted fast-ion distributions in the shots (a) without and (b) with RF. 104

5.18 Fast-ion distributions at the intersectional area (R=83 cm) of the NB source B and the NPA sightline with tangency radius of 70 cm in real space. 106

5.19 Fast-ion distributions at the intersectional area (R=83 cm, Z=0 cm) of the NB source B and the NPA sightline with tangency radius of 70 cm in velocity space. 107

5.20 Comparison of (a) FIDA spatial profiles and (b) FIDA energy spectra of chord 11 with $R_{maj} = 108$ cm from the measurements and simulations. 108

6.1 Magnetic fluctuations in a typical NSTX beam heated plasma. 111

6.2 Temporal evolution of plasma parameters, the E||B type NPA and SSNPA signals in shot 124512. 119

6.3 The Mirnov coil spectrograms show that (a) the bursting events in the time window of $0.32 - 0.37$ second in shot 124512 are $n = 1$ mode and its harmonics, and (b) these modes sweep down rapidly in frequency during the course of bursts during each burst. 120

6.4 The measurements of the soft X-ray array viewing the lower half of plasma suggest that the bursting events in shot 124512 are fishbones. 121

6.5 Normalized cross-correlations (a-e) between the negative derivative of neutron rate and the NPA/SSNPA signals and (f-j) between the edge D-alpha light and the NPA/SSNPA signals in shot 124512. 122

6.6 Temporal evolution of plasma parameters, the E||B type NPA and SSNPA signals in shot 122644. 124

6.7 The Mirnov coil spectrograms show that the (a) bursting events in the time window of $0.59 - 0.65$ second in shot 122644 are mainly $n = 1$ mode and weak $n = 1$ and $n = 2$ continuous mode. (b) The $n = 1$ mode shows similar chirping feature as in the fishbone shot 124512. . 125

6.8 The measurements of the soft X-ray array viewing the lower half of plasma in shot 122644. 126

6.9 The Mirnov coil spectrogram shows there are bursting CAEs in the frequency range of [1500, 2000] kHz during the time window of $0.59 - 0.65$ second in shot 122644. 126

6.10 Normalized cross-correlations (a-e) between the negative derivative of neutron rate and the NPA/SSNPA signals and (e-f) between the edge D-alpha light and the NPA/SSNPA signals in shot 122644. 127

6.11 Temporal evolution of plasma parameters, the E||B type NPA and SSNPA signals in shot 124503. 129

6.12 The Mirnov coil spectrograms show that the bursting events in the time window of $0.32 - 0.39$ second in shot 124503 are $n = 1$ mode and its harmonics. 130

6.13 The measurements of the soft X-ray array viewing the lower half of plasma suggest that the bursting events in shot 124503 are sawtooth oscillations. 131

6.14 Normalized cross-correlations (a-e) between the negative derivative of neutron rate and the NPA/SSNPA signals and (f-j) between the edge D-alpha light and the NPA/SSNPA signals in shot 124503. 132

6.15 The Mirnov coil spectrogram shows there are also some weak CAEs in the frequency range of [800, 1600] kHz during the time window of $0.32 - 0.39$ second in shot 124503. Note that color indicates FFT mode amplitude. 133

6.16 The Mirnov coil spectrograms show that TAE avalanches occur at 0.257, 0.265, 0.275, 0.284, and 0.293 second in shot 128741. 134

6.17 Temporal evolution of plasma parameters, the E||B type NPA and SSNPA signals in shot 124781. 135

6.18 Comparison of the central electron density, electron temperature, fast ion beta, $q_{\min}$, and the frequency sweep range in the fishbone and sawtooth shots. 137

A.1 The Labview control panel for the SSNPA data acquisition system. . 156

B.2 The graphic interface for the SSNPA data analysis. 159

LIST OF TABLES

Page

1.1 Comparison of plasma parameters in NSTX and DIII-D. 13

3.1 Comparison of various fast ion diagnostics in velocity space and real space. 54

6.1 Fishbone and sawtooth database in NSTX. 117

ACKNOWLEDGMENTS

This thesis could not been carried out without the support and advice from many individuals and organizations. First and foremost, I would give my sincere thanks to my advisor Professor William W. Heidbrink for his thoughtful guidance and constant encouragement throughout the whole project. He is a great advisor, teacher and friend. From him I have learned not only plasma physics, but also many principles of being a professional researcher.

The experimental aspects of this thesis were conducted at the fusion facility, National Spherical Torus Experiment (NSTX), located in Princeton Plasma Physics Laboratory (PPPL). Special thanks go to Douglass S. Darrow (PPPL), Kouji Shinohara (Japan Atomic Energy Research Institute), Sidney S. Medley (PPPL), A. Lane Roquemore (PPPL) and Mario Podestá (UC Irvine) who are working or worked there. Doug was my host advisor during my two-year stay at PPPL. He has been there whenever I turned to him for support and encouragement, both professionally and personally. Kouji was my predecessor who initiated the solid state neutral particle analyzer (SSNPA) project on NSTX. He trained me and worked with me during my first month at PPPL. Sid shared his wealth of knowledge and experience about the E||B type neutral particle analyzer (NPA). I also deeply appreciate his patience and help in my first technical writing. Lane is an expert at diagnostics and he helped me design, construct and improve the SSNPA diagnostic. Mario helped me maintain the SSNPA diagnostic after I left PPPL and provided valuable data from the Fast-Ion D-Alpha (FIDA) diagnostic.

I would also like to thank a host of individuals at PPPL that have contributed in some way to this research and background presented in this thesis. Thanks to Eric

Fredrickson, Robert Kaita, Stanley Kaye, Ronald Bell, Nikolai Gorelenkov, and Masa Ono for their useful discussions and suggestions. Thanks to Douglas McCune and Robert Andre for their help in the TRANSP simulation. Thanks to Robert Harvey at CompX for providing the CQL3D simulation results in this thesis. Thanks to Roscoe White for guiding me through his ORBIT code. Thanks to Neal Crocker and Shigeyuki Kubota for reflectometry data and their NOVA-K simulation results. Thanks to Phyllis Roney and Bill Davis for their help and advice concerning IDL and MDSplus data acquisition system. Thanks to John Dong, Tom Holoman and Doug LaBrie for their technical assistance. Thanks to the whole NSTX research team especially the NB team, HHFW team, CHERS team, MPTS team, and soft X-ray team. Without their hard work, dedication, enthusiasm, and long hours, the results in this thesis would not have been possible.

The excellent faculties and researchers at plasma physics program of UC Irvine also deserve recognition. I benefited a lot from the stimulating discussions with Professor Liu Chen, for his always thoughtful and incisive questions and comments. Professor Zhihong Lin's plasma physics classes and suggestions regarding numerical simulations were also very helpful. Professor Roger McWilliams is very kind. I spent my first year's summer research at his big plasma physics lab and got the first hand-on experience. Prof. Chen and Prof. McWilliams also served on my dissertation committee. They gave valuable suggestions and corrections to the dissertation, which made it more readable and accurate. I am also grateful to Yong Xiao and Peter Porazik for proofreading the draft of the dissertation. I also appreciate the help from Emil Ruskov, who taught me to run the TRANSP code and helped maintain the FIDA and FIDA_NPA simulation codes. In addition, there are also a large number of graduate students and friends from UC Irvine and Princeton University that I would like to thank: Liangji Zhao, Yadong Luo, Yang Zhang, Chris Muscatello, Wayne Harris,

Erik Trask, Tommy Roche, Yubao Zhu, Yong Xiao, Welu Zhang, Peter Porazik, Zehua Guo, Wei Liu, Yang Ren, Weihua Zhou and Wubiao Zhu. Thanks for their help in my study and personal life.

Last but certainly not least, I would like to thank my grandmother, my parents, and the rest of my family, who have always wished the best for me and showed all their unconditional love and support. I cannot describe in words how grateful I am for all of you. Without your love, support, understanding, encouragement and prayers, I could not get this far.

This work was supported at PPPL by the DOE contract DE-AC02-09CH11466.

CURRICULUM VITAE

Deyong Liu

EDUCATION

2009 Ph.D. in Plasma Physics	University of California, Irvine
2006 M.S. in Plasma Physics	University of California, Irvine
2002 M.S. in Plasma Physics	Dalian University of Technology, P. R.China
1999 B.S. in Applied Physics	Dalian University of Technology, P. R.China

RESEARCH EXPERIENCE

- 2004∼2009 Research assistant at fusion energy lab, University of California, Irvine

  ♢ Developed and maintained a fast ion diagnostic, solid sate neutral particle analyzer (SSNPA) array, for the National Spherical Torus Experiment (NSTX) including data digital acquisition and post-shot processing

  ♢ Developed a Monte Carlo code to simulate neutral particle analyzer (NPA) and SSNPA signals for comparison with measurements

  ♢ Debugged and optimized the simulation code of fast ion D-alpha (FIDA) diagnostic and applied the code to NSTX

  ♢ Analyzed the NPA and SSNPA data to find the correlation between instability bursts and NPA/SSNPA signals

  ♢ Analyzed the NPA, SSNPA, FIDA data to get radial profiles of accelerated fast ion during high harmonic harmonic wave heating

- 7/2003∼8/2003 Research assistant at basic plasma physics lab, University of California, Irvine

  ♢ Developed a high voltage DC power supply for a Langmuir probe

- 1999∼2002 Research assistant at low temperature plasma simulation group, Dalian University of Technology, P. R. China

  ♢ Simulated the charging and dynamics of dust particles in dusty plasma sheath during plasma source ion implantation in order to investigate their effects on the sheath evolution

  ♢ Simulated the charging and dynamics of dust particles in cathode sheath of glow discharges

PUBLICATIONS

- **D. Liu**, W. W. Heidbrink, M. Podestà, R. E. Bell, E. D. Fredrickson, S. S. Medley, R. W. Harvey, and E. Ruskov, "Profile of fast ions accelerated by high-harmonic fast-wave (HHFW) heating", Plasma Phys. Control. Fusion (2009) submitted

- E. D. Fredrickson, N. A. Crocker, R. E. Bell, D. Darrow, N. N. Gorelenkov, G. Kramer, S. Kubota, F. M. Levinton, **D. Liu**, S. S. Medley, M. Podesta, K. Tritz, R. B. White, H. Yuh, "Modeling Fast Ion Transport in TAE Avalanches in NSTX", Phys. Plasmas (2009) submitted

- M. Podesta, W. W. Heidbrink, **D. Liu**, E. Ruskov, R. E. Bell, D. S. Darrow, E. D. Fredrickson, N. N. Gorelenkov, G. J. Kramer, B. P. LeBlanc, S. S. Medley, A. L. Roquemore, N. A. Crocker, S. Kubota, and H. Yuh, "Experimental studies on fast-ion transport by Alfven waves on the National Spherical Tours Experiment", Phys. Plasmas **16**, 056104, 2009

- J.E. Menard, M.G. Bell, R.E. Bell, S. Bernabei, J. Bialek, T. Biewer, W. Blanchard, J. Boedo, C.E. Bush, M.D. Carter, W. Choe, N.A. Crocker, D.S. Darrow, W. Davis, L. Delgado-Aparicio, S. Diem, C.W. Domier, D.A. D'Ippolito, J. Ferron, A. Field, J. Foley, E.D. Fredrickson, D.A. Gates, T. Gibney, R. Harvey, R.E. Hatcher, W. Heidbrink, K.W. Hill, J.C. Hosea, T.R. Jarboe, D.W. Johnson, R. Kaita, S.M. Kaye, C.E. Kessel, S. Kubota, H.W. Kugel, J. Lawson, B.P. LeBlanc, K.C. Lee, F.M. Levinton, N.C. Luhmann Jr., R. Maingi, R.P. Majeski, J. Manickam, D.K. Mansfield, R. Maqueda, R. Marsala, D. Mastrovito, T.K. Mau, E. Mazzucato, S.S. Medley, H. Meyer, D.R. Mikkelsen, D. Mueller, T. Munsat, J.R. Myra, B.A. Nelson, C. Neumeyer, N. Nishino, M. Ono, H.K. Park, W. Park, S.F. Paul, T. Peebles, M. Peng, C. Phillips, A. Pigarov, R. Pinsker, A. Ram, S. Ramakrishnan, R. Raman, D. Rasmussen, M. Redi, M. Rensink, G. Rewoldt, J. Robinson, P. Roney, A.L. Roquemore, E. Ruskov, P. Ryan, S.A. Sabbagh, H. Schneider, C.H. Skinner, D.R. Smith, A. Sontag, V. Soukhanovskii, T. Stevenson, D. Stotler, B.C. Stratton, D. Stutman, D. Swain, E. Synakowski, Y. Takase, G. Taylor, K. Tritz, A. von Halle, M. Wade, R. White, J. Wilgen, M. Williams, J.R. Wilson, H. Yuh, L.E. Zakharov, W. Zhu, S.J. Zweben, R. Akers, P. Beiersdorfer, R. Betti, T. Bigelow, M. Bitter, P. Bonoli, C. Bourdelle, C.S. Chang, J. Chrzanowski, L. Dudek, P.C. Efthimion, M. Finkenthal, E. Fredd, G.Y. Fu, A. Glasser, R.J. Goldston, N.L. Greenough, L.R. Grisham, N. Gorelenkov, L. Guazzotto, R.J. Hawryluk, J. Hogan, W. Houlberg, D. Humphreys, F. Jaeger, M. Kalish, S. Krasheninnikov, L.L. Lao, J. Lawrence, J. Leuer, **D. Liu**, G. Oliaro, D. Pacella, R. Parsells, M. Schaffer, I. Semenov, K.C. Shaing, M.A. Shapiro, K. Shinohara, P. Sichta, X. Tang, R. Vero, M. Walker and W. Wampler, "Overview of recent physics results from the National Spherical Torus Experiment (NSTX)" Nucl. Fusion **47** S645-S657, 2007

- **D. Liu**, W.W. Heidbrink et al. "Performance of Solid State Neutral Particle Analyzer Array on NSTX", Review of Scientific Instruments, **77**, 10F113, 2006

- S.M. Kaye, M.G. Bell, R.E. Bell, S. Bernabei, J. Bialek, T. Biewer, W. Blanchard, J. Boedo, C. Bush, M.D. Carter, W. Choe, N. Crocker, D.S. Darrow, W. Davis, L. Delgado-Aparicio, S. Diem, J. Ferron, A. Field, J. Foley, E.D. Fredrickson, D.A. Gates, T. Gibney, R. Harvey, R.E. Hatcher, W. Heidbrink, K. Hill, J.C. Hosea, T.R. Jarboe, D.W. Johnson, R. Kaita, C. Kessel, S. Kubota, H.W. Kugel, J. Lawson, B.P. LeBlanc, K.C. Lee, F. Levinton, R. Maingi, J. Manickam, R. Maqueda, R. Marsala, D. Mastrovito, T.K. Mau, S.S. Medley, J. Menard, H. Meyer, D.R. Mikkelsen, D. Mueller, T. Munsat, B.A. Nelson, C. Neumeyer, N. Nishino, M. Ono, H. Park, W. Park, S. Paul, T. Peebles, M. Peng, C. Phillips, A. Pigarov, R. Pinsker, A. Ram, S. Ramakrishnan, R. Raman, D. Rasmussen, M. Redi, M. Rensink, G. Rewoldt, J. Robinson, P. Roney, A.L. Roquemore, E. Ruskov, P. Ryan, S.A. Sabbagh, H. Schneider, C.H. Skinner, D.R. Smith, A. Sontag, V. Soukhanovskii, T. Stevenson, D. Stotler, B. Stratton, D. Stutman, D. Swain, E. Synakowski, Y. Takase, G. Taylor, K. Tritz, A. von Halle, M. Wade, R. White, J. Wilgen, M. Williams, J.R. Wilson, W. Zhu, S.J. Zweben, R. Akers, P. Beiersdorfer, R. Betti, T. Bigelow, M. Bitter, P. Bonoli, C. Bourdelle, C.S. Chang, J. Chrzanowski, C. Domier, L. Dudek, P.C. Efthimion, M. Finkenthal, E. Fredd, G.Y. Fu, A. Glasser, R.J. Goldston, N.L. Greenough, L.R. Grisham, N. Gorelenkov, L. Guazzotto, R.J. Hawryluk, J. Hogan, W. Houlberg, D. Humphreys, F. Jaeger, M. Kalish, S. Krasheninnikov, L.L. Lao, J. Lawrence, J. Leuer, **D. Liu**, N.C. Luhmann, E. Mazzucato, G. Oliaro, D. Pacella, R. Parsells, M. Schaffer, I. Semenov, K.C. Shaing, M.A. Shapiro, K. Shinohara, P. Sichta, X. Tang, R. Vero, D. Walker and W. Wampler, "Progress towards high performance plasmas in the National Spherical Torus Experiment (NSTX)", Nucl. Fusion **45** S168-S180, 2005

- **Deyong Liu**, Dezhen Wang, Xiaogang Wang, and Jiuyuan Liu, "Charging effects on temporal and spatial evolution of the dust plasma sheath in plasma source ion implantation", Phys. Plasmas **8**, 1427, 2001

- Dezhen Wang, **Deyong Liu**, and Jinyuan Liu, "Dust charging and levitating in cathode sheath of glow discharges of with energetic beam", J. Appl. Phys. **88**, 1276, 2000

- **Deyong Liu**, Dezhen Wang, Jinyuan Liu, "Dynamics and suspension of dust particles in cathode sheaths of dc glow discharge", Acta Physica Sinica **49**, 1094, 2000 (in Chinese)

ABSTRACT OF THE DISSERTATION

Fast-ion studies in the National Spherical Torus Experiment:
Transport by instabilities and acceleration by high harmonic fast waves

By

Deyong Liu

Doctor of Philosophy in Physics

University of California, Irvine, 2009

Professor William W. Heidbrink, Chair

An extensive set of fast-ion diagnostics, including neutron detectors, a E||B type neutral particle analyzer (NPA) and the newly built four-chord solid state neutral particle analyzer array (SSNPA) and a 16-channel Fast-ion D-alpha (FIDA) diagnostic, provides a good test-bed to study fast ion physics in the National Spherical Torus Experiment (NSTX). During combined neutral beam injection (NBI) and High-Harmonic Fast-Wave (HHFW) heating, the acceleration of fast ions is evident in all fast ion diagnostics. The neutron rate is about three times larger during the HHFW heating. A fast-ion tail above the beam injection is observed in the NPA, SSNPA and FIDA diagnostics. It is also shown that the accelerated fast ions observed by the NPA and SSNPA diagnostics mainly come from passive charge exchange reactions at the edge due to the NPA/SSNPA localization in phase space. The spatial profile of accelerated fast ions that is measured by the FIDA diagnostic is much broader than in conventional tokamaks because of the multiple resonance layers and large orbits in NSTX. The fast-ion distribution function calculated by the CQL3D Fokker-Planck

code differs from the measured spatial profile, presumably because the current version of CQL3D uses a zero-banana-width model. In addition, the effects of bursting instabilities on the fast ion distribution in neutral beam heated plasmas are examined. Fishbone events generally have a minor effect on the fast ion distribution and no clear correlation is observed in the NPA and SSNPA diagnostics. However, sawteeth or the combinations of fishbones and CAEs always cause neutron rate drops up to 25% and bursts at outer chords of the SSNPA, which indicate fast ion loss. It is also observed that high energy fast ions respond earlier than low energy fast ions.

Chapter 1

Introduction

1.1 Fusion Energy

Experts predict that fossil fuels will become depleted within the next fifty years even at the present consumption rate, while the global energy demand will double due to a rise in the world's population and higher per-capita consumption. To meet the increasing global energy demand and limit green house gas emissions, a new generation of energy production technologies is required. Fusion energy, which powers the sun and other stars, is being considered as one of the most promising candidates for the world's long-term energy supply because of its environmental benefits, safety of operation and abundant availability of the fuels [1, 2].

The basis for fusion energy is fusion reaction, in which light atomic nuclei are pushed close enough so that they combine and form heavier nuclei. The mass difference (Δm) between the reactants and products is converted to the kinetic energy (ΔE) of the products according to Einstein's famous formula $\Delta E = \Delta m c^2$, where $c = 3 \times 10^8$ m/s is the speed of light. Because of the enormous conversion factor c^2, a

small mass loss can create a large amount of kinetic energy. In order to make fusion reactions occur, the fuels must be heated up to 100 million degrees Celsius and held at high pressure long enough to overcome the Coulomb barrier between the reacting nuclei. At such high temperatures and high pressures, the fuel atoms are completely ionized and form a plasma, i.e. a mixture of electrons and fully stripped ions. The plasma must also be confined in order for fusion to take place. The sun and other stars use their huge gravitational force to squeeze the particles together, which is called gravitational confinement. However, on Earth, this is not feasible since the gravity of the earth is only 1/28 of that of the sun. Instead, the confinement can be achieved on earth via one of following two methods: inertial confinement and magnetic confinement [3]. In inertial confined fusion, powerful energy beams such as laser beams are used to compress the hydrogen fuel to an extremely high density and temperature in a very short time. The confinement of the fuel is based on the inertia of the pellet fuel mass, which resists the natural expansion when it is heated to thermonuclear fusion temperatures. On the other hand, in magnetic confined fusion, strong magnetic fields are used to confine the plasma, heated by ohmic heating and other means. Thermonuclear fusion occurs at a slow rate with continuous burning and addition of fuel. Research on controlled fusion started in the 1950s. Tremendous progress has been made since then although some extreme scientific and technological difficulties remain. As of the present, near break-even controlled fusion has been achieved in a few fusion devices around the world, such as JET, and TFTR (see, e.g. review in Ref. [4] and references therein), and this led to the joint international research and development project, International Thermonuclear Experimental Reactor (ITER) [5], with aims to introduce a full-scale demonstration fusion power plant in the mid 2030s and a commercial version capable of generating at least $1,000$ megawatts of electricity in the 2040s. As to inertial confinement fusion, it is less developed than magnetic confinement fusion with respect to the realization of a power plant and it faces some

challenges, including low repetition rates, expensive laser and optic upkeep [6, 7]. But it is expected to receive enhanced attention with the planned demonstration of inertial confined fusion ignition at the US National Ignition Facility (NIF) in $2010-2011$ and at the French Laser Mega-Joule (LMJ) in $2012-2013$ (see, e.g. review in Ref. [8]).

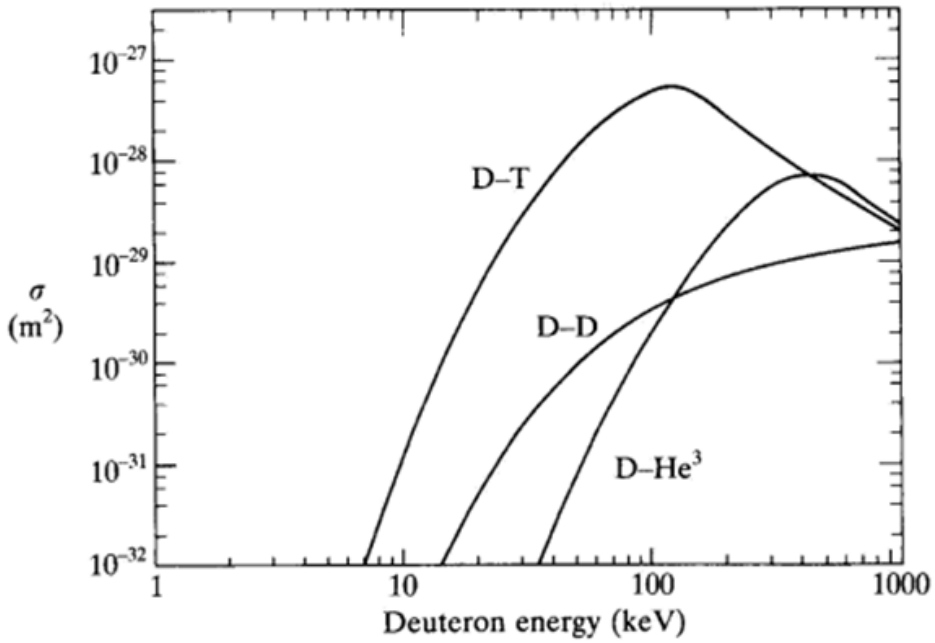

Figure 1.1: Fusion cross-sections vs deuteron kinetic energy for fusion reactions D-T, D-D and D-He^3. The two D-D reactions have similar cross-sections, the graph gives their sum. (Fig. 1.2.2 in Ref. [9])

Although there are numerous nuclear fusion processes that in principle could be used to deliver energy, only a few reactions are of practical value for potential energy production on the earth, which include

$$D^2+D^2 \rightarrow He^3\ (0.817\text{MeV})+n^1\ (2.45\text{MeV}) \tag{1.1}$$

$$D^2+D^2 \rightarrow T^3\ (1.008\text{MeV})+H^1\ (3.024\text{MeV}) \tag{1.2}$$

$$D^2 + T^3 \rightarrow He^4\ (3.517\text{MeV}) + n^1\ (14.069\text{MeV}) \tag{1.3}$$

$$D^2 + H_e{}^3 \rightarrow He^4 (3.67\text{MeV}) + H^1\ (14.681\text{MeV}) \tag{1.4}$$

The most favorable fusion reaction, as seen from Fig. 1.1, is the D-T reaction in Eq. (1.3) because it has the largest cross section (with its maximum lying at a lower energy than the other reactions) and largest released energy. In order to reach the "ignition" point where the fusion-born particles can heat the fuels and compensate for the heat losses, the D-T plasma must be heated to high temperature , eg. $10 - 20$ keV, and must be confined and satisfy the Lawson criterion [10]:

$$n\tau_E > 1.5 \times 10^{20}\ \text{m}^{-3}\text{s} \tag{1.5}$$

where n is the plasma density and τ_E is the energy confinement time. Figures 1.2 and 1.3 illustrate the progress in reaching the reactor regime in magnetic confinement and inertial confinement fusion. In present experiments, usually D fuel is used to avoid the large neutron flux produced in the reaction (1.3) as well as the T-handling. The D-D reaction can provide valuable information regarding the confinement of hot plasmas in D-T reaction.

Magnetic confinement fusion uses magnetic fields to confine the plasma and keep it away from the chamber walls. This is made possible by the Lorentz force which guides charged particles to move in helical trajectories around the magnetic field lines. This also acts to confine the charged fusion products (for example, helium nuclei, also known as alpha particles.). The produced neutrons have no charge and can pass freely through the magnetic field and penetrate the wall of the confinement chamber. These neutrons can be used to drive a thermal cycle to produce electricity.

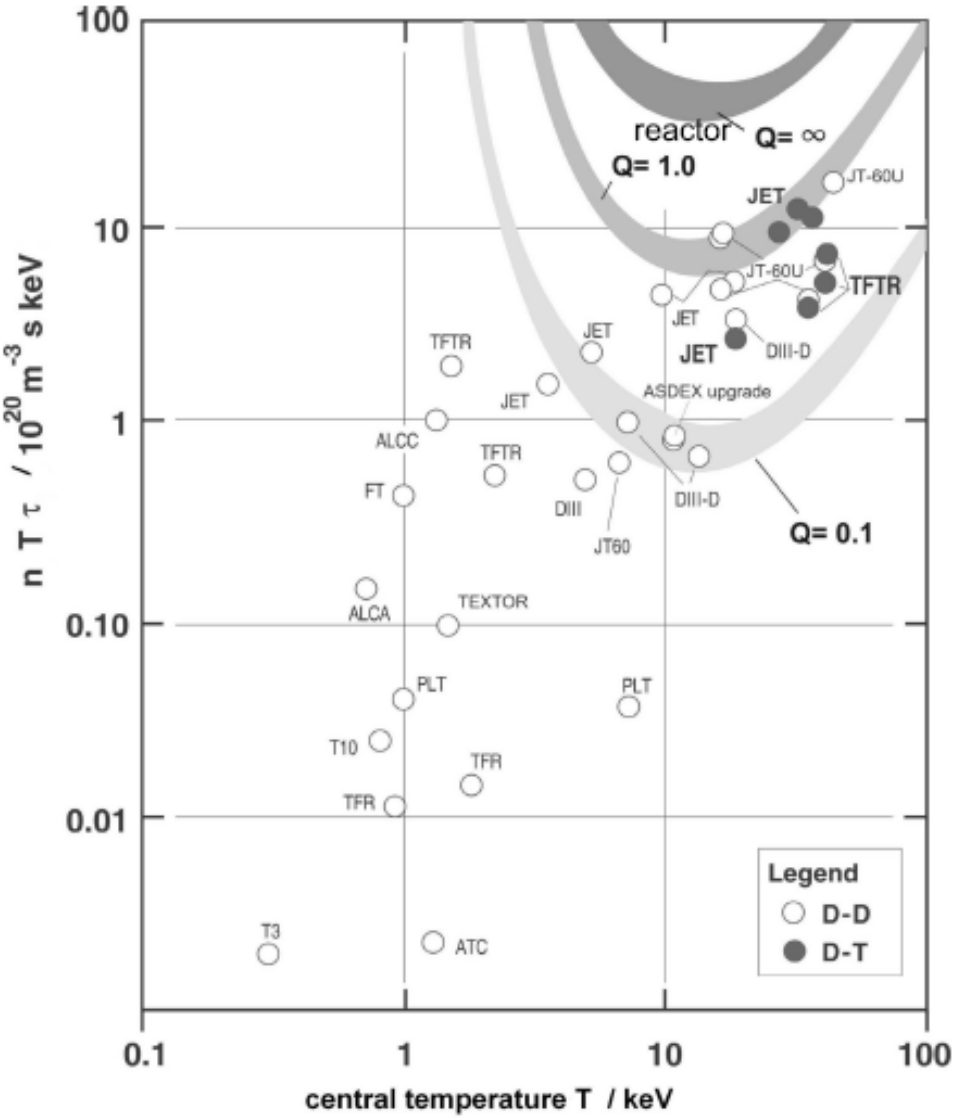

Figure 1.2: Compilation of $nT\tau_E$ progress in magnetic confinement fusion. Note that the Lawson criterion for magnetic confinement fusion is modified to $nT\tau_E > 3 \times 10^{21}\mathrm{m}^{-3}\mathrm{keVs}$ because the fusion reactivity is a function of temperature T. The next generation tokamak experiment, ITER, is expected to deliver ten times more fusion energy than the amount of energy needed to heat the plasma. (Reproduced from Fig. 1 in Ref. [4])

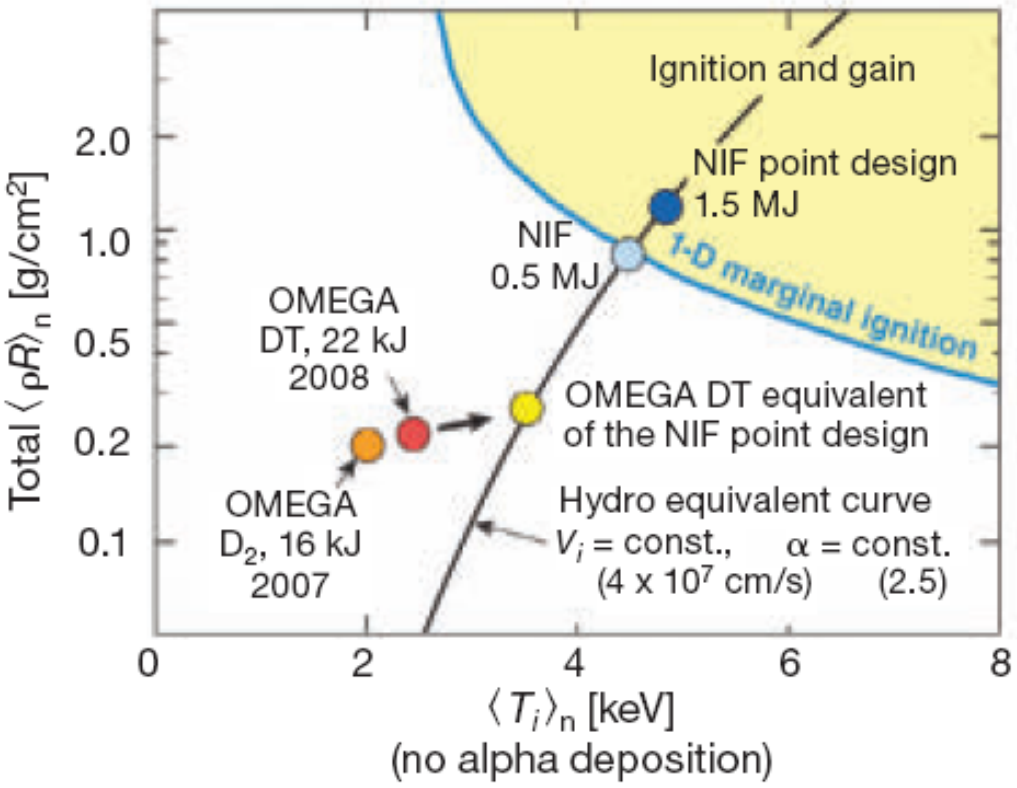

Figure 1.3: Progress towards ignition in inertial confinement fusion. Note that in inertial confinement fusion, the modified version of Lawson criterion is $\rho R > 1 g/cm^3$, where ρ and R are the fuel density and radius respectively. (From Ref. [11])

A toroidal topology for the magnetic field has been most successful for keeping the particles bound because of the avoidance of end losses by closing the surfaces formed by magnetic field lines.

1.2 Tokamaks

The word tokamak comes from Russian, which means toroidal chamber with magnetic field. The tokamak concept was first proposed in 1950s by two Soviet physicists Igor E. Tamm and Andrei D. Sakharov [12]. To date, the tokamak is the most advanced toroidal magnetic confinement concept and leading candidate for producing fusion in the future. The ITER tokamak is most likely the first system to be converted to a fusion reactor that is capable of producing thermal energy at the level of an electricity-producing power station. A comprehensive overview about tokamaks can be found in Ref. [9]. There are also some other magnetic confinement concepts and some may usurp the tokamak. For example, compared with tokamaks, stellarators have the advantages of not having the disruptive instability, not requiring current drive and being relatively easy to operate in steady state, but their coil system is technically complicated [13].

The tokamak is an axisymmetric doughnut-shaped device characterized by a strong magnetic field in the toroidal direction and a weaker poloidal magnetic field. The toroidal magnetic field is produced by the external coils wound around the torus in the poloidal direction. According to the Ampere's law, the toroidal magnetic field is proportional to $1/R$, where R is the distance to the main torus axis and is termed major radius as shown in Fig. 1.4 (b). (The radius of the plasma, a, is called the minor radius. The ratio of the major radius to minor radius is typically 3 for conventional tokamaks. The poloidal magnetic field is generated by plasma current, which is

induced through transformer action by a solenoid coil wound around the central axis. Typically, the poloidal field is approximately one order of magnitude smaller than the toroidal field. The combination of the toroidal field and poloidal field results in a helical magnetic field line structure around the torus. These fields and currents are illustrated in Fig. 1.4 (a). In addition to the toroidal and poloidal magnetic field, position control coils are used to control positions and the shape of confined plasma. They also play a basic role in the three dimensional toroidal stability. Generally, the plasma density, n_e, temperatures, T_e and T_i, and toroidal current density j_ϕ in tokamaks are all peaked functions of the minor radius r, falling to small values at the plasma boundary, where the edge plasma is in direct contact with a set of limiting structures (limiter plasmas) or is defined by a magnetic separatrix (divertor plasmas).

In order to attain the necessary temperatures in a fusion reactor, the tokamak plasma is first heated to temperatures of a few keV by the ohmic dissipation of the induced plasma current. However, since the classical resistivity of the plasma scales as $\mathrm{T}_e^{-3/2}$, ohmic heating is usually supplemented by other means of heating to reach ~ 10 keV. There are two main auxiliary heating methods. The first method involves the injection of energetic neutrals which is known as neutral beam injection (NBI). The energetic atoms penetrate the plasma and eventually give their power to it through collisions. The second approach utilizes high-frequency electromagnetic waves. If the waves have the correct frequency and polarization, their energy can be transferred to the charged particles in the plasma, which in turn collide with other plasma particles, thus increasing the temperature of the bulk plasma.

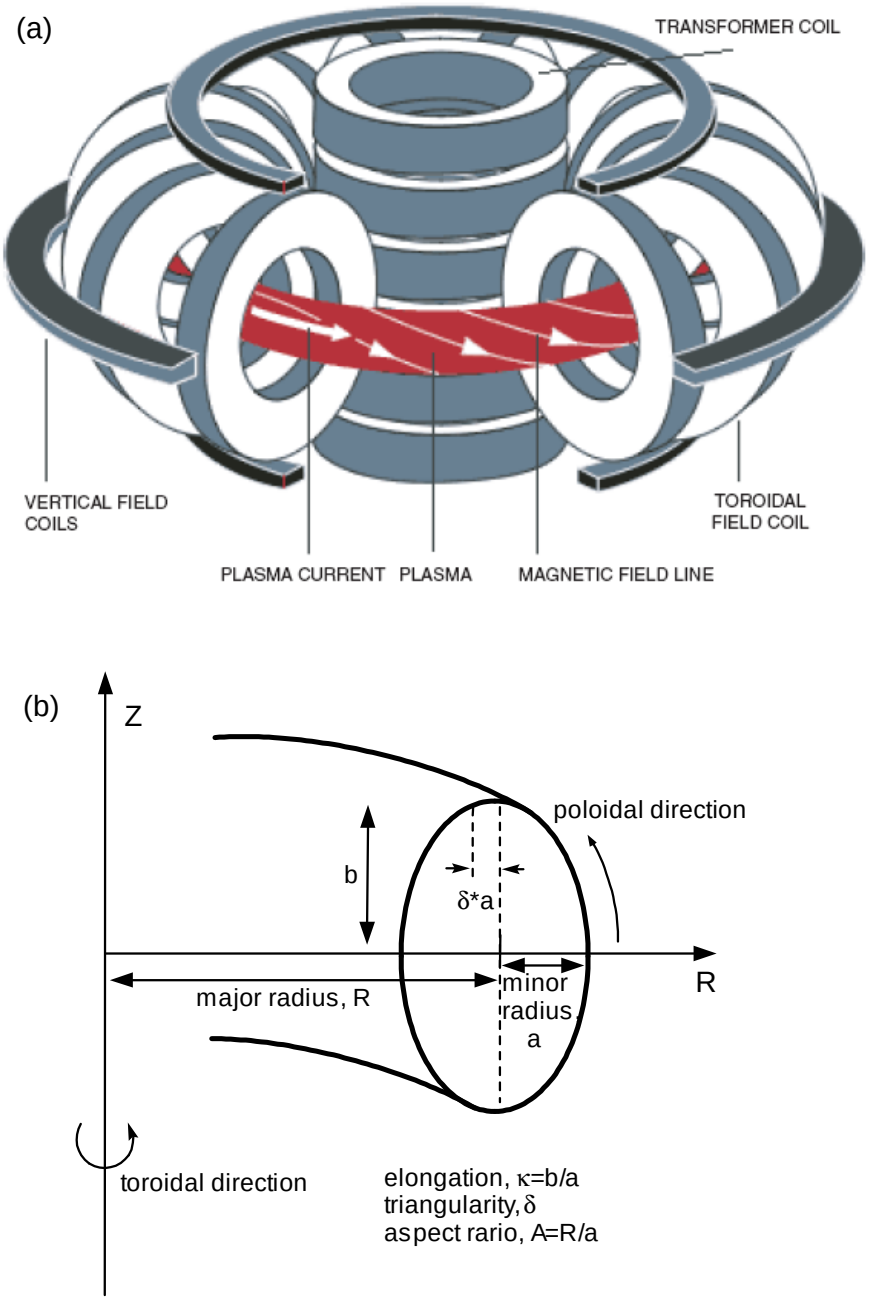

Figure 1.4: (a) Schematic of Tokamak (Fig. 2 (a) in Ref. [14]); (b) cross section of toroidal plasma.

1.3 Spherical Torus

The spherical torus (ST) is a tokamak with the central hole reduced to the minimum technically feasible size. (Thus the major radius is close to its minor radius.) While tokamak is often described as a large metal doughnut shell, the ST is more like a cored-out apple. The ST configuration was firstly proposed by M. Peng and D. J. Strickler in 1986 and it may have several advantages over a conventional tokamak [15]. One main advantage is the higher efficiency, which is measured in the value of the plasma parameter β_T ($\beta_T \equiv \frac{2\mu_0 <P>}{B_0^2}$, where P is the plasma pressure, and B_0 is the magnitude of toroidal magnetic field at the plasma geometric centre field) [16]. The toroidal magnetic field needed to keep the plasma stable in a ST can be a factor of 10 less than in a conventional tokamak carrying the same plasma current. Since the amount of fusion power is roughly proportional to the square of the plasma pressure and the cost of a fusion power plant will rise with the size and strength of the magnetic field coils, the ST concept can play an important role in the development of smaller and more economical fusion reactors. In addition, STs are predicted to be more stable due to maximization of the field line path over the inboard, or "good" curvature region, as shown in Fig. 1.5.

Generally, STs have low aspect ratio A ($A \equiv R_c/a$ where R_c is the major radius at the geometric center and a is the midplane minor radius), high plasma elongation κ (the plasma vertical extent divided by its horizontal extent), and high triangularity. They can access an expanded range of plasma parameters and operating regimes relative to conventional aspect ratio tokamaks. The first major ST experiment, Small Tight Aspect Ratio Tokamak (START), at UK, achieved $\beta_T = 40\%$, a world record in 1999 [18, 19].

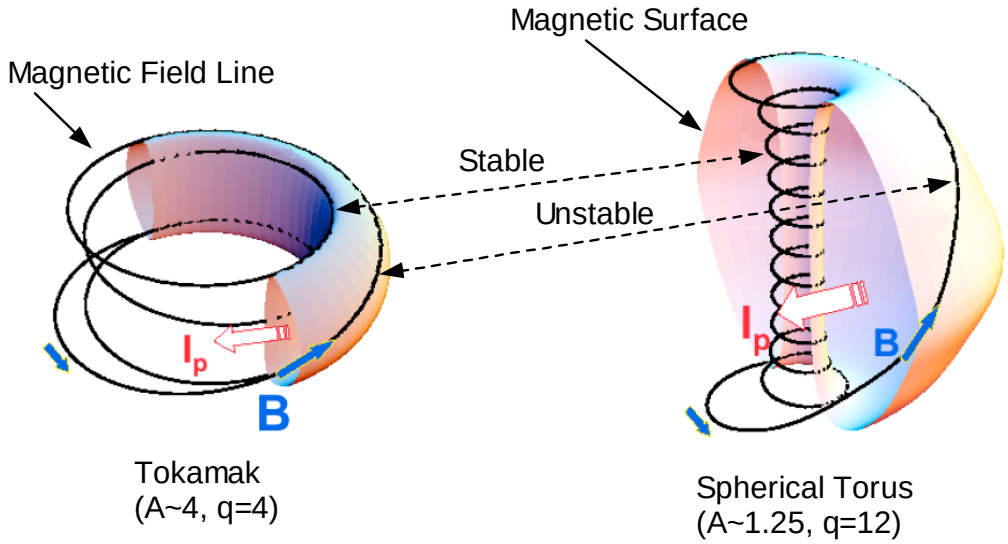

Figure 1.5: The shape and magnetic topology for a conventional Tokamak and a spherical torus. In the ST, a larger fraction of a magnetic field line is on the inboard (stable side of the device) than the tokamak. (Modified from Fig.2 in Ref. [17])

1.4 National Spherical Torus Experiment

The experimental research presented in this thesis was performed on the National Spherical Torus Experiment (NSTX) [20, 21] at the Princeton Plasma Physics Laboratory (PPPL) and the data were taken in 2007 and 2008 run campaigns. The NSTX is one of the two largest ST experiments in the world, the other one being the Mega-Amp Spherical Tokamak (MAST) [22, 23] at Culham, UK. The main mission of NSTX is to extend the understanding of toroidal plasma physics to high-β, low collisionality regimes at low aspect ratio, which are not available in conventional tokamaks [20, 24].

The NSTX is an ultra-low-aspect-ratio ($A \equiv R_0/a \simeq 1.26$) ST with nominal major and minor radii of $R_0 \simeq 0.85$ m and $a \simeq 0.67$ m, elongation up to 2.2 and triangularity up to 0.5. A schematic view of NSTX's cross section is displayed in Fig. 1.6. During the 2007 and 2008 run campaigns, NSTX is equipped with three co-injected

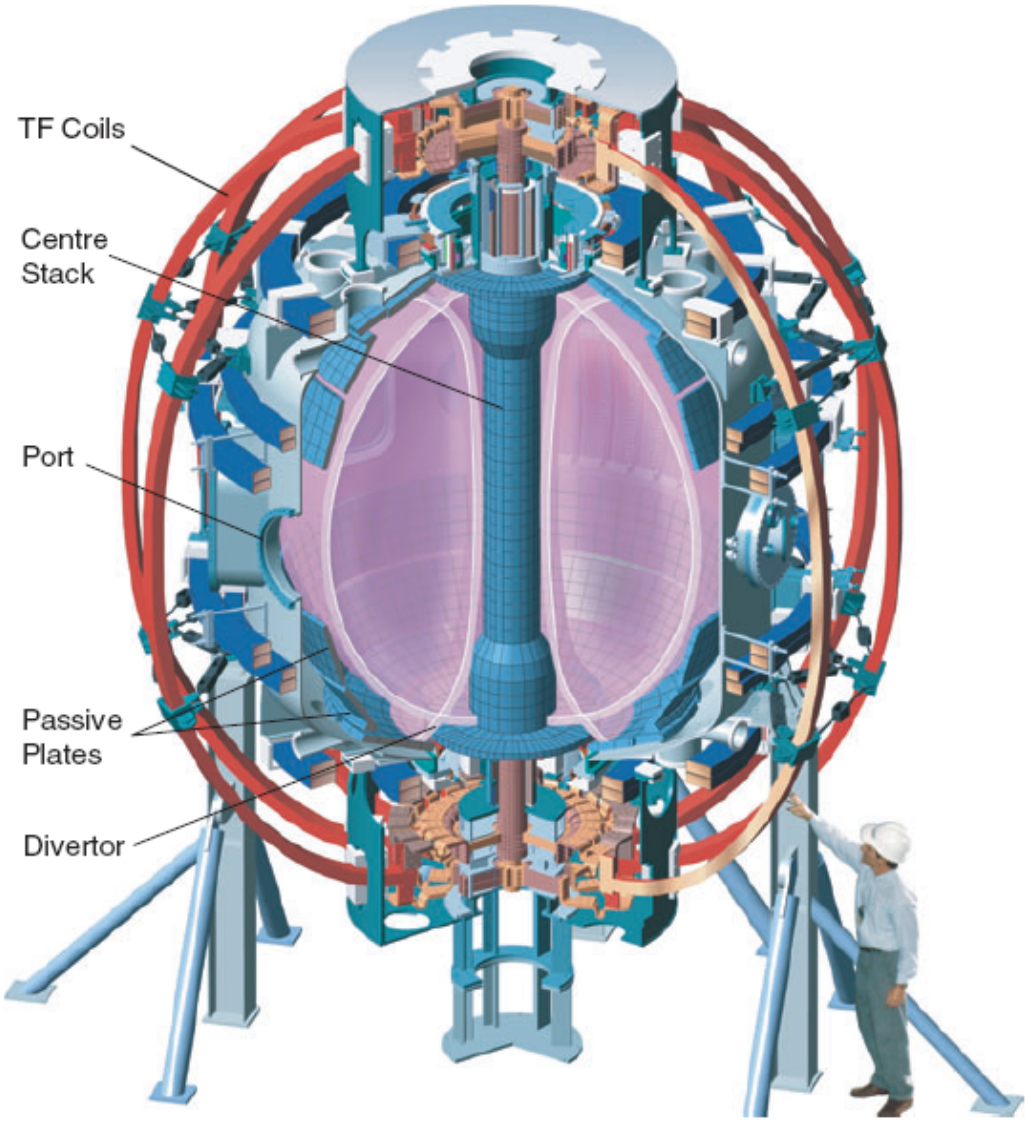

Figure 1.6: A cutaway view of the NSTX device. (Fig. 1 in Ref. [25])

Table 1.1: Comparison of plasma parameters in NSTX and DIII-D.

Plasma Parameters	**NSTX**	**DIII-D**
Major radius (R_0)	0.85 m	1.67 m
Midplane minor radius (a)	0.65 m	0.67 m
Aspect ratio (A$\equiv R_0/a$)	$1.25 - 2.5$	$2.5 - 5.3$
Plasma elongation (κ)	$1.7 - 3.0$	$1.0 - 2.6$
Plasma Triangularity (δ)	$0.3 - 0.8$	$\lesssim 1.0$
Toroidal magnetic field (B_T)	$0.3 - 0.6$ T	$0.6 - 2.2$ T
Plasma current (I_p)	1.4 MA	< 2.5 MA
Central electron density (n_{e0})	$1.5 - 8 \times 10^{19}$ m^{-3}	$\lesssim 1.0 \times 10^{20}$ m^{-3}
Central electron temperature (T_{eo})	$0.3 - 4$ keV	$\lesssim 6$ keV
Neutral beam power (P_{NB})	$\lesssim 7.5$ MW	$\lesssim 20$ MW
Ion cyclotron heating power (P_{RF})	$\lesssim 6$ MW	$\lesssim 3$ MW
Fast ion Larmor radius (ρ_f)	$\lesssim 20$ cm	$\lesssim 2$ cm
v_f/v_{alfven}	$1 - 4$	$0.4 - 1$

neutral beam (NB) sources and a 12-strap High-Harmonic-Fast-Wave (HHFW) heating system. These auxiliary heating systems strongly affect the plasma density and temperature range in NSTX. Typical plasma parameters in NSTX are shown in Table 1.1 and compared with a conventional tokamak named DIII-D [26] (The DIII-D plasma parameters from Ref. [27].). A more detailed description of the fusion device NSTX can be found in Ref. [20, 28] and a review of the NBI and HHFW heating systems and major diagnostics in NSTX will be given in Chapter 2.

1.5 Fast Ions

Fast ions in tokamaks refer to the ions with energies much higher than typical thermal ion temperature. They are usually generated from fusion reactions (for example, alpha particles produced from the deuterium-tritium (D-T) fusion reactions) and plasma heating systems such as neutral beam injection (NBI) and radio-frequency (RF) waves in the ion cyclotron (ICRF) and lower hybrid (LH) range of frequencies. Since fast ions are not in thermal equilibrium, their distribution function can not be simply described with a shifted Maxwellian distribution. Instead, it is generally a function of position $\mathbf{r}$, velocity $\mathbf{v}$, and time t. Fast ions born in nuclear reactions generally have a well defined initial energy. The spatial distribution is centrally peaked because both the plasma density and temperature peak on axis. The angular distribution is nearly isotropic. Hydrogenic fast ions created by NBI (usually Deuterium beam) have three energy components (known as the full energy, the half energy, and the third energy components). The initial pitch angle, defined as $\arccos(v_{||}/v)$ with $v_{||}$ the fast ion parallel velocity relative to the magnetic field, depends on the injection angle of neutral beams. The acceleration of fast ions by ICRF occurs in the perpendicular direction to magnetic field and around resonance layer(s). In this thesis, it mainly focuses on the fast ions that are generated from the NBI and RF heating systems.

Although the fast-ion density is generally one order of magnitude less than the background plasma density, fast ions can play an important role in several aspects of magnetic confined fusion. Fast ions are a major source of energy and momentum for the plasma. Adequate confinement of energetic ions is essential to provide efficient heating of the bulk plasma and achieve a high fusion power gain. Moreover, the fast-ion pressure and driven current can have a significant impact on macroscopic stability properties. Although dilute populations of fast ions often behave classically, intense fast ions can drive instabilities that redistribute or expel the fast ions from

the plasma, which can cause damage to in-vessel components or diagnostics. Fast ion physics, like the acceleration of fast ions by RF heating, losses or redistribution of fast ions due to magnetic field topology and fast-ion driven instabilities, have been extensively studied in conventional tokamaks and remain a hot topic in the fusion research. A comprehensive review of fast ion physics and diagnostics in conventional tokamaks is available in Ref. [29, 30, 31].

1.6 Thesis Objective and Organization

NSTX is an excellent testbed to study ITER relevant physics of fast ion confinement. The fast ions in NSTX have similar orbital parameters to the fusion α particles originating from D-T reactions in the next-step fusion devices such as ITER. Of particular importance for fast ion behavior and confinement in NSTX is the low toroidal magnetic field and its strong variation between the inboard and outboard plasma edges. As shown in Table 1.1, the toroidal magnetic field B_T is about $0.3-0.6$ T (compared to ~ 2 T in DIII-D) and it is comparable to the poloidal magnetic field. In conjunction with a relatively small major radius relative to the minor radius, the low toroidal field can alter the orbit topologies [32, 33] and particle drifts [34]. For example, the gyroradius ρ of an 80 keV deuterium ion in NSTX can be ~ 0.3 m at the outboard midplane of the plasma. This gyroradius is a large fraction of the 0.68 m minor radius of typical plasmas in NSTX. As a result, fast ion orbits in NSTX exhibit some features not seen in conventional tokomak orbits. For instance, banana orbits have larger radial excursion near the banana tip than near their midplane crossings, which is the widest part of the orbit in a conventional tokamak. Moreover, the large fast-ion gyroradius in NSTX can be comparable to the gradient scale length of the magnetic field, i.e. $\rho \nabla B/B$ is appreciable. This means that the fast-ion magnetic

moment μ may not be well conserved. However, due to the conservation of the canonical angular momentum, the net effect of the loss of invariance μ is relatively small and changes in magnetic moment are not expected to lead to a significant reduction in the confinement of co-injected beam ions in NSTX [34, 35]. In addition, NSTX is susceptible to fast-ion driven instabilities due to its relatively low toroidal magnetic field and the low aspect ratio. The Alfven modes can be easily excited in NSTX because the fast ion velocity is two to four times larger than the Alfven speed. The large Larmor radius of the fast ions compared to the minor radius can also enhance mode–particle interactions. A wide variety of Alfvėn eigenmodes (AEs) and Energetic Particle Modes (EPMs) have been observed in NSTX and some evidence of energetic ion losses or redistributions has been seen [36, 37, 38].

The main objective of this thesis is to gain better understanding about fast ion physics in ST using the newly developed 4-chord Solid State Neutral Particle Analyzer (SSNPA) array and 16-channel Fast-Ion D-Alpha (FIDA) diagnostics as well as the existing fast ion diagnostics in NSTX. The effort includes the diagnosis of fast ions created from or accelerated by the plasma heating systems, and comparisons with theories and simulations. The measurements in this work show that fast-ion density during combined NBI and HHFW is significantly enhanced in a very broad region and that the fast ion tail observed by the neutral particle analyzer in the previous work is from the passive charge exchange reactions at the edge. The quantitative comparison between measurements and simulations suggest that the large Larmor radius and banana width of fast ions could the fast ion spatial profile during HHFW heating. In addition, this work also examines experimentally the fast ion redistribution or loss in the presence of bursting instabilities.

The thesis is organized as follows. Chapter 2 reviews the main auxiliary heating systems as well as the existing plasma and fast ion diagnostics in NSTX. Chapter 3

contains a description of the newly developed fast ion diagnostic – SSNPA [39, 40]. Chapter 4 introduces the simulation code used in this work especially the development of FIDA_NPA simulation code. Chapter 5 presents the results of fast ion profile measurements during combined NBI and HHFW heating and comparisons with numerical modelling. The acceleration of fast ions during HHFW heating is clearly observed in many fast ion diagnostics. The measurements suggest that the fast ion tail observed by the NPA diagnostics is from the passive charge-exchange reactions at the edge due to their localization in velocity space and that fast-ion density is enhanced in a very broad region because of the multiple resonance layers and large orbits in a spherical tokamak. Some discrepancies between the measurements and simulations have been observed and they are likely due to the zero-banana-width assumption in theory. Chapter 6 shows the results of fast ion diagnostics during fishbone and sawtooth instabilities and explains why the sawtooth events have a bigger effect on fast ion confinement in NSTX. The thesis concludes with a summary and suggestions for future work in Chapter 7. Possible future fast ion experiments involving the FIDA and SSNPA diagnostics are discussed and reasonable upgrades for the SSNPA diagnostic are proposed.

Chapter 2

Plasma Heating Systems and Diagnostics in the National Spherical Torus Experiment

The NSTX device has mega-ampere plasmas for plasma physics and fusion research. In this chapter, the major plasma heating systems and diagnostics on NSTX are reviewed.

2.1 Plasma Heating Systems

The NSTX plasma first is heated to temperatures of a few keV by ohmic heating. It is further heated by two main auxiliary heating systems: Neutral Beam Injection (NBI) and High Harmonic Fast Wave (HHFW) heating.

2.1.1 Ohmic Heating System

Because the plasma can be regarded an electrical conductor, it is possible to heat the plasma by inducing a current through it. This is termed as ohmic heating (OH). The current is induced by slowly increasing the current through an electromagnetic winding coil linked with the plasma torus. In the mean time, the plasma torus can also be viewed as the secondary winding of a transformer.

The 962-turn OH coil system in NSTX consists of four layers which are double wound, forming a total of eight sub-windings which are electrically connected in series, but which are water cooled in parallel by eight individual cooling paths. Each winding is formed using extruded copper conductors with central passage for water cooling, and insulated using a B-staged kapton/epoxy glass composite. The coil is wound over a stainless steel tension tube, covered with Teflon. A detailed description of the ohmic heating system of NSTX is available in Ref. [28].

2.1.2 Neutral Beam Injection System

The Neutral beam injection (NBI) system in NSTX injects up to three beam lines of $60 \sim 100$ keV deuterium atoms into the plasma. These energetic neutral atoms are created by extracting positive ions from suitable ion sources, accelerating the ions to the high energies, and finally neutralizing the energetic ions by collisions with a gas target in a neutralizer. However, not only deuterons are created in the ion source, but also the deuterium molecular ions D^{+2} and D^{+3}. These molecular ions are also extracted, accelerated and dissociated in the neutralizer. Thus, the final neutral beam has three energy components known as the full, the half and the third energy components, respectively. The species fraction and power distribution depend on the specific conditions in the ion source. After passing through the magnet, which deflects

the non-neutralized ions, the neutral atoms are injected into the plasma through the duct. By undergoing charge exchange or electron/ion impact ionization reactions, the injected neutral atoms become ionized and are then confined by the magnetic fields. A small fraction of beam particles could pass through the plasma unaffected and impact the far vessel wall as a shinethrough beam. To protect the vessel wall, neutral beam armor was designed and installed to receive the shinethrough beam particles. A general description of the NBI system in tokamaks can be found in Chapter 5 of Ref. [9] and a detailed description of the NBI system in NSTX is available in Ref. [41]

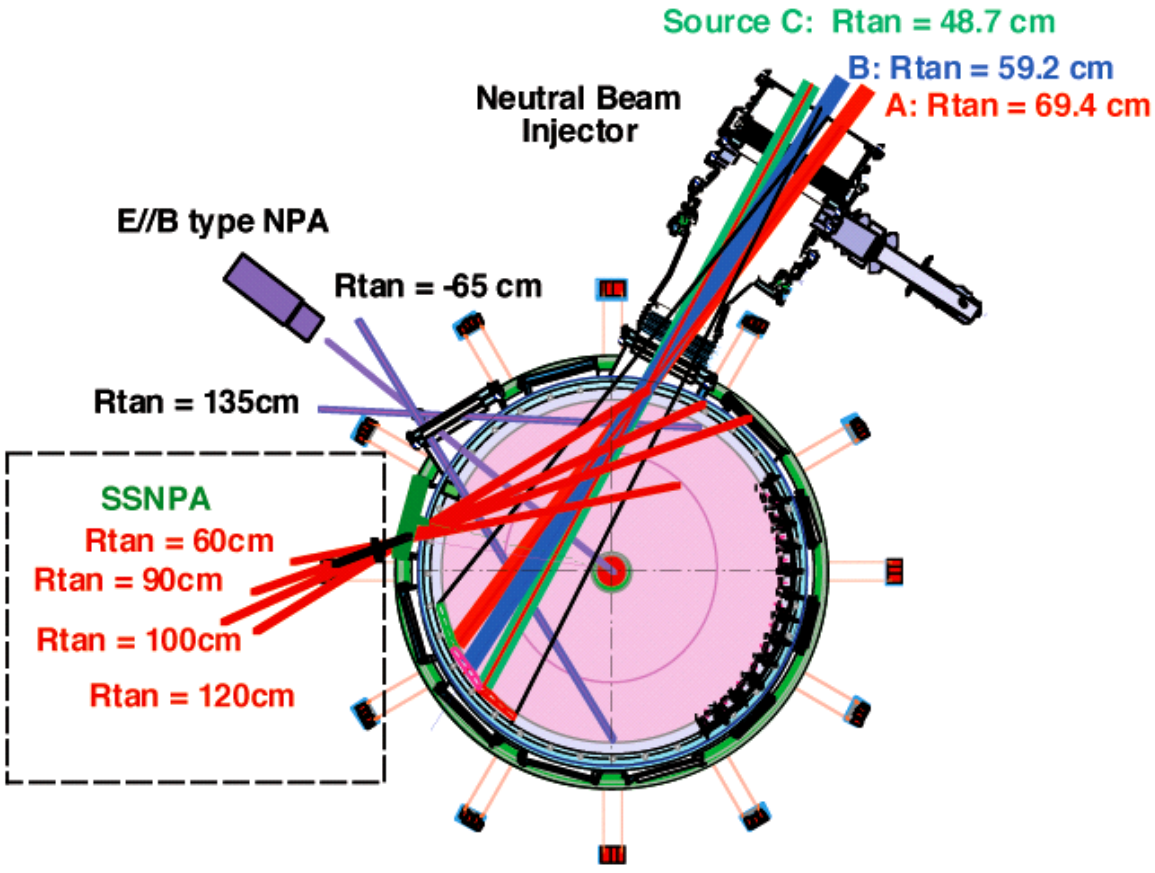

Figure 2.1: Layout of injection lines of three neutral beam sources in NSTX with solid state neutral particle analyzer array and E||B type neutral particle analyzer. (Fig. 3 in Ref. [39])

The NBI system in NSTX consists of three beam lines with tangential radii of 0.69 m (source A), 0.59 m (source B) and 0.49 m (source C) and a top view is shown in Fig. 2.1. A total power of 7.5 MW of D^0 can be deposited into the NSTX plasmas. The NBI system serves a variety of functions, including heating the plasma, fueling it, simulating the hot ion component that will escape from the plasma in a reactor, and acting as a critical component to various diagnostics that include the E||B type Neutral particle Analyzer (NPA), Sold State Neutral particle Analyzer (SSNPA), Fast-Ion D-Alpha (FIDA), Charge-Exchange Recombination Spectroscopy (CHERS) and Motional Startk Effect (MSE).

2.1.3 High Harmonic Fast Wave Heating System

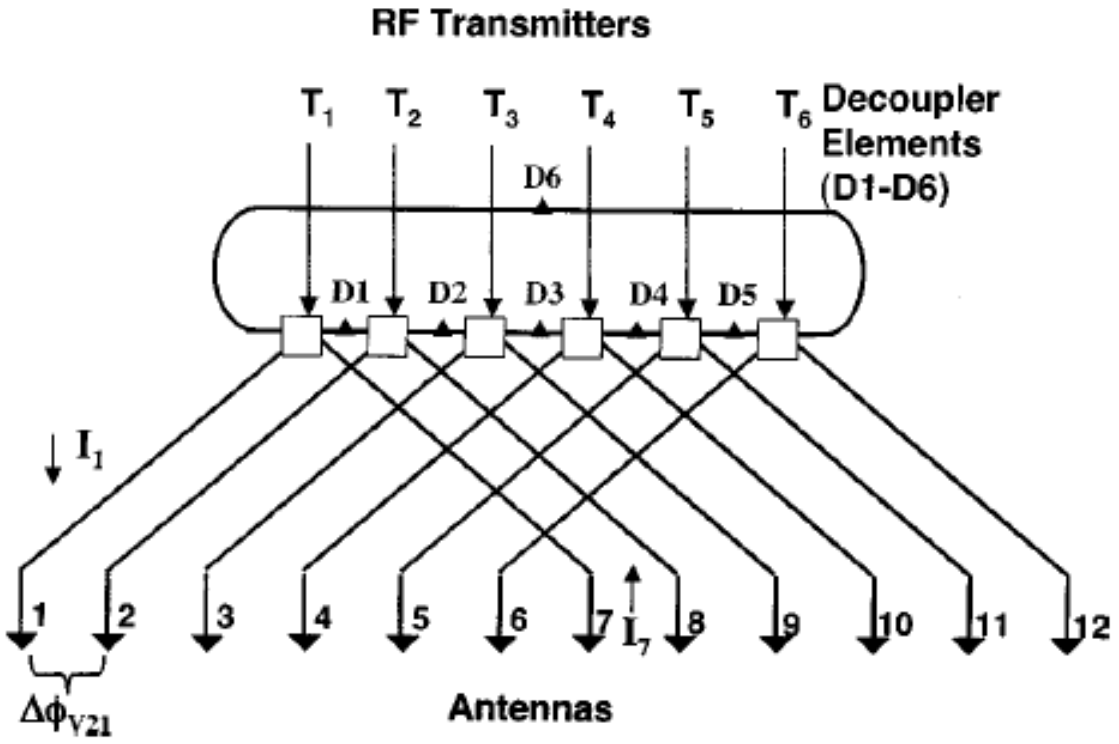

Figure 2.2: Schematic diagram of the rf distribution system showing the twelve antenna elements, the six RF inputs (T1– T6) and the splitting decoupling network (D1–D6). (Fig. 1 in Ref. [42])

The High Harmonic (> 10) Fast Wave (HHFW) heating system in NSTX is designed to provide electron heating and current drive for the NSTX plasmas. The system is a 12-element array, fed by six transmitters, which subtends almost a full toroidal quadrant of NSTX. Each of the twelve straps is 0.85 m long by 0.075 m wide and is protected by a molybdenum Faraday shield and a boron nitride shield. The six Radio Frequency (RF) transmitters operate at a frequency of 30 MHz, corresponding to the 15th harmonic of the ion cyclotron resonant frequency at B_T=3 kG. The RF power is split and fed to the antenna such that the phase between the first 6 straps is arbitrary and controlled at the generator while a strap in the second 6 will be π out of phase with its partner in the first 6. A schematic of the power dividing and decoupling network is shown in Fig. 2.2. A detailed description of the HHFW system in NSTX is available in Ref. [28]

Theoretical analyses and modelling calculations suggest that the HHFW power absorption can be one to two orders of magnitude larger in the NSTX parameters than in conventional tokamaks [43]. Theoretically, the strong absorption together with the real time antenna phasing capability allows efficient current drive by HHFW.

2.2 Major Diagnostics

The NSTX is equipped with many advanced diagnostics for the purpose of the understanding of NSTX plasmas. Plasma parameters (electron density, electron temperature, ion temperature, and impurity and rotation information) are monitored by the Thomson scattering diagnostic and charge exchange recombination spectroscopy. The magnetic structure is diagnosed by a set of Mirnov coils and the internal plasma behavior is monitored by the soft X-ray diagnostic. They can provide useful information for the study of plasma instability and confinement. Fast ion diagnostics include

neutron detectors, a fast ion loss probe, an E||B type neutral particle analyzer, a 4-chord solid state neutral particle analyzer array, a 16-channel fast-ion D-alpha diagnostic and a fast ion loss probe. In this section, a brief review of these diagnostics is given in this section since they are extraordinarily useful over the experiments in this thesis. More Detailed descriptions of the various diagnostics in NSTX can be found in Ref. [25]. The hardware project of this thesis, solid state neutral particle analyzer array, will be described in Chapter 3

2.2.1 Thomson Scattering Diagnostic

The Multipoint Thomson Scattering (MPTS) diagnostic in NSTX provides time-resolved electron temperature and density information at 30 radial locations. The electron temperature is calculated from the Doppler broadening of the scattered light and the electron density is determined from the amount of light scattered. A detailed derivation of the theory behind this diagnostic technique is available in Ref. [44].

The MPTS system in NSTX currently uses two 30-Hz Nd:YAG lasers, which are directed through the machine on the horizontal midplane. Part of the laser system is illustrated in Fig. 2.3. Because the equilibria for high beta in NSTX tend to have flux surfaces compressed on the outboard side of the plasma, the MPTS system uses a backscattering geometry (Fig. 2.4). This geometry gives nearly full radial coverage on the horizontal midplane, with high sensitivity and high spatial resolution at the outer edge. The scattered light is collected by a spherical mirror optics and is imaged on a curved array of 36 fiber-optic bundles. The bundles transport the imaged light to filter polychromators, which are housed in an accessible, shielded room near the lasers. A detailed description of the MPTS diagnostic in NSTX can be found in Ref. [45, 46]. The spatial resolution from the MPTS system is about 1.0 cm at the

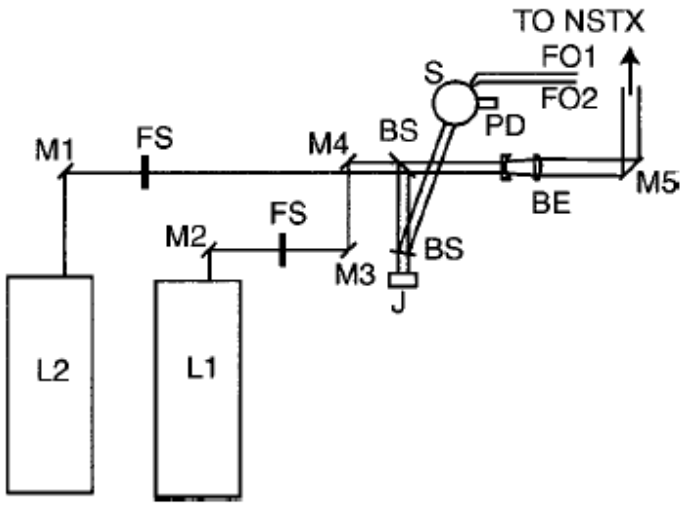

Figure 2.3: Laser systems of the MPTS system. Laser beams from Nd:YAG lasers L1 and L2 are combined side by side with mirrors M1–M4. Two fast shutters (FS) release the beam for delivery after warming up. Energy monitoring is done through beam splitters (BS). The main beams enter expanding doublet BE before being reflected off mirror M5 toward NSTX. (Fig. 1 in [45])

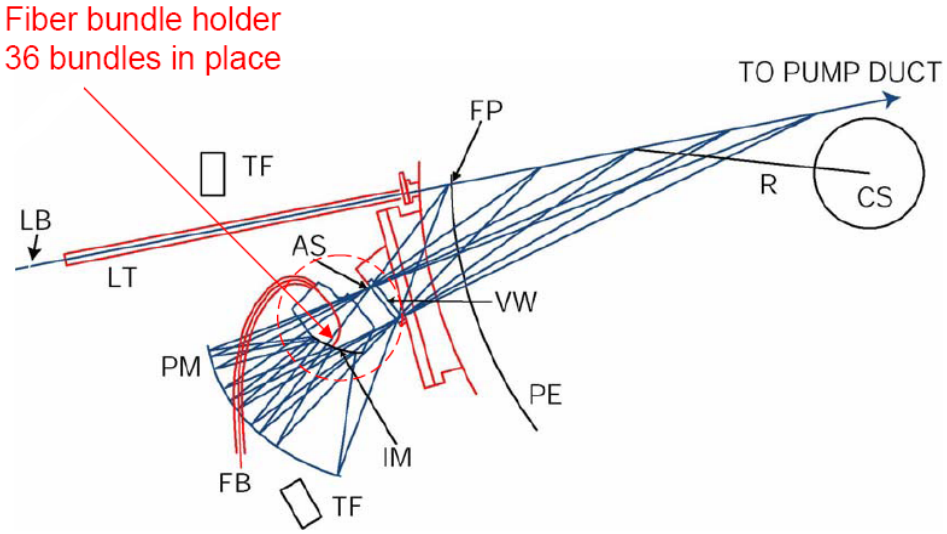

Figure 2.4: Collecting optics of the MPTS system. Spherical mirror PM images laser path onto surface IM, where the fiber bundle (FB) collects light. Only one out of 36 bundles is shown. Aperture stop (AS) is located next to the vacuum window (VW). The optics sees the main plasma and scrape-off layer. (Fig. 2 in Ref. [45])

plasma outer edge, $3-4$ cm at the magnetic axis, and $8-10$ cm at the inner edge [46]. The system is capable of accurate measurements of the electron temperature from less than 5 eV to greater than 5 keV for plasma densities ranging from less than 1×10^{18} m^{-3} to more than 1×10^{20} m^{-3} [47]. The absolute calibration of the density measurement for each channel is performed by Rayleigh scattering measurements [48].

2.2.2 Charge Exchange Recombination Spectroscopy

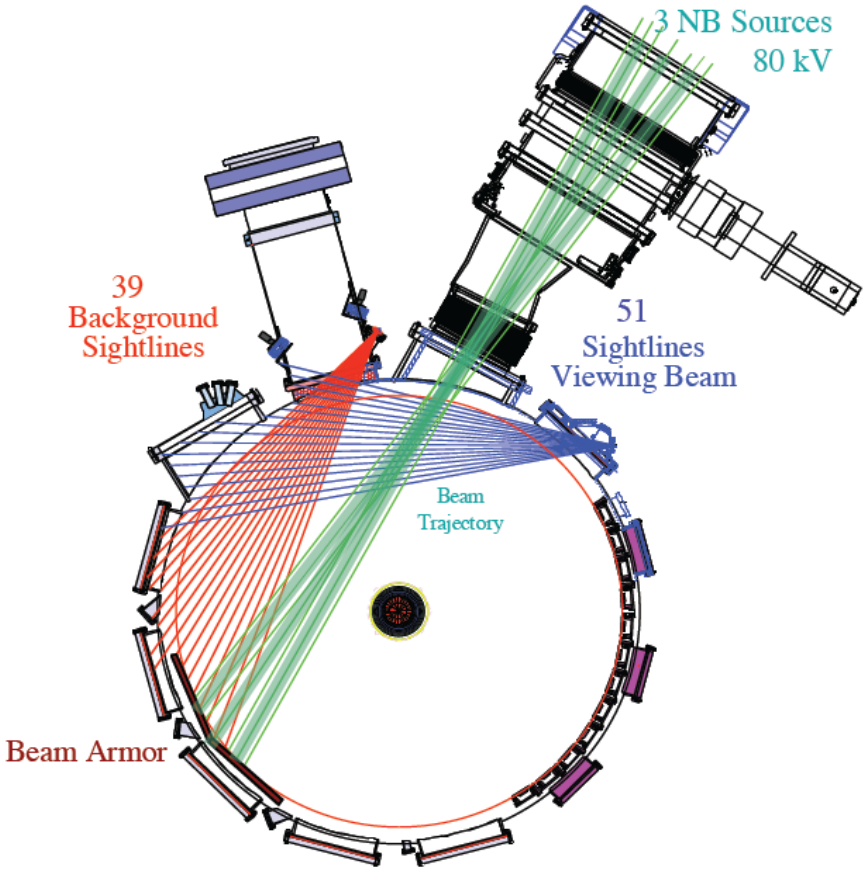

Figure 2.5: CHERS viewing geometry. (From Ref. [49])

The Charge Exchange Recombination Spectroscopy (CHERS) diagnostic provides profile measurements of ion temperature T_i, toroidal rotation $V\varphi$, and carbon density N_{carbon} [25, 50]. The diagnostic utilizes the C VI ($n = 8-7$) line at the optic

wavelength of 529.1 nm emitted by the ions that are excited by charge exchange collisions with the injected beam atoms. Currently, 51 midplane sightlines intersect the neutral beams nearly tangent to the flux surfaces for good radial resolution and 39 background sightlines are used to measure the contribution due to edge emission with views adjacent to the three NSTX neutral beam sources. The layout of the sightlines is shown in Fig. 2.5. The time resolution of the system is 10 ms and the spatial resolution ranges from ~ 0.5 cm at the edge to ~ 3.0 cm in the core [25]. A vertically viewing CHERS system also became available starting from the 2009 run campaign.

2.2.3 Motional Stark Effect Diagnostic

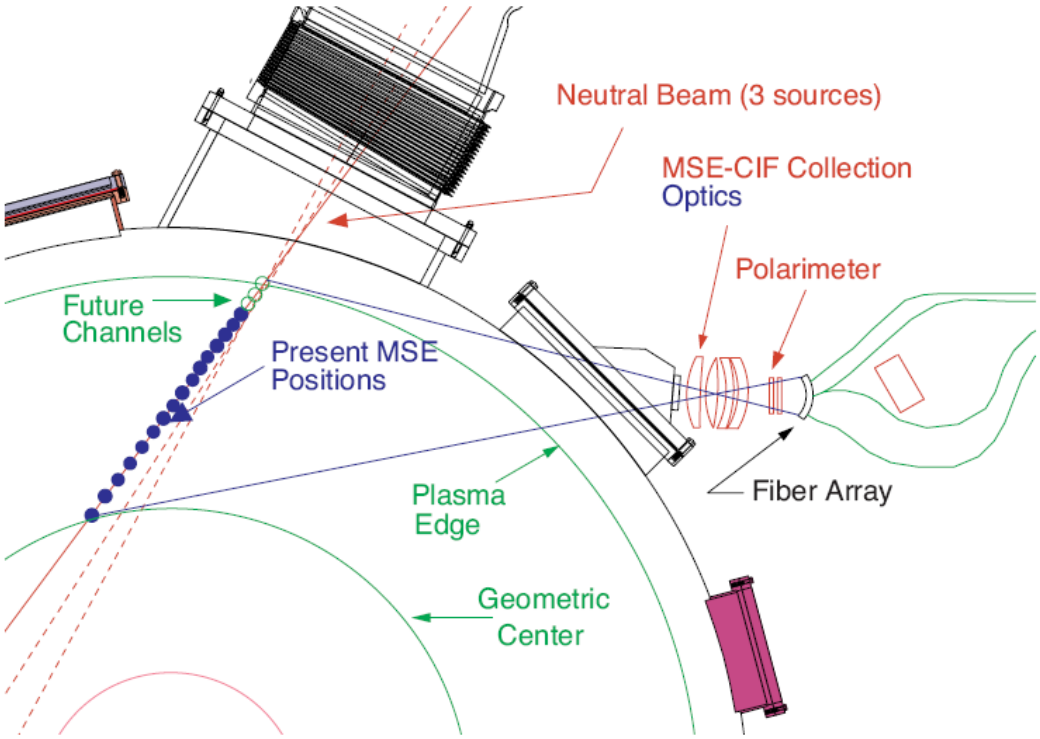

Figure 2.6: Plan view of the MSE-CIF diagnostic layout on NSTX. (Fig. 6 in Ref. [51])

The Collisionally-Induced Fluorescence Motional Stark Effect (MSE-CIF) diag-

nostic in NSTX provides internal magnetic pitch angle measurements for equilibrium reconstruction [51] (Fig. 2.6). The system relies on the motional Stark effect [52, 53] from the Lorentz electric field, $\mathbf{E} = \mathbf{v} \times \mathbf{B}$, as an energetic neutral hydrogenic atom passes across a magnetic field. (The Stark effect causes a splitting of spectral lines of the neutral atom with the shift proportional to the magnetic field.) The MSE system in NSTX uses a novel optical design that reduces the geometric Doppler broadening, and a high throughput, high resolution, and narrow bandpass Lyot filters to operate at low magnetic field. The system presently has 19 channels that spread from $10 - 20$ cm inboard of the magnetic axis to near the outboard edge of the plasma. The system has a spatial resolution of $2 - 3$ cm and a time resolution of 5 ms. A complete description of the NSTX MSE diagnostic is available in Ref. [51]

2.2.4 Mirnov Coil Arrays

The NSTX uses a comprehensive set of 1-dimensional and 2-dimensional magnetic pickup coils ("Mirnov coils") to measure local magnetic flux fluctuations. The MHD mode numbers can be inferred from the phase difference between the Mirnov coils located at different poloidal and toroidal positions. The full set of signals with other magnetic measurements is used for equilibrium reconstruction with the EFIT code [54]. The Mirnov coils are also used in combination with the arrays of ultra-soft X-ray detectors for characterizing MHD instabilities.

2.2.5 Soft X-Ray Arrays

The soft X-ray emissivity strongly depends on electron density and temperature; therefore, measurements of soft X-ray emissions can provide valuable information for the study of MHD phenomena (fishbone and sawtooth in particular) and impu-

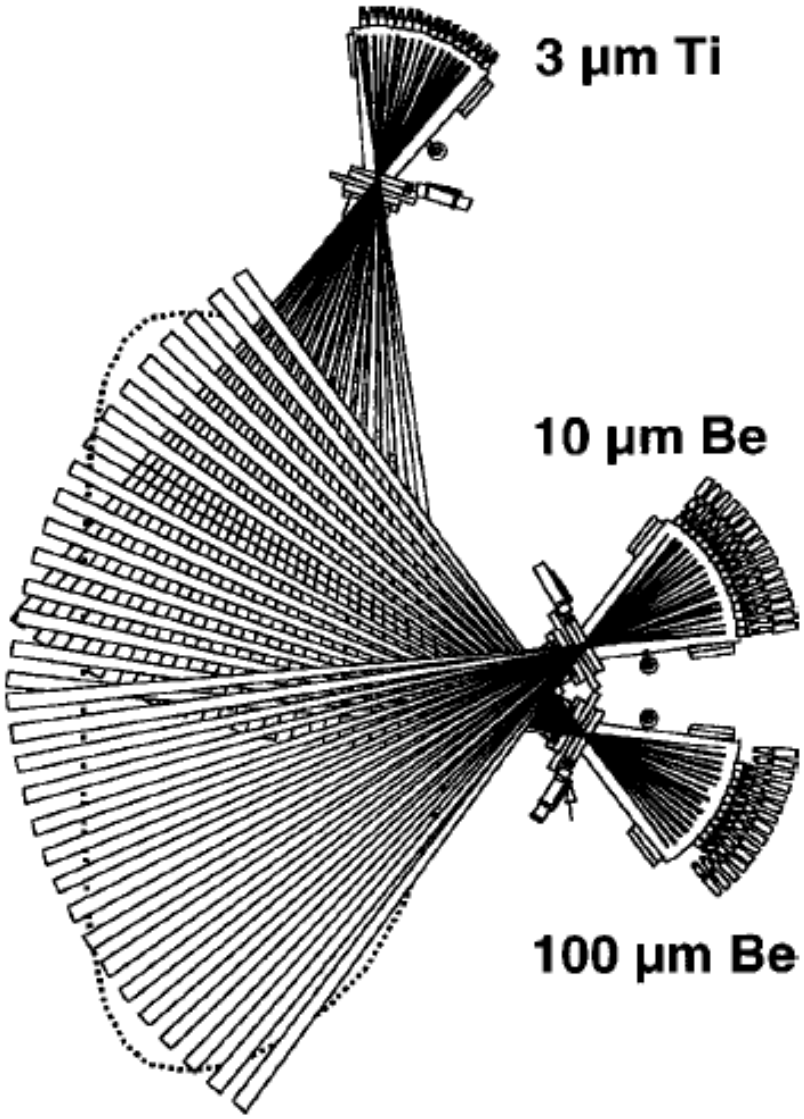

Figure 2.7: Layout of the Ultrasoft X-ray (USXR) system on NSTX. (Fig. 2 in Ref.[55])

rity transport effects. The NSTX ultrasoft X-ray (USXR) system [55, 56] has three broadband filtered arrays of absolute photodiodes: two are located at midplane ports viewing the upper and lower halves of the plasma, and the third is mounted on a top flange, viewing the plasma from above. The sightlines and locations for the USXR arrays are shown in Fig. 2.7 The system has good spatial and temporal resolution of ∼a few cm and several ms respectively, but a low-energy resolution of ∼hundreds of eV [55]. The arrays can be independently filtered in several spectral ranges, being mainly used for imaging of MHD fluctuations up to 100 kHz in the plasma core and periphery.

2.2.6 Neutron Detectors

The neutron detectors on NSTX consist of both ^{235}U fission chambers and plastic scintillators. They give an absolutely-calibrated measure of the volume-averaged 2.5 MeV neutron rate R_n from the D-D fusion reactions between NB ions and bulk plasma ions. During beam injection, the beam-plasma reaction rate is typically one order of magnitude larger than the beam-beam or thermonuclear rate. The emission rate R_n depends strongly on the density of high-energy, centrally confined fast ions due to the energy dependence of the fusion cross-section and to the higher density of target ions in the plasma core. Thus the neutron rate is a measure of the fast ion population in the plasma.

2.2.7 Fast Ion Loss Probe

The scintillator based energetic ion loss detector in NSTX [57] measures the pitch angle and gyroradius of the lost ions as a function of time. The probe acts as a magnetic spectrometer, using a pair of apertures and the confining magnetic field of

the plasma to disperse the lost fast ions onto a scintillator plate, where their strike points are determined by their individual pitch angle and gyroradius. The luminosity pattern on the scintillator plate is imaged by a fast framing rate intensified video camera.

2.2.8 E||B Type Neutral Particle Analyzer

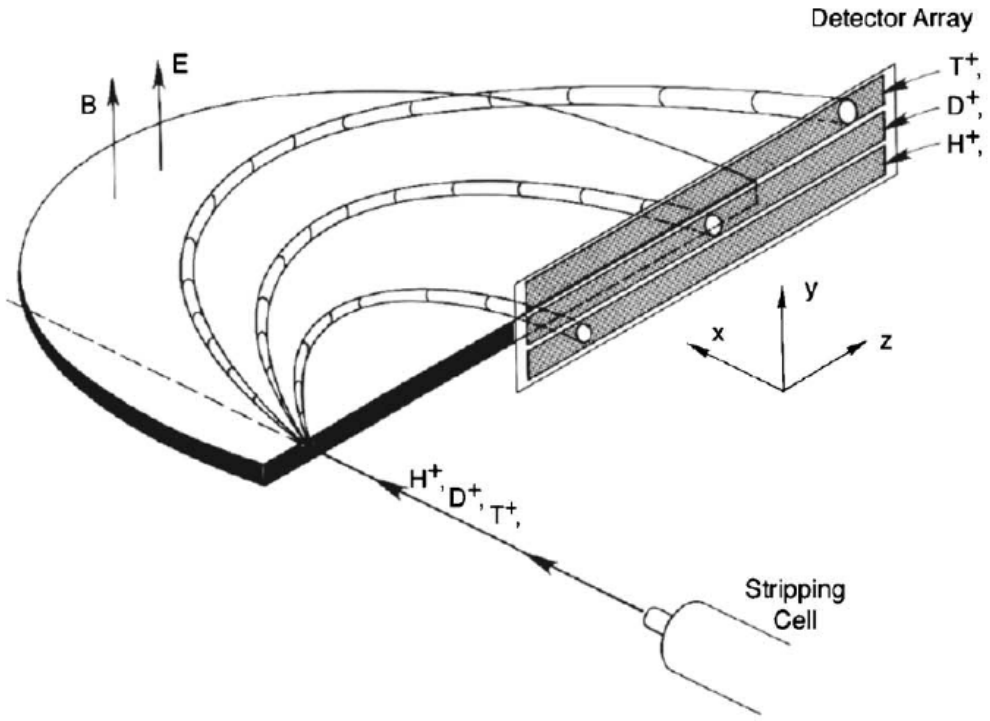

Figure 2.8: Illustration of the E||B spectrometer concept. After reionization of the charge exchange neutrals in the stripping cell, the ions enter perpendicularly into a semicircular region of parallel magnetic and electric fields and emerge energy dispersed into linear, mass-resolved rows on the detector plane.(Fig.1 in Ref.[58])

The Neutral Particle Analyzer (NPA) diagnostic is widely used in fusion devices to get the line-integrated fast ion density distribution by measuring charge exchange neutral particles escaping from plasmas. An overview of the developments in the instrumentation and application of charge exchange neutral particle diagnostics is avail-

able in Ref. [59].)The E||B type NPA diagnostic in NSTX is thoroughly described in Ref. [60] with the layout shown in Fig. 2.1. The system utilizes a PPPL-designed E||B spectrometer [58] (in a D-shaped parallel electric and magnetic field configuration), illustrated in Fig. 2.8, to discriminate between different ion species and record their energy spectra. The detector consists of a large-area microchannel plate which is provided with two rectangular, semi-continuous active area strips, one coinciding with each of the mass rows for detection of H^+ and D^+ respectively. Each mass row has 39 energy channels. The time resolution of the E||B type NPA diagnostic is ~ 1 ms and the energy resolution varies from $\Delta E/E = 7\%$ at low E to $\Delta E/E = 3\%$ at high E with calibrated energy range E from 0.5 to 150 keV. The E||B type NPA diagnostic can scan both horizontally and vertically on a shot-to-shot basis to map the fast ion energy distribution in both space and pitch angle.

2.2.9 Fast-Ion D-Alpha Diagnostic

$$D^0 + D^+ \Longrightarrow D^+ + D^{0*} \Longrightarrow D^+ + D^0 + \gamma \tag{2.1}$$

The Fast-Ion D-Alpha (FIDA) diagnostic is a type of charge exchange recombination diagnostic [61]. It measures the D_α light emitted by fast ions that neutralize when they pass through a heating beam and undergo $n = 3 \rightarrow n = 2$ transitions (see Eq. 2.1 and Fig. 2.9). Since the Doppler shift of the D_α line depends on the energy component of fast ions along the viewing channel, the FIDA diagnostic performs an effective average in velocity space over this and higher energies. The FIDA diagnostic in NSTX has two complementary instruments: a spectrometer-based FIDA system (s-FIDA) and a filter-based FIDA system (f-FIDA). The s-FIDA system has good spatial and spectral resolutions of 5 cm and 10 keV, but a temporal resolution limited to 10 ms. The f-FIDA integrates the D_α light over a convenient spectral range and it is aimed at high temporal resolution of <1 ms, but with limited spatial and

energy resolutions. Each channel of the two systems consists of two paired views, spaced toroidally by 30°, intercepting and missing the NB at the same radial location (see Fig. 2.10 (a)) and they are called active views and passive views respectively. The net signals from fast ions can be obtained either from the difference between active and passive views or from active views using the beam modulation technique. All the FIDA data used in this paper are from the 16 active channels with background subtraction obtained through beam modulation. Since the FIDA signals are proportional to the product of injected neutral density and the fast-ion density, the wavelength-integrated (or energy-integrated) FIDA signals are usually divided by the injected neutral density (as calculated by a pencil-beam code) to obtain "FIDA density" [62]. More details about the FIDA concepts and diagnostic in NSTX can be found in Ref. [61, 62, 63]

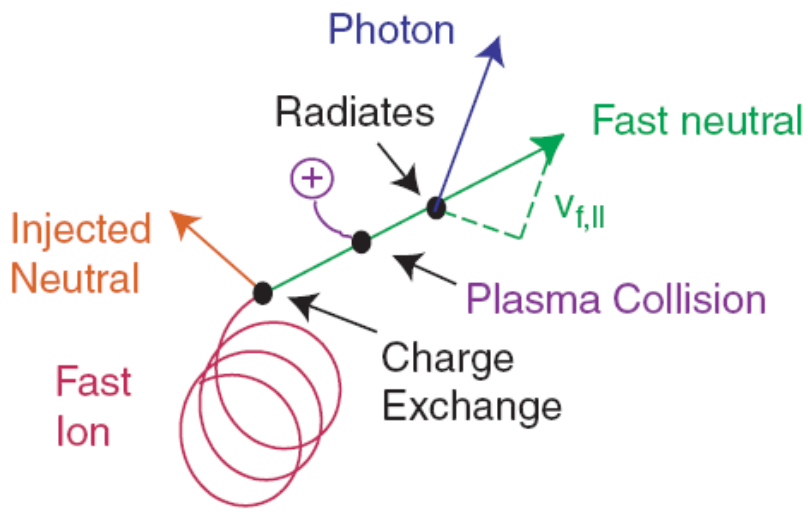

Figure 2.9: Three types of atomic processes are involved in the emission of a photon by a fast ion. The first reaction is a charge-transfer event between an orbiting fast ion and an injected neutral. The second reaction is the changes in energy levels caused by the collisions between the neutralized fast ion and the plasma. The third reaction is the atomic transition that produces the measured photon. The Doppler shift of this photon is determined by the component of the fast-ion velocity in the direction of observation, v_f. (Ref. 8 (a) in Ref. [61])

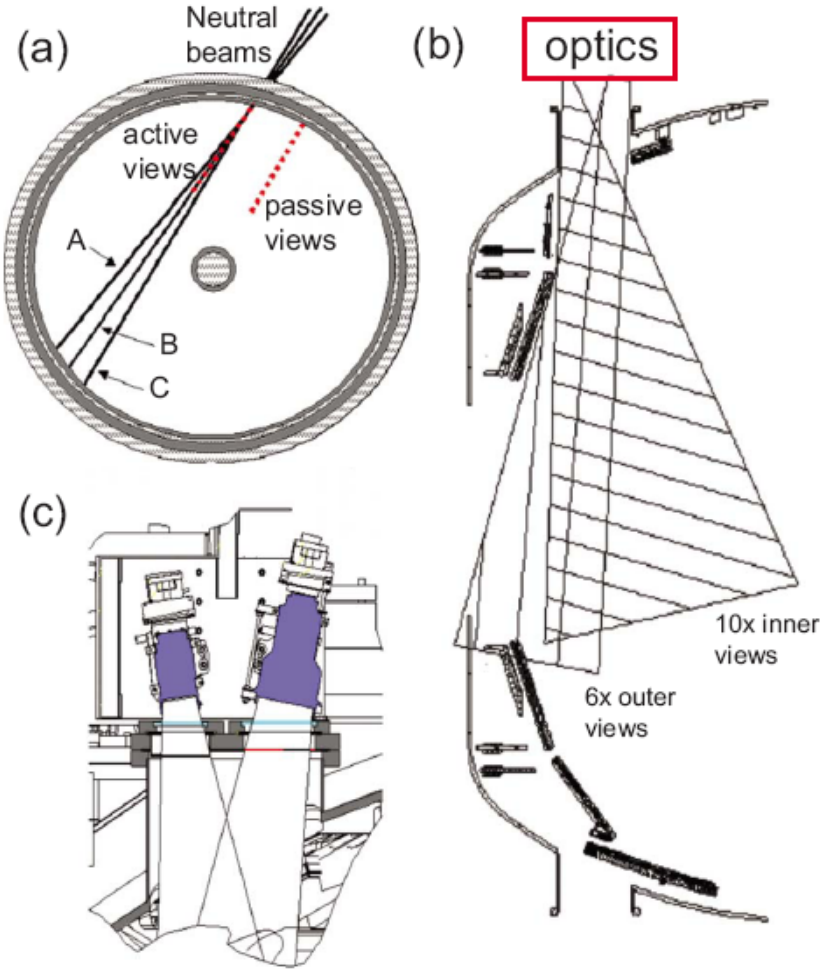

Figure 2.10: (a) Equatorial cross section of NSTX showing the paths of the three NB sources A, B, and C and the location of the FIDA active and passive views. (b) Poloidal cross section and field of view of the "top" lenses, used for the s-FIDA views, highlighted. The "bottom" lenses, used for the f-FIDA fibers, are symmetric with respect to the equatorial plane. (c) Details of the two lenses installed at each of the four ports occupied by the FIDA views.(Fig. 1 in Ref. [62])

Chapter 3

Solid State Neutral Particle Analyzer

In this chapter, a detailed description of the newly developed Solid Sate Neutral Particle Analyzer (SSNPA) array is given. This SSNPA diagnostic is the main hardware part of this thesis project and involves several innovations, such as post-shot analysis and noise reduction techniques, which are important for the successful operation of the diagnostic in NSTX's challenging plasma environment. The SSNPA array on NSTX consists of four chords with tangency radii of 60, 90, 100, and 120 cm that view across the three co-injection neutral beam lines (Fig. 2.1). Each chord utilizes a silicon photodiode that is coupled to fast digitizers to measure the energy distribution of charge-exchange fast neutral particles from 35 to 120 keV. The system has an energy resolution and time resolution of 10 keV and 5 ms respectively.

The rest of this chapter is divided into five sections. First, the working principles and the advantages of the SSNPA diagnostic are discussed. Second, the SSNPA setup, noise reduction techniques and fast digitization of raw signals are described.

Third, the software-based pulse height analysis, calibration results, and noise analysis are given. Fourth, it explains the sources of the SSNPA signals and compares the characteristics of the NPA diagnostics with other fast ion diagnostics. Finally, the measurements of the SSNPA diagnostic in quiescent plasmas prove that it works properly in NSTX. Part of this chapter is published in Refs. [39, 40].

3.1 Working Principles

Neutral Particle Analyzer (NPA) diagnostic is a well established diagnostic tool used to infer the fast-ion energy and spatial distribution inside the plasma. As shown in Sect. 2.2.8, the traditional E||B type NPA uses a stripping cell to reionize the neutrals and electric and magnetic fields to deflect the particles on to a microchannel plate detector. But the large size and high cost of this diagnostic make it difficult to build a multichannel system. Recently, compact semiconductor detectors[64] (natural diamond detectors (NDDs) and silicon diodes) have been proposed as an alternative way of measuring the energy of charge exchange particles and have been tested on several magnetic fusion experiments [65, 66, 67, 68, 69, 70, 71]. The working principle is simple. When a particle hits a semiconductor detector (for example, a silicon detector), it produces a pulse of electron-hole pairs and form a small current with the magnitude of a nA. The current is converted to a voltage pulse by a charge sensitive preamplifier and amplified by a second stage amplifier. The final pulse height has a linear relation with the incident particle energy. In this way, the energy spectrum of the escaping neutral particles can be obtained through analog circuits or digital pulse height analysis. A four-chord SSNPA array was installed on NSTX in 2004 [39] and improved in the 2005 experimental campaign [40]. Although the SSNPA system has the advantages of compact size, lower equipment cost, and relatively simple design,

there are some trade-offs compared with the traditional E||B type NPA. First, it does not have the ability to diagnose different types of particles. For NSTX, this is not an issue since we are mostly interested in the energetic particles in the energy range of $30 - 120$ keV and they are generated from the deuterium NBI. Second, the system may be susceptible to some soft X-ray and electromagnetic (EM) noise. The SSNPA system also has lower counting capability than the E||B type NPA because it works in pulse mode and it does not have many detectors. These constraints impose some limits on the time resolution and energy resolution of the SSNPA system. Possible upgrades for the SSNPA diagnostic are proposed in Chapter 7 of this thesis.

3.2 Hardware Description

3.2.1 Setup

Figure 3.1: Silicon photodiodes used in the SSNPA diagnostic.

The SSNPA diagnostic is based on using silicon photodiodes (AXUVHS4 or AXUVHS11 from International Radiation Detectors Inc. [72]) as detectors for energetic neutral particles (Fig. 3.1). These detectors have a diameter of $0.16 - 1$ mm and are operated at a bias of -50 V at room temperature. At the front of each detector, there

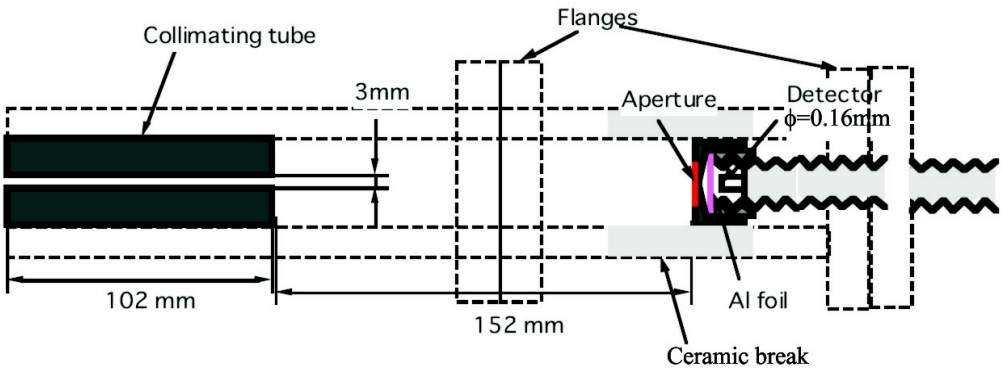

Figure 3.2: Schematic view of collimating tube, aperture, Al foil, and detector. (Fig. 1 in Ref. [39])

is a very thin layer of platinum silicide (a dead layer) whose thickness is 7 nm and the energy loss from this layer is less than 1 keV. In order not to be affected by the visible radiation or low energy X-ray from the plasma, a thin (150 nm) Aluminum foil is placed in front of each detector as shown in Fig. 3.2. The stopping power due to this foil is estimated to be around 9 keV for deuterons of energy between 40 and 120 keV based on TRIM simulation [73]. A copper cap is placed in front of the aluminum foil and covers the detector with a $20 \sim 50\ \mu m$ aperture in the middle. With the combination of collimating tube and aperture, the solid angle for each chord of SSNPA is $\sim 1 \times 10^{-4}$ sr (the Solid angle of the collimating tube is $\sim 7.4 \times 10^{-4}$ sr). The collimation is so sharp that the viewing chord can be regarded as a line. (The small fraction of neutrals that scatter off the tube wall without significant energy loss is neglected in the analysis. The edge of the pinhole of the collimating tube is tapered to a knife edge finish to minimize possible reflections.) It is expected that the sensitivity to X ray, gamma ray and neutron emissions directly from the plasma is small because of the small field-of-view and small size of detector. There is another copper foil covering each flight tube and the detector from the outside of flight tube. The copper foil, copper aperture holder and aluminum foil work as three EM noise shielding layers. For each chord, there are two flanges with a ceramic break in the

flight tube and a long length of $\sim$ 3 cm between the detector and the feedthrough. A small declination or obliquity of these flange attachments can prevent the aperture from aiming inside the sight line of collimating tube. Thus, careful installation of the detector and aperture structure is one of the key points for this collimating structure. Each detector is connected to a charge sensitive preamplifier directly so that no additional capacitance is added to the preamplifier input side. The output signal from the preamplifier is sent to a second stage amplifier via a $\sim$ 7 meter-long cable. The block diagram and photo of the SSNPA setup are shown in Fig. 3.3 and Fig. 3.4 respectively.

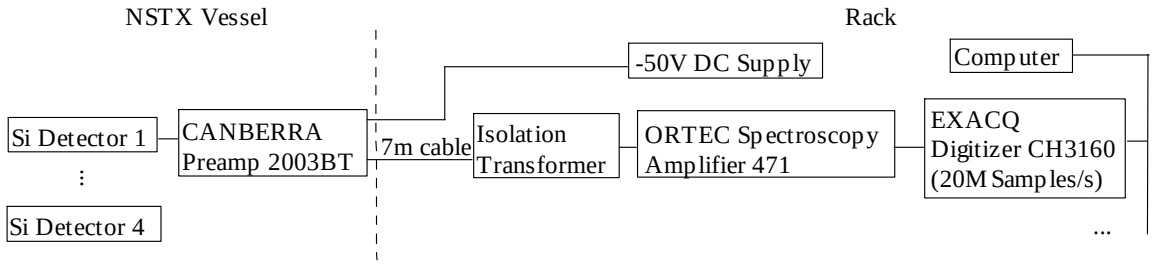

Figure 3.3: Schematic diagram of the SSNPA electronics.

3.2.2 Noise Reduction Techniques

The electronics before the second stage amplifier, including the detector, the preamplifier and a long signal cable are most sensitive to EM pickup since they are very close to the toroidal and poloidal coils (only 10 cm from the toroidal field coils and 50 cm from the poloidal field coils) and any EM pickup will be amplified by the second stage amplifier. Several improvements were made to reduce the noise in the NSTX 2005 experimental campaign: (1) low capacitance and low dark current detectors (AXUVHS4 or AXUVHS11 detectors) were carefully selected since they would finally determine the energy resolution and low-energy limit of the measurable energy range;

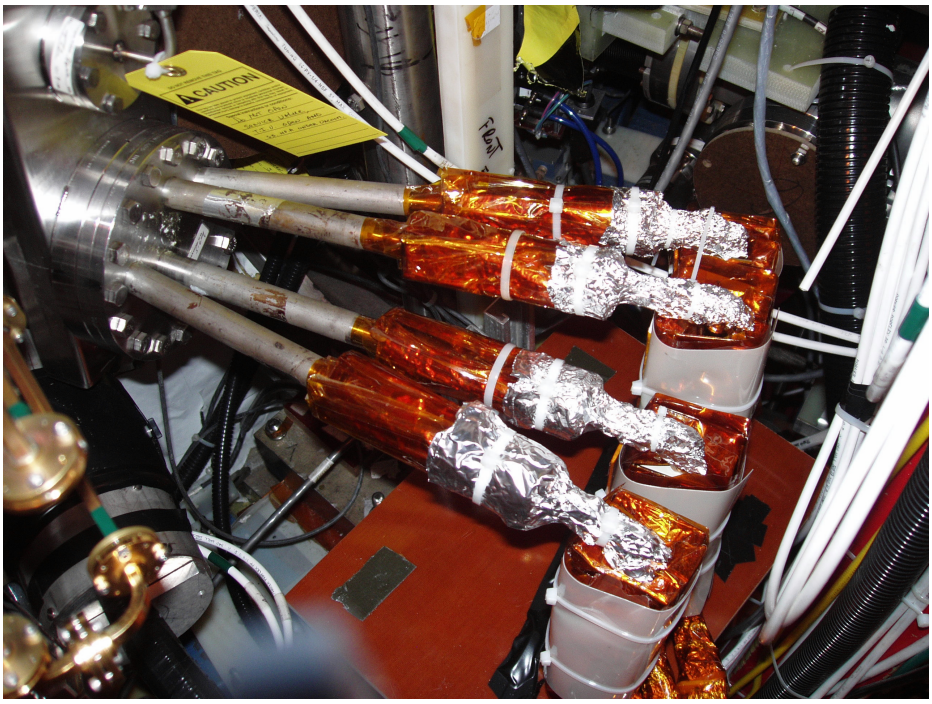

Figure 3.4: A photo of the SSNPA diagnostic, which shows the flight tubes and preamps in copper shielding boxes.

(2) the preamplifiers and connectors were shielded in a copper box that was grounded to the instrument rack; (3) the cables between the preamplifiers and the amplifiers were shortened from 10 to 7 meters and the coaxial signal cables were replaced by shielded twisted-pair cables; (4) the cables for one chord that consist of one bundle were gently twisted and covered with a grounded braid and magnetic shielding foil (METGLAS 2605CO) [74]; (5) the four bundles were put in an aluminum conduit, which was also grounded to the instrument rack, and a wide bandwidth transformer was inserted in series with the signal cable to eliminate possible ground loops. With these improvements, the detector, preamplifier and cables have good EM shielding that significantly reduced the noise pickup in plasma discharges. Charge sensitive preamplifiers (CANBERRA 2003BT) with a sensitivity of 20 mV/MeV, a fast shaping amplifier (ORTEC 471) with shaping time 0.5 μs and two digitizer boards (that will be described below) are used in the current SSNPA array design.

3.2.3 Fast Digitization of Raw Signals

Since the NSTX 2005 experimental campaign, the conventional analog pulse height analysis module of the SSNPA has been replaced by a digital pulse height and shape analysis system. The output signal of the second stage amplifier was directly connected to a PCI digitizer board (EXACQ CH3160) [75] with an onboard memory of 64 MB. The digitizer board provides either one input channel with a sampling rate at 40 MHz, or two input channels at 20 MHz, or four input channels at 10 MHz. Input signals up to ± 5 V can be fed in and the energy resolution is 12-bit. Standard TTL signals are used for triggering. Currently two digitizer boards are used at a 20 MHz sample rate for two channels on each board. Data are sampled continuously after a start trigger until either a preset time arrives or the onboard memory is full. Afterwards, the data are transferred to a local programmable computer. Dedicated Labview and IDL programs were developed for data acquisition and analysis, respectively. This novel digital approach provides several important features: accurate pulse height measurement, pulse shape discrimination, post experiment data re-processing, pulse pile-up identification and treatment, and possible high count rate operation. In addition, this digitization method is also very useful in identifying noise sources. Through this digitization method, it was found that the EM noise had a fixed frequency related to the coil system used for resistive wall mode control [76].

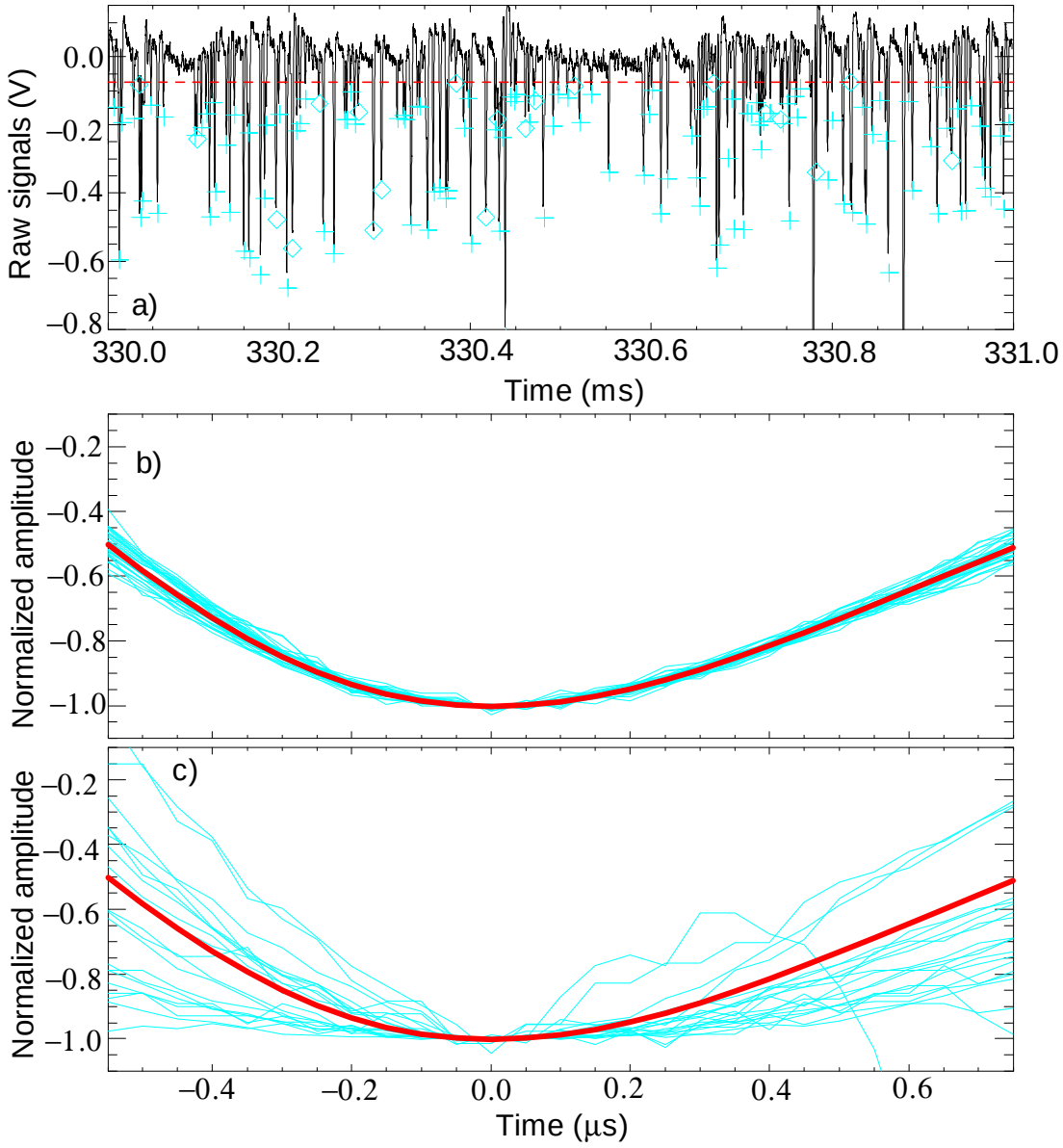

Figure 3.5: (a) Raw data for chord 1 of the SSNPA with true signals marked with plus and noise marked with diamond; (b) pulse shape comparison of the true signals (solid blue curves) with the pulse model(bold red curve); and (c) pulse shape comparison of noise (solid blue curves) with the pulse model (bold red curve).

3.3 Data analysis

3.3.1 Software-based Pulse Height Analysis

The software-based pulse height analysis (PHA) consists of several stages: (a) filtering to remove low frequency noise and smooth the raw data; (b) rejection of pulses below a preset threshold; (c) peak location for pairs of adjacent overlapping pulses that exceed the threshold and (d) determination of the baseline, peak position, peak value and pulse width for individual pulse. The pulse height equals the peak value minus the baseline and each pulse is normalized to its pulse height and compared with the model pulse shape. If the reduced chi-squared is smaller than a specified value (which means the measured pulse shape is very similar to the model pulse), that pulse is accepted as a true signal pulse. Otherwise, the pulse is rejected as EM noise. In contrast to a conventional analog PHA, this digitization method, in principle, also enables disentangling of two overlapping pulses and determinating of the pulse height for both pulses [77]. If any pulse width is larger than a certain maximum value, it is considered a possible pulse pile-up event. In such cases, the first signal is fitted up to the start of the second one. The analytical function obtained from the fitting is subtracted, thus isolating the second pulse, which can then be separately analyzed. But this reconstruction still requires a minimum fit interval between two pulses in order to obtain stable results for the first pulse. An example of this digitization method is shown in Fig. 3.5 with (a) the raw signals with true peaks marked with a plus and noise marked with a diamond; (b) pulse shape comparison of the true signals (solid blue curve) with the pulse model (bold red curve); and (c) pulse shape comparison of noise (solid blue curves) with the pulse model (bold red curve). With this digitization method, pulse height is accurately measured and obvious noise pulses since the EM pickup are rejected. However, the ideal arrangement for the digitization

method is to sample the raw signals right after the preamplifiers [78]. Unfortunately, the available preamplifiers do not have sufficient gain (the output signals are only the order of a millivolt). More details about the data acquisition and pulse height analysis for the SSNPA diagnostic are presented in Appendices.

3.3.2 Energy Calibration

3.3.2.1 Energy Calibration with a Mono-energetic Source

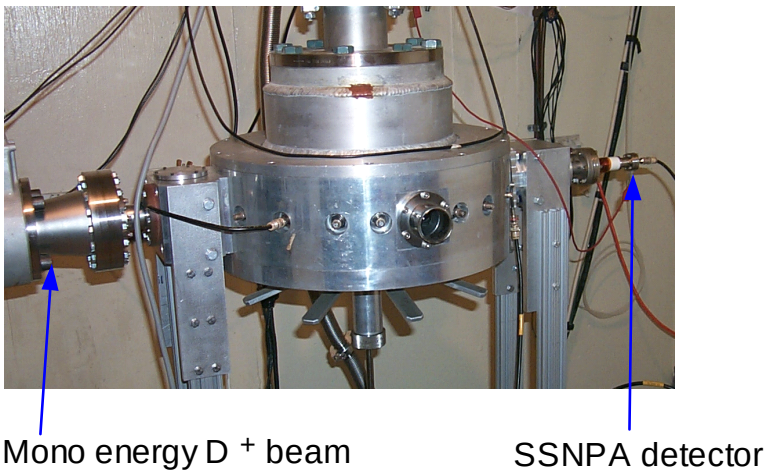

Figure 3.6: Layout of the energy calibration of SSNPA detectors. A mono-energetic D^+ source is produced by a small accelerator and it is perpendicular to the detector surface.

An energy calibration was carried out using a mono-energetic source of deuterons from the low energy charged particle accelerator at the Colorado School of Mines with the layout shown in Fig. 3.6. The output of the second stage amplifier was measured using a multi-channel analyzer (MCA), which was calibrated by using a pulser. The results are shown in Fig. 3.7. The peak position in the MCA waveform is plotted versus the beam energy in Fig. 3.7(a). There is good linearity in the range of 35 to 120 keV when the beam is perpendicular to the detector surface. (The angle sensitivity

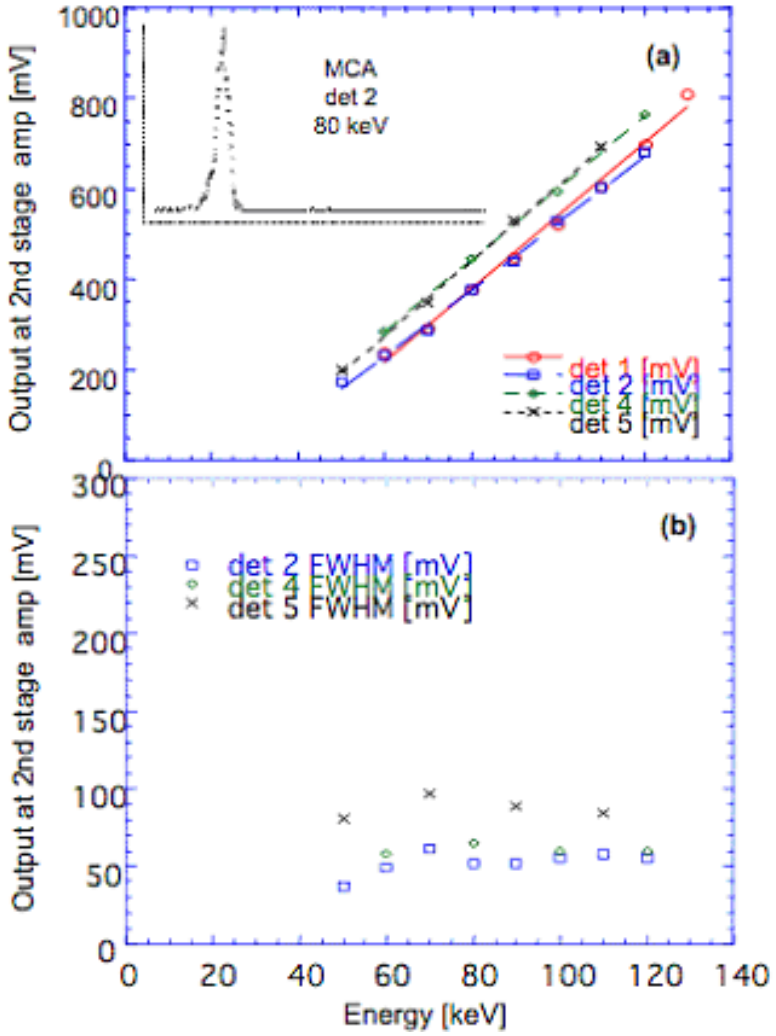

Figure 3.7: (a) Peak position of spectrum versus energy of beam source. One of spectra of MCA is also shown as an example in this panel (count vs channel), (b) FWHM of spectrum versus energy of beam source. (Reproduced from Fig. 2 in Ref. [39])

of the SSNPA detectors is not tested in the energy calibration. The effect should be small since the solid angle of each chord is around 1×10^{-4} sr.) It is also shown in Fig. 3.6.that only the particles with energy larger than 35 keV can be detected. The energy resolution (FWHM in the MCA waveform) is about 10 keV and it is almost a constant in the range of 35 to 120 keV. This lack of dependence on the energy suggests that electronic noise is dominant in the present setup. These calibration results were also consistent with calibration using an alpha source (^{241}Am) with energy of 5.49 MeV.

3.3.2.2 Energy Calibration with Gas-filled-torus Shots

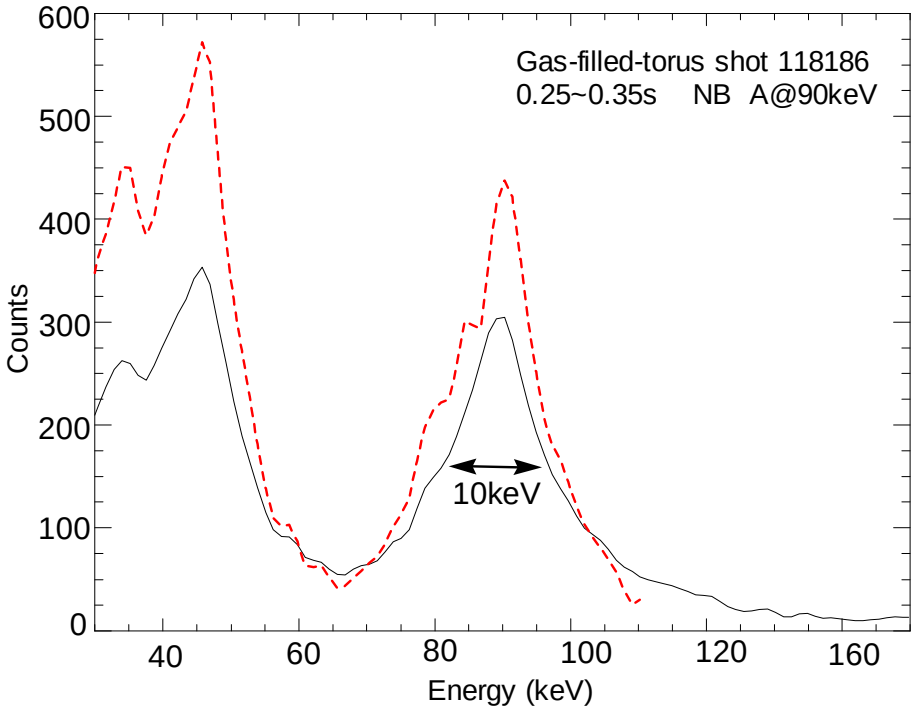

Figure 3.8: Measured energy spectrum (solid black curve) for chord 1 of the SSNPA in a gas-filled shot 118186 and the real energy spectrum (dashed red curve) inversely derived from the Monte Carlo simulation.

Gas-filled-torus shots can also be used for energy calibration [69] or validity checking of the SSNPA performance. During the calibration of the motional Stark

effect diagnostic, neutral beams (NB) are injected into the NSTX vessel without a target plasma in what is referred to as gas-filled-torus shots. In these shots, some of the NB-injected particles are ionized by collisions with the residual gas and captured on the toroidal magnetic field lines. The electron density is very low, hence the slowing-down time is long and particle loss by charge exchange is significant. Therefore, the spectra obtained on a sightline close to the tangency radius of the injected NB should be the same as that of the injected neutrals. The solid black curve in Fig. 3.8 shows a typical measured energy spectrum obtained on Chord 1 of the SSNPA in the gas-filled-torus shot 118186 in which NB source A was injected at 90 keV. Full and half energy components of the injected NB (Deuterium) are clearly seen and an energy resolution of 10 keV is achieved.

3.3.3 Noise Analysis

The noise on the SSNPA diagnostic comes from two main sources: pulse pile-up and neutron/gamma ray radiation. The pulse pile-up can generate a high-energy tail above the beam injection energy in the energy spectra, but it does not significantly distort the spectral shape. The high-energy tail above the beam injection energy (90 keV) in gas-filled-torus shots (Fig. 3.8) is such an example. Because there is no plasma in the gas-filled-torus shots and hence no neutron/gamma ray radiation, the high-energy tail can only come from by pulse pile-up. A Monte-Carlo code [79] can be used to simulate pulse pile-up trains if the real count rate and spectrum are available. In our analysis, the real count rate can be obtained by numerical inversion from the paralyzable model [80] and the measured energy spectrum can be used as the initial estimate of the real spectrum. With iteration, the real energy spectrum can be inversely derived from the uncorrected experimental spectra. The dashed red curve in the Fig. 3.8 shows the derived real energy spectrum. It is clearly seen that pulse

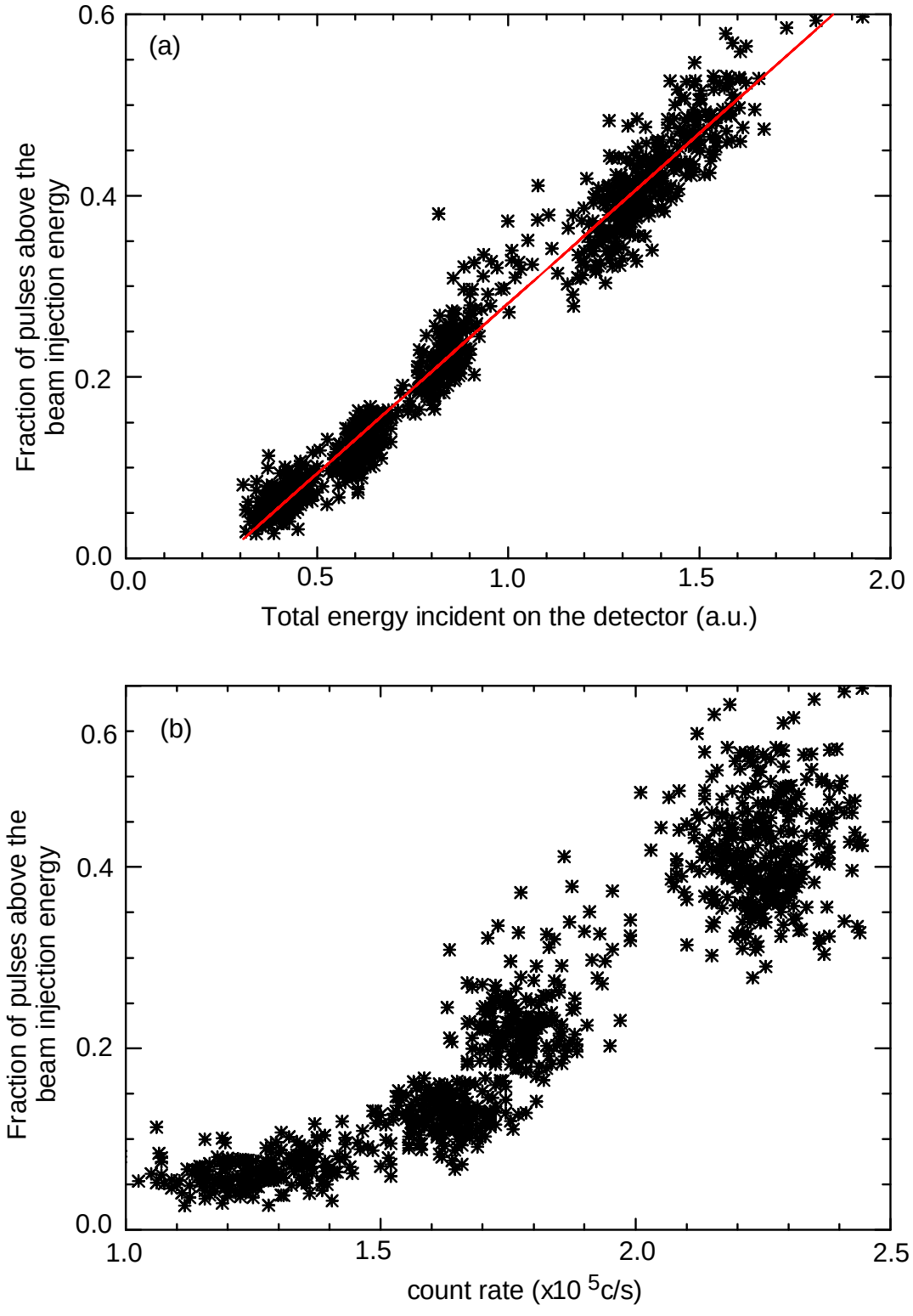

Figure 3.9: The fraction of pulses above the injection energy increases monotonically with (a) incident energy and (b) count rate in the gas-filled-torus shots.

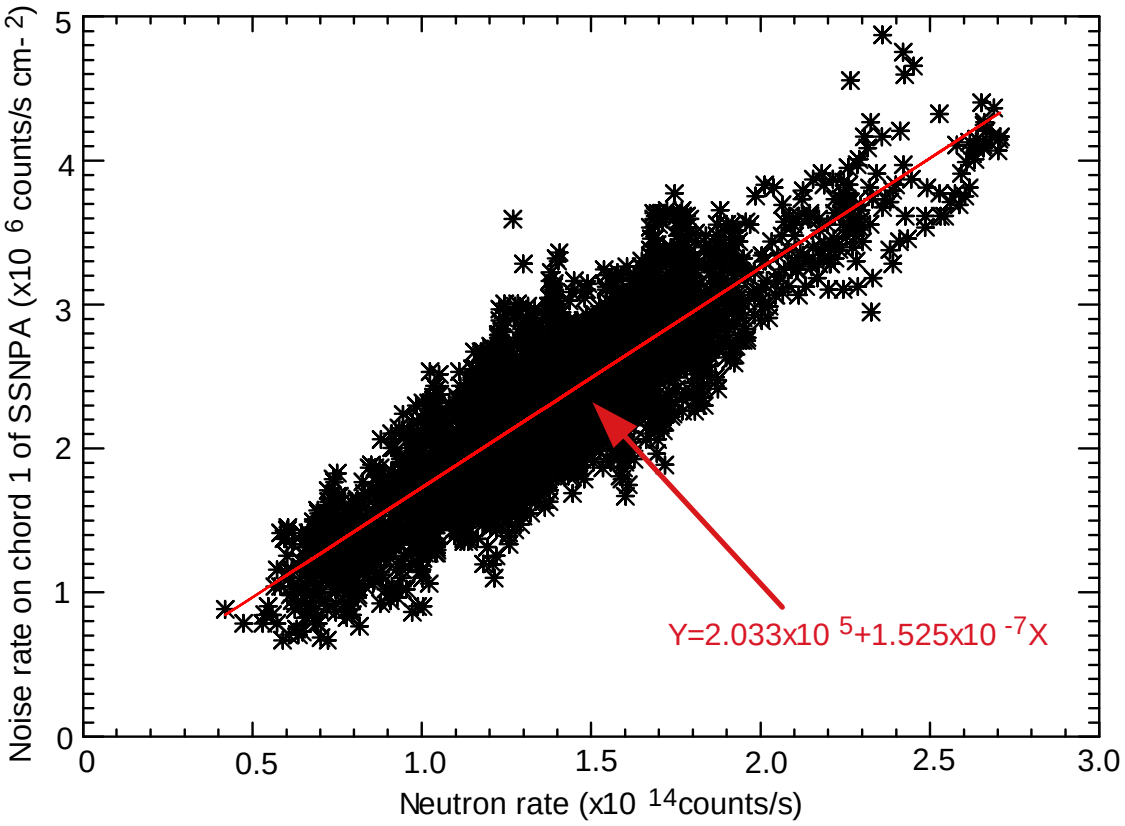

Figure 3.10: The linear relation between the neutron rate and SSNPA noise in a set of shots with the closed SSNPA valve, in which only neutron/gamma ray can strike the SSNPA detectors.

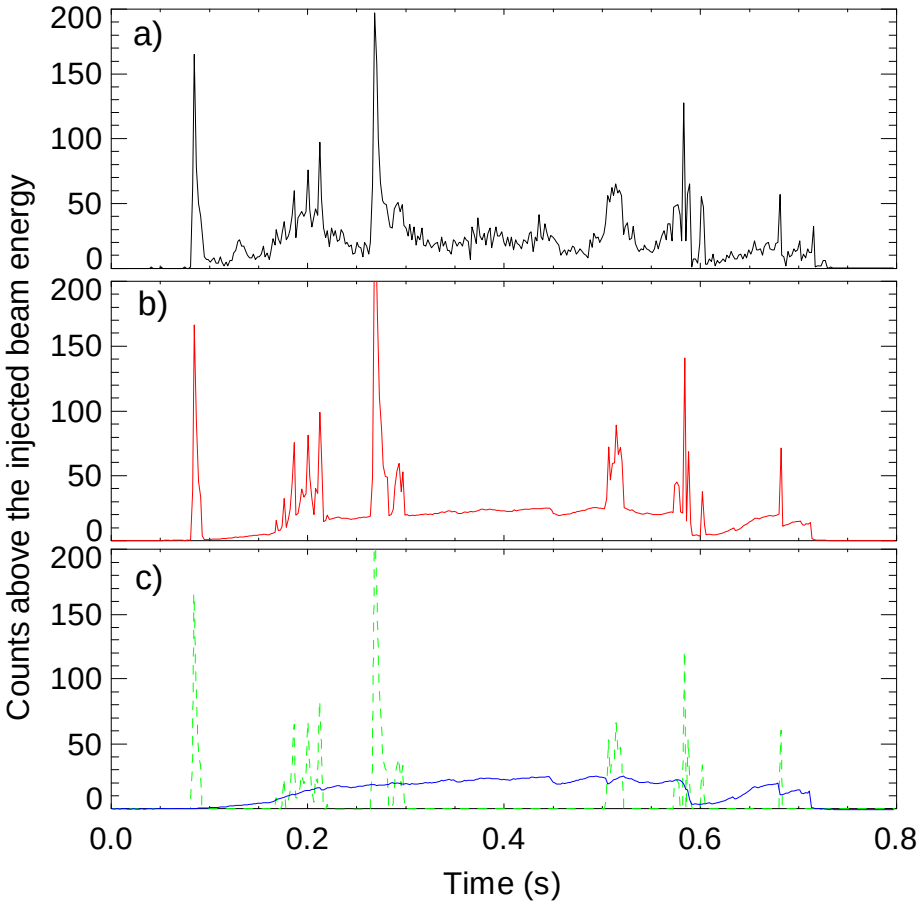

Figure 3.11: (a) Temporal evolution of the counts above the beam injection energy; (b) the empirical linear combination of pulse pile-up and neutron/gamma ray radiation; and (c) contribution from pulse pile-up (dashed green curve) and neutron/gamma ray radiation (solid blue curve). This suggests that the pulses above the beam injection energy are from pulse pile-up and neutron/gamma ray radiation.

pile-ups generate the high-energy tail, but it does not significantly distort the spectral shape below the injection energy. Examination of a number of discharges indicates that the fraction of pulses above the injection energy increases monotonically with the count rate. One example is shown in Fig. 3.9, in which eight reproducible gas-filled-torus shots were chosen to estimate the coefficient between the pulse counts above the beam injection energy and the total neutral flux incident on the detector. The neutron/gamma ray's contribution to the SSNPA signals can be measured by closing the SSNPA valve to eliminate the neutral flux onto the detectors. Figure 3.10 shows a strong linear relation between the neutron emission rate and the SSNPA signals in a series of shots with the SSNPA valve closed.

These noise coefficients from gas-filled torus shots and valve-closed shots can be used to estimate the contributions of pile-up and neutron/gamma ray radiation contributions to the SSNPA noise. One example is shown in Fig. 3.11. The empirical linear combination (red curve) of pulse pile-up (solid blue curve in Fig. 3.11) and neutron/gamma ray radiation noise (dashed green curve in Fig. 3.11) is in good agreement with the experimental pulse count evolution above the beam injection energy (solid black curve in Fig. 3.11). This confirms that pulse pile-up and neutron/gamma ray radiation are the two major sources for the SSNPA noise. Note that the SSNPA diagnostic can pick up a fixed frequency EM noise from the coil system used for resistive wall mode control. This problem has not been resolved yet. For all the SSNPA data presented in this thesis, neutron/gamma ray radiation induced noise is subtracted and the circuits for resistive wall mode control are disconnected from the NSTX machine.

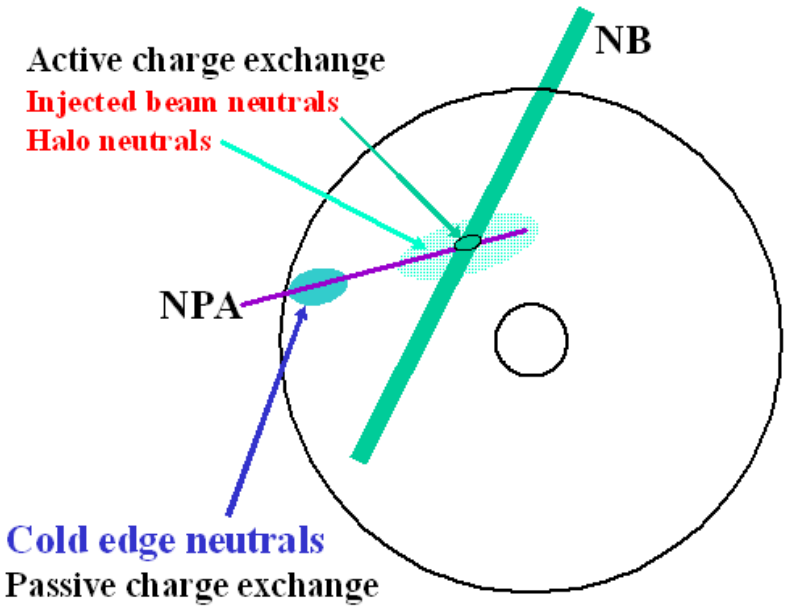

Figure 3.12: Schematic view of the NSTX device showing a neutral beam source and a NPA/SSNPA sightline. Injected beam neutrals are in the green beam footprint, warm halo neutrals are in a cloud around the injected beam, and cold edge neutrals are near the walls of the chamber.

3.4 Characteristics of the NPA Diagnostics

Both NPA and SSNPA diagnostics measure fast ions that charge exchange with neutral particles. In NSTX, there are three types of hydrogenic neutral particles. Neutrals from NBI is the major population and they have three energy components (refer to Sect. 2.1.2). The velocities and densities of these neutrals are determined by the injection energy, injection power and species fractions. The small divergence of the neutral beam source implies that both the direction of the velocity vector and the spatial extent of the injected neutrals is well defined. When a primary beam neutral is deposited via charge exchange on a thermal ion, the thermal ion in turn becomes a neutral known as a halo neutral. Around the footprint of the injected beam there is a halo neutral cloud whose density can be comparable with the injected neutral density. The velocity distribution of this population is approximately the local velocity

distribution of the plasma ions. Near the plasma edge, there are some relatively cold neutrals from the wall or gas puff. Since these three types of neutrals exist in the NPA/SSNPA sightlines, the signals of the NPA/SSNPA also come from three parts, as shown in Fig. 3.12.

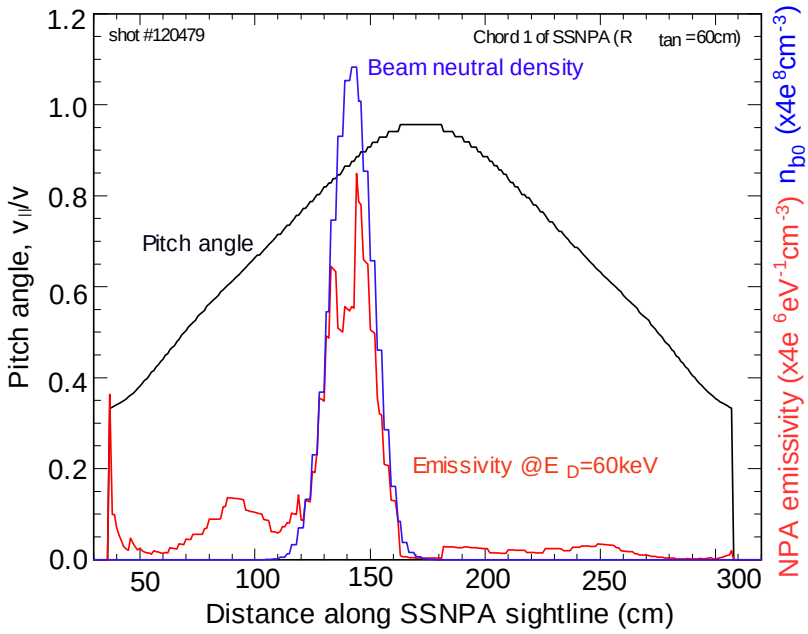

Figure 3.13: The SSNPA (chord 1) signal is localized to a significant extent by beam neutrals in real space and a small pitch range in velocity space. For the sightlines that intersect with the NB, approximately 2/3 of the integrated flux originates from the intersection region.

Figure 3.13 shows a calculation of the charge exchange emissivity (red line) of chord 1 (R_{tan}=60 cm) of SSNPA for a deuteron energy of 60 keV overlaid with the beam neutral density for source A (blue line) as a function of distance along the SSNPA sightline. It clearly shows that the SSNPA emissivity is mainly localized due to charge exchange on the beam primary and halo neutrals. The range of pitch detected by the NPA and SSNPA is plotted in Fig. 3.14 by noting the values at the rising and falling edges of the beam neutral density line. It suggests that the pitch detected by the NPA/SSNPA is well localized and that the fast ions sampled by the

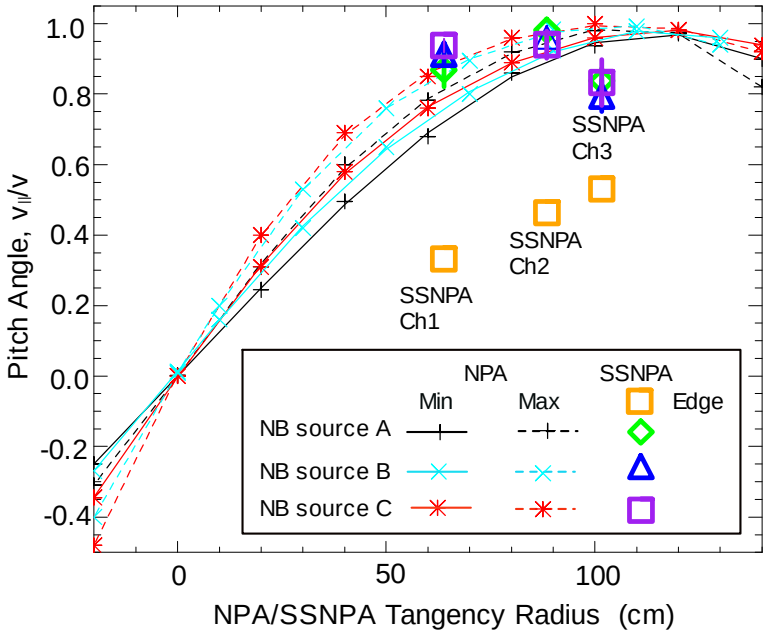

Figure 3.14: The pitch of fast ions that can be sampled by the NPA and SSNPA diagnostics as a function of the NPA/SSNPA viewing tangency radius. (The data for NPA diagnostics is reproduced from Ref. [60])

NPA/SSNPA are mainly from passing particles. Generally, for the sightlines that intersect with the injected NB, the NPA/SSNPA signal is dominated by the charge exchange reactions with beam neutrals and halo neutrals at the intersectional area, which is called active charge exchange. The charge exchange with cold edge neutrals contribute only 1/4 to 1/3 of the total NPA signal and it is called as passive charge exchange. Note that the most outboard chord of SSNPA misses the injected NB (Fig. 2.1), so the signal of that chord mainly comes from the charge exchange reactions with halo neutrals and edge neutrals.

Table 3.1 compares the NPA/SSNPA diagnostic with other fast ion diagnostics in real space and velocity space. The fast ion loss probe diagnostic is also a local measurement in real space, while the neutron diagnostic is volume-averaged. The signals from the line-integrated NPA and FIDA diagnostics are mainly core-weighted due to active CX reactions with beam neutrals in the intersectional area. However,

Table 3.1: Comparison of various fast ion diagnostics in velocity space and real space.

Diagnostics	**Velocity Space**	**Real Space**
Neutron detectors	weights high energies	volume averaged
Fast ion loss probe	a small volume	lost fast ions
FIDA	a region, weights high energies	mainly the intersection region
NPA and SSNPA	a small volume	mainly the intersection region

under certain conditions, the signals from the NPA diagnostics can be edge-weighted due to passive CX reactions with wall neutrals. These diagnostics also measure different portions in velocity space. The fast ion loss probe, E||B type NPA and SSNPA diagnostics measure a very small volume in velocity space, while the FIDA diagnostic measures a region. The neutron emission rate measurements are also averaged in velocity space although they weight high energies (because the D-D fusion cross section increases rapidly with energy) and counter-going ions (due to plasma rotation) most heavily.

3.5 SSNPA Measurements in Quiescent Plasmas

The study of the confinement of dilute populations of the fast ions in NSTX suggests that the fast ions decelerate classically and hardly diffuse in MHD quiescent plasmas. Thus the SSNPA measurements in quiet plasmas can be used to validate the diagnostic. Figure 3.15 shows the temporal evolution of plasma current, injected NB power, neutron yield, 80 keV neutral flux measured by the E||B type NPA (with tangency radius 63.5cm) and Chord 1 of the SSNPA (with tangency radius 60 cm) in shot 119598. The NB (source A) is modulated and short neutral beam pulses (beam blips) are injected at a full energy of 90 keV with 10 ms on and 20 ms off.

The signals of SSNPA Chord 1 are clearly synchronized to the modulation of the NB and the temporal evolution is similar to that obtained with the E||B type NPA. The fast-ion slowing down process during the beam off period is also observed with the SSNPA diagnostic and one example is shown in Fig. 3.16. The measured slowing down process can be fitted to an exponential curve E=$E_{inj}\exp(-t\gamma_E)$, where E_{inj} is the beam injection energy, E is the energy peak during beam-off period, t is time and γ_E^{-1} is the experimental fast ion slowing down time. The experimental slowing down time can be compared with the calculated classical slowing down time ${\gamma_s}^{-1}$ using the measured plasma profiles, where $\gamma_s = 2(1+\frac{m_f}{m_e})\psi(x)\gamma_0$ [81], $\gamma_0 = 4\pi e^4 n_e \ln\Lambda/m_f^2 v_f^3$, $x = m_e v_f^2/2kT_e$, $\psi(x)$ is the error function, $\ln\Lambda$ is Coulomb logarithm, m_e, n_e, and T_e are electron mass, electron density and electron temperature respectively, and m_f and v_f are fast-ion mass and velocity respectively. $\ln\Lambda = 24 - \ln({n_e}^{1/2}{T_e}^{-1})$ for $T_e < 10$ keV and $v_f \ll v_e$, T_e is in eV and others are in CGS units. (The value of $\ln\Lambda$ has been used in the previous comparison of fast ion slowing down in DIII-D and reasonable agreement is obtained [82]). Figure 3.17 shows the experimental slowing-down time from a series of shots in NSTX is consistent with the theoretical prediction.

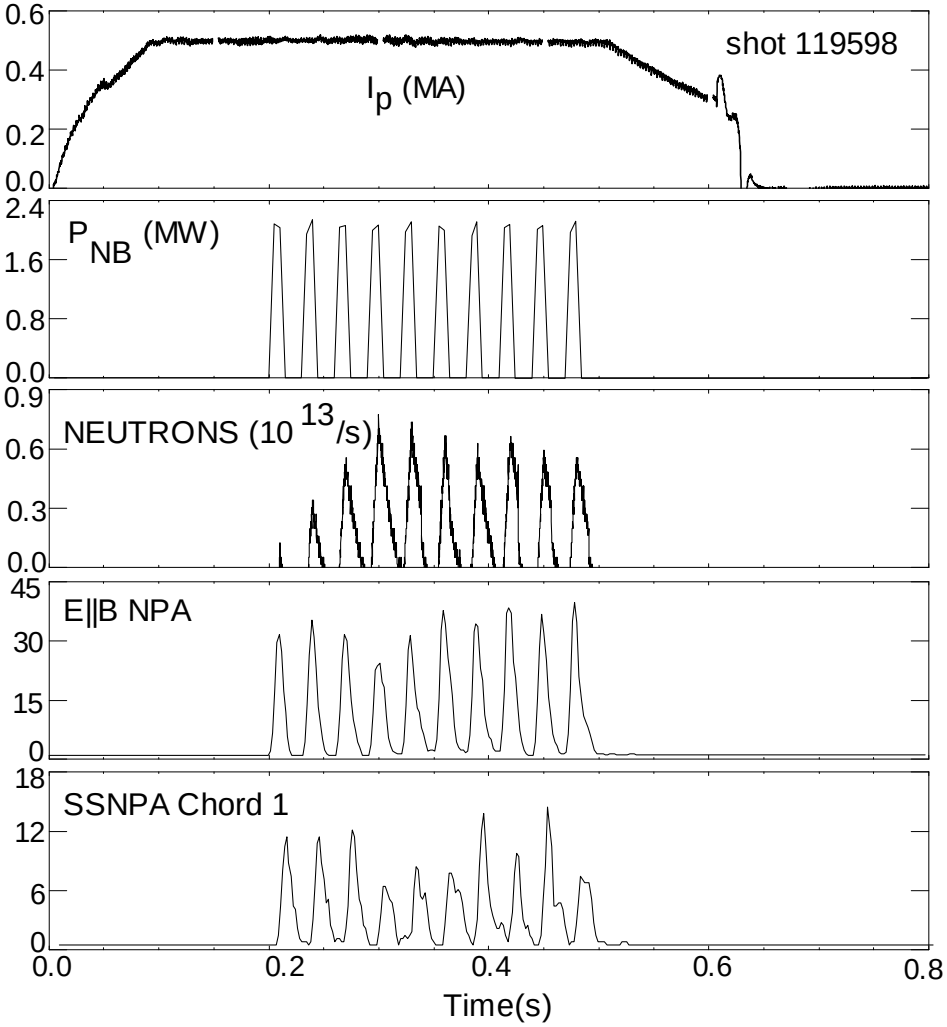

Figure 3.15: Temporal evolution of plasma current, NB power, neutron yield, counts in Chord 1 of the SSNPA, and the E||B NPA signal in shot 119598

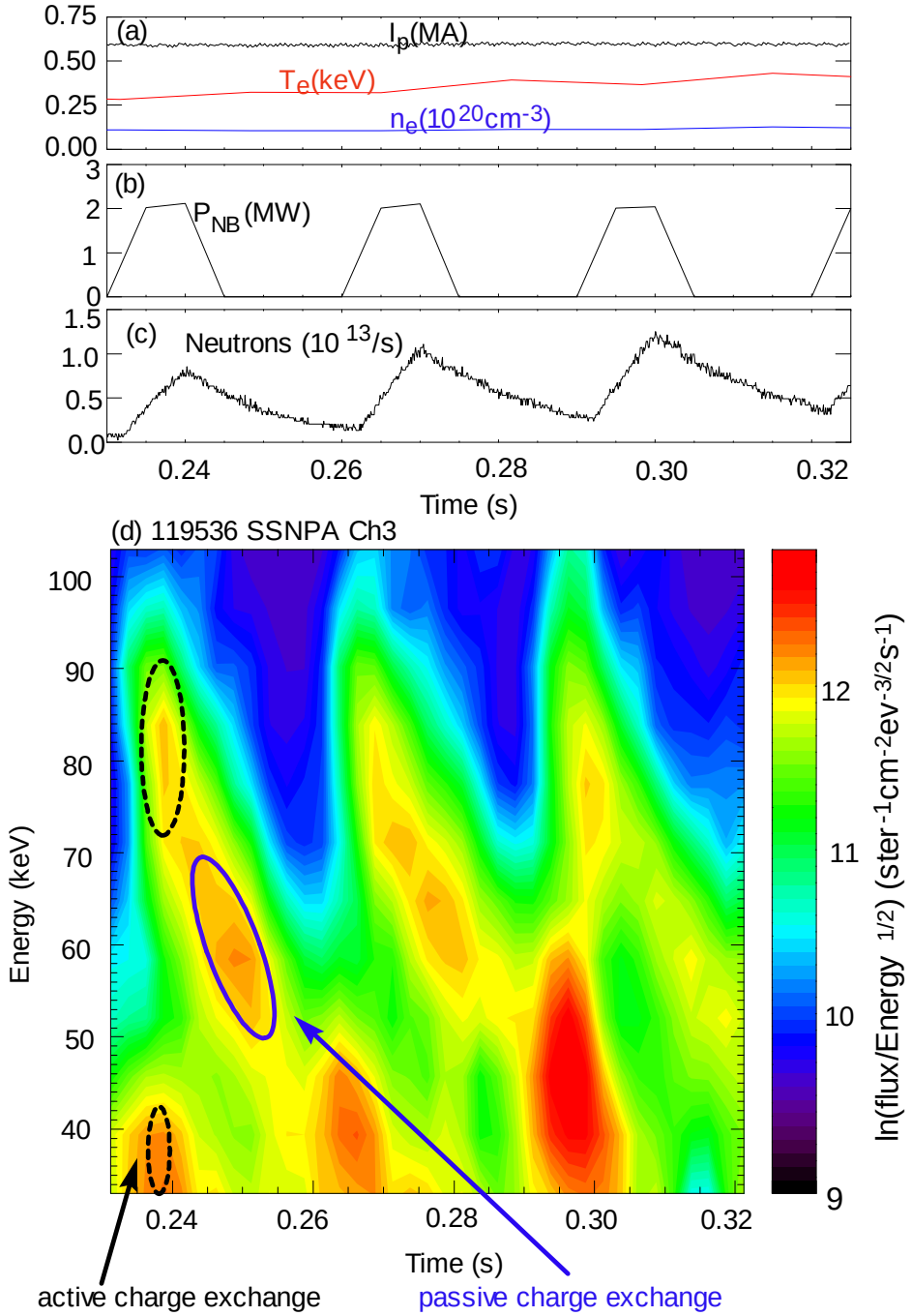

Figure 3.16: Temporal evolution of (a) plasma current, central electron temperature, and central electron density; (b) injected NB power, (c) neutron rate and (d) measured signals of chord 3 of the SSNPA diagnostic. The full energy (90 keV) and half energy (45 keV) components are observed on the SSNPA during the neutral beam injection. During the beam off period, fast-ion slowing down process is also clearly shown.

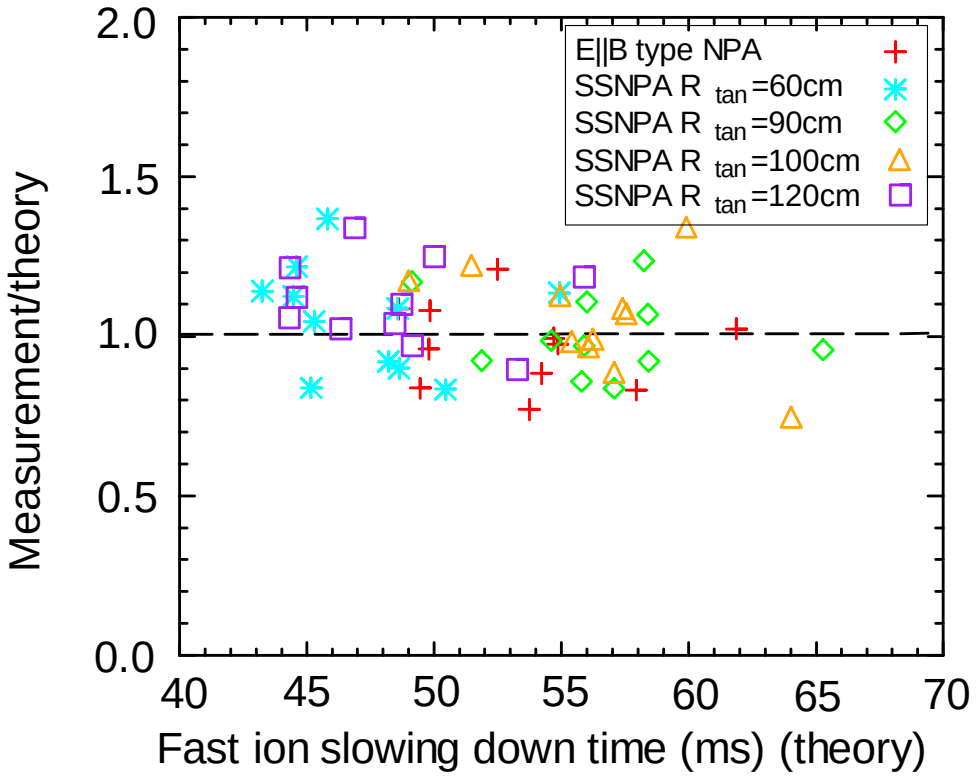

Figure 3.17: Comparison of fast-ion slowing down time from experimental data fitting and classical Coulomb collision theory.

Chapter 4

Simulation Codes

In this thesis, the NPA and FIDA measurements are often compared with numerical simulations to understand the underlying physics. The simulation codes include TRANSP, CQL3D and our self-developed FIDA_NPA simulation codes. In this chapter, a brief review of TRANSP, CQL3D and FIDA simulation codes is given with appropriate references. The TRANSP-based NPA simulation code and our self-developed NPA simulation code are described in the Sect. 4.4.1 and 4.4.2.

4.1 TRANSP Code

The TRANSP code [83, 84, 85, 86] is one of the primary transport codes used in the fusion community for time dependent analysis of tokamak experiments. It uses the measured plasma density, temperature, rotation and current profiles and assumes that fast ions behave classically. One essential element of the TRANSP code is the NUBEAM module [87], a Monte Carlo package for the neutral beam injection physics. With the NUBEAM module, the TRANSP code can simulate neutral beam

deposition, fast ion orbiting, power deposition, beam driven current and momentum transfer, which account for particle collisions, charge exchange loss and recapture and transport of beam neutral particles. In this thesis, the TRANSP code is mainly used to predict the fast-ion distribution at guiding center in quiet plasmas. Note that the TRASNP simulation code has considered the effects of large Larmor radius and finite orbit width of fast ions, but it currently does not include the interactions between fast ions and RF waves.

4.2 CQL3D Code

The CQL3D code[88] is generally used for modelling auxiliary heating in tokamaks. As described in detail in Ref. [88], the code consists of an array of 2D-in-momentum space, bounce-averaged, collisional quasilinear Fokker-Planck equation solvers running on noncircular magnetic flux surfaces. It is coupled to ray-tracing codes for electron cyclotron, lower hybrid, and fast waves, to a neutral beam deposition code, and to a noncircular equilibrium code. Neoclassical diffusion and finite orbit size effects are not implemented in the version of CQL3D code employed here. In this thesis, the CQL3D code is mainly used to predict the fast-ion distribution during NBI with/without RF heating.

4.3 FIDA Simulation Code

The FIDA simulation code is a forward and weighted Monte Carlo simulation code for the FIDA diagnostic. It predicts fast-ion D_α spectra based on a given fast-ion distribution function and measured plasma profiles and electric and magnetic fields. All the relevant atomic physics effects have been included. A detailed description

of the FIDA simulation code can be found in Refs. [89, 90]. In this thesis, we use the FIDA simulation code to predict FIDA spectra and spatial profile during HHFW heating with the fast-ion distributions dumped from CQL3D or TRANSP.

4.4 NPA Simulation Codes

There are two NPA simulation codes used in this thesis. One is the TRANSP-based NPA simulator, which is a module inside the TRANSP code. However, the TRANSP-based NPA simulation is not accurate enough since it does not handle halo neutrals properly. In TRANSP, halo neutrals are volume averaged both poloidally and toroidally rather than remaining near the beam footprint. But the fact is halo neutrals spread out into 4π and "linger" in the NPA field of view because of multi-generations and they have comparable density as primary beam neutrals. It is conceivable that the temporal evolution of the NPA neutral fluxes produced by charge exchange on the primary and halo neutrals may be different. Aside from this, proper treatment of halo neutrals is crucial for the accurate simulation of NPA horizontal and vertical scan measurements. In the horizontal scan case, primary neutrals attenuate as a function of distance along the beam line whereas the halo neutrals can grow following the neutral beam deposition profile. In the vertical case, the halo neutrals effectively extend the vertical dimension of the beam footprint. To clarify the effect of halo neutrals on the temporal evolution of NPA flux and the shape of NPA energy spectra, a new NPA simulation code called FIDA_NPA has been developed and the code shares many physics modules with the FIDA simulation code (Both NPA and FIDA diagnostics rely on charge exchange neutrals.) The results will be compared with TRANSP predictions and experimental measurements.

Before introducing the NPA simulation codes, it is useful to derive the formula

for the signals detected by the NPA diagnostics. As introduced in Sect. 2.2.8 and Chapter 3, the NPA diagnostics measure charge exchange neutral particles. The neutral production rate into 4π space due to charge exchange reactions between a fast ion distribution $n_i(\mathbf{r})f_i(\mathbf{r},E_i)$ $(cm^{-3}eV^{-1})$ and a neutral population $n_n(\mathbf{r})$ (cm^{-3}) is

$$R_0(E_i) = n_i(\mathbf{r})f_i(\mathbf{r},E_i)n_n(\mathbf{r})\sigma_{cx}(E_{rel}^{i,n})V_{rel}^{i,n} \quad (cm^{-3}eV^{-1}s^{-1}) \tag{4.1}$$

where $n_i(\mathbf{r})$ is the fast ion density, $f_i(\mathbf{r},E_i)$ is the energy distribution function of the fast ions, $\sigma_{cx}(E_{rel}^{i,n})$ is the charge-exchange cross section and $V_{rel}^{i,n}$ is the relative velocity between the ions and neutrals. These charge exchange neutrals fly out at all directions and only the part in a certain phase space can strike the NPA or SSNPA detectors. The input at one NPA/SSNPA detector is

$$R(E_i) = \int n_i(\mathbf{r})f_i(\mathbf{r},E_i)n_n(\mathbf{r})\sigma_{cx}(E_{rel}^{i,n})V_{rel}^{i,n}\frac{\triangle\Omega}{4\pi}e^{-\lambda}Adl \quad (eV^{-1}s^{-1}) \tag{4.2}$$

where $\triangle\Omega$ is the solid angle of the analyzer system, $e^{-\lambda}$ is the attenuation factor of the neutrals during escape from the plasma (the attenuation is caused by either another charge exchange event or particle impact ionization) and Adl is the volume of the plasma viewed by the NPA analyzer. Note that $A \triangle \Omega$ doesn't vary along the NPA/SSNPA sightline. The count rate at the NPA/SSNPA detector is

$$C(E_i) = R(E_i)\cdot K(E_i) = \int n_i(\mathbf{r})f_i(\mathbf{r},E_i)n_n(\mathbf{r})\sigma_{cx}(E_{rel}^{i,n})V_{rel}^{i,n}\frac{\triangle\Omega}{4\pi}K(E_i)Adl\ (s^{-1}) \tag{4.3}$$

where $K(E) = \varepsilon(E)\ \triangle(E)$ is the detector response function depending on detection efficiency, detector energy width etc. For historical reasons, the "NPA neutral flux" is defined as

$$\Phi(E) = \frac{C}{\frac{\triangle\Omega}{4\pi}K(E)A} = \int n_i(\mathbf{r}) f_i(\mathbf{r},E_i) n_n(\mathbf{r}) \sigma_{cx}(E_{rel}^{i,n}) V_{rel}^{i,n} e^{-\lambda} dl \quad (cm^{-2}eV^{-1}s^{-1}) \quad (4.4)$$

since the slope of $\ln(\Phi(E)/E^{1/2})$ in a Maxwellian plasma can be used to estimate thermal ion temperature [91]. For the NSTX experimental data and simulation results, the NPA energy spectra are also plotted as $\ln(\Phi(E)/E^{1/2})$ versus E with units of $cm^{-2}eV^{-3/2}s^{-1}$.

4.4.1 TRANSP-based NPA Simulation

The TRANSP code is capable of simulating the NPA flux measurements and it includes five types of neutrals: beam neutrals (from injected neutral beams), halo neutrals (from charge exchange reactions between thermal ions and beam neutrals), fast neutrals (from charge exchanged fast ions), warm neutrals (from wall recycling), and cold neutrals (from gas puffing). Each type of neutrals can be set as on or off in the TRANSP namelist. The neutral production rates between fast ions and neutrals are calculated using the formula (4.1) with look-up tables for charge exchange cross section from Ref. [92, 93]. The attenuation factor of these neutrals during the exit from the plasma is computed using the look-up tables for charge exchange cross section and particle impact ionization cross section from Ref. [94]. It should be noted that in TRANSP, the NPA flux comes from a cylindrical tube pointing into the plasma along the sightline rather than the measured cone. The tube is typically artificially enlarged to improve Monte Carlo statistics. So when comparing the TRANSP NPA simulation results with experimental measurements, the TRANSP signals should be multiplied by a factor of ~ 0.16 [95], which was obtained from a rough calculation based on the actual solid acceptance angle of $\sim 5.9 \times 10^{-5}$ sr and the enlarged cylindrical tube diameter of 5 cm. More details about the TRANSP-based NPA simulator can be

found in the TRANSP help file [86] and Sect. 3.6 in Ref. [95]. Note that the effect of the collimating tube on incoming particles is not considered in the TRANSP-based NPA and FIDA NPA simulations.

4.4.2 FIDA_NPA Simulation

The FIDA_NPA simulation code also calculates the NPA neutral flux from charge exchange reactions. But it differs from the TRANSP-based NPA simulation in the following five aspects. Firstly, only primary beam and halo neutrals are included in the FIDA_NPA simulation code. The other types of neutrals, i.e. fast neutrals, warm neutrals and cold neutrals, are ignored. This assumption is reasonable because on NSTX, the sightlines of NPA/SSNPA intersect the injected neutral beams and that the NPA neutral flux is strongly localized to the intersectional area as found in TRANSP-based NPA simulation. The NPA/SSNPA signal is mainly affected by the beam neutrals and halo neutrals. Secondly, halo neutrals are correctly treated in the FIDA_NPA simulation using Monte-Carlo method and random walk model. Thirdly, the FIDA_NPA simulation code calculates the NPA neutral flux from the measuring cone, instead of an artificially enlarged tube as assumed in TRANSP. It is consistent with the real experimental setup. Fourthly, the FIDA_NPA simulation code calculates NPA energy spectra based on a given fast ion distribution, which can be either the results of an analytic model, a Fokker-Planck model calculation or a numerical output from the codes like TRANSP, ORBIT [96] or CQL3D. In contrast TRANSP assumes that fast ions behave classically and the TRANSP-based NPA simulation code can not use fast-ion distribution codes from other codes. In addition, the charge exchange cross sections and particle impact ionization cross sections in the FIDA_NPA simulation code came from a more recent reference [97], and they should be more accurate than the cross sections used in TRANSP.

The neutrals can exist in different quantum states, determined by the principle quantum numbers n and the angular momentum states l. The strong fine-structure mixing allows the assumption that the population of each quantum state may be grouped as a single population based on the principle quantum number n [98]. In the FIDA_NPA simulation, states with $n > 4$ are neglected since these energy levels are sparsely populated and the cross sections seem uncertain. The required cross sections and reactivities for the neutrals in the states with $n = 1 - 4$ are available in Ref. [97], and they are consistent with the data in the Atomic Data and Analysis (ADAS) compilation (Ref. [99, 100])

4.4.2.1 Code Structure

The flow diagram of the FIDA_NPA simulation code is outlined in Fig. 4.1. The first part is the input and initialization module, in which the geometry of NBs and NPA detectors are given. Because neutrals travel in straight lines, a Cartesian coordinate (xyz coordinate) system is employed (Fig. 4.2). The geometrical information about the NBs and NPA detectors are specified either in TRANSP coordinates or in typical North-South-East-West coordinates and both need to be converted to be xyz Cartesian coordinates. Then a regular Cartesian mesh is established along the centerline of one injected neutral beam. All the plasma profiles, electric field and magnetic field are mapped onto this mesh. Next, all the atomic rates that do not depend on the neutral velocity, such as electron impact ionization rate, are computed. In addition, the volume weight of each cell for the NPA measurements and the direction of the velocity vector from each cell to the center of each NPA detector are calculated. All these quantities are stored in a large structure.

The second part of the code calculates the primary neutral and halo neutral density distributions in real space, velocity space, and energy levels using a Monte-

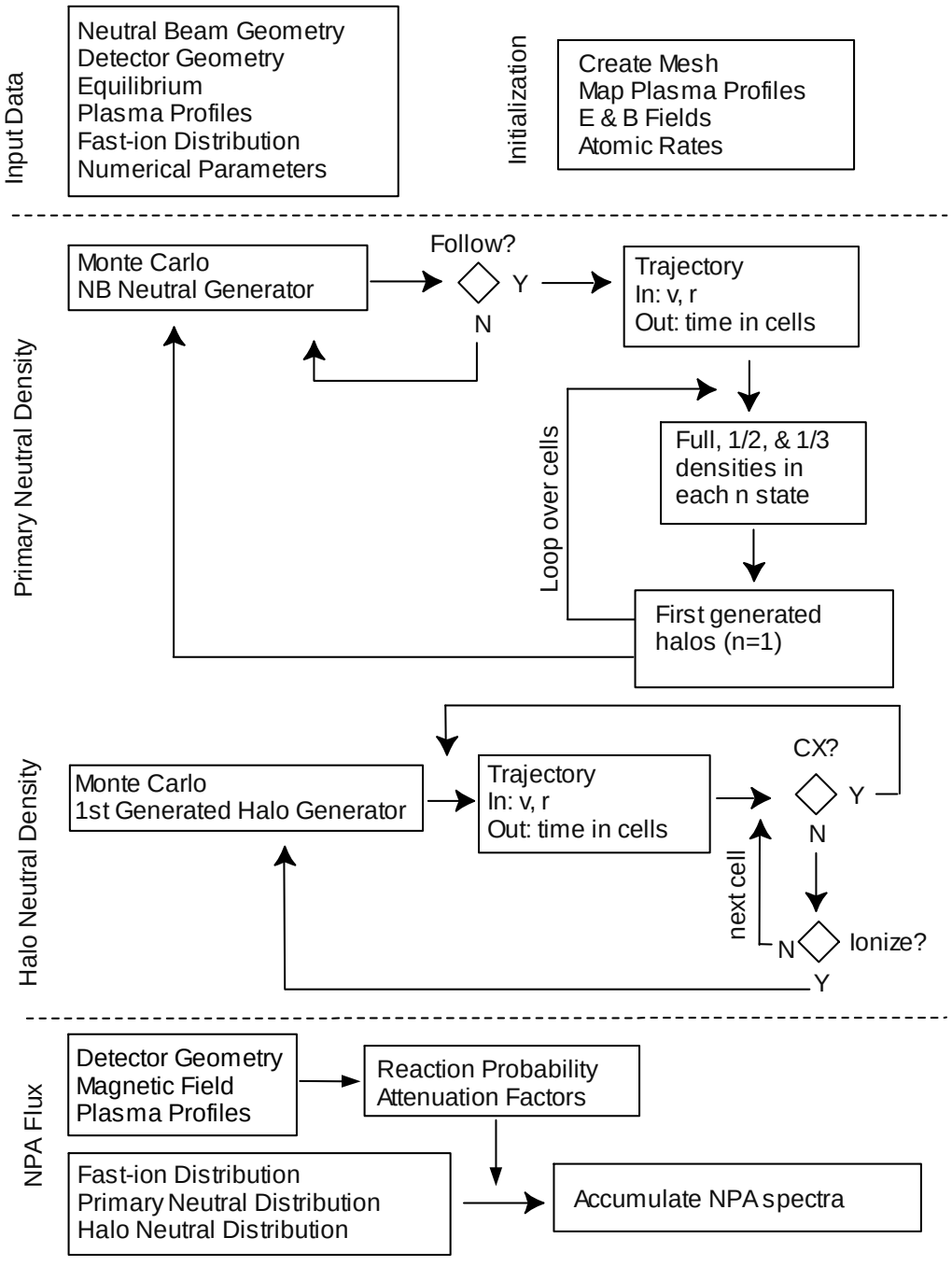

Figure 4.1: Flow diagram of the FIDA_NPA simulation code.

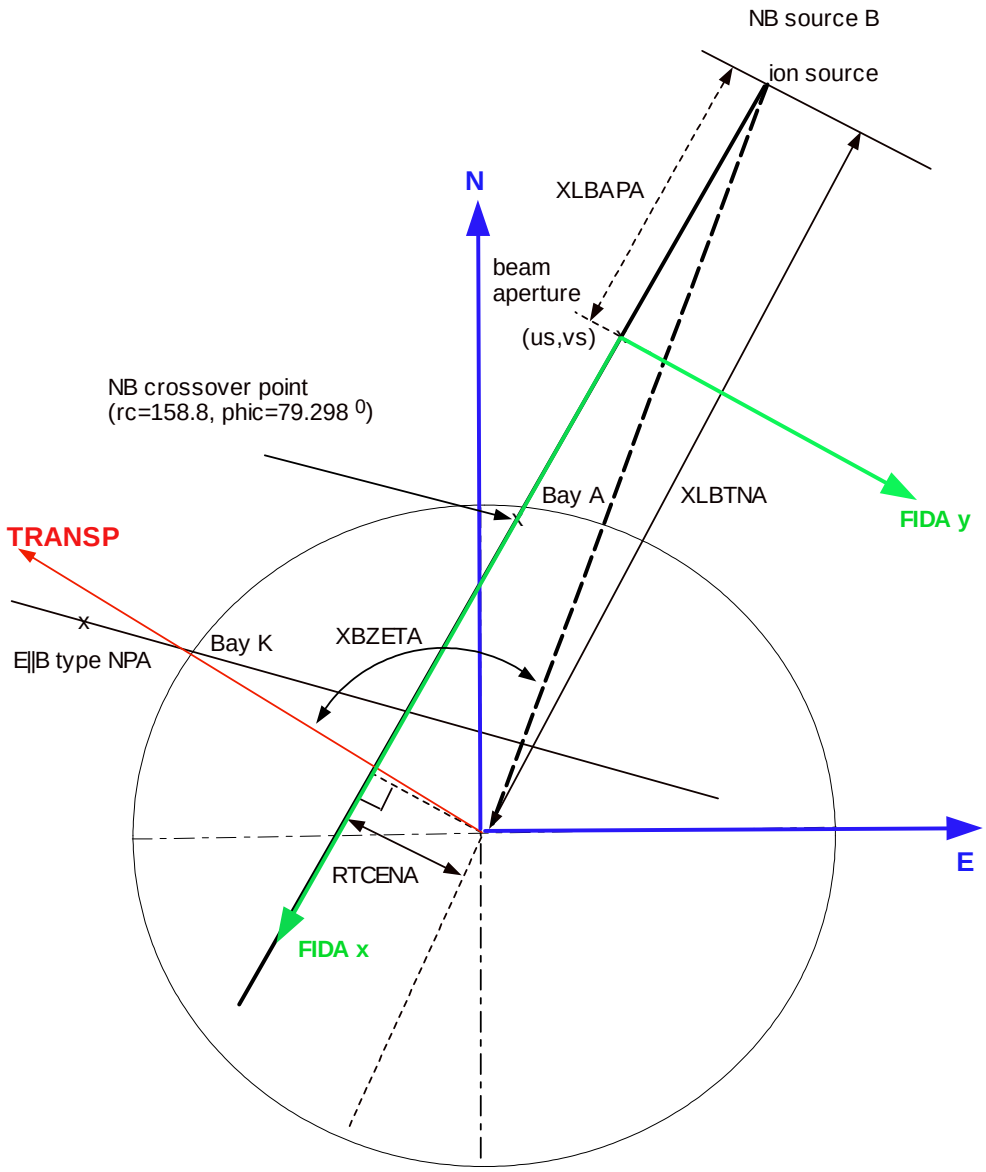

Figure 4.2: Coordinates used in TRANSP and FIDA_NPA simulations and general North-South-East-West coordinates. Since some geometrical parameters (like neutral beam parameters) are either specified in TRANSP coordinates or in ordinary N-S-E-W coordinates, coordinate conversion is performed in the FIDA_NPA input program.

Carlo method. To calculate the primary neutral density, about $50,000$ beam rays for each beam source are launched using the known beam geometry and divergence. Then the code follows the spatial trajectories and energy level transitions of each beam ray, solves the radiation equation in each cell and gets the densities and velocities of the full, half, and third energy neutrals, with each as a function of energy level n. The Charge exchange events for the injected neutrals are the source of halo neutrals. With the calculated primary neutral density, the number of first generation halos (assumed to be $n = 1$ state only) in each cell is determined. These new halo neutrals can have charge exchange reaction again with another bulk ion and hence they participate in pseudo-random walk diffusion from the original birth location. Another Monte-Carlo procedure is implemented to simulate the halo diffusion process. If a charge exchange event happens in a cell, the particle is restarted with a new random velocity based on the local ion temperature and rotation. The neutral is traced until it ionizes or goes outside of the plasma.

After obtaining the primary and halo neutral density, we can accumulate the NPA energy spectra. For each cell inside the NPA/SSNPA viewing cone, the pitch angle ($v||/v$) of charge exchange neutrals that can reach the NPA detector and their charge-exchange reaction rate can be calculated from the geometry of the NBs, NPA detectors and magnetic field profile. The charge exchange neutral production rate in a cell is the product of the fast-ion density, which is a function of position, energy and pitch angle, the primary and halo neutral density, and the charge exchange rate coefficient. The fraction of the neutrals that can reach the NPA detector is equal to the solid angle of the NPA detector opened for that cell divided by 4π. The attenuation factor of the neutrals during the exit from the plasma is calculated with a pencil beam code [101]. The outputs of the main program are neutral particle rate, pitch angle and energy of the neutrals, and attenuation factors for each cell inside the NPA viewing cone.

4.4.2.2 Benchmark

Several benchmarks of the FIDA_NPA code have been performed. The primary beam neutral density profile was compared with the TRANSP simulation as shown in Fig. 4.3. The primary neutral profiles along the y axis (perpendicular to the neutral beam source A) and z axis (vertical to the neutral beam source A) from the FIDA_NPA simulation at the beam tangency point agree well with the TRANSP simulation results and neutral beam calibration data [102]. It should be pointed out that only beam neutrals are considered in the TRANSP simulation in this specific case.

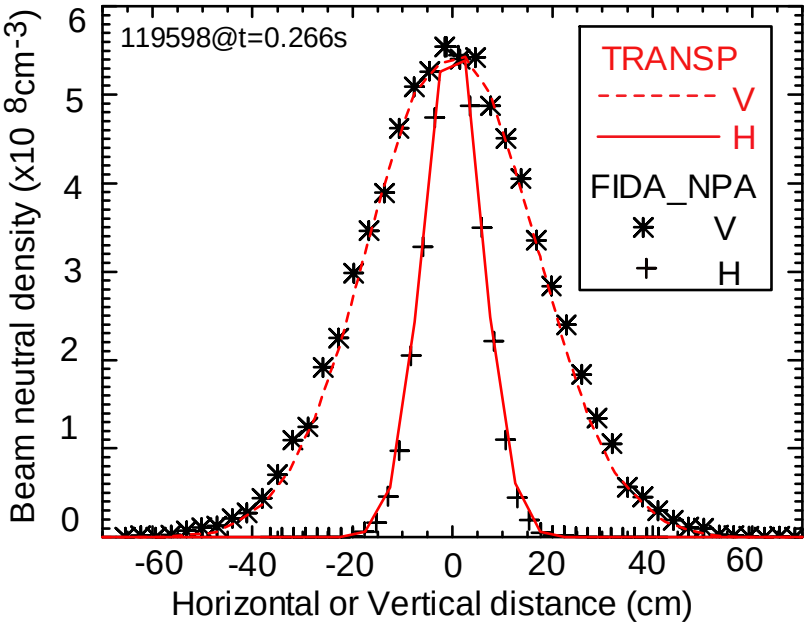

Figure 4.3: Comparison of beam neutral density profile along the y axis. i.e. perpendicular to the neutral beam source, and z axis, vertical to the neutral beam source, from the FIDA_NPA simulation and TRANSP simulation at the beam tangency point (Rmaj=70cm). Both the magnitude and shape agree well, which verifies the calculation of primary beam neutral density in the FIDA_NPA code.

The halo neutral simulation portion of the code was verified by comparing with a relatively simple 1-D diffusion model. If we assume: (1) a uniform plasma with a circular NB beam injection and (2) no beam attenuation along the NB centerline,

the halo neutrals will diffuse only in the radial direction and the density can be determined from the following simple 1-D diffusion model [103]

$$D_{n0}\frac{\partial}{r\partial r}(r\frac{\partial n_h}{\partial r}) = n_h n_e \langle\sigma v\rangle_{ei} - \sum_{k=1}^{k=3} n_i n_{b,k}(r)\,\langle\sigma v\rangle_{cx,k} \tag{4.5}$$

where n_i, n_e, $n_{b,k}$, n_h are ion density, electron density, kth component of primary beam neutral density and halo neutral density respectively, $D_{n0} = k_b T_i/m_d\gamma_{cx}$ is the diffusion coefficient and γ_{cx} here is estimated by the most probable $n_i\langle\sigma v\rangle_{cx}$ based on the ion temperature. The leftmost term in Eq. 4.5 represents the halo neutral diffusion. The term $n_h n_e\langle\sigma v\rangle_{ei}$ is the halo decay term due to the collisions with electrons and the rightmost term is the halo formation term due to charge exchange reactions between the primary beam neutrals and thermal ions. The halo neutral losses through impurity impact ionization and impurity charge exchange are not included in this simple diffusion model, but they are included in the FIDA_NPA simulation code and they have a minor effect (less than 5%) on halo neutral density. Equation 4.5 is an inhomogeneous modified Bessel's equation. In theory, it is not easily solved analytically for a spatially varying beam neutral profile, but a solution exists for a constant source. For example, the radial direction is divided into many regions in the FIDA_NPA programming and plasma parameters like n_i, n_e, and $n_{b,k}$ are constants in each region. Then the halo neutral density solutions for these regions

can be generally expressed as

$$
\begin{aligned}
n_h(r)_I &= C_1 I_0(\lambda r) + \gamma_I/\beta \\
n_h(r)_{II} &= C_2 I_0(\lambda r) + E_2 K_0(\lambda r) + \gamma_{II}/\beta \\
&\cdots \\
n_h(r)_{n-1} &= C_{n-1} I_0(\lambda r) + E_{n-1} K_0(\lambda r) + \gamma_{n-1}/\beta \\
n_h(r)n &= E_n K_0(\lambda r)
\end{aligned}
\tag{4.6}
$$

where I_0 and K_0 are modified Bessel functions, $\lambda = \sqrt{n_e \langle \sigma v \rangle_{ei}/D_{n0}}$, $\gamma_j = \sum_{k=1}^{k=3} n_i n_{b,k}(r) \langle \sigma v \rangle_{cx,k}$ for each region, and $\beta = n_e \langle \sigma v \rangle_{ei}$. The coefficients C_j and E_j are constants that are determined by the boundaries between each region (i.e. $n_i(a) = n_{i+1}(a)$ and $n_i'(a) = n_{i+1}'(a)$).The halo neutral density in the whole region can be obtained by combining all of these analytical solutions. Figure 4.4 shows the halo neutral densities calculated from the diffusion model and the Monte-Carlo halo simulation code for the same given plasma profiles with $n_i = n_e = 1.1 \times 10^{14}$ cm, $T_e = 2.5$ keV and $T_i = 1.25$ keV. The three dashed steps are the input primary neutral density of NB's three energy components in the radial direction. The solid black line is the solution of this 1-D diffusion model and the light blue steps are the halo neutral density from the FIDA_NPA simulation code. They agree pretty well with each other, which verifies the halo neutral simulation module in the FIDA_NPA simulation code. It is also shown in Fig. 4.4 that the halo neutral density can be comparable to the primary neutral density and hence contribute significantly to the NPA flux.

To test the collisional-radiative model, the attenuation factors of the primary beam neutrals along the neutral beam centerline were compared with TRANSP simulation and they are in reasonable agreement. A summary of one of these comparisons is shown in Fig. 4.5. Figure 4.5 (a) shows the neutral density along the NPA sightline

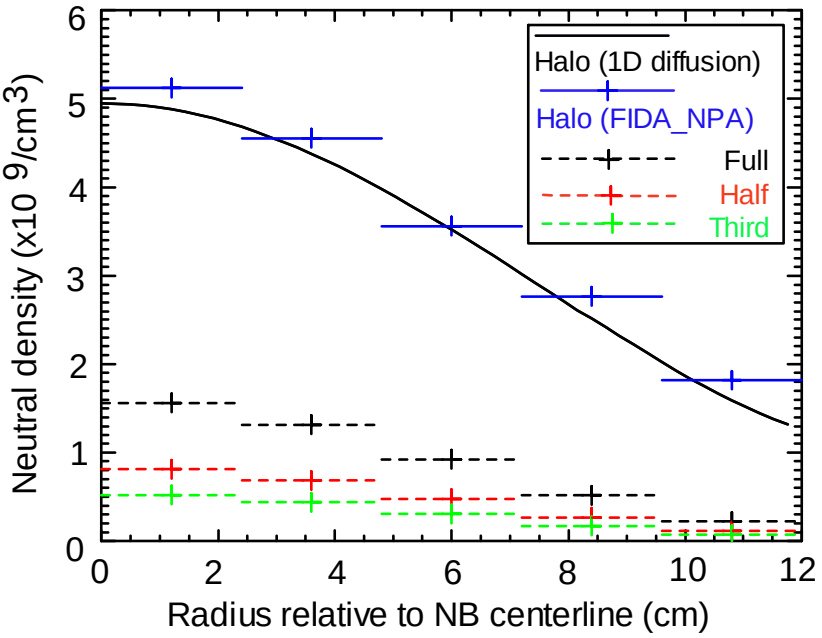

Figure 4.4: Comparison of halo neutral densities calculated from a 1-D diffusion model and the Monte-Carlo halo simulation code for the same given plasma profiles with $n_i = n_e = 1.1 \times 10^{14}$ cm^{-3}, $T_e = 2.5$ keV and $T_i = 1.25$ keV. The three dashed steps in black, red and green colors represent the densities of the full, the half and the third energy components of primary neutrals used in both codes. The halo neutral density from the FIDA_NPA simulation code agrees well with the 1-D diffusion model, which verifies the calculation of halo neutrals in the FIDA_NPA code.

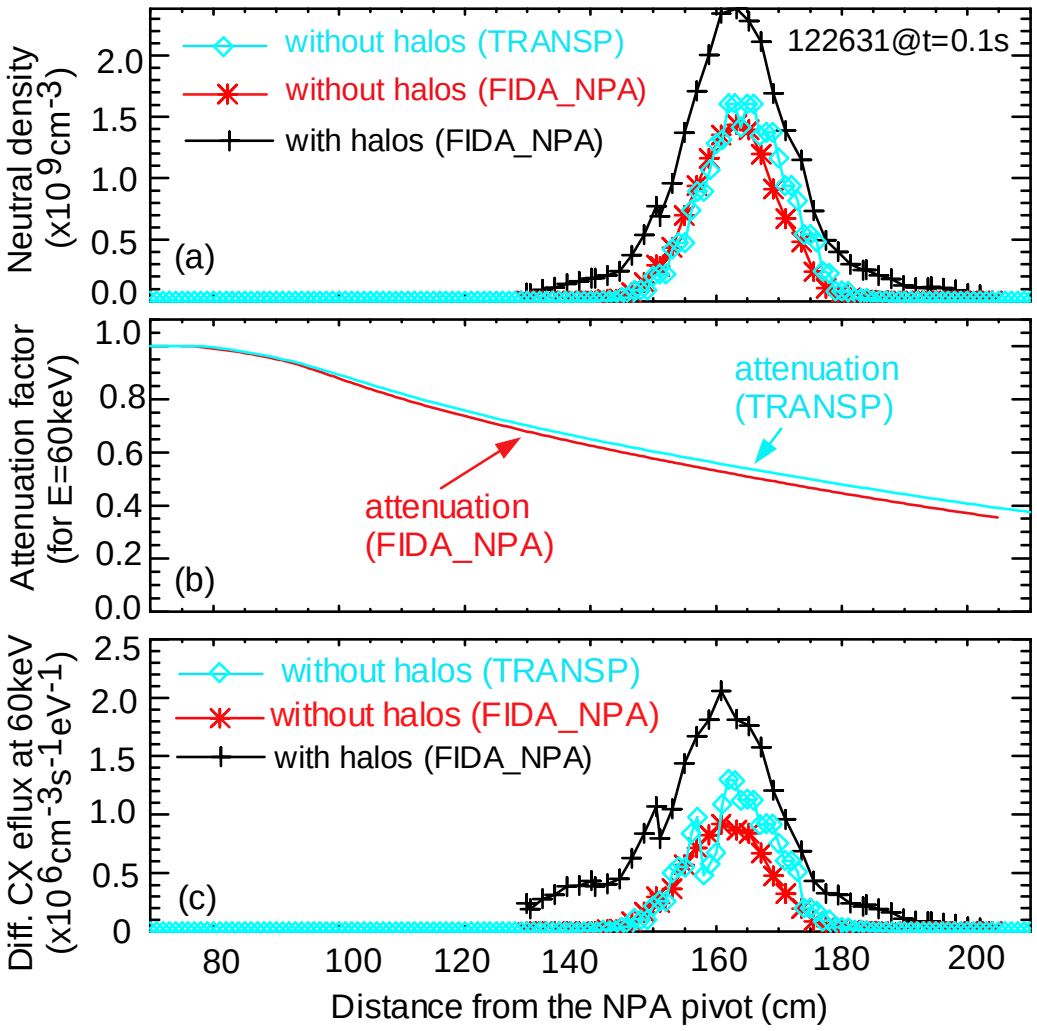

Figure 4.5: Comparison between the FIDA_NPA simulation and TRANSP simulation in shot 122631 and t=0.1s. (a) Neutral density along the NPA sightline; (b) Attenuation factor for neutrals of 60keV along the NPA sightline; (c) Differential CX efflux along the NPA sightline.

from TRANSP simulation and FIDA_NPA simulation. When halo neutrals are not considered, both codes give very similar neutral density. It is also shown in Fig. 4.5 that the halo neutral density can be comparable to the primary neutral density so that the total neutral density almost doubles when halo neutrals are included in the FIDA_NPA simulation code. Figure 4.5 (b) and (c) show the attenuation factors and differential charge exchange flux along the NPA sightline for neutrals with energy of 60 keV from the TRANSP simulation (light blue line) and the FIDA_NPA simulation (red line) respectively. The small discrepancies between two simulations in Fig. 4.5 are likely due to different atomic cross sections being used (Sect. 4.4.2.1).

4.4.2.3 Effect of Halos on NPA Measurements

Figure 4.6 shows an example of NPA energy spectra from the TRANSP-based NPA and FIDA_NPA simulation codes. When only primary beam neutrals are considered in the two codes, they predict very similar NPA energy spectra. When halo neutrals are included in the FIDA_NPA simulation code, they contribute significantly to the NPA flux, but they barely change the shape of the energy spectra. In principle, a difference could appear since $\sigma_{cx}(E_{rel}^{i,n})V_{rel}^{i,n}$ depends on $V_{rel}^{i,n}$, which is not the same for primary neutrals and halo neutrals. But, the actual effect is small.

Figure 4.7 shows the temporal evolution of (a) plasma current, electron temperature and electron density,(b) neutral beam power and (c) NPA flux from FIDA_NPA simulation. It is shown that the charge exchange reactions between fast ions and halo neutrals can change the temporal evolution of NPA flux. This is because the ratio of beam neutrals to halo neutrals can vary with the plasma parameters, for example, electron temperature and electron density. The primary beam neutral and halo neutral density along the NPA sightline at six selected time slices are shown in Figure 4.8.

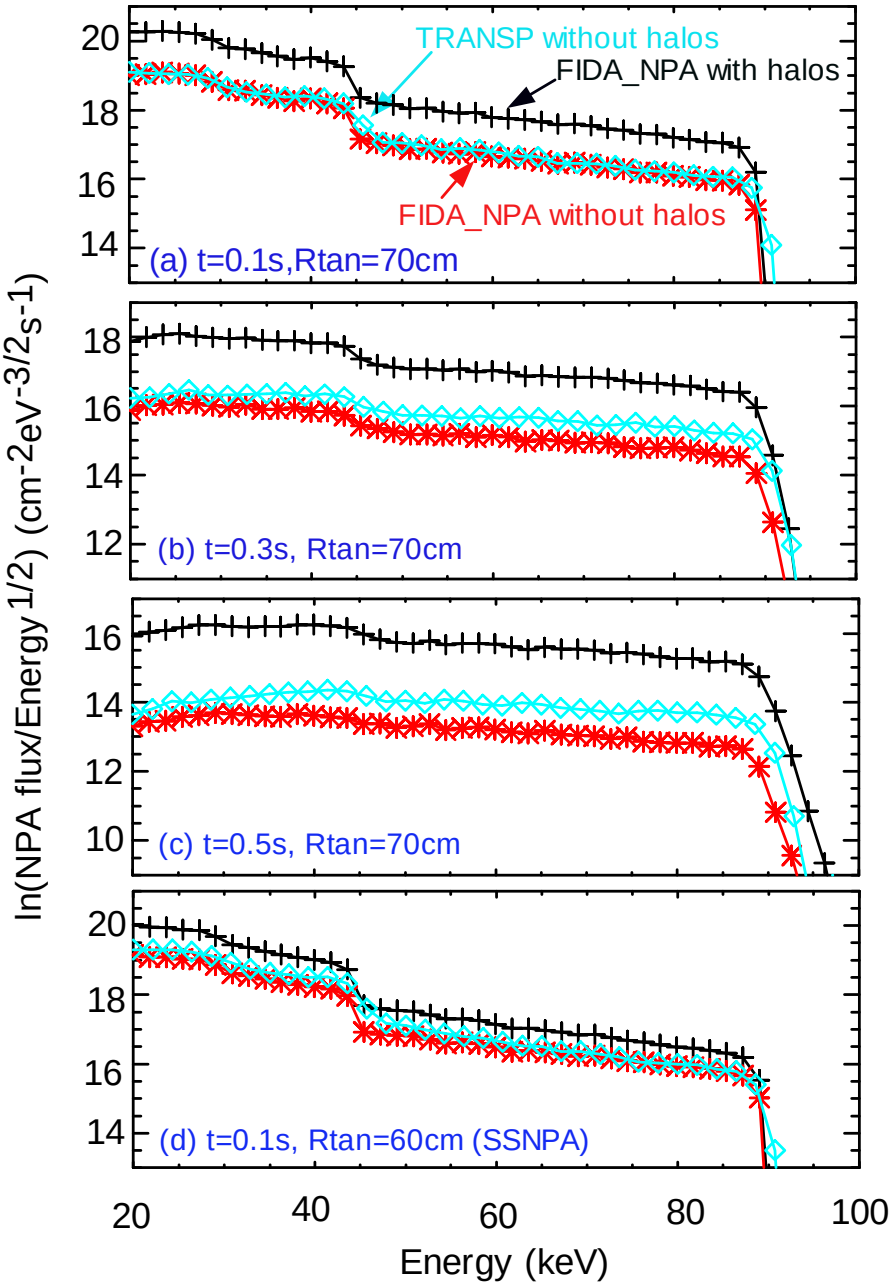

Figure 4.6: Energy spectra from the FIDA_NPA (red lines without halo neutrals and black lines with halo neutrals) and TRANSP (light blue lines) simulations at (a) t=0.1 s, (b) t=0.3 s, and (c) t=0.5 s for shot 122631.

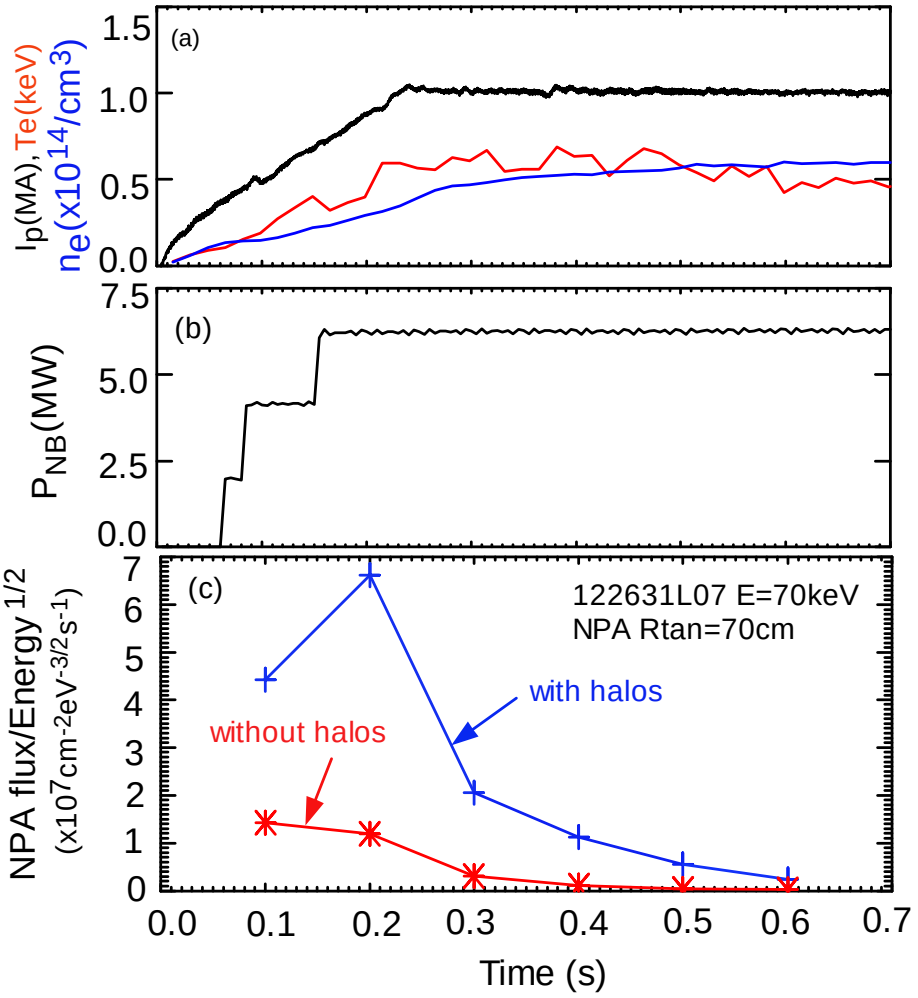

Figure 4.7: Temporal evolution of (a) plasma current, electron temperature and electron density, (b) neutral beam power, and (c) NPA flux at E=70 keV from the FIDA_NPA simulation.

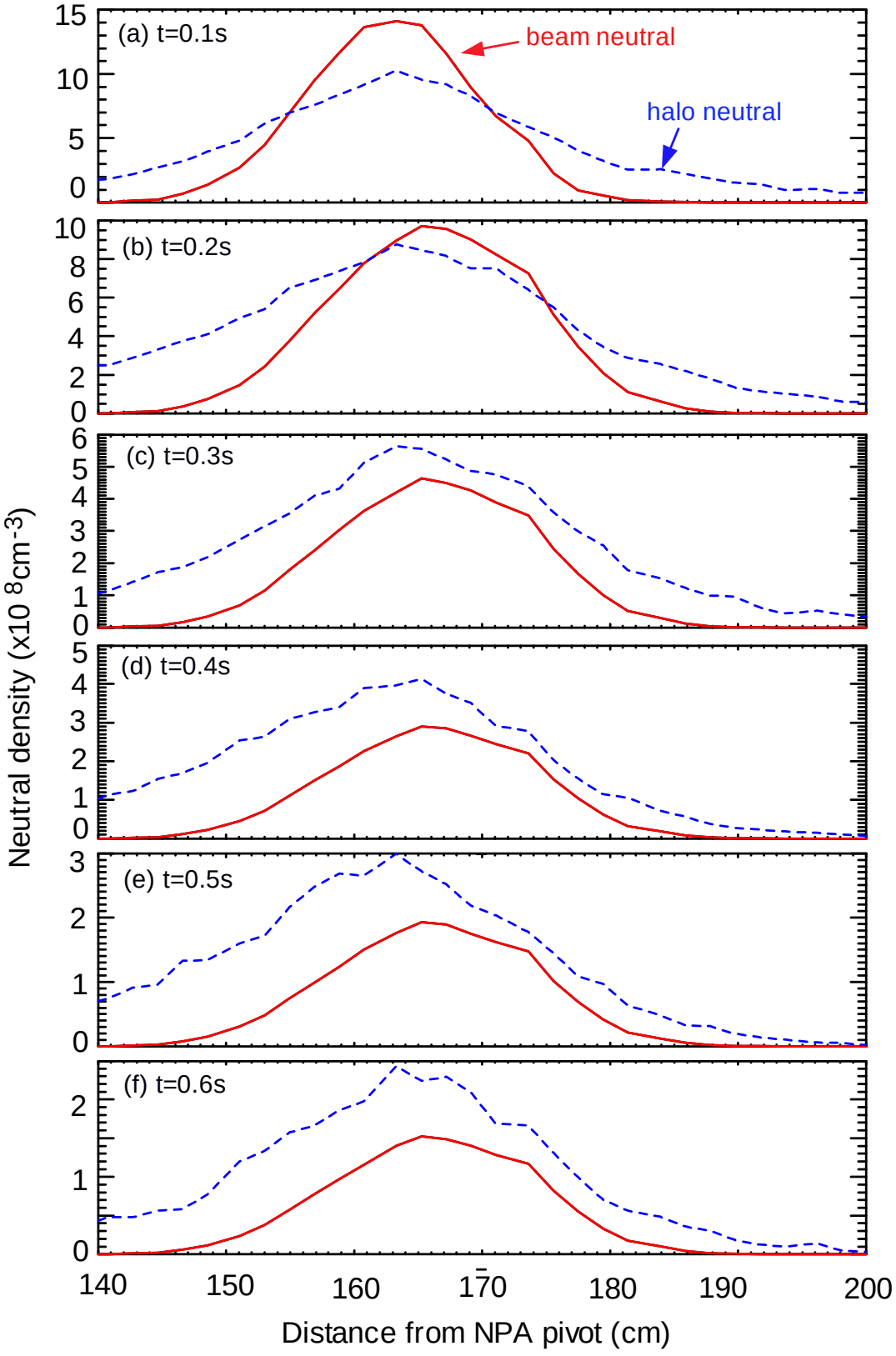

Figure 4.8: Primary beam neutral and halo neutral density along the NPA sightline at (a) t=0.1 s, (b) t=0.2 s, (c) t=0.3 s, (d) t=0.4 s, (e) t=0.5 s, and (f) t=0.6 s from the FIDA_NPA simulations for shot 122631.

Chapter 5

Profiles of Fast Ions that are Accelerated by High Harmonic Fast Wave Heating

5.1 Introduction and Motivation

As described in Sect. 2.1, NBI and HHFW are the two major auxiliary heating systems in NSTX. Up to 7.5 MW of NBI power and 6 MW of HHFW power can be deposited into bulk deuterium plasmas in NSTX. The interactions between fast waves and fast ions from NBI have been extensively studied in many toroidal fusion devices [30, 104, 105, 106, 107, 108, 109, 110, 111, 112, 113, 114]. The wave absorption by fast ions at the fundamental cyclotron frequency or low harmonics can form an energetic, anisotropic tail distribution and this wave absorption competes with electron

absorption, which reduces the available power for electron heating and current drive by the fast waves. Acceleration of fast ions at the third, fourth and fifth harmonics is now an established technique and has been demonstrated in many recent experiments [112]. In particular, the $k_\perp \rho_f$ dependence, where $k_\perp$ is the perpendicular wavenumber and ρ_f is the fast-ion gyroradius, is well established. The discharges in NSTX provide a unique opportunity for studying the interactions between HHFW and fast ions at high β and dielectric constant ($\varepsilon \equiv {\omega_{pe}}^2/{\Omega_{ce}}^2 \sim 50$). Because of the relatively low magnetic field, fast ions produced during NBI in NSTX are super-Alfvenic and the ratio of the gyroradius to the perpendicular wavelength is very large. In addition, the spacing between harmonic layers is much narrower than in conventional aspect-ratio tokamaks especially when compared with orbit size. Significant absorption of HHFW power at multiple cyclotron harmonics is expected. These differences of NSTX from conventional tokamaks motivate this careful comparison between theory and experiment in this unusual regime.

The acceleration of fast ions by HHFW in NSTX was previously studied by Rosenberg et al. with neutron and E||B type Neutral Particle Analyzer (NPA) measurements [113]. Although the acceleration was observed by both diagnostics, little information was obtained on the spatial profile of the absorption. The newly installed FIDA diagnostic makes radially-resolved measurements of the fast-ion profile possible. (The FIDA measurements of accelerated beam ions by high harmonic cyclotron heating in DIII-D were recently published [114].) In Sect. 5.2 and 5.3, the measurements of accelerated fast ions in a variety of fast ion diagnostics are shown and compared with the predictions from the Fokker–Planck CQL3D code.

5.2 Experimental Conditions and Results

5.2.1 Experimental Conditions

The data presented here are from a half day run during the 2008 experimental campaign. In all the shots of this experiment, the toroidal magnetic field is about 0.55 T at the magnetic axis, the plasma current is about 800 kA, the outer gap is about $3-4$ cm, and the central density is around 3.0×10^{13} cm^{-3}. Neutral beam source A (R_{tan}=0.69 m) at 90 keV was applied at two times of $0.06-0.15$ s and $0.42-0.57$ s to obtain MSE data. During the time of $0.15-0.4$ s, short pulses of neutral beam source B (R_{tan}=0.59 m) injected approximately 1.1 MW of ~ 65 keV deuterons into deuterium NSTX plasmas (Fig. 5.2 (a)). Beam modulation technique is applied here to minimize fast-ion driven instability and to perform background subtraction for fast ion diagnostics. The 30 MHz HHFW system couples $\sim$ 1.1 MW of power between 0.21 and 0.37 s with parallel (to the magnetic field) wavenumber $k_{||}$ =7 m^{-1}. At such a wave number, fast waves propagate mostly in the co-current direction and resonate with deuterium cyclotron harmonics at multiple radial locations with the central resonance corresponding to the eighth harmonic and the outer edge resonance corresponding to the eleventh harmonic (Fig. 5.1).

The temporal evolution of plasma parameters in the discharges with and without HHFW heating is shown in Fig. 5.2. For comparison, the NB timing and power are exactly the same in the shots with RF as in the no-RF reference shot. As shown in Fig. 5.2(b), plasma parameters (plasma current and electron temperature) in the three nominally identical RF shots and the no-RF reference shot are similar except that the electron density n_e is slightly larger in the RF shots. As expected, there is no robust MHD activity in the spectra of Mirnov signals (Fig. 5.2(c)), since the beam modulation technique and relatively low injection energy are used to reduce

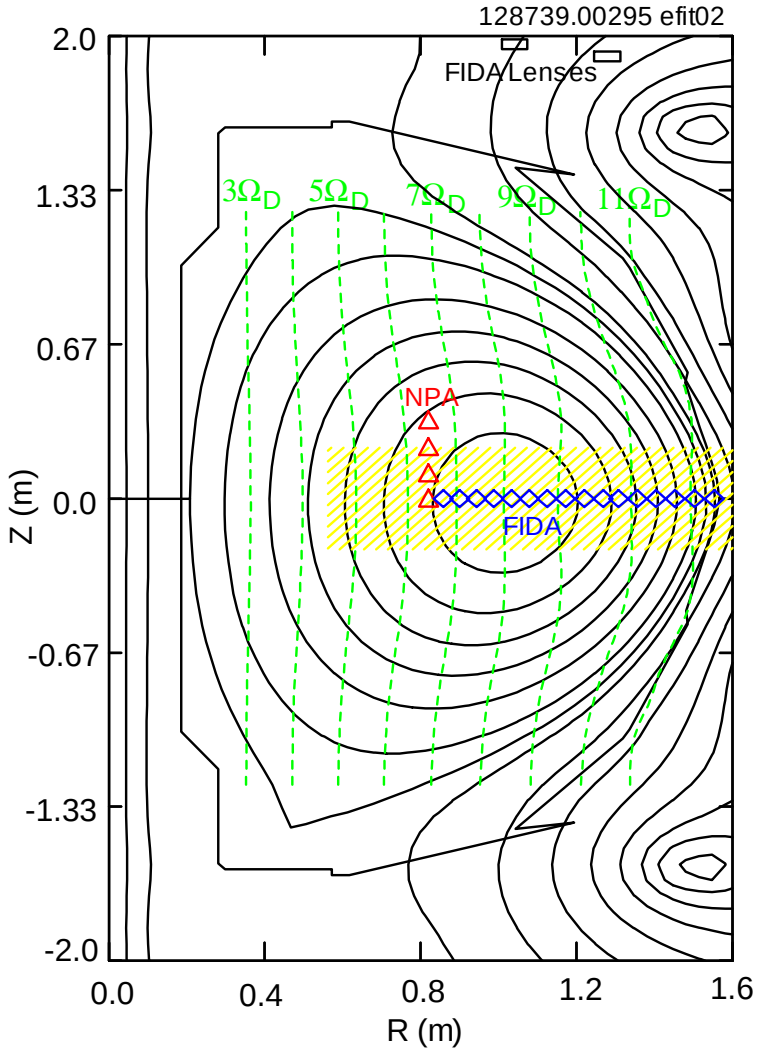

Figure 5.1: Elevation of the NSTX vacuum vessel, showing the flux surfaces (solid black curves), the locations where ω_{RF} equals the $3rd - 11th$ deuterium cyclotron harmonics (dashed green lines), the midplane locations of the FIDA channels (diamonds) and elevation minor radii of the E||B type NPA during the four-shot vertical scan (triangles). The hashed region represents the approximate extent of the neutral beam that produces the FIDA and NPA signals. The rectangles indicate the approximate locations of the FIDA lenses.

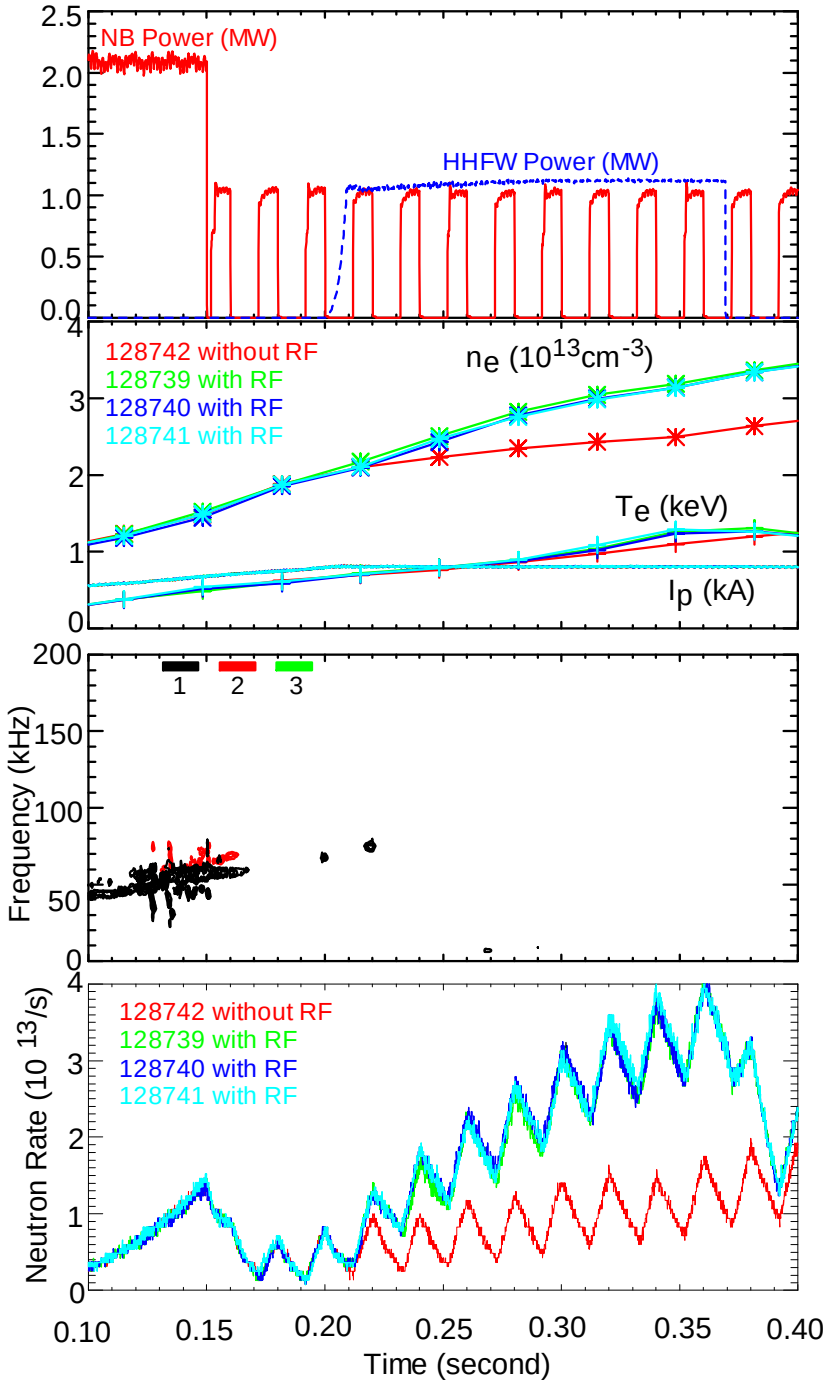

Figure 5.2: (a) Temporal evolution of NB power and HHFW power in the three nominally identical RF shots. (b) Temporal evolution of central electron density, electron temperature and plasma current in the no-RF reference shot 128742 and the three nominally identical shots 128739 – 128741. (c) Spectrum of Mirnov coils of shot 128739 in the low frequency range of $[0, 200]$ kHz. The color indicates toroidal mode number. (d) The d-d neutron emission rates in the no-RF reference shot 128742 and the three nominally identical shots 128739 – 128741.

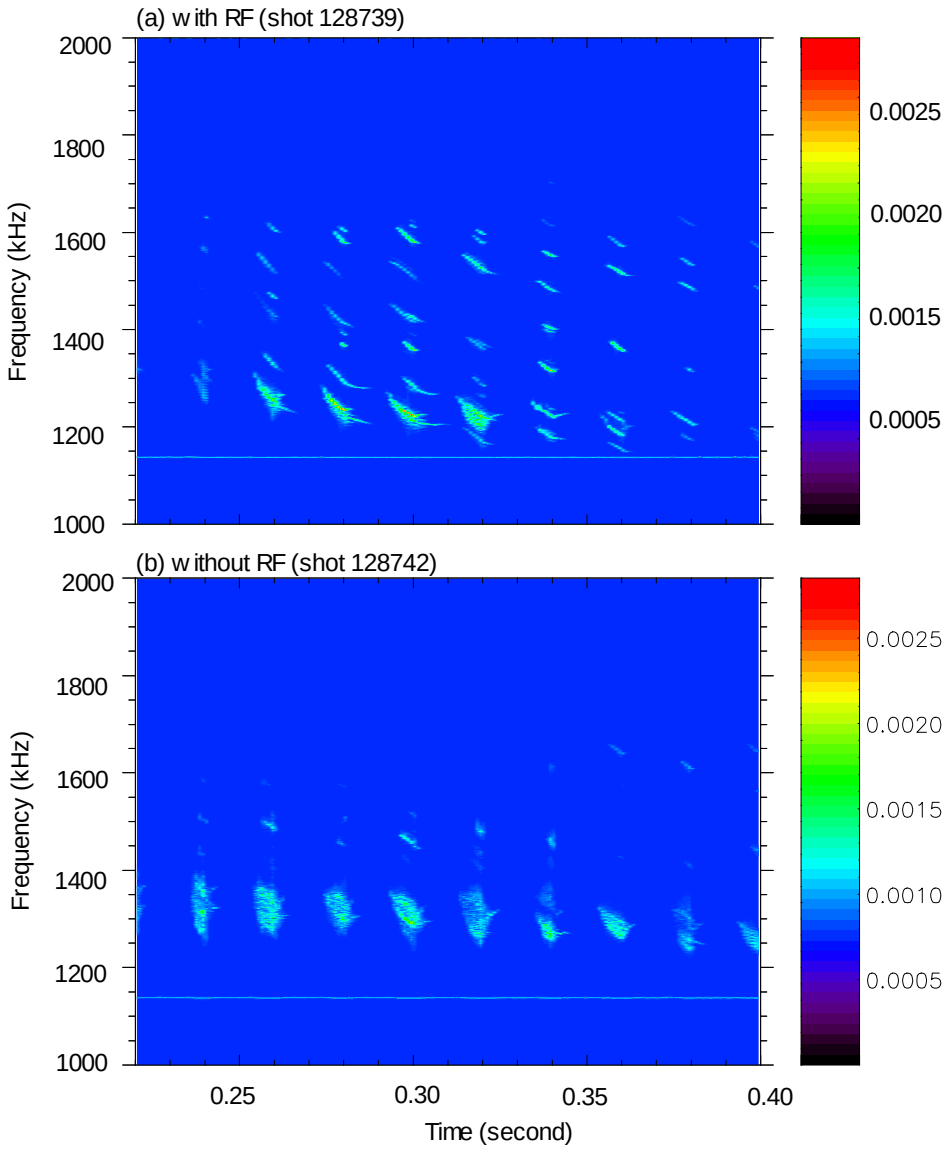

Figure 5.3: Spectra of Mirnov coil signals in the frequency range of [1000, 2000] kHz in the discharges with and without RF. Note that color indicates FFT mode amplitude. The FFT mode amplitude in our experiment is relative weak (less than 1/4 of that in typical NSTX plasmas).

the fast-ion population. However, weak Compressional Alfven Eigenmodes (CAEs) exist in all shots (Fig. 5.3). As shown in Fig. 5.3 (a), the CAEs during the HHFW heating are about 25 percent stronger in mode magnitude and show some chirping feature with frequency sweep of 150 kHz. This may affect the fast ion spatial profile.

5.2.2 Neutron Measurements

Neutron measurements clearly show that fast ions are accelerated by the HHFW heating. Since the NB is modulated, the neutron emission rate shows similar modulation trend as the injected NB (5.2(d)). The time-averaged level of neutron emission rate rises by about a factor of three during the HHFW heating. Because the neutron rate is dominated by beam-plasma reactions, this indicates that a significant fraction of high-energy fast ions are accelerated by the HHFW heating. The pulses in the neutron rate between 0.17 and 0.37 second were analyzed using the technique described in Ref. [115]. For each pulse, the neutron emission R_n rises nearly linearly during the beam injection, then decays approximately exponentially following the pulse (Fig. 5.4). Because the rise depends on the number of confined beam ions and the decay depends on beam ion slowing down and loss, the neutron signal can be fit to the equation $\frac{dR_n}{dt} = c - \frac{R_n}{\tau_n}$ during the beam pulse and to $\frac{dR_n}{dt} = -\frac{R_n}{\tau_n}$ after the pulse, where the constant c reflects the prompt confinement of the injected beam ions and is proportional to $(dN_b/dt)n_d \langle\sigma v\rangle$. Here dN_b/dt is the rate at which full-energy beam ions are injected into the device, n_d is the deuterium density in the center of the device, $\langle\sigma v\rangle$ is the averaged D-D reactivity, and τ_n is the neutron decay time. As shown in Fig. 5.5(a), the rise rate c of the neutron emission in the HHFW heating shots agrees well with that in the no-RF reference shot prior to the injection of HHFW power, but it is slightly larger upon the injection of HHFW power. This is because the deuterium density n_d is slightly larger due to the higher electron density during the HHFW heat-

ing. As shown in Fig. 5.5(b), the neutron decay time τ_n in the HHFW heating shots agrees well with the no-RF reference shot prior to the injection of HHFW power, but increases substantially upon injection of HHFW power. This is because the size of the tail of the distribution is determined by a competition between Coulomb drag and acceleration by cyclotron absorption. The fast ion distribution function f can be described by the Fokker-Planck equation

$$\frac{\partial f}{\partial t} = C + Q + S \tag{5.1}$$

where C represents the collision operator, Q represents RF acceleration and S represents particle sources and sinks. When the NB is turned off, $S \simeq 0$ at high energies. Then the neutron decay during the beam turn-off period reflects the competition between Coulomb deceleration and HHFW acceleration. From Fig. 5.5(b), it can be estimated that the high-energy ions that dominate the D-D beam-target fusion neutron rate experience strong acceleration that, on average, is nearly $0.5 - 0.7$ of the Coulomb drag in the shots of $128739 - 12841$. The experimental data (discrete points with vertical error bars in Fig. 5.5) are also compared to the predictions (solid lines in Fig. 5.5) from the TRANSP simulation, which uses measured temperature, density, impurity and rotation profiles and assumes fast ions behave classically, but does not include any model for HHFW-induced acceleration. The rise rate of the neutron pulses is accurately modeled by TRANSP both before and during HHFW injection, because the beam ions that have just been injected have not had enough time to be accelerated, so they produce the same number of neutrons before and during the HWFW heating. The predicted neutron decay time is in good agreement with the measured values prior to the HHFW injection, but it is much smaller than the measurements during the HHFW heating. This indicates that fast ions are accelerated by the HHFW heating, which increases the slowing-down time above the

classical value and consequently the fast ion density.

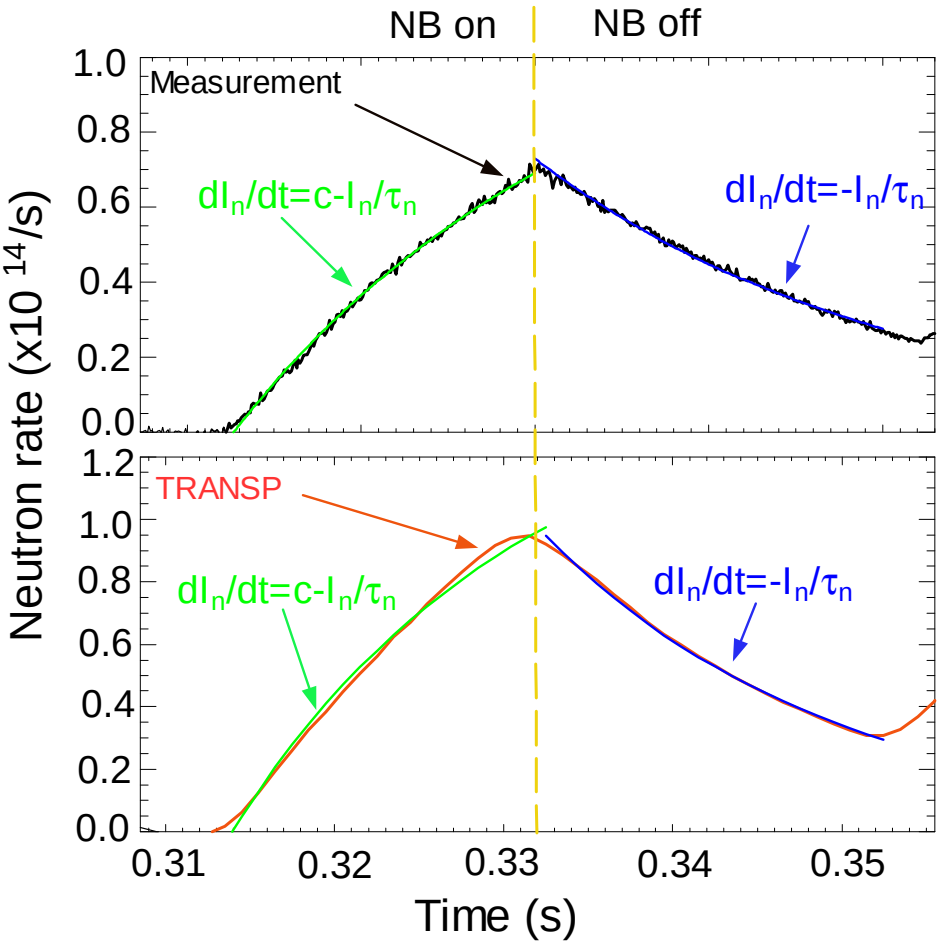

Figure 5.4: Details of a neutron pulse in the measurements and TRANSP simulations. The neutron rate rises nearly linearly during the NB injection, and then decays approximately exponentially when the NB is turned off.

5.2.3 NPA and SSNPA Measurements

The application of HHFW gives perpendicular energy to fast ions through cyclotron resonance. In Ref. [113], a clear fast ion tail due to HHFW heating in NSTX was observed on the E||B type NPA diagnostic when HHFW and NBI were active simultaneously. Furthermore, the tail decayed to the no-RF spectrum after RF turnoff with NBI remaining active. Unfortunately, in our experiment, the NPA energy spec-

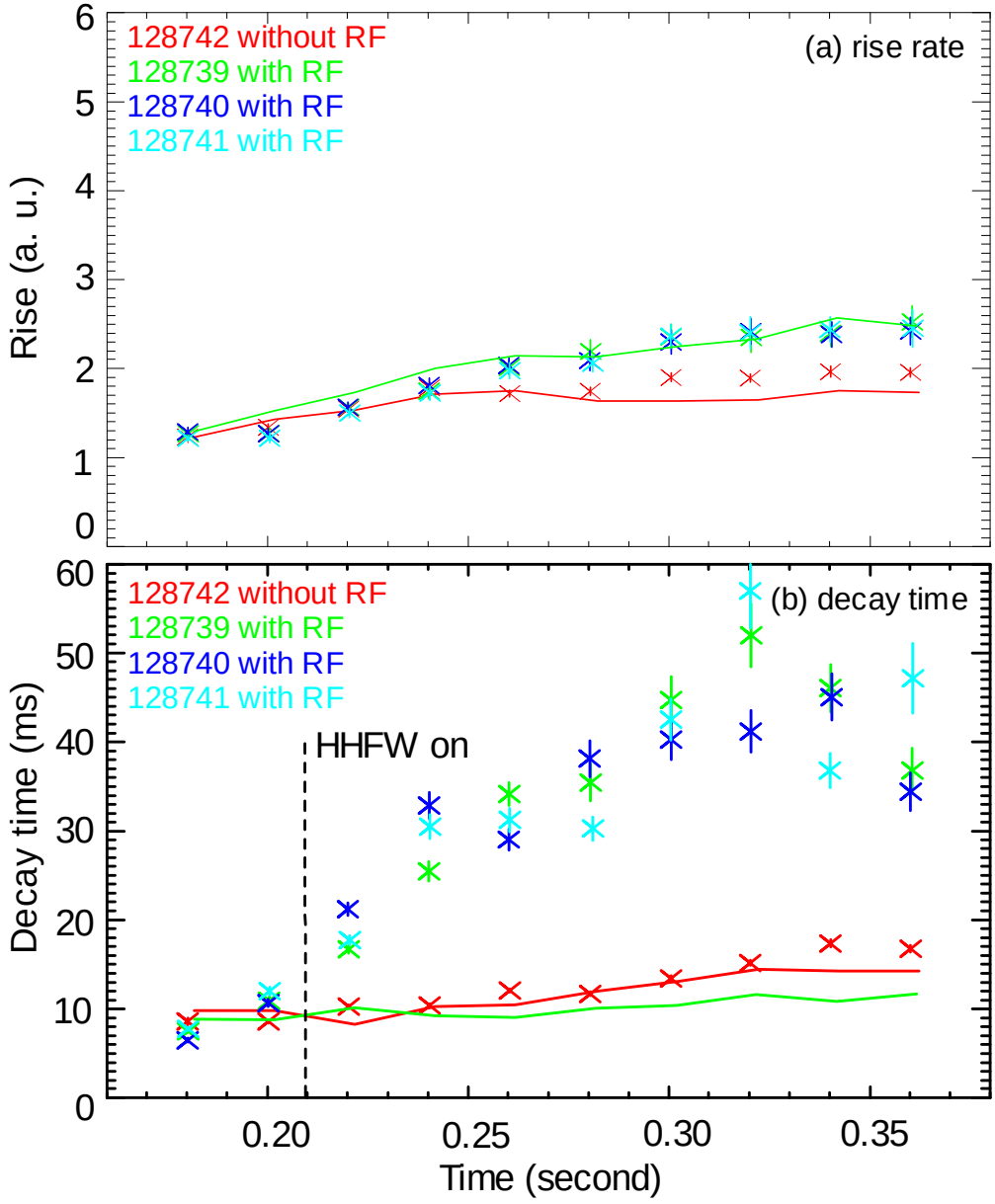

Figure 5.5: (a) Rise rate and (b) decay time of neutron emission rate versus time in the discharges with and without HHFW heating. The symbols represent experimentally measured values. The solid lines are TRANSP predictions that employ the measured profiles but do not take into account HHFW-induced acceleration of the beam ions.

tra were contaminated by RF-induced noise. However, with the assumption that the RF-induced noise is unaffected by the modulated NB, active CX energy spectra can be obtained by subtracting the NPA signal in the beam-off period from that in the beam-on period. In this way, the RF-induced noise and the passive CX signal are effectively removed. As shown in Fig. 5.6, the active CX energy spectrum of the E||B type NPA during the HHFW heating shot shows only a small D^+ tail above the beam injection energy. Similarly, the active CX energy spectra from the SSNPA do not show any obvious D^+ tail (not shown here), but the total energy spectra (which is the summation of active and passive signals) of SSNPA show a D^+ tail up to 100 keV (Fig. 5.7). (Note that the energy spectrum which shows an accelerated fast ion tail in Ref. [113] is also the energy spectrum of the NPA total signals.) This suggests that the accelerated fast ions that are observed by the NPA diagnostics are mainly from the passive CX reactions at the edge. The reason why the active CX signals do not show an obvious D^+ tail is that the small portion of phase space observed by the NPA was weakly affected by the HHFW heating. More details will be presented in Sect. 5.3. The active CX signals from this pitch-angle scan show fast ions are accelerated ~ 10 keV above the injection energy and a strong fast ion tail is observed at the vertical angle of 12 degrees with the elevation minor radius of 33 cm (Fig. 5.15). The energy spectra of total signals from the SSNPA measurements (Fig. 5.16) during these nominally identical shots show that the acceleration of fast ions is strong in the chords $1-3$ whose pitches at the edge are between 0.3 and 0.5. It also suggests that the acceleration is strong in the more perpendicular direction, as expected for fast wave heating.

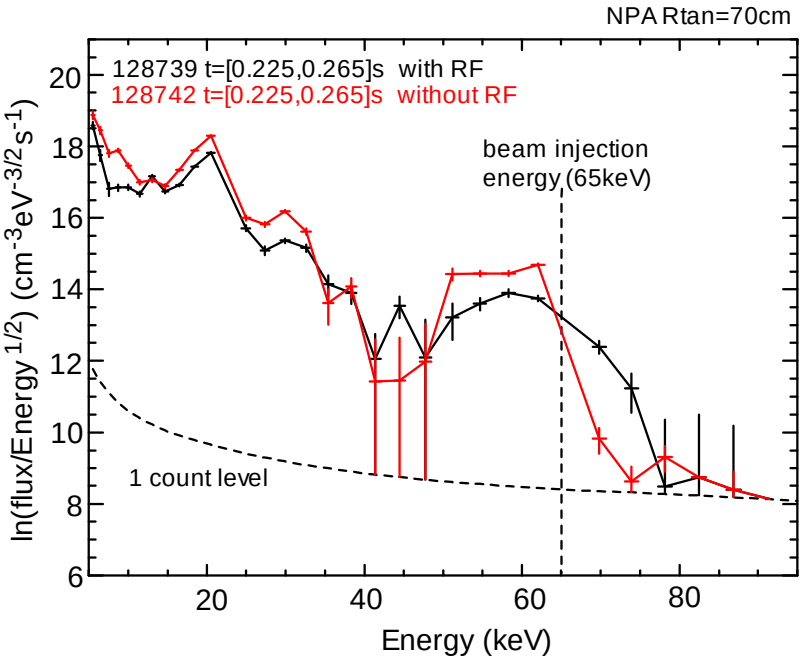

Figure 5.6: Energy spectra of active CX signals from the E||B type NPA at a sightline tangency radius of 70 cm for NSTX shots 128739 (with RF) and 128742 (without RF).

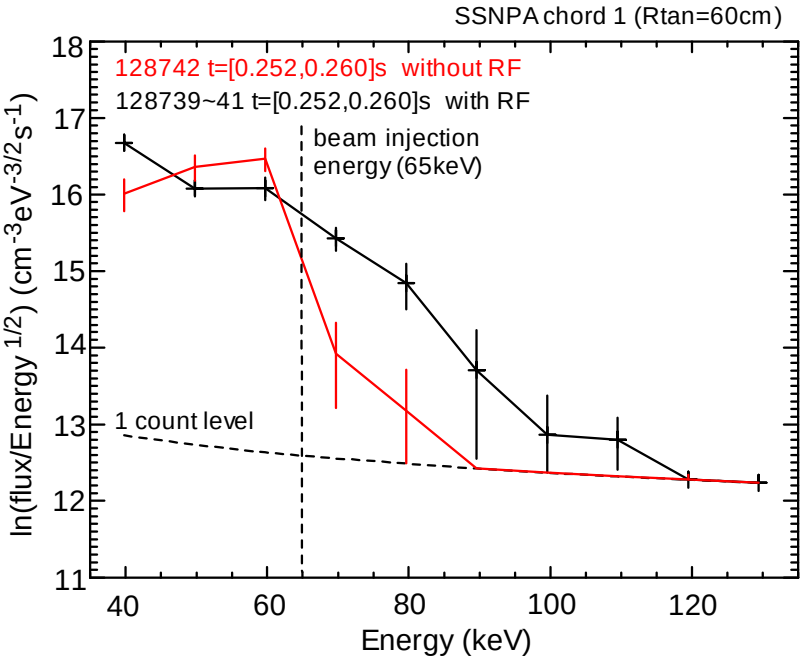

Figure 5.7: Energy spectra of total CX signals of chord 1 of SSNPA with tangency radius of 60 cm in shots 128739 (with RF) and 128742 (without RF).

5.2.4 FIDA Measurements

FIDA data also confirm that fast ions are accelerated by fast waves. Figure 5.8 shows the comparison of the FIDA energy spectra in the discharges with and without HHFW heating. It shows that the FIDA density, which is proportional to the local fast ion density, of channel 11 with $R_{maj} = 108$ cm in the energy range of $E_\lambda = 15 - 65$ keV is much larger in the discharges with RF than without RF. For example, the FIDA density for $E_\lambda \simeq 42$ keV, which is actually dominated by the fast ions with beam injection energy and angle ($E_\lambda \simeq 65$ keV, $p = 0.6$) increases by a factor of 2 in the RF shots. The data indicate that fast ions are accelerated and some of them are above the beam injection energy.

The acceleration of fast ions during the HHFW heating can also be observed in the spatial profile of energy-integrated FIDA density (Fig. 5.9). To determine the radial position of the fast-ion acceleration, Fig. 5.10 shows the enhancement of the energy-integrated FIDA density in the HHFW heating shots as a function of major radius. For both energy integration ranges in Fig. 5.10, the FIDA density increases significantly in the RF shots in a very broad region. The enhancement is largest between the 7 Ω_D and 8 Ω_D harmonic resonance layers. (The magnetic axis $R_{maj} \simeq 100$ cm is also in that region.) This is different from the observations in DIII-D [114]. More details will be presented in Sect. 5.3. The peak in the FIDA density enhancement around $R_{maj} = 150$ cm occurs near the 11 Ω_D harmonic resonance layer; this increase in signal is also accentuated because the channel is close to the plasma boundary where the FIDA density in the no-RF reference shot is small. Figure 5.10 shows that the enhancement of the FIDA density in the energy integration range of $E_\lambda = 30 - 65$ keV (Fig. 5.10 (b)) is about twice as large as the FIDA density enhancement (~ 1.5) in the energy integration range of $E_\lambda = 10 - 65$ keV (Fig. 5.10 (a)). This is because HHFW heating is a finite Larmor radius effect that depends

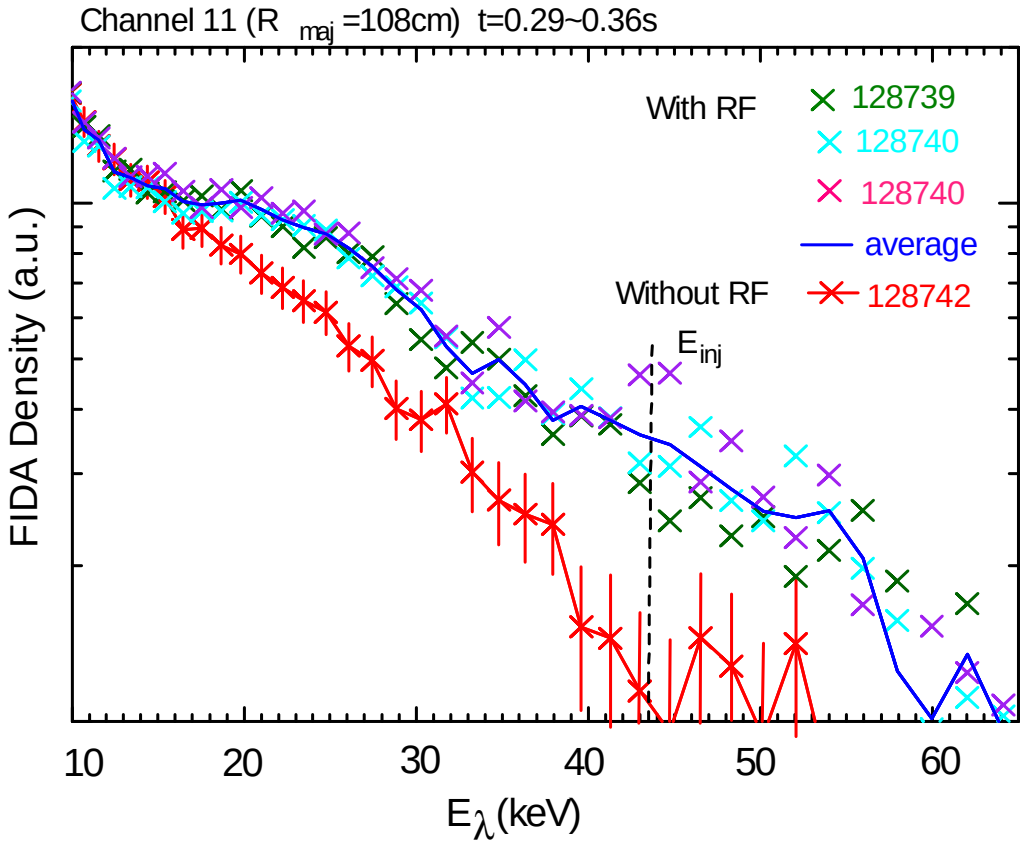

Figure 5.8: Energy spectra of channel 11 (R_{maj} = 108 cm) of the FIDA diagnostic in the no-RF reference shot 128742 and three nominally identical RF shots 128739 – 128741 (where the red line is the average of the three RF shots). The vertical error bars in shot 128742 show typical statistical error in these shots. Note that the energy axis E_λ is the energy component of fast ions along the viewing sightline.

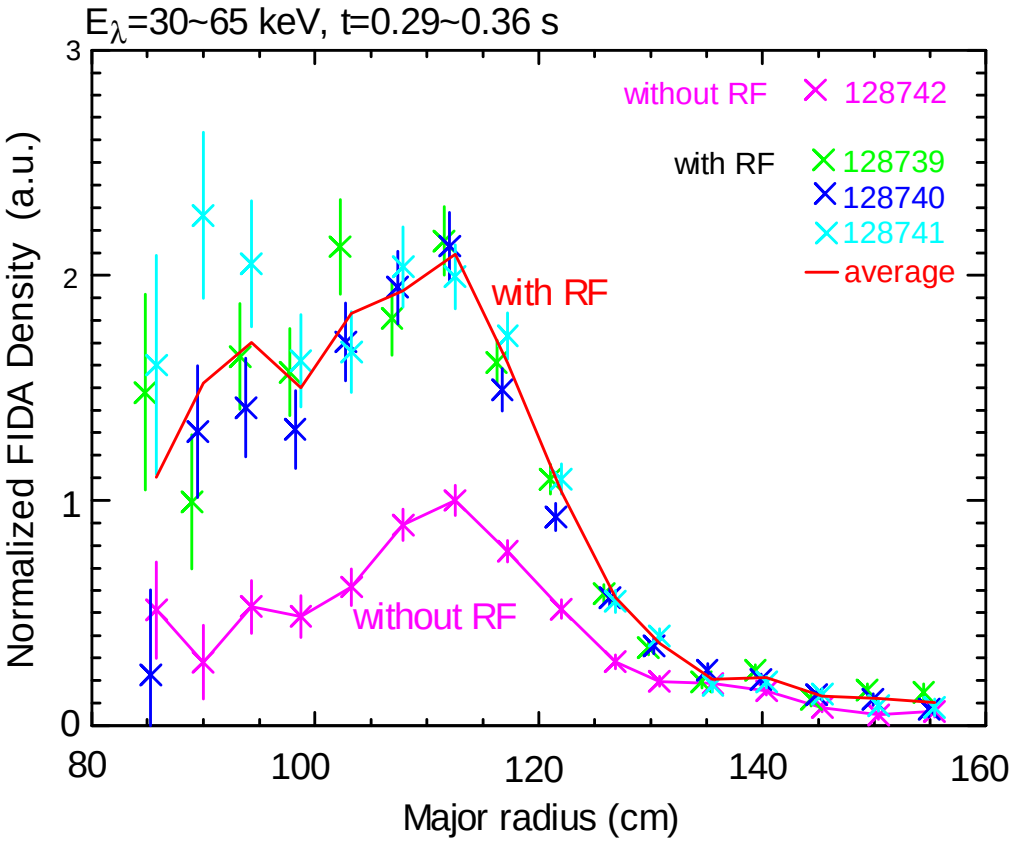

Figure 5.9: Integrated FIDA density ($E_\lambda = 10 - 65$ keV) vs major radius. The blue, light blue and pink symbols represent the FIDA enhancement in three nominally identical RF shots (128739, 128740 and 128741) relative to the no-RF reference shot 128742. The red line is the average of the three RF shots. The vertical error bars are statistical error.

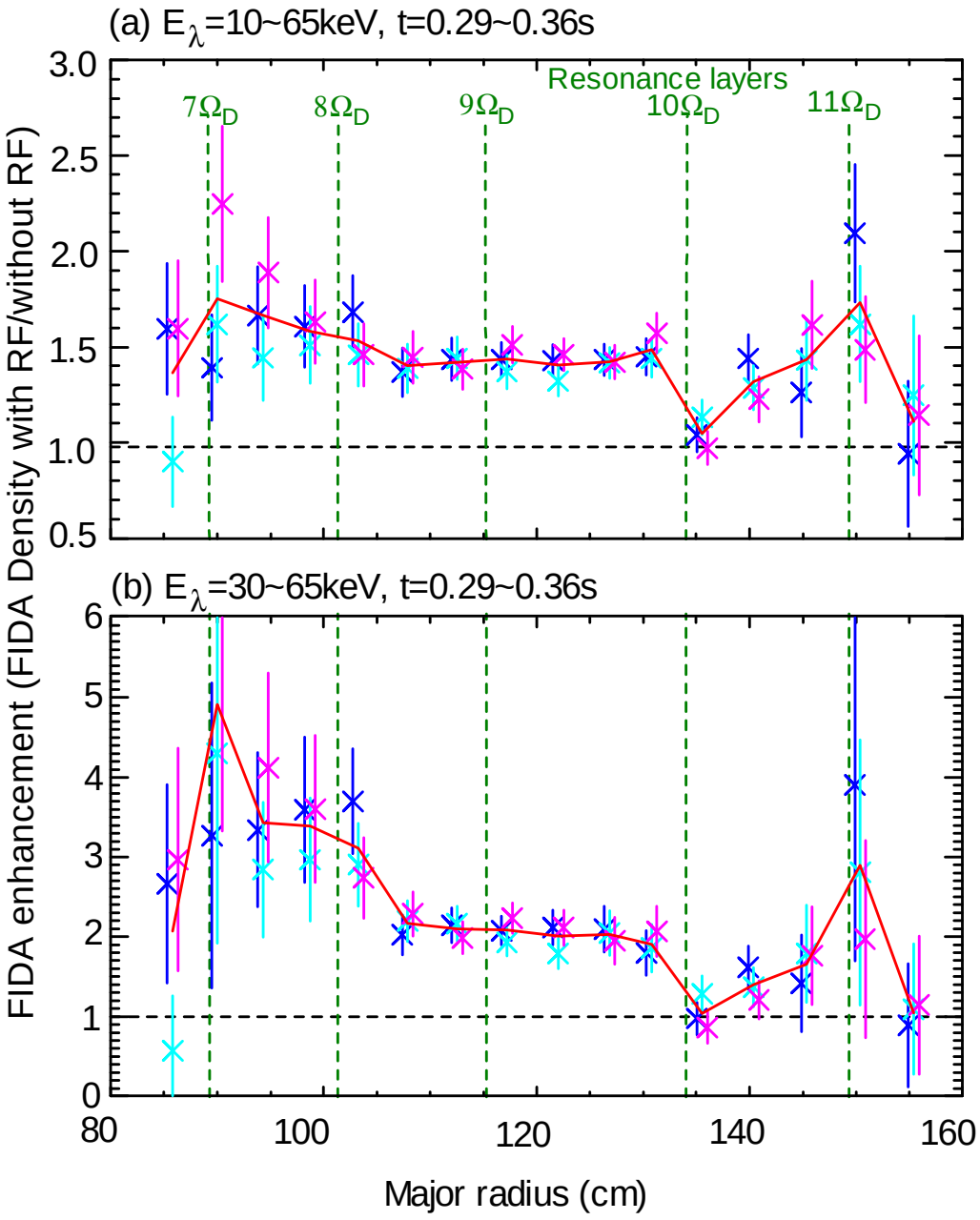

Figure 5.10: Relative change in integrated FIDA density in the discharges with and without HHFW heating for energy integration range of (a) $E_\lambda = 10 - 65$ keV and (b) $E_\lambda = 35 - 65$ keV during the time window $0.29 - 0.35$ s. The blue, light blue and pink symbols represent the FIDA enhancement in three nominally identical RF shots (128739, 128740 and 128741) relative to the no-RF reference shot 128742. The red line is the average of the three RF shots. The vertical error bars are statistical error. The dashed green lines are nominal resonance layers.

upon the value of $k_\perp \rho_f$. The observation is consistent with the theoretical expectation that higher energy ions should be most strongly affected.

5.3 Discussion and Comparison with Theory

Before the comparisons between measurements and simulations are shown, a qualitative picture of fast ion behavior during RF heating is given. When a resonance layer is tuned to a particular major radius of the plasma, fast ions gain a small amount of perpendicular energy every time when they pass through that major radius. As the wave heats the fast ions to higher energies, it pushes them into the trapped region in velocity space. The banana tips of the fast ions are also driven towards the heating resonance layer. This process is illustrated in Fig. 5.11 and this feature is called resonance localization. Furthermore, the fast ions with banana tips near the resonance are actually preferentially heated because their $v_{||}$ is small and thus they spend the longest amount of time around the resonance.

As shown in Sect. 5.2.3, the fast ion tail above the beam injection energy observed by the NPA diagnostics is mainly from the passive CX reactions at the edge, not from the active CX reactions at the intersectional area. This can be understood by looking at the fast-ion distribution in velocity space. Fast ions produced by NBI are mainly confined around the magnetic axis. The initial pitch of fast ions in our experiment is ~ 0.6 due to the injection angle of NB source B. Since the plasma density is relatively low, pitch angle scattering is small. The pitch of the confined fast ions is in a small region around the initial pitch. The main pitch is shown as the blue line in Fig. 5.12 in velocity space with diamond symbols representing the full, half and third energy components of NB injection energy. As shown in Sect. 2.4, the geometry of the NPA/SSNPA sightlines determines the pitch at which fast ions can contribute

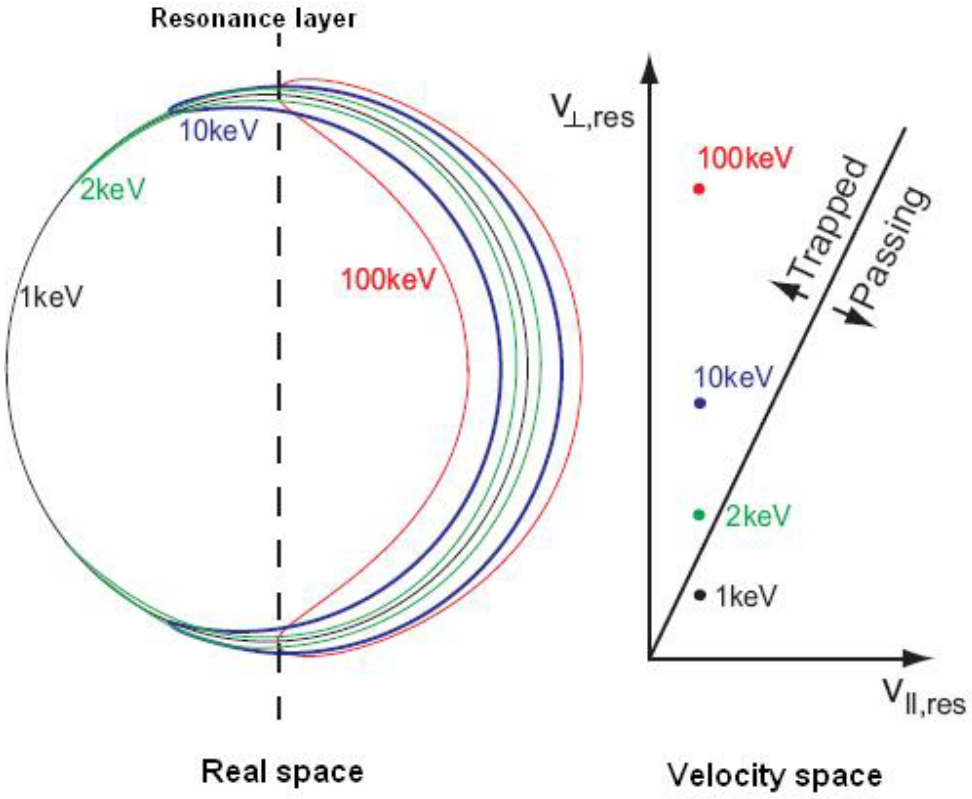

Figure 5.11: Fast ion orbits during successive passes through a resonance layer. The ICRF wave gives perpendicular energy to fast ions and thus pushes them into the trapped particle region. The particle's banana tips eventually end up close to the resonance layer. (Modified from Fig. 1.7 of Ref. [116] and Fig. 2.3 in Ref. [103])

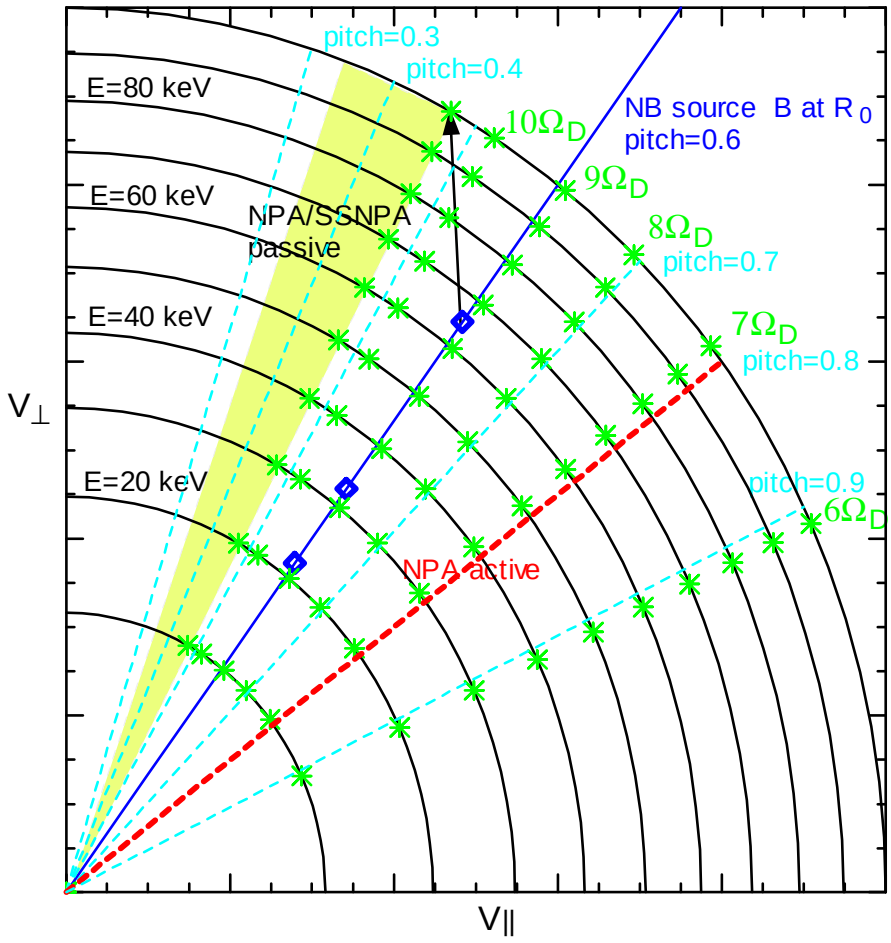

Figure 5.12: Velocity space of fast ions. The blue line shows the pitch of fast ions from NBI at the magnetic axis with diamond symbols representing the full, half and third energy components of the NB injection energy. The dashed red line shows the pitch at which fast ions can contribute to the NPA active CX signals. The pitch range for SSNPA active CX is $0.75 - 0.9$. The shaded yellow region shows the pitch range in which fast ions can contribute to the NPA and SSNPA passive CX signals. The green symbols represent the pitches of fast ions at nominal resonance layers.

to the NPA/SSNPA active CX signals. That pitch is ~ 0.8 (obtained from Fig. 3.14) for the E||B type NPA at tangency radius of $= 70$ cm and it is shown as the red line in Fig. 5.12 in velocity space. For the SSNPA sightlines, the pitch range for active CX signals is $0.75 - 0.9$ (not shown in Fig. 5.12.). The shaded yellow region in Fig. 5.12 represents the pitch range in which fast ions can contribute to the NPA and SSNPA passive CX signals. During the HHFW heating, a fast ion gains perpendicular energy through cyclotron resonance and thus the pitch shifts upward in velocity space. For example, when a 65 keV fast ion gains 35 keV of perpendicular energy, it can move upward in the velocity space and enter the shaded region. Then it becomes detectable for the NPA/SSNPA passive CX signals. For the fast ions with pitch less than 0.8, when they gain perpendicular energy, they move farther away from the red line and they can not be detected by the NPA diagnostic. In addition, very few fast ions are in the region with pitch between 0.9 and 1.0 and the wave electric field at the 6 Ω_D harmonic is relatively small. The combination of these effects explains why the NPA diagnostics measure little fast ion acceleration in the active CX signals but clearly observe the tail in the passive CX signals.

Since fast wave heating imparts only perpendicular energy to fast ions, it will produce fast ions with banana tips or turning points near resonance layers, i.e. resonance localization effect. So the other way to understand the NPA/SSNPA observations is to trace back the trajectories of fast ions before the CX reaction. One example is shown in Fig. 5.13. The fast ion that can contribute to the SSNPA passive CX signals is a barely passing particle and the turning point is near the central resonance layers (Fig. 5.13 (a) and (b)) and the fast ion spends much of its orbit at resonance layers. This is the result of gaining perpendicular energy. In Fig. 5.13 (c) and (d), the fast ion that can contribute to the SSNPA active CX signals is a well confined passing particle. This type of particle is not produced by fast wave heating. This is consistent with our observations that the SSNPA active CX signal does not see a 100

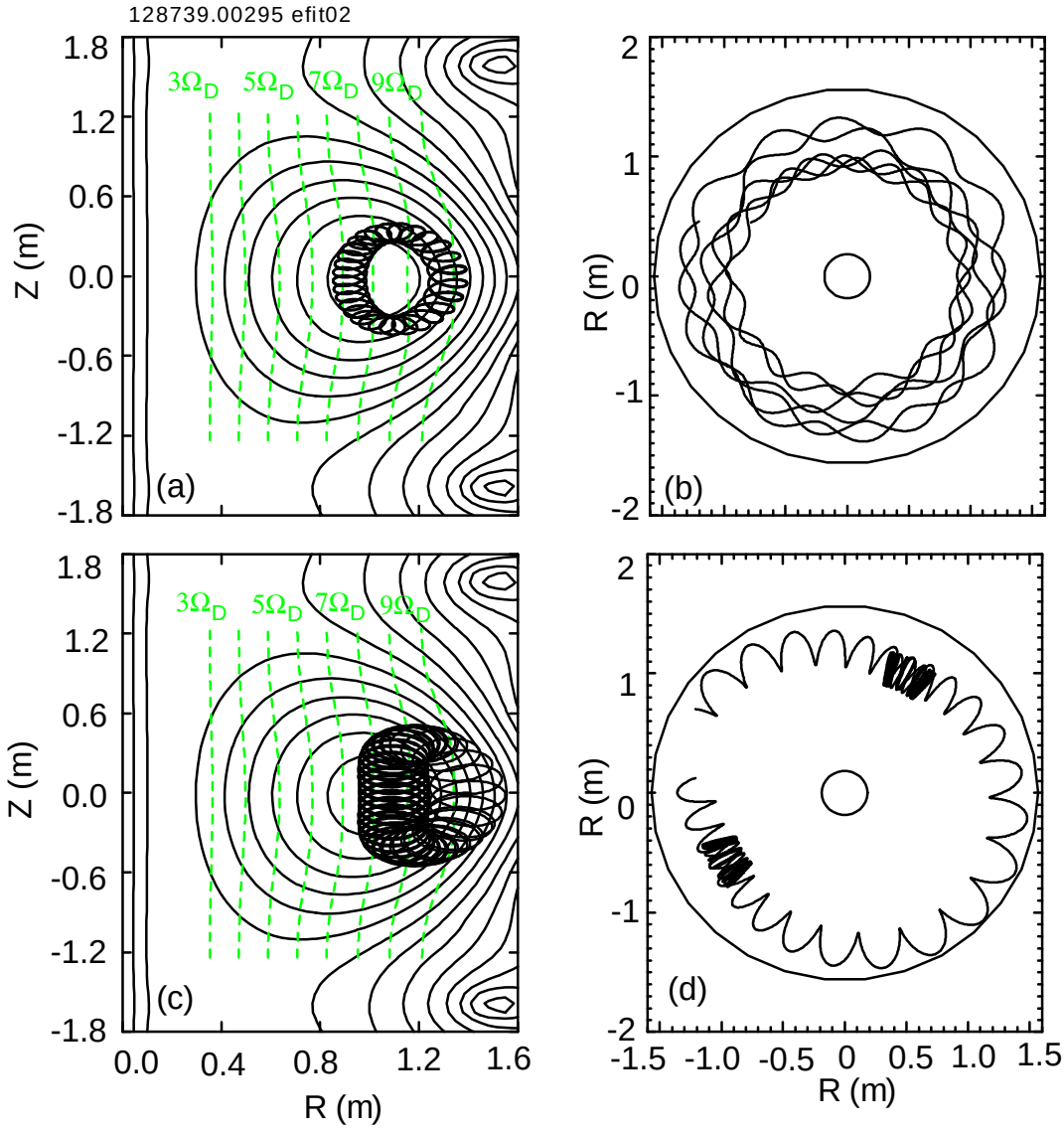

Figure 5.13: (a) Elevation and (b) top view of trajectory of a fast ion (E=100 keV and pitch=0.8) that can CX at R=0.9 m and contribute to the active CX signals of chord 1 of SSNPA; (c) elevation and (d) top view of trajectory of a fast ion (E=100 keV and pitch=0.4) that can CX at R=1.4 m and contribute to the passive CX signals of chord 1 of SSNPA.

keV fast ion tail, but the SSNPA passive CX signal does.

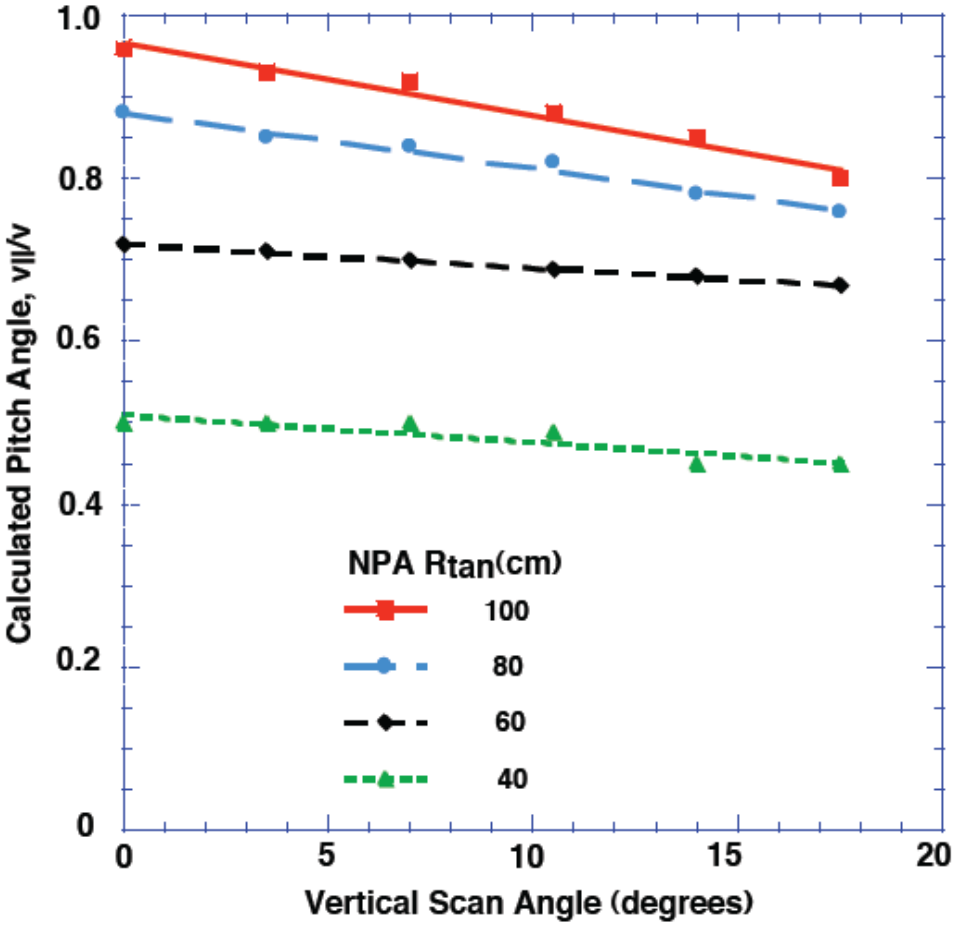

Figure 5.14: The pitches of the E||B NPA at different tangency radii vs vertical angle. Generally the pitch goes down when the E||B NPA scans vertically from zero vertical angle. (Modified from Ref. [117])

The pitch of the observed orbits also explains the results in the E||B type NPA vertical scan, in which the pitch ($p = v_{||}/v$) changes from more parallel (~ 0.8) to more perpendicular (~ 0.72). The pitches of the E||B type NPA at different tangency radii as a function of the vertical angle above the midplane is shown in Fig. 5.14. The similarity between the NPA signals at vertical angles of 0, 4 and 8 degrees (with elevation minor radii of 0, 11 and 22 cm) can be understood by noting that the magnitude of NPA signals is due to the competing effects of pitch angle and neutral

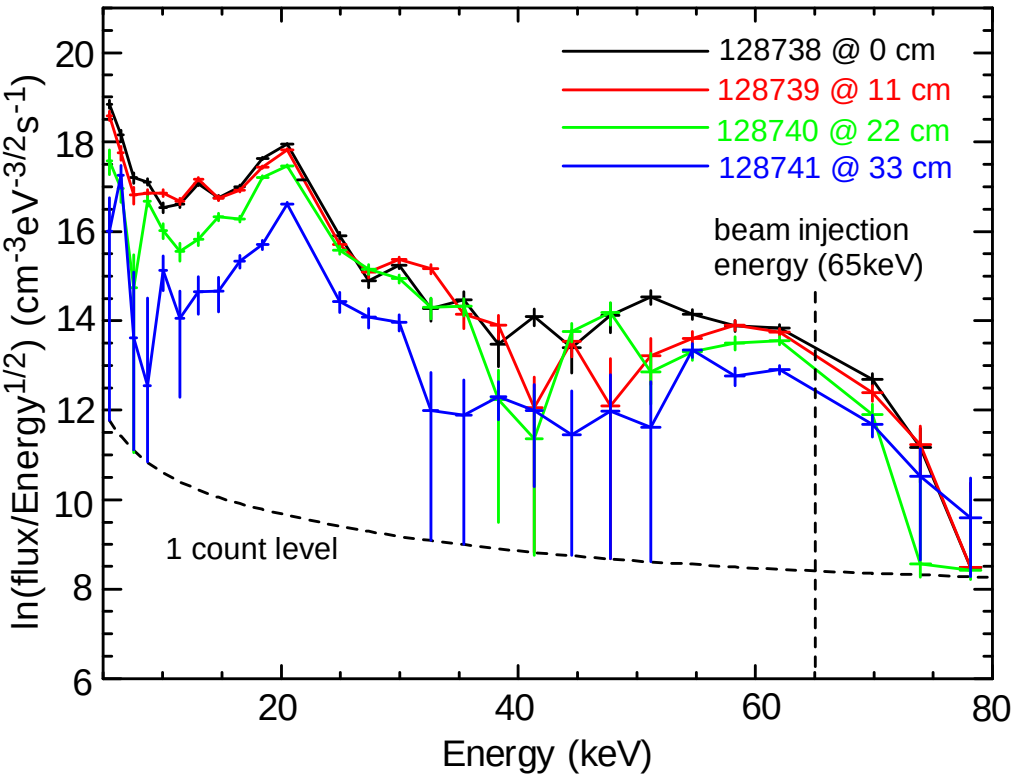

Figure 5.15: Energy spectra of active signals from the E||B type NPA during four nominally identical discharges, in which the NPA scanned vertically with vertical angles of 0, 4, 8 and 12 degrees above the midplane (corresponding elevation minor radius at beam intersection of 0, 11, 22, 33 cm respectively). The NPA tangency radius is 70 cm.

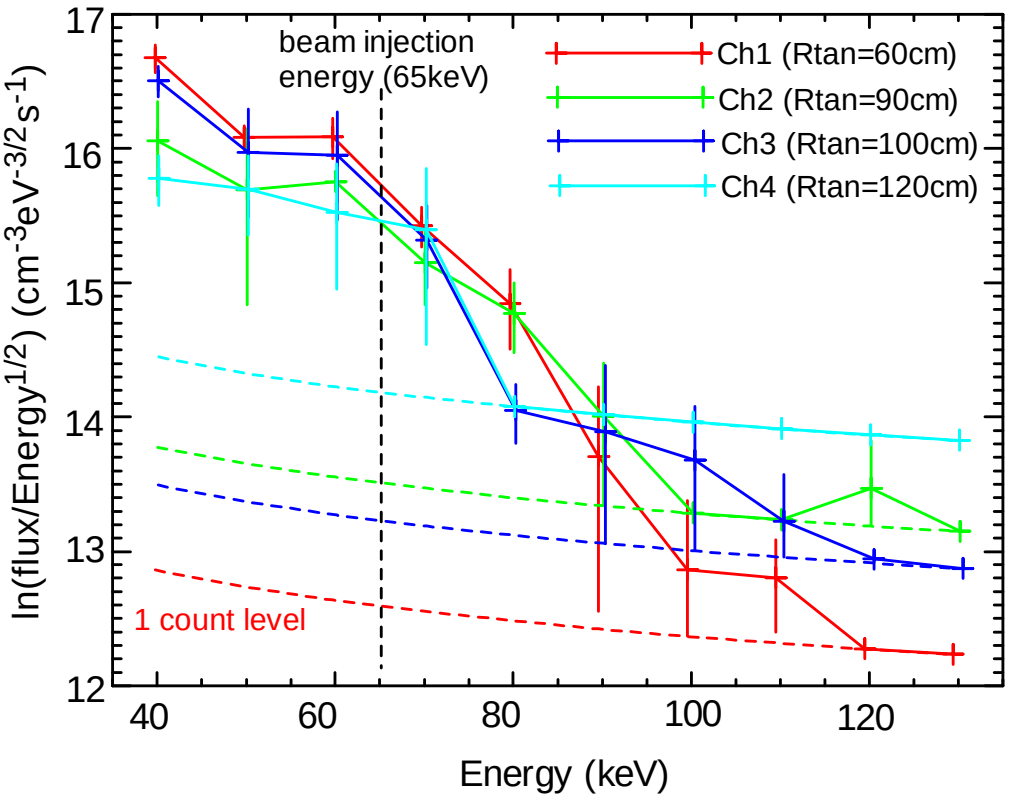

Figure 5.16: Averaged energy spectra of total CX signals of four chords of SSNPA in four nominally identical discharges 128738 – 128741 with HHFW heating. The vertical error bars are the standard deviation of SSNPA signals in these identical discharges. The acceleration of fast ions is strong in chords 1-3 whose pitches at the edge are between 0.3 and 0.5.

particle density localization. With the increase of vertical angle (or elevation minor radius), the beam neutral density is lower and the pitch becomes modestly closer to the pitch (0.6) of the injected NB. For example, the beam neutral density at a vertical angle of 4 degrees is lower than that at 0 degree. But a particle at a vertical angle of 4 degrees would have to pitch angle scatter less to find its way to the E||B type NPA. Thus, the final NPA signals are comparable for vertical angles at 0 and 4 degrees. At the vertical angle of 12 degrees, the beam neutral density decreases dramatically. So the lower signal is understandable. More importantly, a fast ion tail is seen at the vertical angle of 12 degrees because the NPA is in a more perpendicular direction.

As shown in Fig. 5.10 of Sect. 5.2.4, the FIDA density is enhanced significantly in a very broad range from the 6 Ω_D to 10 Ω_D harmonic resonance layers. The enhancement region is much broader than that in the DIII-D [114] case, in which the FIDA spatial profile peaks about $8 - 10$ cm farther out in radius than the nominal resonance layer (due to the nature of banana orbits) and the full width at half maximum (FWHM) is about 15 cm. The difference can be explained by the multiple and closely spaced resonance layers in NSTX and the large gyroradius of fast ions. In NSTX, there are four or five resonance layers in typical discharges from plasma center to plasma edge as shown in Fig. 5.1. The gyroradius of the fast ions with perpendicular energy of 50 keV is about 8.3 cm at the usual NSTX toroidal magnetic field of 0.55 T. (In contrast, in DIII-D there are only one or two resonance layers and the gyroradius of the fast ions is around 2.3 cm at a toroidal magnetic field of 2 T). In addition, the orbit drift displacement is about 20 cm (Fig. 5.13) and is comparable to the spacing between resonance layers in NSTX. The combination of these factors results in accelerated fast ions throughout the plasma cross section, in contrast to the localized profiles observed in conventional tokamaks [118, 119, 120].

The Fokker–Planck equation for the fast-ion distribution function during the

HHFW heating can be solved with the CQL3D code and it can be used as an input in a forward-modelling NPA and FIDA simulation code [61] to compare with measurements. In the version of the CQL3D code employed here, the fast-ion orbits are treated in a zero banana-width approximation and the wave fields in the quasilinear RF operator Q are calculated using ray tracing. Two cases were simulated with the CQL3D code. In the first case, only NBI is considered and it is similar to the no-RF reference shot 128742. The second case includes the interactions between HHFW and fast ions from NBI and it is similar to the three nominally identical RF shots. In both cases, the modulated NB in experiments is replaced with a steady beam that injects the average power. The CQL3D simulations predict a fourfold increase in the neutron emission rate with RF; the measured neutron rate increase is a factor of three. The calculated fast-ion distributions are mapped into the coordinates used in the NPA and FIDA simulation code, namely $F(E, p, x, y, z)$, where E is the energy, p is the pitch of fast ions and (x, y, z) are Cartesian coordinates along the neutral beam that produces the NPA and FIDA signals. Then the code uses the F and the computed injected beam neutral and halo neutral densities to predict the NPA signal and the FIDA spectral intensity. The FIDA simulation code has been verified in quiescent plasmas in the DIII-D tokamak [121] using the fast-ion distribution calculated by TRANSP. In the DIII-D case, the simulation gives good agreement with the measured FIDA intensity and spectral shape.

Figure 5.17 shows the comparison between the NPA simulations and measurements. Since there is no robust MHD instability in the no-RF reference shot (as shown in Fig. 5.2(c)), the simulated NPA energy spectra are expected to agree with the measurements. As shown in Fig. 5.17 (a), the simulated magnitude roughly agrees with the measurement, but it does not show the strong drop between the NB full and half energy components. In other words, the NPA simulations predict that slowing down fast ions fill up the energy range between the full and half energy components,

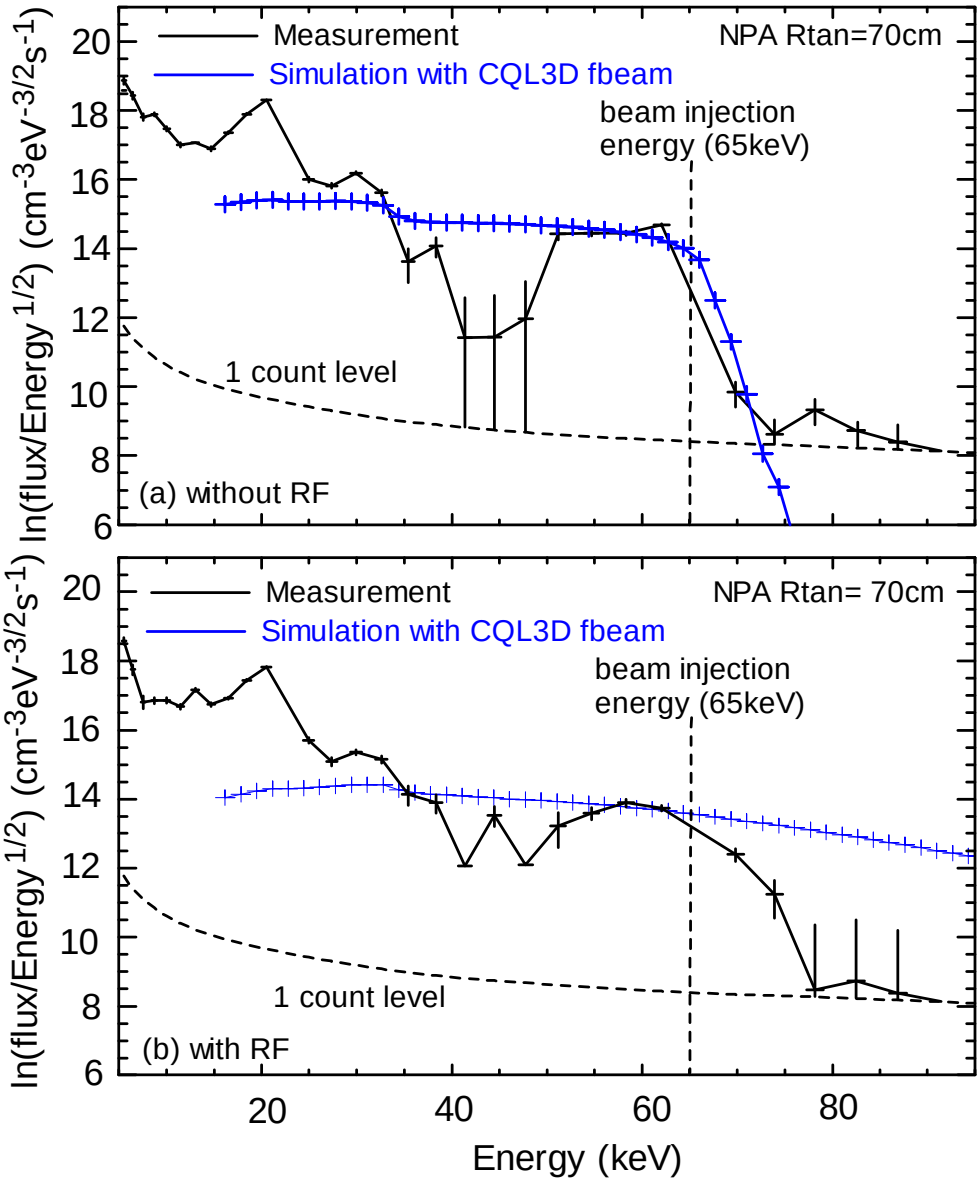

Figure 5.17: Comparison of the measured NPA energy spectra and NPA simulations using CQL3D predicted fast-ion distributions in the shots (a) without and (b) with RF.

but that is not observed experimentally. Figure 5.17 (b) shows that the NPA simulations predict that the NPA should see a fast ion tail in the active CX signals during the HHFW heating, which is also contrary to our observations. A possible reason for these discrepancies is that the input fast-ion distribution is not sufficiently accurate, especially in velocity space because of the zero-banana-width assumption in the CQL3D code and the large gyroradius of fast ions in NSTX. The fast-ion distributions calculated by TRANSP and CQL3D codes are shown in Figs. 5.18 and 5.19. They are expected to match each other in the no-RF case. However, the two calculated fast-on distributions are quite different in velocity space although they have similar spatial distribution in real space. The fast-ion distribution from CQL3D code shows more trapped particles and counter-going particles 5.19. Note that the NPA diagnostics measure a small portion of velocity space of the fast-ion distribution. A small variation of fast-ion distribution in velocity space can result in quite different NPA energy spectra in our simulations. That is why it is so difficult to get quantitative agreement between the NPA measurements and simulations.

The simulated FIDA spatial profiles and energy spectra are compared with the measurements in Fig. 5.20. In the no-RF reference case, the shape of the spatial profile from a FIDA simulation based on the TRANSP fast-ion distribution agrees well with the measurement. However, the FIDA simulations that uses the CQL3D fast-ion distribution predict that the peak of the FIDA spatial profile is closer to the magnetic axis ($R_0 \simeq 100$ cm) and narrower than the measurements (Fig. 5.20 (a)). During RF, the simulations predict a signal enhancement of about 3.5, while the measured enhancement is about 2 in the energy integration range of $30-60$ keV. This difference is also evident in the energy spectra (Fig. 5.20 (b)). These discrepancies are likely due to the zero-banana width approximation in CQL3D simulation.

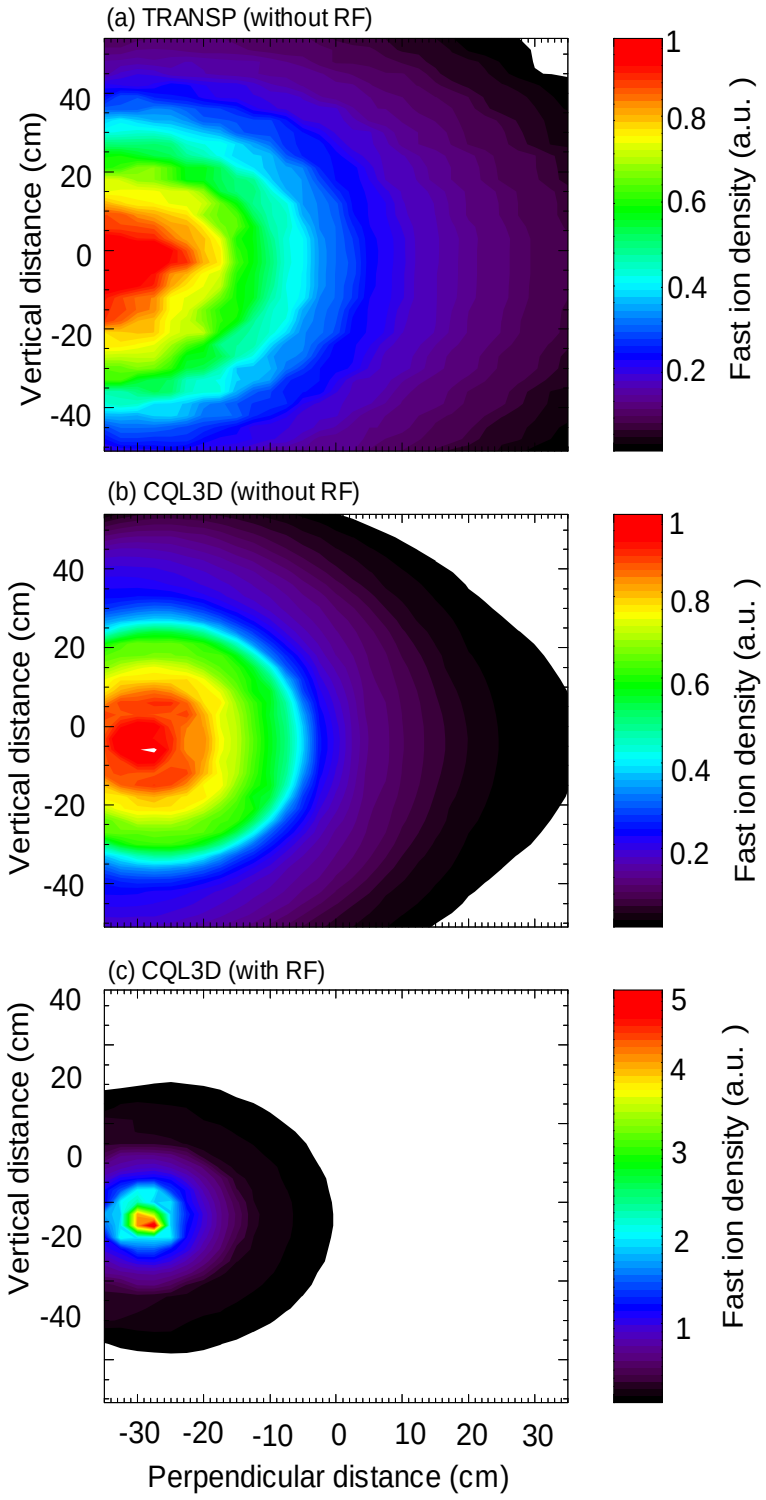

Figure 5.18: Fast-ion distributions at the intersectional area (R=83 cm) of the NB source B and the NPA sightline with tangency radius of 70 cm in real space. The distributions are calculated by (a) TRANSP code, (b) CQL3D code without RF and (c) CQL3D code with RF.

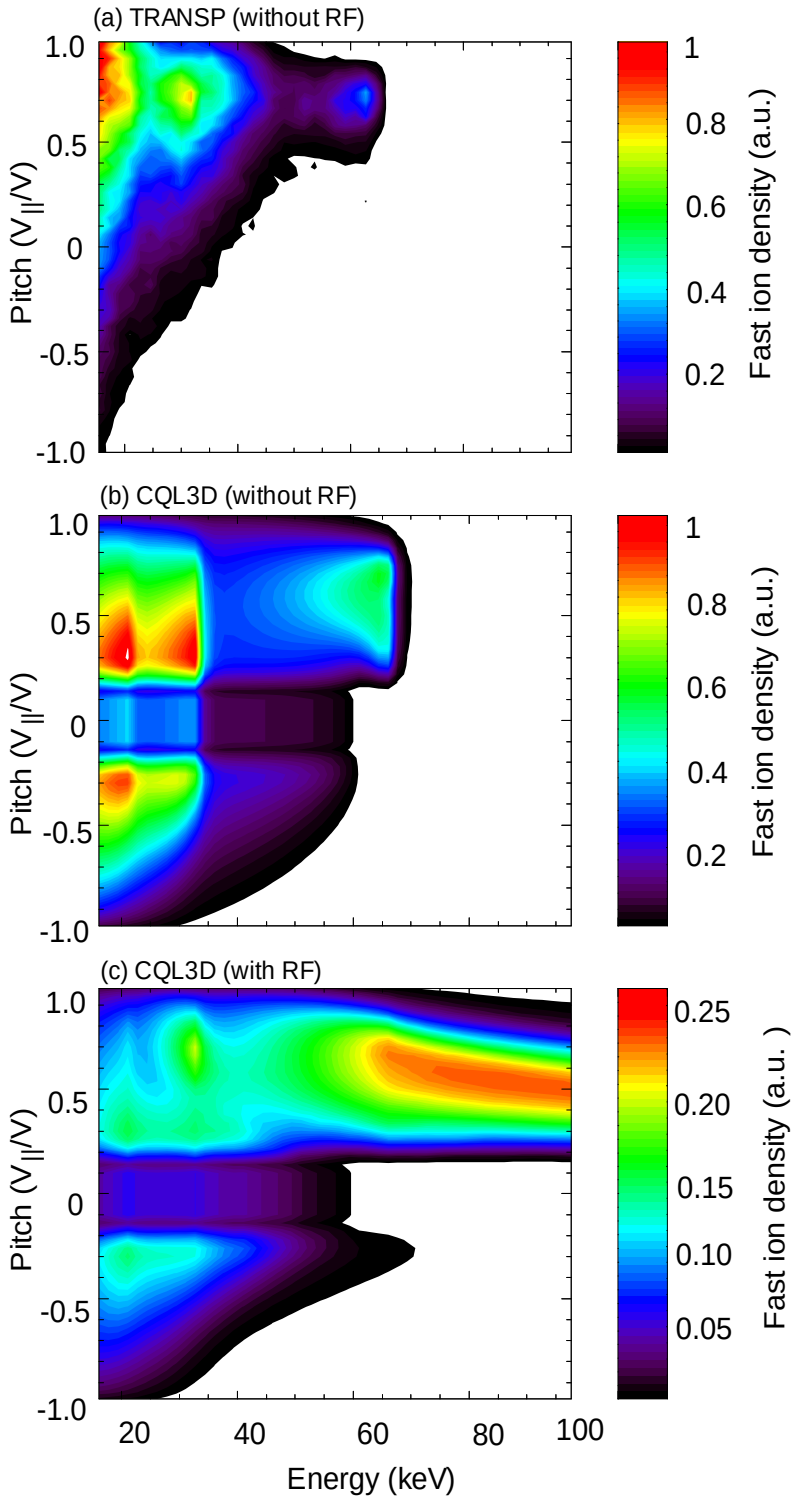

Figure 5.19: Fast-ion distributions at the intersectional area (R=83 cm, Z=0 cm) of the NB source B and the NPA sightline with tangency radius of 70 cm in velocity space. The distributions are calculated by (a) TRANSP code, (b) CQL3D code without RF and (c) CQL3D code with RF.

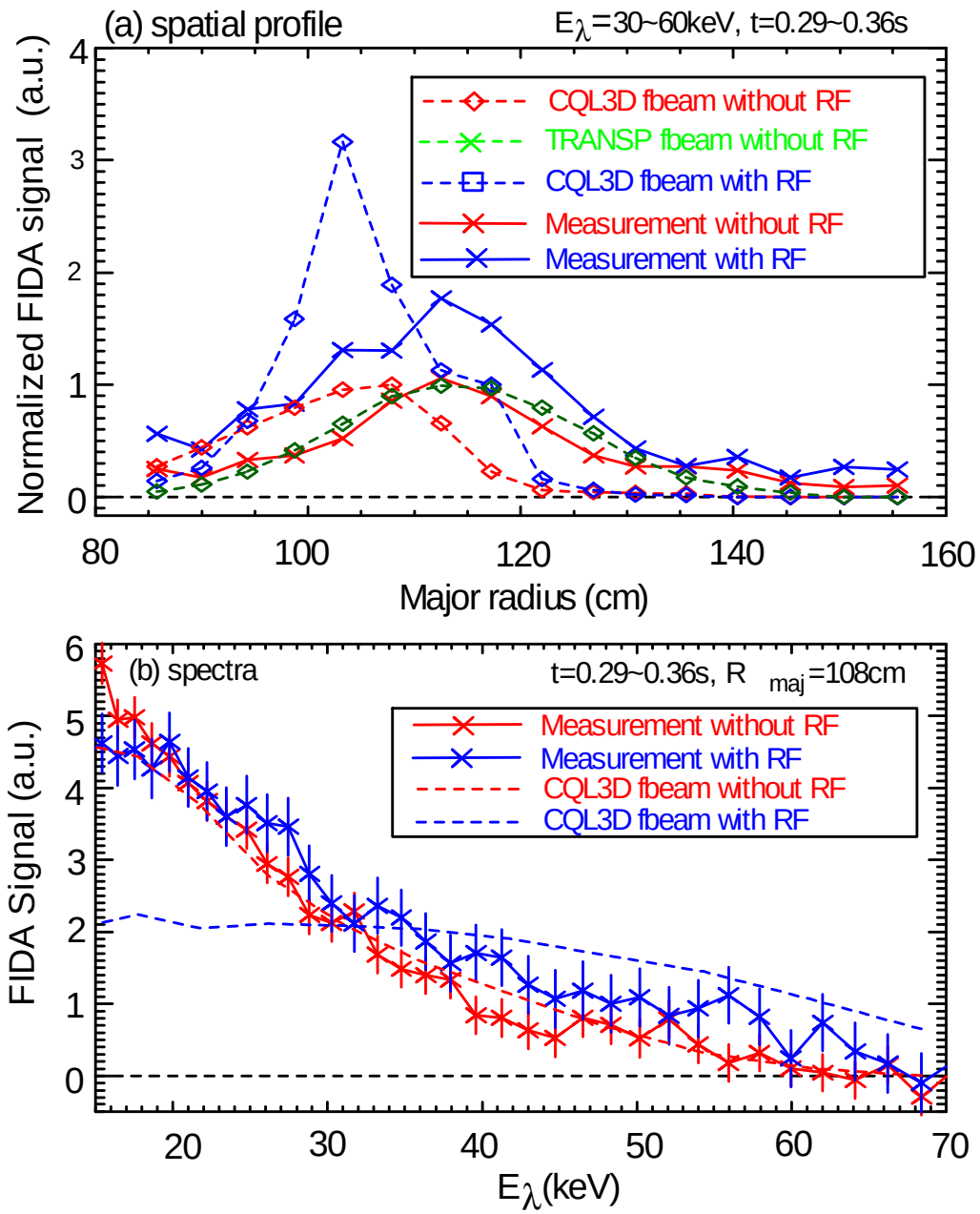

Figure 5.20: Comparison of (a) FIDA spatial profiles and (b) FIDA energy spectra of chord 11 with $R_{maj} = 108$ cm from the measurements and simulations.

5.4 Conclusion

The acceleration of fast ions due to HHFW heating in NSTX is clearly observed with the neutron, E||B type NPA, SSNPA and FIDA diagnostics. With 1.1 MW of HHFW power, the neutron rate is about three times larger than in the comparison discharge without HHFW heating. At some tangency radii, the SSNPA can detect neutrals at twice the injection beam energy. The fast ion tail above the injection energy observed by the NPA and SSNPA diagnostics is mainly from the passive charge exchange reactions at the edge, not from the active charge exchange reactions in the intersectional area. For the measurement geometry, the passive NPA signals are more sensitive to the perpendicular part of phase space than the active signals. The SSNPA measurements also suggest that the acceleration of fast ions is greatest in the perpendicular direction. All of these observations are consistent with theories of RF heating. The measurements by the FIDA diagnostic indicate that the acceleration is mainly in higher energy beam ions and the fast ion density can be increased by a factor of two at the beam injection energy. The measured FIDA spatial profile of accelerated fast ions shows that the enhancement is in a much broader region than in conventional tokamaks due to the multiple and closely-spaced resonance layers and large orbits in NSTX. The energy dependence of the fast-ion distribution function calculated by the CQL3D Fokker-Planck code is fairly consistent with the measurements but the predicted profile differs from the measurements. The peak of the simulated FIDA spatial profile is closer to the magnetic axis and the FWHM is narrower than the measurements. These differences are probably attributable to the zero-banana-width assumption in the current version of CQL3D code. Comparison with the finite banana-width treatment implemented in ORBIT-RF[122, 123] is in progress. In a future work, the combination of temporal, spectral and spatial resolution should allow for stringent tests of theoretical models of wave absorption.

Chapter 6

Redistribution and Loss of Fast Ions during Instability Bursts

6.1 Introduction

Fast ions in fusion plasmas provide a source of free energy to excite instabilities and, in turn, can be affected by the instabilities during their slowing down. Redistribution or loss of the fast ions due to plasma instabilities has been observed in many toroidal fusion devices [29, 30, 124]. The fast-ion redistribution and loss is of concern since the heating of D-T plasmas in the future fusion reactors is also expected to be primarily by fast ions in the form of super-Alfvénic fusion alphas. The NSTX fusion research facility, with low magnetic field and small aspect-ratio, provides a unique window to study deuterium fast ion behavior in the super-Alfvénic regime. The NB heated plasmas in the NSTX typically have a wide variety of instabilities with frequency ranges from a few kilohertz to a few megahertz (Fig. 6.1) [125]. These modes include energetic particle modes (EPM), Toroidal Alfvén Eigenmodes (TAE), and Compressional

and Global Alfvén Eigenmodes (CAE and GAE, respectively). This chapter mainly focuses on the bursting instabilities, such as fishbone and sawtooth oscillations, because they have repetitive patterns and they are easy to analyze and compare with theory.

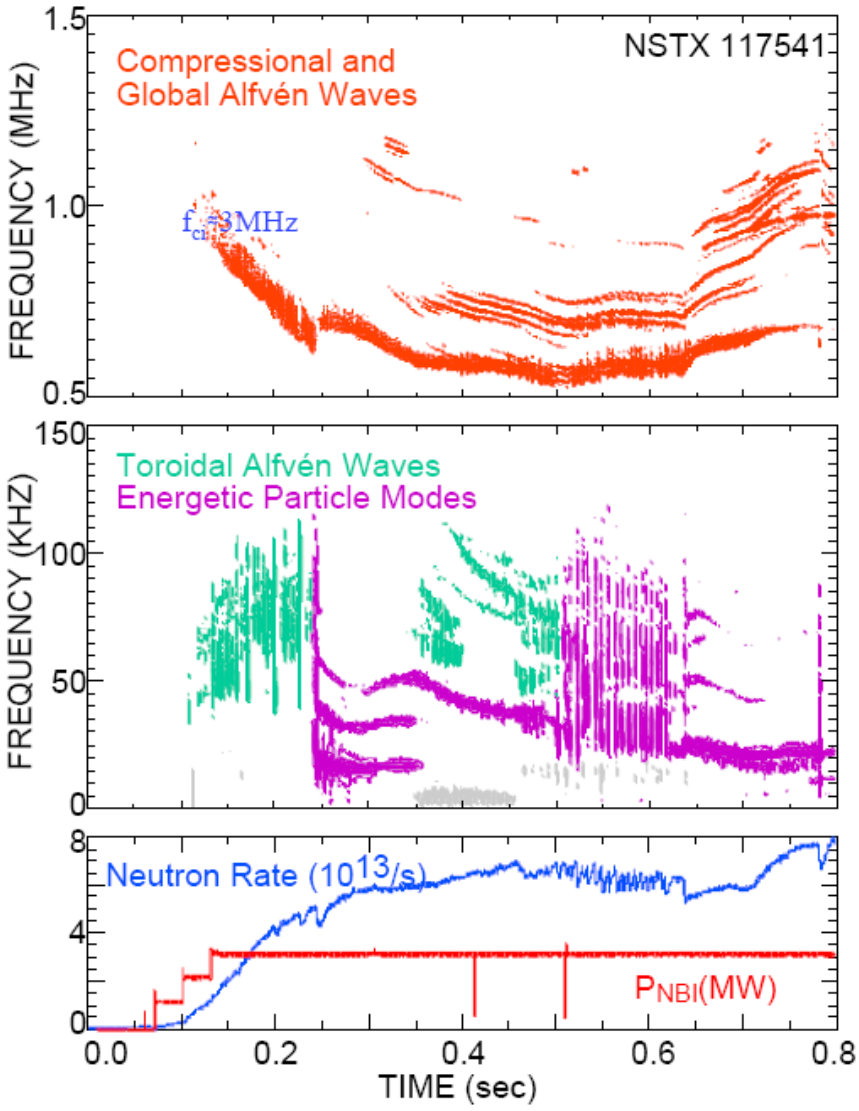

Figure 6.1: Magnetic fluctuations in a typical NSTX beam heated plasma. (a) compressional and global Alfvén eigenmodes orange; (b) toroidal Alfvén eigenmodes and energetic particle modes; (c) neutral beam heating power and a global neutron rate. (Reproduced in Fig. 1 in Ref. [125])

The rest of this chapter is organized into four sections. In Sect. 6.2, a brief

review of sawtooth and fishbone instabilities is given with appropriate references. Sect. 6.3 shows the measurements from the E||B type NPA, SSNPA, neutron detectors, Mirnov coils, and soft X-ray diagnostics during bursting events. The correlation between the NPA/SSNPA measurements and these instability bursts is analyzed by a cross-correlation technique. In Sect. 6.4, simulations with the ORBIT code are proposed to explain the different effects of sawtooth and fishbones on the fast ion distribution. The chapter concludes with a summary in the last section.

6.2 Overview of Fishbone and Sawtooth

Fishbone and sawtooth instabilities are two common bursting instabilities and have been observed in many diagnostics in all tokamaks. Both of them are n=1, m=1 (n and m are the toroidal and poloidal mode numbers) kink modes and can have repetitive patterns. They have been extensively studied experimentally and theoretically (see, e.g. review in Ref. [29, 30] and references therein). Before we show the experimental observations, we briefly review the fishbone and sawtooth instabilities in conventional tokamaks and NSTX.

6.2.1 Fishbone Instability

The well-known fishbone instability in conventional tokamaks is an $n = m = 1$ internal kink mode with frequency comparable to either the toroidal precession frequency (ω_{pre}) of the beam ions or the bulk ion diamagnetic frequency (ω_{*i}) [126, 127, 128, 129]. The fishbone instability generally has bursting character and can result in a considerable loss or redistribution of the fast ions [126, 130]. Since fishbones generally occur near the center of the machine, the loss of fast particles from fishbones is not

expected to be severe unless particle orbit is large enough to reach the plasma edge.

The fishbone instability in the NSTX may differ from conventional fishbones because of the low magnetic field, small aspect-ratio and high β. The precession-drift resonance could excite conventional n=m=1 fishbones under some conditions in NSTX, but the precession frequency in the NSTX is often low or even negative due to small aspect-ratio and high β. Thus fishbones in NSTX can be driven through a fast-ion bounce resonance, rather than the fast-ion precession-drift resonance [131]. These bounce-resonance fishbones are important especially in low shear and high-q discharges, which are desired for an ST (or advanced tokamak) reactor. In addition, fishbone-like EPMs[132] are often observed in NSTX. But the inferred central safety factor q(0) can be larger than one and the toroidal mode number is not limited to $n = 1$, but ranges up at least $n = 5$ [131]. For comparison with sawtooth events, we consider only the conventional n=m=1 fishbones in this thesis.

6.2.2 Sawtooth Instability

The sawtooth instability manifests itself as a regular periodic reorganization of the core plasma surrounding the magnetic axis in tokamaks [133]. The complete cycle of a sawtooth oscillation can be subdivided into three phases: (i) the sawtooth ramp phase; a quiescent period during which the plasma density and temperature increase approximately linearly with time in the plasma core; (ii) the precursor oscillation phase, during which a helical magnetic perturbation ($n = 1$, $m = 1$ kink mode) grows and, due to toroidal rotation of the plasma, the soft X-ray emission, electron cyclotron emission, and interferometric data show growing oscillatory behavior; (iii) the collapse phase, in which plasma density and temperature and soft X-ray intensity fall rapidly to lower values. Generally, the sawtooth oscillations are radially inverted

so that a sudden fall in the temperature in the plasma center is associated with a increase in the plasma temperature outside the q=1 surface. The sawtooth itself may not affect the overall performance significantly, but it can affect plasma performance and confinement by coupling to other non-ideal MHD instabilities, such as neoclassical tearing modes (NTMs) and edge localized modes (ELMs).

The sawtooth instability is complex and remains incompletely explained in theory, even with the most advanced computer simulations. Kadomtsev [134] gave a first insight into the complete reconnection process: the hot core region with the $q = 1$ surface undergoing magnetic reconnection along a helical X-line is replaced by a unstable $n = m = 1$ magnetic island. However, this model fails to describe many sawtooth oscillations observed in the plasmas with high beta. For example, the Kadomtsev relaxation model predicts that the central safety factor, $q(0)$, equals unity after the crash. This often contradicts some experimental data. Some further development of the Kadomtsev relaxation model and other alternative theories of sawtooth crash were proposed in the 1980s and 1990s, for example, the quasi-interchange model by Wesson [135] and the ballooning mode model by Park and Nishimura [136, 137]. As of the present date, no concrete theory can explain all phenomena observed in the sawtooth crashes.

The sawtooth instability can strongly interact with fast ions in two ways: it can be either stabilized by the fast ions or it can affect the fast ion radial profile [29, 30]. In this work, we mainly focus on the effects of sawtooth events on the fast ion distribution in NSTX. The theoretical description of the effects of the sawtoooth instability on the fast ions is available in Refs. [138, 139, 140] and can be briefly summarized as follows. The sawtooth-induced particle redistribution is a result of competition of several processes. First, the electric field associated with the plasma flow tends to move particles together with the flow. The characteristic time is the sawtooth

crash duration. Second, the toroidal precession tends to move a particle so that its radial coordinate, r, is constant, and hence preventing the particle redistribution. The characteristic time is the precession period. Third, the longitudinal motion tends to move particles along the displaced flux surfaces. The characteristic time of this motion is the period of the particle trip around a magnetic surface. The resulting particle motion depends on the relative characteristic times of the three processes, which in turn depends on the particle energy and pitch angle.

6.3 Measurements and Data Analysis

The experiments on NSTX show that sawtooth events often result in strong drops in the neutron emission rate of a factor of two. The E||B type NPA and SSNPA diagnostics also show bursts or drops at some tangency radii. These suggest that high energy fast ions are redistributed or are expelled from the plasma. However, the fishbone events generally have much weaker effects on the neutron emission rate (less than 5% neutron rate drop), E||B type NPA and SSNPA signals. These could indicate either that the fast ions are just redistributed within the plasma, or that only the lower energy fast ions are expelled. To understand the different effects of fishbones and sawteeth on the fast ion distribution, a database of NSTX discharges that have fishbones and/or sawteeth is built using the data from the 2007 experimental campaign. A subset of the most relevant discharges is given in Table 6.1. In these shots, the toroidal magnetic field is about $0.39 - 0.44$ T at the magnetic axis, the plasma current is about 800 kA (except in shot 125281, where the plasma current is 1.2 MA), the outer gap is about $9 - 12$ cm, the central electron temperature is around 1.0 keV, and the central density is around $2 - 5 \times 10^{13}$ cm^{-3}. Fast ions are produced by the deuterium neutral beam source(s) with the injection energy of

$65 - 90$ keV. The background plasma is either helium plasma or deuterium plasma. It is very interesting that some shots, for example, 124518, 124519 and 124769, have both fishbones and sawteeth simultaneously (Table 6.1).

6.3.1 Experimental Measurements during Fishbone Events

Conventional $n = m = 1$ fishbones are observed during plasma current ramp up or steady state in NSTX. One example is shown in Fig. 6.2. There are about 13 bursts in the Mirnov signals during the time widow of $0.315 - 0.375$ second in shot 124512. The Mirnov coil spectrograms (Fig. 6.3) show rapid downward sweep (chirping) in frequency for each burst. The changes in the mode frequency occur in a time scale of 3 msec and they are very unlikely to represent changes in equilibrium plasma profiles. Because of the mode number $n = 1$ (Fig. 6.3(a)) and the chirping feature, the bursting events are believed to be fishbones, like those observed in PDX [126]. This is further confirmed by the soft X-ray data, as shown in Fig. 6.4. Figure 6.2 (f) shows that these fishbones cause about 4% drops in the neutron emission rate. The small neutron-rate drops in the neutron rate during the fishbone events could indicate either that the fast ions are just redistributed within the plasma, or that only the lower energy fast ions are expelled. The signals of the E||B type NPA and SSNPA are hardly affected by these fishbones except that the signal in the chord 4 of SSNPA may have some weak correlation. As shown in Fig. 6.2 (g) and Fig. 6.4, the mode amplitude of these fishbones gradually increase from 0.315 second, ending up with a sawtooth crash at 0.370 second. At the crash, the neutron rate decreased by 55% and the E||B type NPA and chord 1 of SSNPA also show a drop in the measured signal. However, the most outboard chord of SSNPA and fast ion loss probe show a burst at the sawtooth crash. All these facts suggest that the conventional $n = m = 1$ fishbone instability has weak effects on the confinement of fast ions in NSTX, at least for high

Table 6.1: Fishbone and sawtooth database in NSTX.

Fishbones	
Helium plasma	
Shot Num.	Time (msec)
124510	316-346
124511	320-355
124512	315-365
124514	300-328
124518	290-331
124519	304-340
124524	310-380
124525	310-343
124526	310-340
124529	310-350
124530	315-345
124764	320-350
124765	320-365
124769	305-335
124771	310-336
124786	270-298
124790	260-292
Deuterium Plasma	
125281	705-760

Sawteeth	
Helium plasma	
Shot Num.	Time (msec)
124503	320-390
124505	330-400
124518	350-465
124519	405-495
124520	380-480
124522	350-410
124523	375-450
124636	380-440
124769	350-435
Deuterium Plasma	
Shot Num.	Time (msec)
124362	430-480
124643	380-460
124646	410-520
124647	390-470
124649	545-656

energy fast ions.

Since the signal-to-noise ratio (SNR) of the SSNPA diagnostic is not very large, the discharges with repetitive instability bursts are chosen for our study and the cross-correlation technique is applied to look for the correlation between the bursts and the NPA/SSNPA signals. Generally, The normalized cross-correlation function $R_{xy}(L)$ of two signals x(t) and y(t) is defined as

$$R_{xy}(L) \equiv x(t) * y(t) \equiv \frac{\sum_{i=0}^{i=N-L-1} (x_{i+L} - \bar{x})(y_i - \bar{y})}{\sqrt{\sum_{i=0}^{i=N-1} (x_i - \bar{x})^2 (y_i - \bar{y})^2}} \text{ for } L < 0$$

$$R_{xy}(L) \equiv x(t) * y(t) \equiv \frac{\sum_{i=0}^{i=N-L-1} (x_i - \bar{x})(y_{i+L} - \bar{y})}{\sqrt{\sum_{i=0}^{i=N-1} (x_i - \bar{x})^2 (y_i - \bar{y})^2}} \text{ for } L \geq 0$$

where i is the index, L is the time lag, and $\bar{x}$ and $\bar{y}$ are the means of the signals $x(t)$ and $y(t)$ respectively. The correlation coefficient has a value of 0 if the two signals completely uncorrelated and a value of $+1$ or -1 if they are perfectly positively or negatively correlated. This method is insensitive to the amplitude of the signals; only the shape and phase are important.

The measured neutron rate is a good monitor of the fast ion behavior in NSTX since it is dominated by the beam–plasma reactions. To find out the correlation between the instability bursts and the NPA or SSNPA signals, the normalized cross-correlation coefficient between the negative derivative of neutron rate and the NPA/SSNPA signals is calculated. The cross-correlation between the edge D-alpha light and the NPA/SSNPA signals is also monitored because the edge D-alpha light measures the

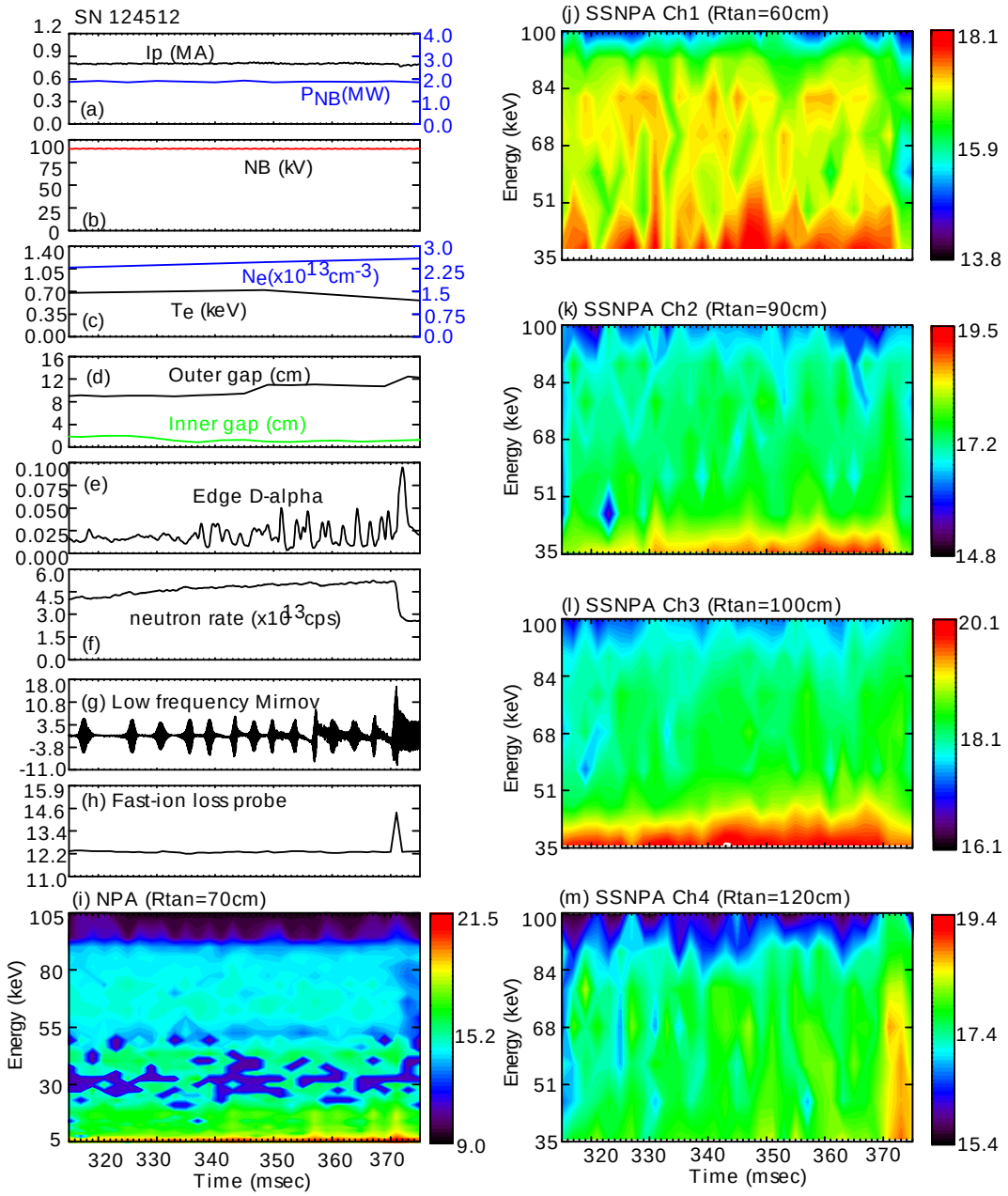

Figure 6.2: Temporal evolution of (a) the plasma current and injected NB power, (b) the beam injection energy, (c) the electron temperature and density, (d) the inner and outer gap width, (e) the edge D–alpha light, (f) the neutron emission rate, (g) the low pass filtered Mirnov signal in the frequency range of $0.2 - 40$ kHz, (h) the fast-ion loss probe signal, (i) the E||B type NPA signal, and (j-m) the SSNPA raw data during the fishbone events in shot 124512. A sawtooth crash occurs at $t = 0.370$ second, which caused a 55% drop in the neutron rate and a burst at the fast ion loss probe and the most outboard chord of the SSNPA diagnostic.

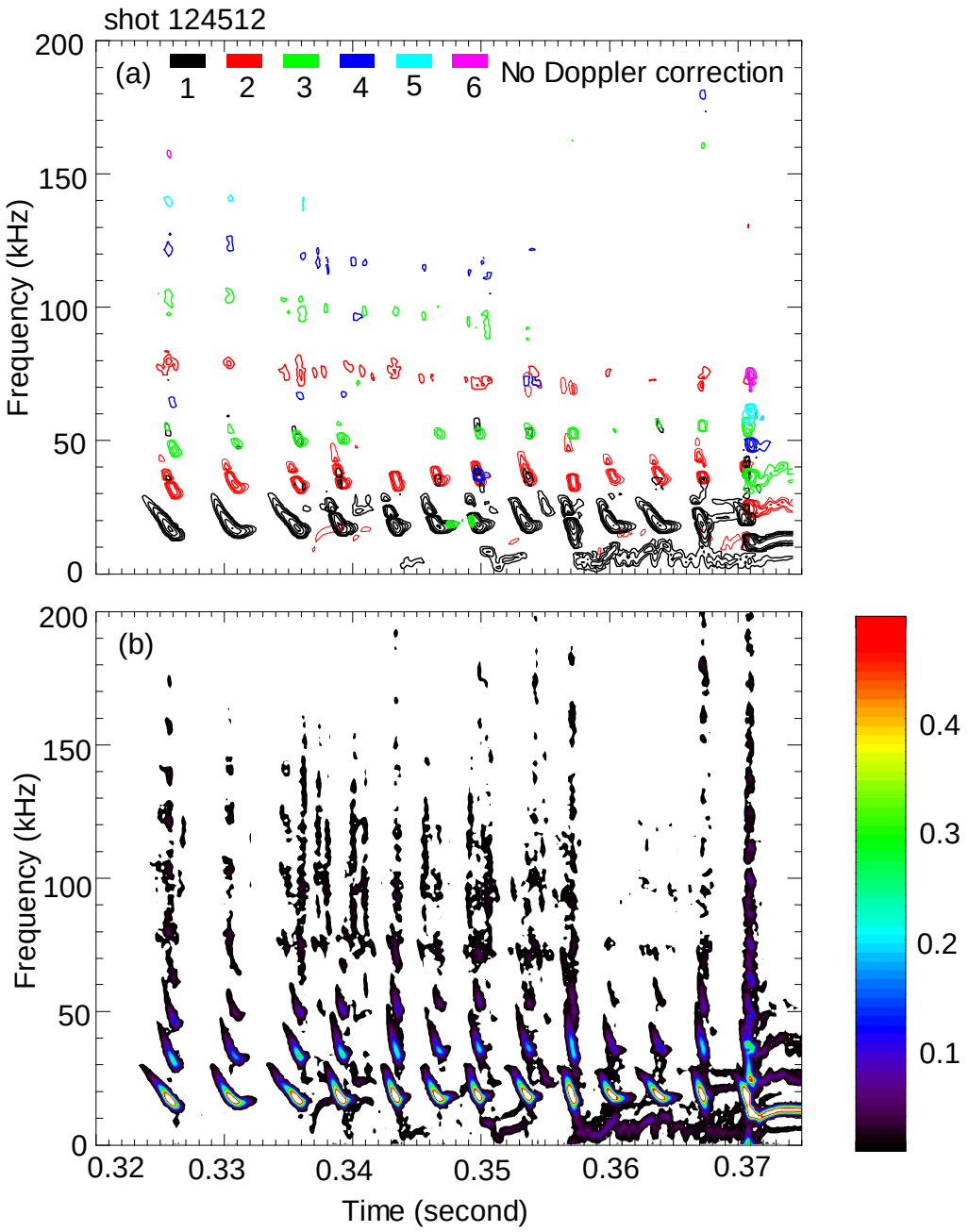

Figure 6.3: The Mirnov coil spectrograms show that (a) the bursting events in the time window of $0.32 - 0.37$ second in shot 124512 are $n = 1$ mode and its harmonics, and (b) these modes sweep down rapidly in frequency during the course of bursts during each burst. The mode number ($n = 1$) and the chirping feature suggest these bursts are fishbones. Note that color in (a) indicates toroidal mode number and color in (b) represents FFT mode amplitude.

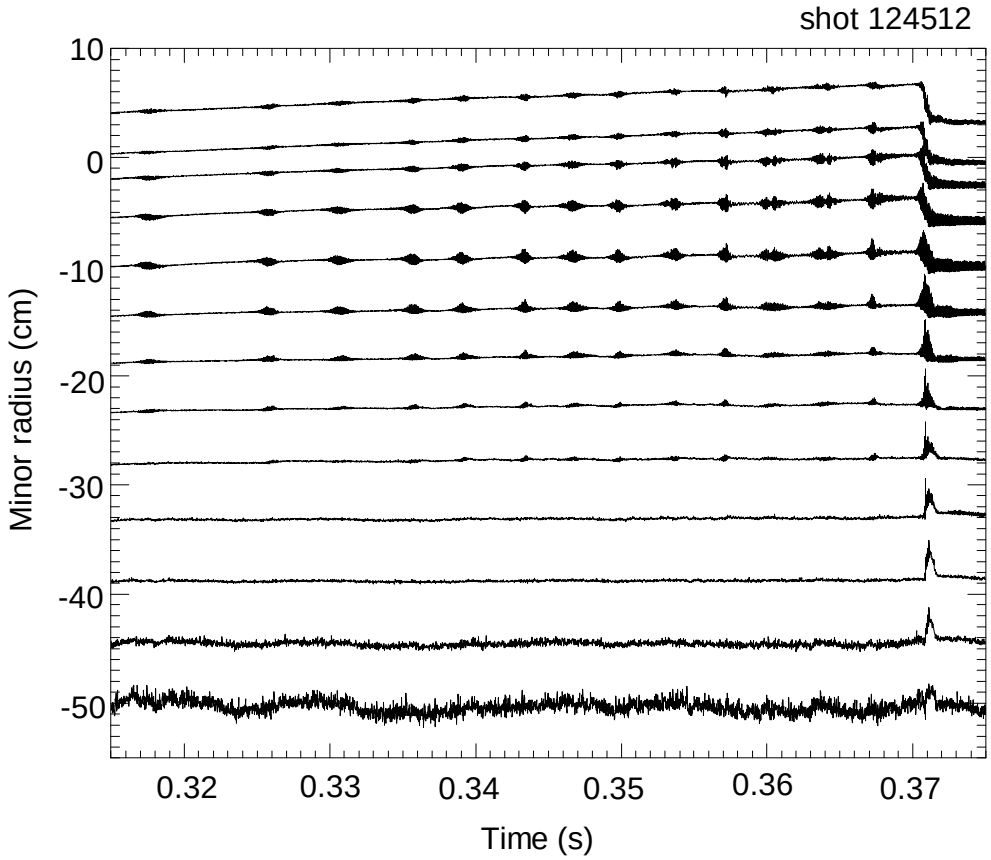

Figure 6.4: The measurements of the soft X-ray array viewing the lower half of plasma suggest that the bursting events in shot 124512 are fishbones since the oscillations grow and decay with time for each burst. The fluctuations are auto-scaled and the tangency radii are mapped to the midplane minor radius using EFIT.

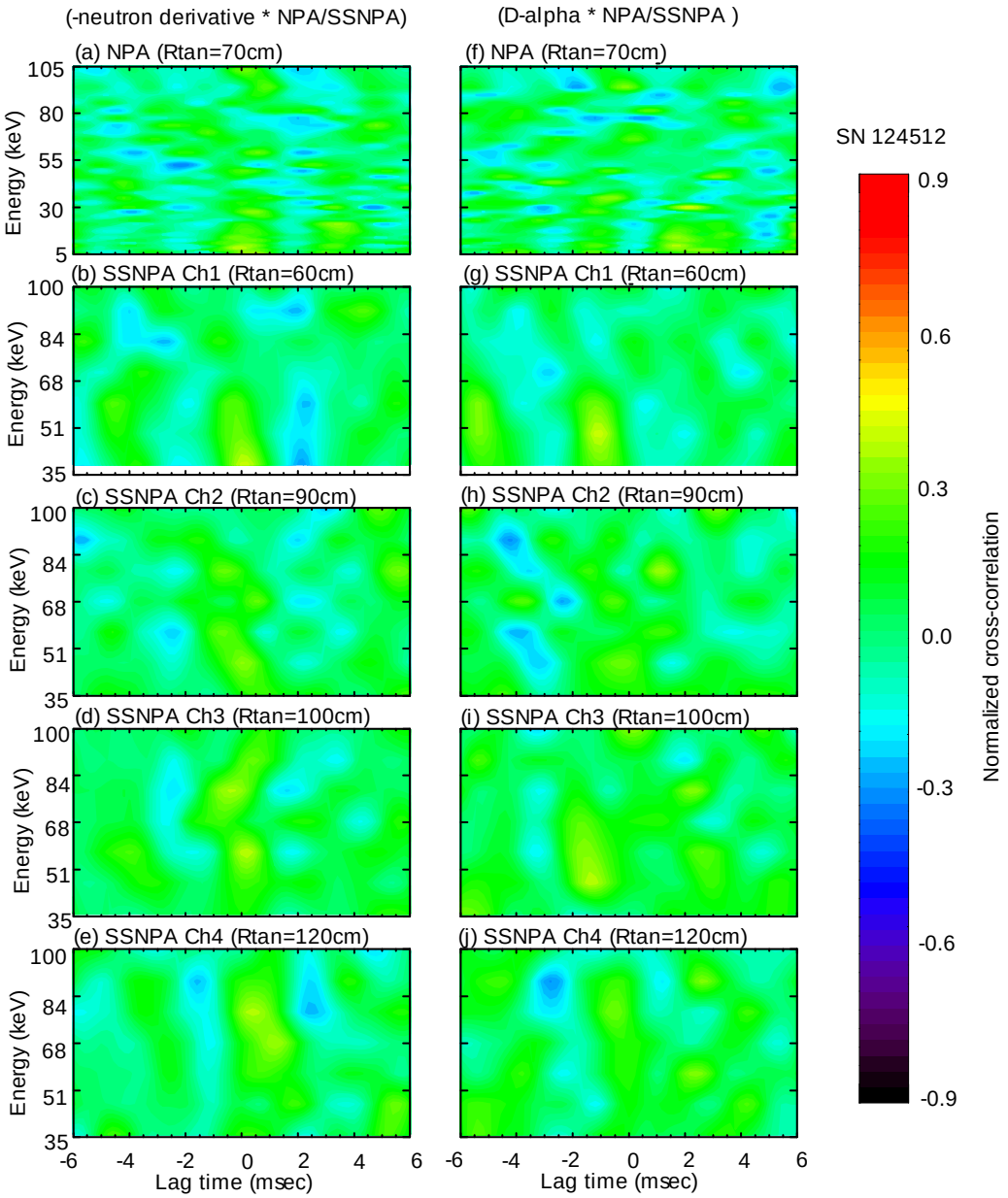

Figure 6.5: Normalized cross-correlations (a-e) between the negative derivative of neutron rate and the NPA/SSNPA signals and (f-j) between the edge D-alpha light and the NPA/SSNPA signals in shot 124512.

edge neutral density, whose change can also affect the NPA/SSNPA signals due to passive charge exchange reactions. For the fishbone events between 0.315 and 0.365 second in shot 124512, these correlation coefficients are plotted in Fig. 6.5. The cross-correlation between the envelope of Mirnov coil signal and the NPA/SSNPA signals is also checked and it is similar Fig. 6.5. It shows that the NPA/SSNPA signals have very weak correlation with the neutron rate or Mirnov coil signal during the fishbone events. It indicates that the fast ions cause only modest transport of fast ions. Similar analysis is applied to all of the fishbone shots in our database and all of them show no or weak correlation between the instability bursts and NPA/SSNPA signals. This is consistent with the measurements in the Small Tight Aspect Ratio Tokamak (START), in which circulating particles dominate in the fast ion population and the fishbone instability tends to be stabilized when β is high [141]. The stabilizing effect of high β in STs was discovered theoretically in Refs. [142, 143, 144], where the trapped-particle-induced fishbone mode was considered.

One interesting observation is that the combination of $n = 1$ fishbones and CAEs could lead to significant fast ion loss. Figure 6.6 (f) shows that the neutron rate dropped $\sim 25\%$ for each burst in shot 122644. The E||B type NPA and SSNPA diagnostics also observe a strong correlation with these bursts (Fig. 6.6 (h)-(l)). The Mirnov spectrograms (Fig. 6.7) suggest that these bursting events at low frequency range of [0, 200] kHz are $n = 1$ chirping modes. The soft X-ray data (Fig. 6.8) also show that they are similar to the $n = 1$ fishbones observed in shot 124512. The difference is that, in shot 122644, strong bursting CAEs appear in the Mirnov spectrogram at the frequency range of [1500, 2000] kHz. The cross-correlations of the E||B type NPA and SSNPA signals with neutron rate are much stronger than their cross-correlations with the edge D-alpha light (Fig. 6.10). In addition, Fig. 6.10 also shows that fast ions with energies ~ 90 keV arrive at the edge ~ 0.5 ms prior to ~ 45 keV fast ions. Note that a change in the edge neutral density would

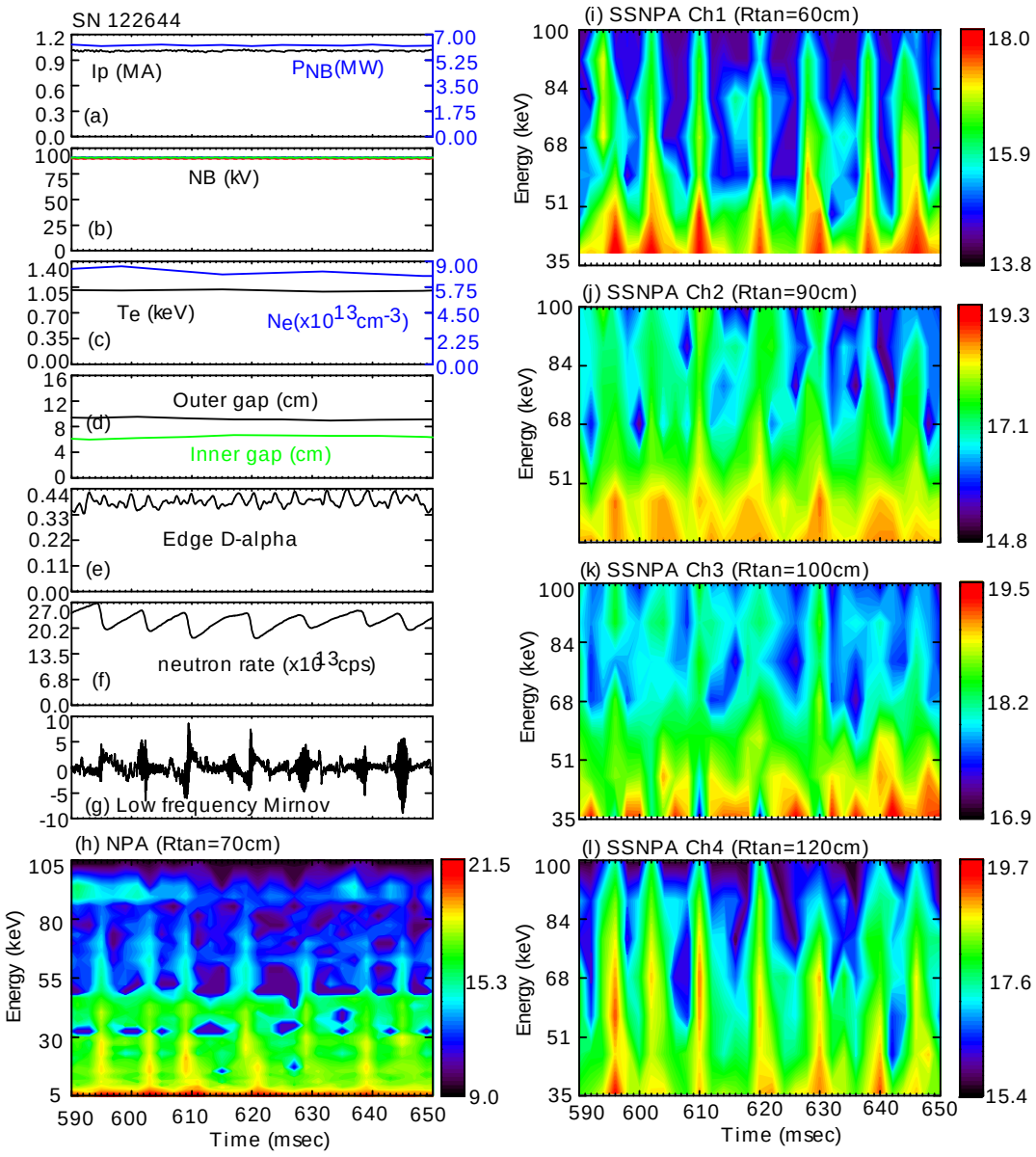

Figure 6.6: Temporal evolution of (a) the plasma current and the injected NB power, (b) the beam injection energy, (c) the electron temperature and density, (d) the inner and outer gap width, (e) the edge D–alpha light, (f) the neutron emission rate, (g) the low pass filtered Mirnov signal in the frequency range of $0.2 - 40$ kHz, (h) the E||B type NPA signal, and the SSNPA raw data (i-l) during the bursting events in shot 122644. Each burst caused a 25% drop in the neutron rate and a burst at the signals of the E||B type NPA and the SSNPA diagnostics. Note that the signals of E||B type NPA and SSNPA diagnostics are plotted as $\ln(NPA\ Flux/E^{1/2})$ in the units of $cm^{-2}eV^{-3/2}s^{-1}$.

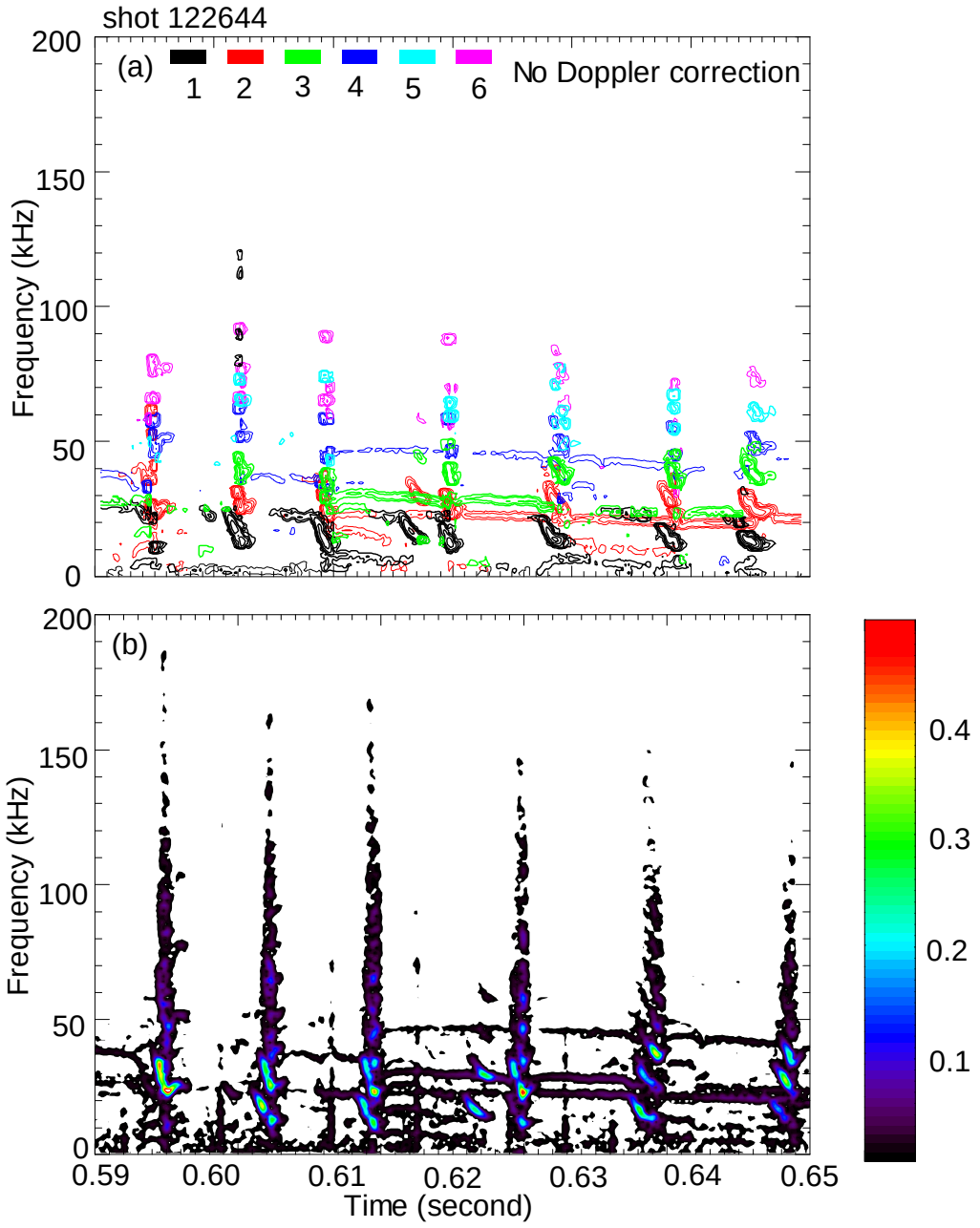

Figure 6.7: The Mirnov coil spectrograms show that the (a) bursting events in the time window of $0.59 - 0.65$ second in shot 122644 are mainly $n = 1$ mode and weak $n = 1$ and $n = 2$ continuous mode. (b) The $n = 1$ mode shows similar chirping feature as in the fishbone shot 124512. Note that color in (a) indicates toroidal mode number and color in (b) represents FFT mode amplitude.

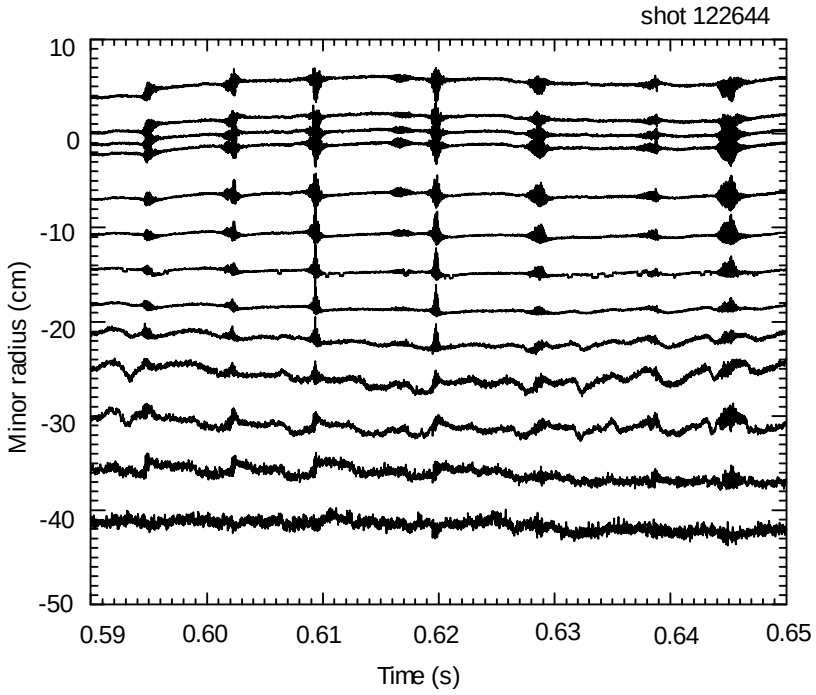

Figure 6.8: The measurements of the soft X-ray array viewing the lower half of plasma in shot 122644. They have similar features as in the fishbone shot 124512.

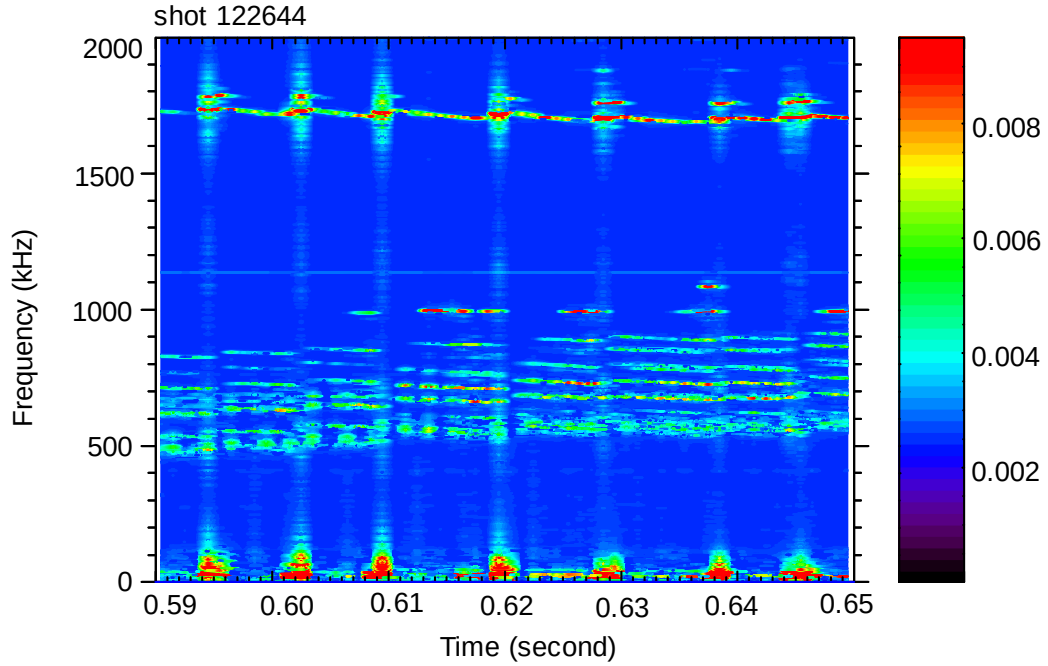

Figure 6.9: The Mirnov coil spectrogram shows there are bursting CAEs in the frequency range of [1500, 2000] kHz during the time window of $0.59 - 0.65$ second in shot 122644.

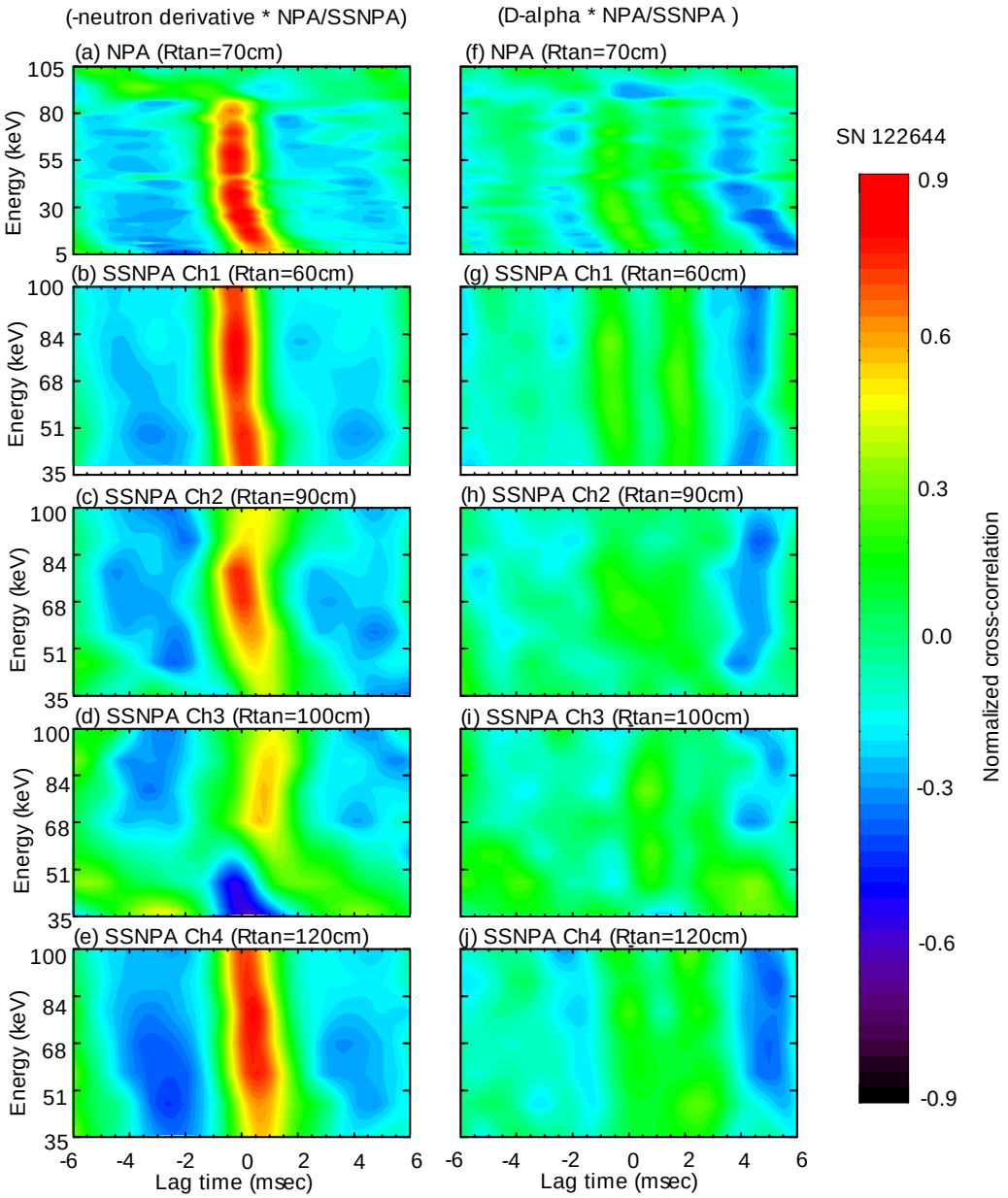

Figure 6.10: Normalized cross-correlations (a-e) between the negative derivative of neutron rate and the NPA/SSNPA signals and (e-f) between the edge D-alpha light and the NPA/SSNPA signals in shot 122644.

affect the NPA/SSNPA signals in all energy channels at the same time. The stronger correlation between the negative derivative of neutron rate and the NPA/SSNPA signals and the energy dependence clearly show that the bursts in the NPA/SSNPA signals are mainly due to fast-ion transport into the higher neutral density region, not due to the change of the edge neutral density.

6.3.2 Experimental Measurements during Sawtooth Events

Sawtooth oscillations often result in strong drops of the neutron rate. An example is given in Fig. 6.11. There are six bursting events during the time of $0.32-0.039$ second in shot 124503, as shown in the Mirnov coil signal (Fig. 6.11 (g)), and each burst cause $\sim 22\%$ neutron rate drop (Fig. 6.11 (f)). These bursting events are identified as sawtooth crashes, rather than Internal Reconnection Events (IRE) or fishbones, because there is no noticeable current spikes (Fig. 6.11 (a)) and the mode number is $n = 1$ in the Mirnov spectrograms (Fig. 6.12). This is further confirmed by the soft x-ray data (Fig. 6.13). The raw data of chords 3 and 4 of the SSNPA diagnostic show bursting feature during the sawtooth events (Fig. 6.11 (h-l)). The cross-correlation analysis shows that, although there is also some weak correlation with the edge D-alpha light, the NPA/SSNPA signals are mainly correlated with the instability bursts (Fig. 6.14). The NPA (with Rtan=70 cm) signal drops at each burst (Fig. 6.14 (a)), while the signals from outboard chords of the SSNPA increase at each burst (Fig. 6.14 (d) and (e)). More importantly, the fast ions with high energies first respond and then the ones with lower energies respond. This also suggests the bursts or drops observed in the NPA/SSNPA signals are associated with the instabilities, not with the edge neutral density change. The bursts of the neutral flux at the outboard chords of the SSNPA and the strong drops in the neutron rate during sawtooth crashes indicate the loss of the most energetic fast ions that are responsible for most of the neutron

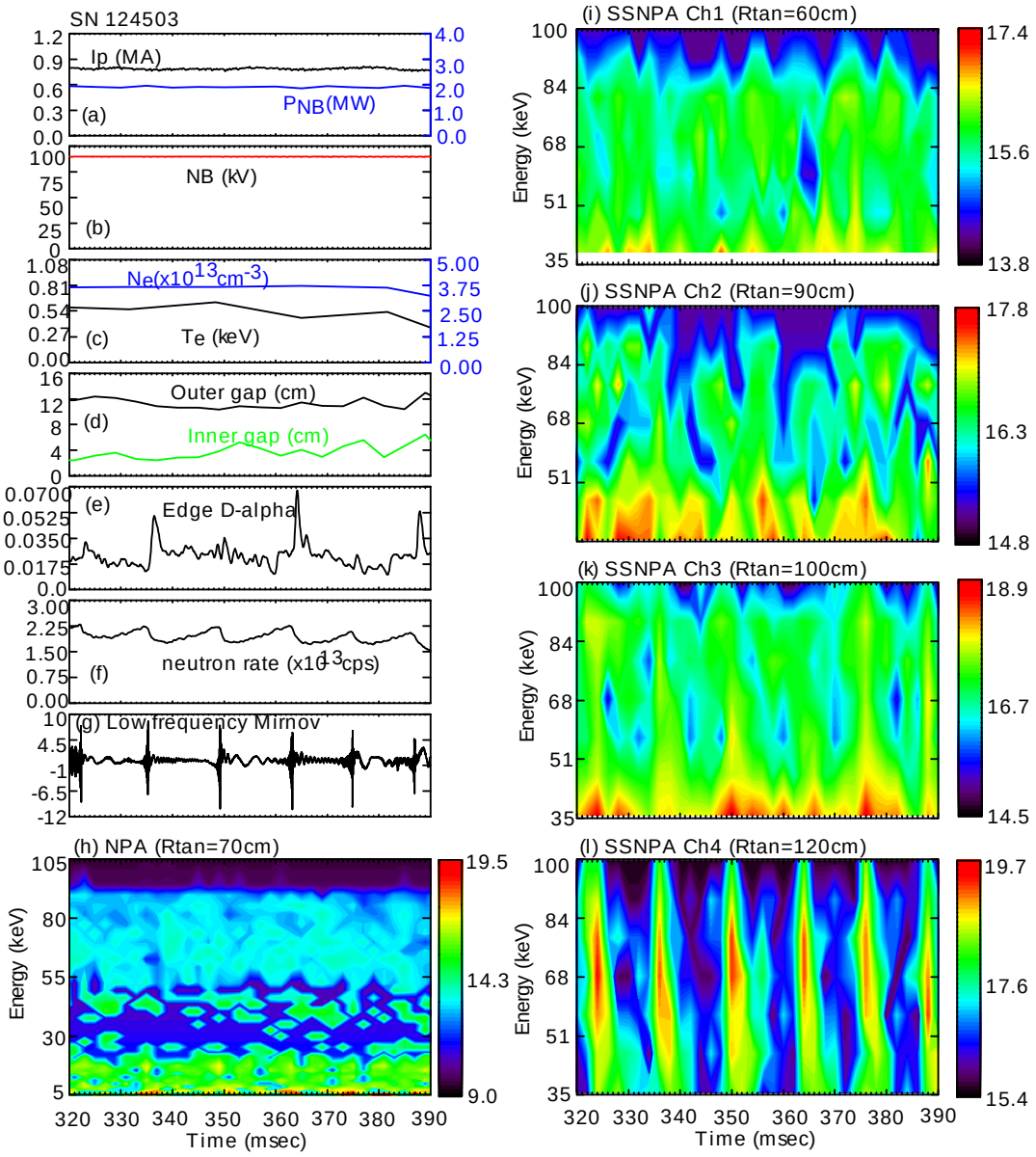

Figure 6.11: Temporal evolution of (a) the plasma current and the injected NB power, (b) the beam injection energy, (c) the electron temperature and density, (d) the inner and outer gap width, (e) the edge D–alpha light, (f) the neutron emission rate, (g) the low pass filtered Mirnov signal in the frequency range of $0.2-40$ kHz, (h) the E||B type NPA signal, and (i-l) the SSNPA raw data during the bursting events in shot 124503. Each burst caused a 22% drop in the neutron rate and a burst at chords 3 and 4 of the SSNPA diagnostic. Note that the signals of E||B type NPA and SSNPA diagnostics are plotted as $\ln(NPA\ Flux/E^{1/2})$ in the units of $cm^{-2}eV^{-3/2}s^{-1}$.

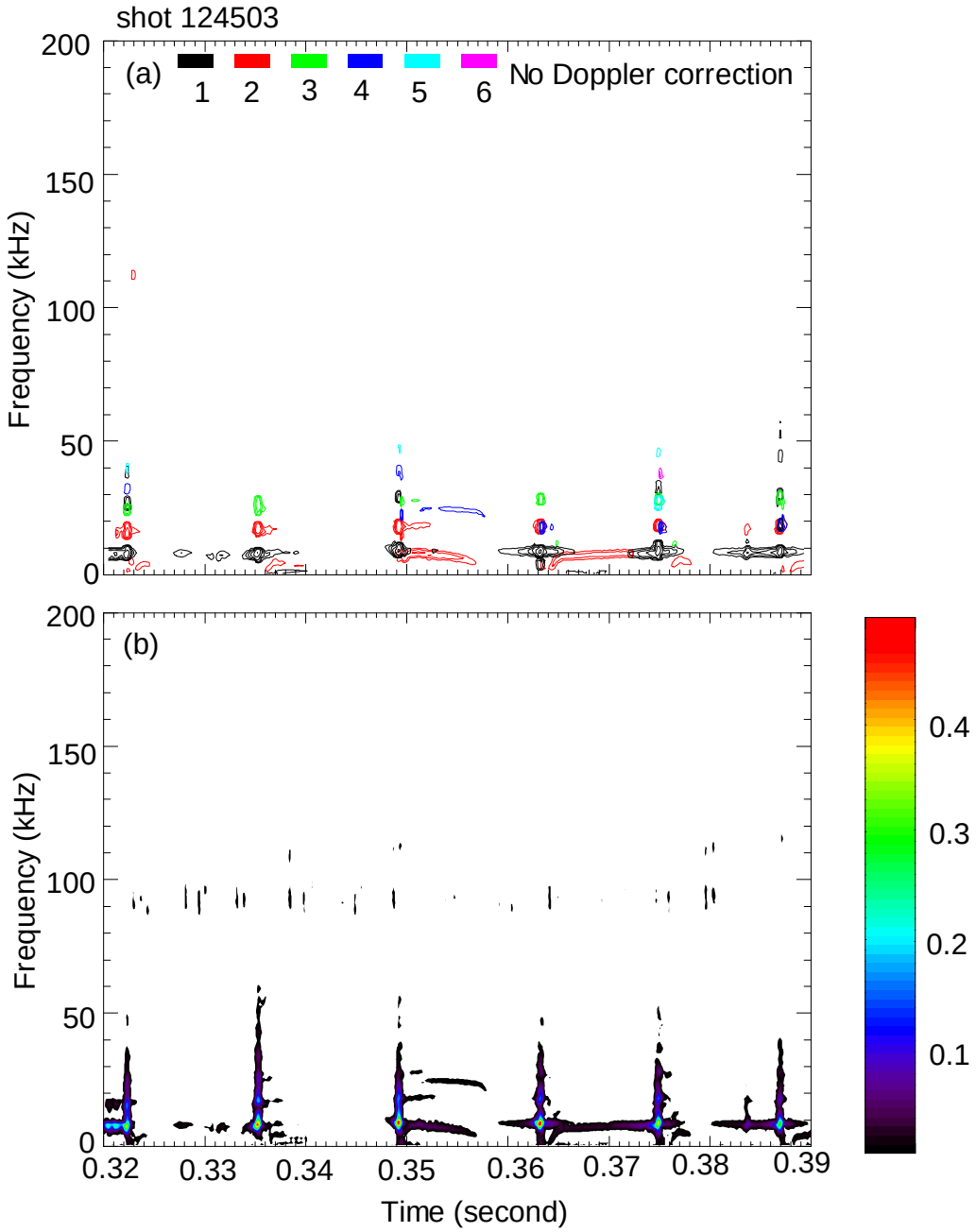

Figure 6.12: The Mirnov coil spectrograms show that the bursting events in the time window of $0.32 - 0.39$ second in shot 124503 are $n = 1$ mode and its harmonics. Note that color in (a) indicates toroidal mode number and color in (b) represents FFT mode amplitude.

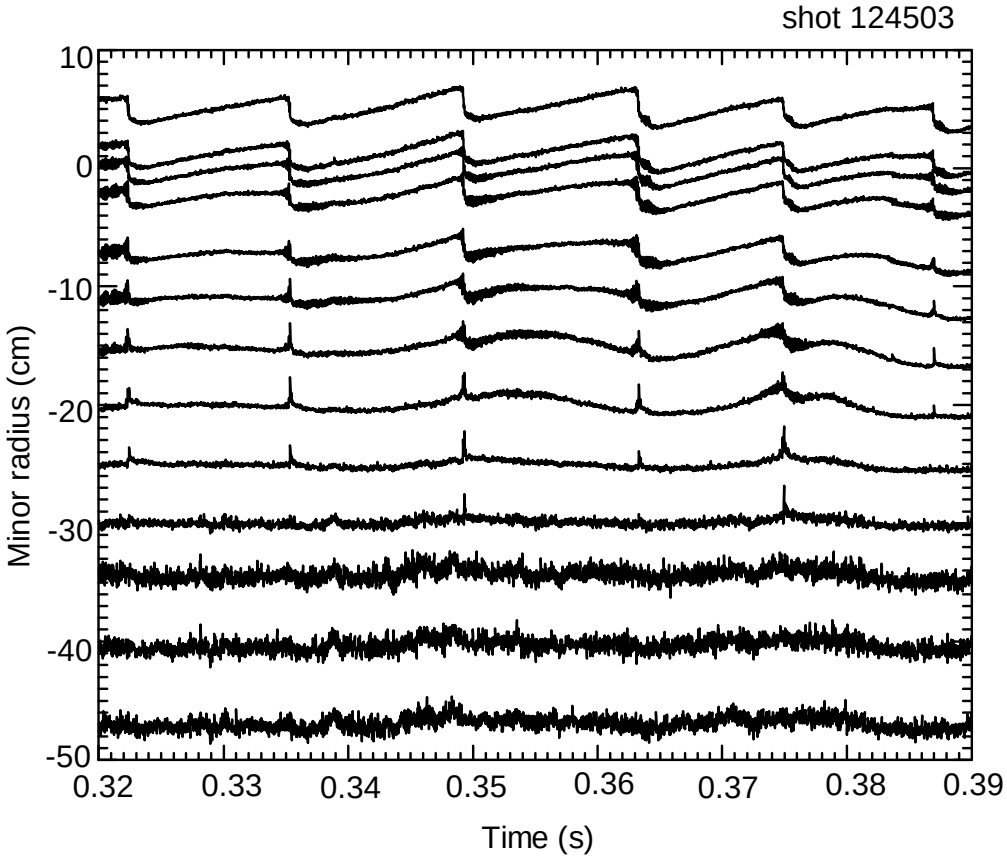

Figure 6.13: The measurements of the soft X-ray array viewing the lower half of plasma suggest that the bursting events in shot 124503 are sawtooth oscillations since each oscillation ends abruptly when a reconnection occurs. The fluctuations are auto-scaled and the tangency radii are mapped to the midplane minor radius using EFIT.

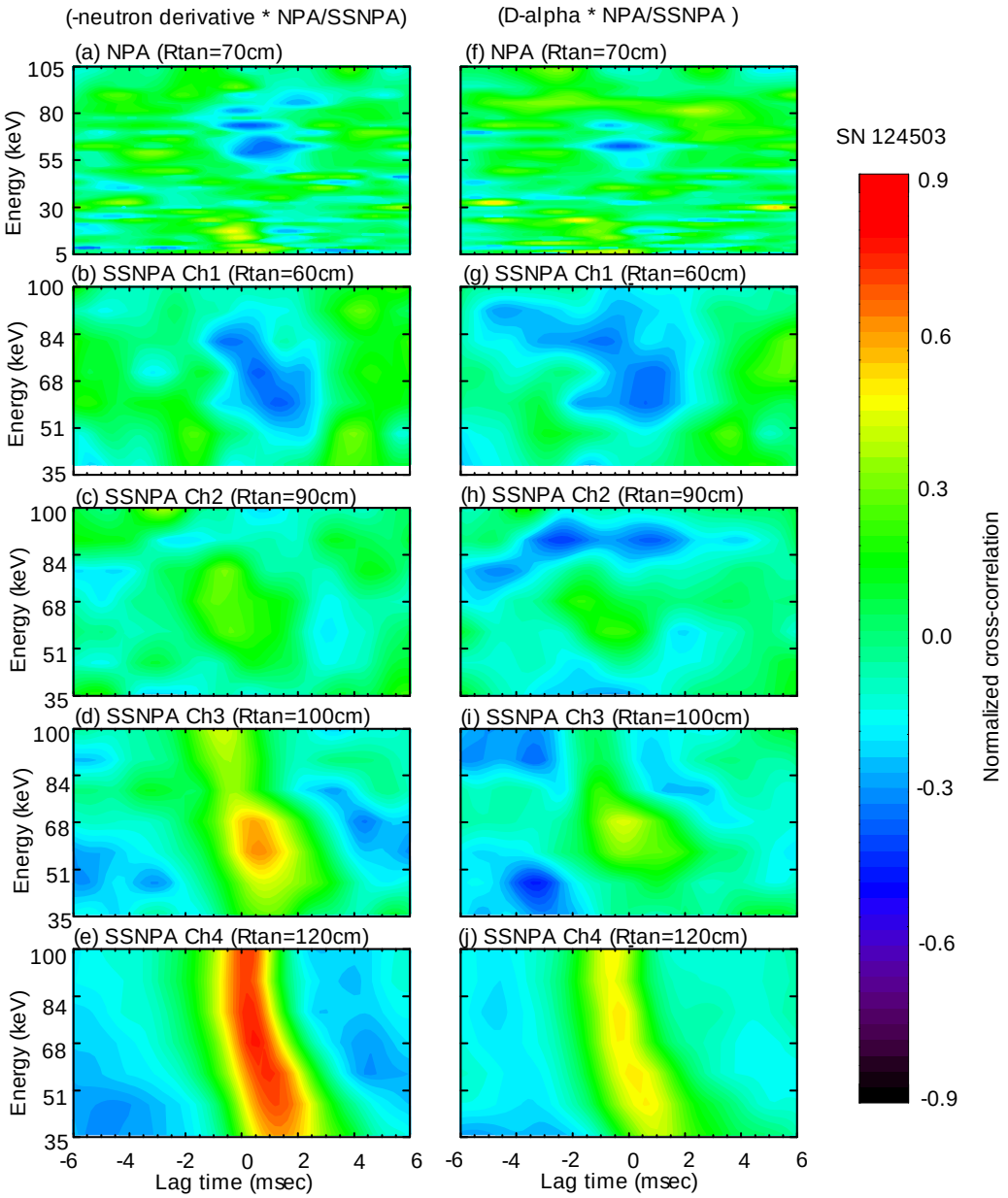

Figure 6.14: Normalized cross-correlations (a-e) between the negative derivative of neutron rate and the NPA/SSNPA signals and (f-j) between the edge D-alpha light and the NPA/SSNPA signals in shot 124503.

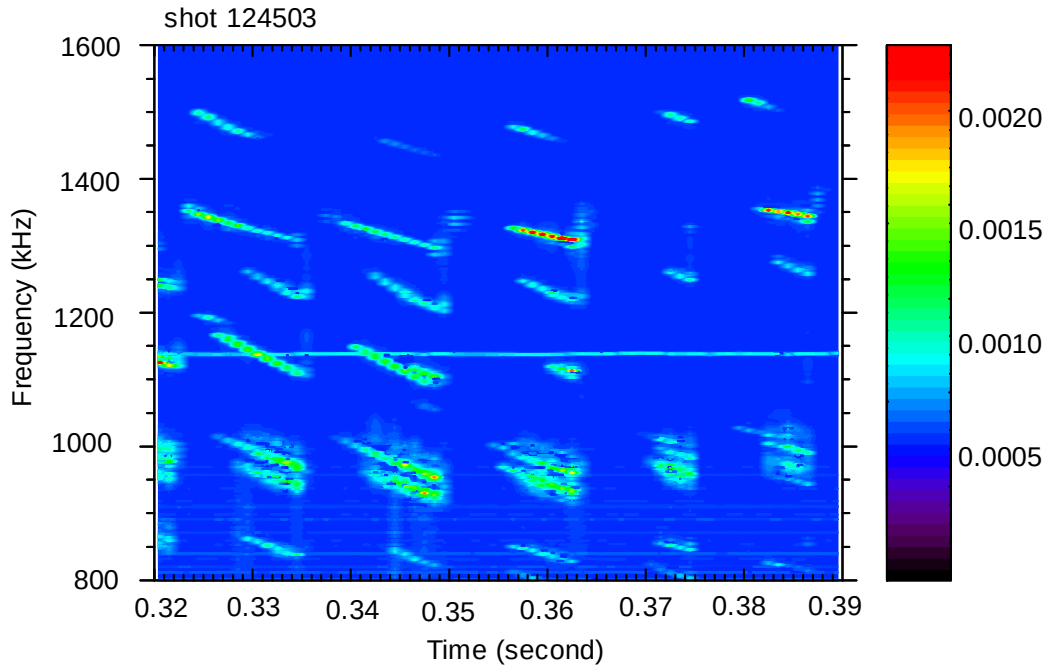

Figure 6.15: The Mirnov coil spectrogram shows there are also some weak CAEs in the frequency range of [800, 1600] kHz during the time window of $0.32 - 0.39$ second in shot 124503. Note that color indicates FFT mode amplitude.

production. Note that there are also very relative weak and chirping CAEs in the frequency range of [800, 1600] kHz in the Mirnov spectrogram 6.15. These CAEs may also affect the fast ion distribution.

6.3.3 TAE Avalanches

Bursts of multiple TAE-like instabilities (i.e. TAE avalanches) are observed to cause fast ion loss in NSTX [145]. In the example shown in Fig. 6.16(a), $n = 2$, 3, and 4 modes are present during the large TAE bursts at 0.257, 0.265, 0.275, 0.284 and 0.293 second in shot 124781. Coincident with the large TAE bursts are drops in the neutron rate of $10\% - 15\%$ and bursts of D_α light, as shown in Fig. 6.17 (e) and (f)). The chords 2 and 3 of the SSNPA diagnostic also show strong correlations with the large TAE bursts. All these observations indicate that some fast ions are lost.

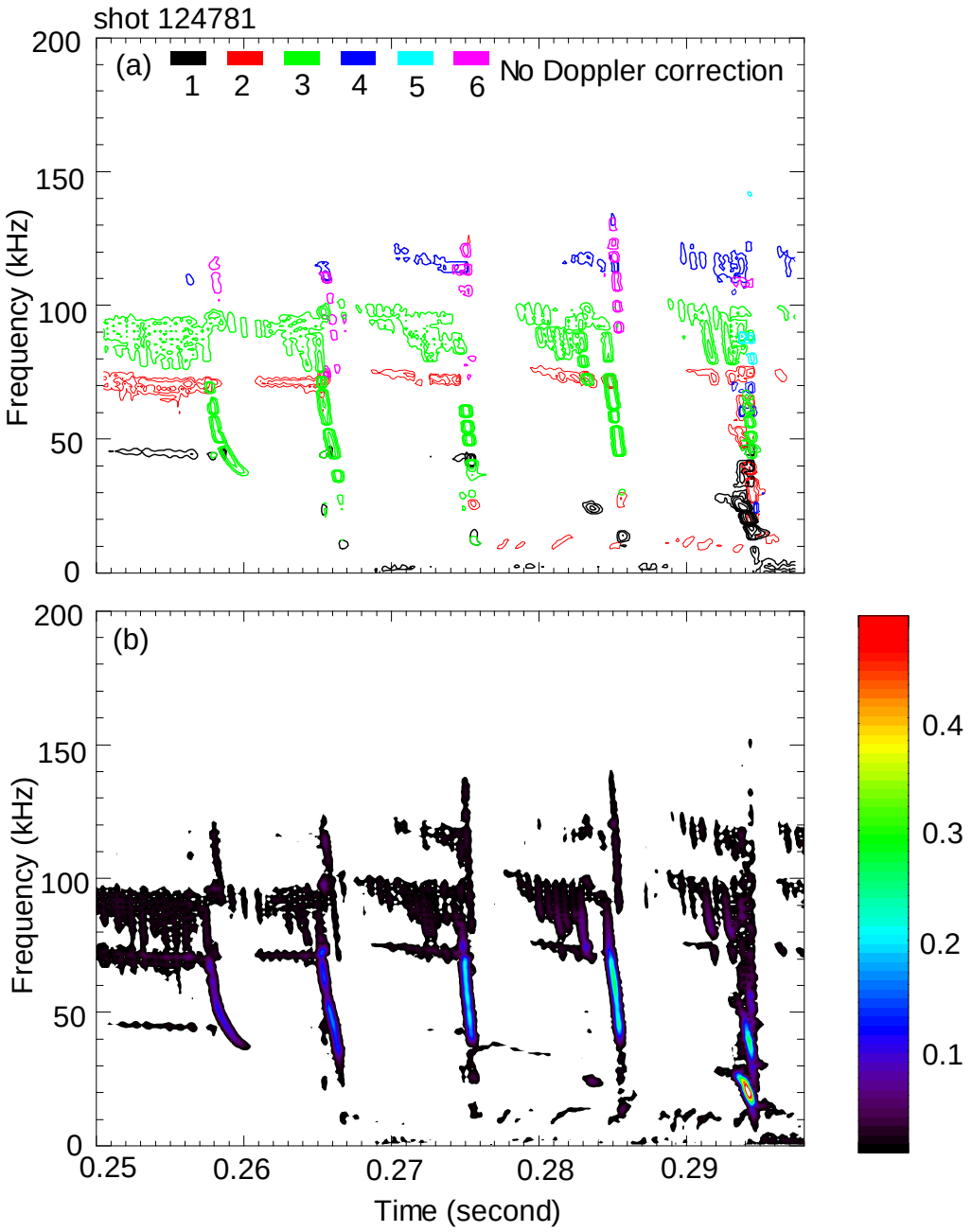

Figure 6.16: The Mirnov coil spectrograms show that TAE avalanches occur at 0.257, 0.265, 0.275, 0.284, and 0.293 second in shot 128741. Note that color in (a) indicates toroidal mode number and color in (b) represents FFT mode amplitude.

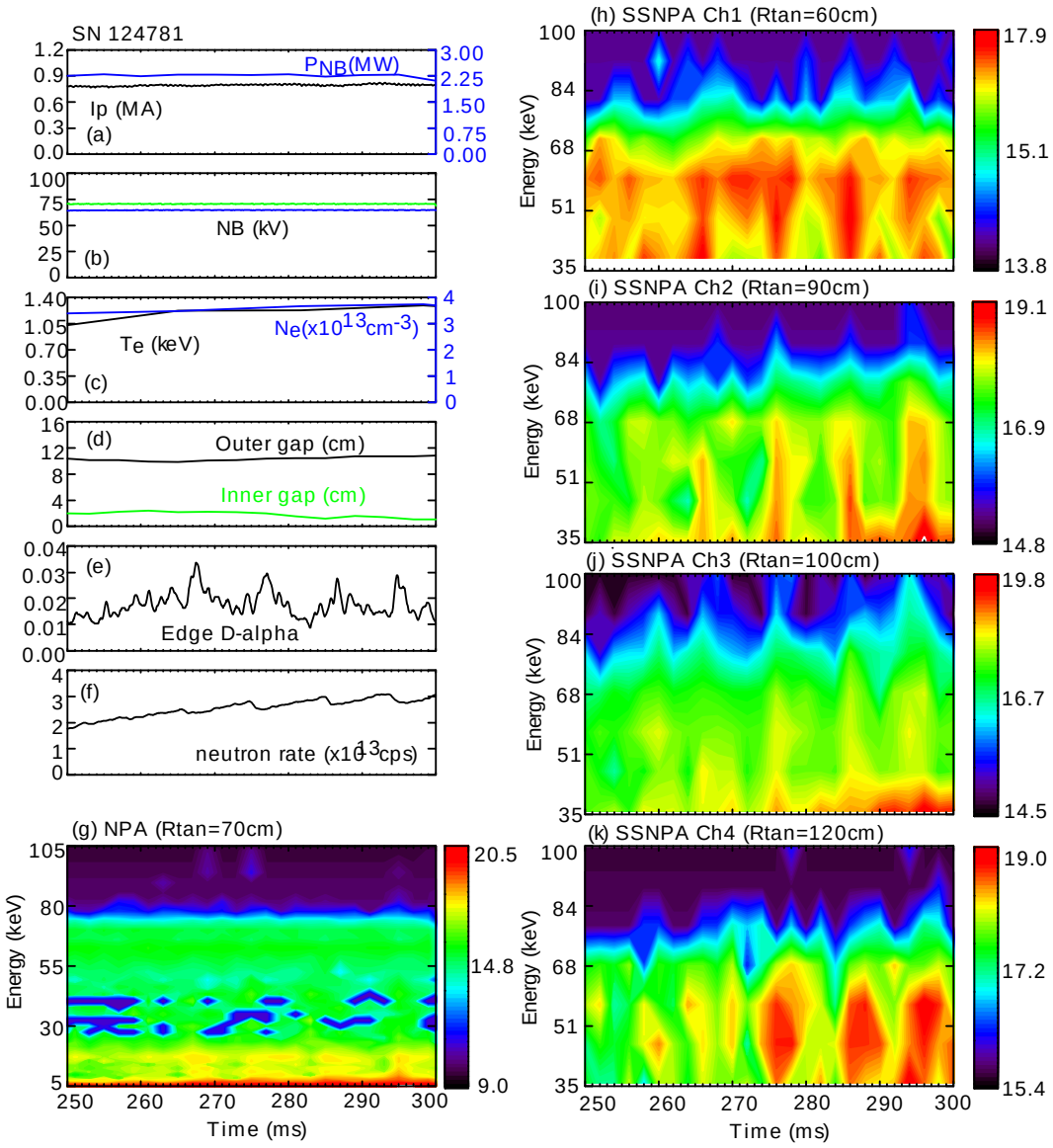

Figure 6.17: Temporal evolution of (a) the plasma current and injected NB power, (b) the beam injection energy, (c) the electron temperature and density, (d) the inner and outer gap width, (e) the edge D–alpha light, (f) the neutron emission rate, (g) the E||B type NPA signal, and (h-k) the SSNPA raw data during the TAE avalanches in shot 124781. Each TAE avalanche causes a $10\% - 15\%$ drop in the neutron rate and a burst at chords 2 and 3 of the SSNPA diagnostic. Note that the signals of E||B type NPA and SSNPA diagnostics are plotted as $\ln(NPA\ Flux/E^{1/2})$ in the units of $cm^{-2}eV^{-3/2}s^{-1}$.

It is proposed that when multiple modes with resonances closely spaced in phase space reach sufficient amplitude so that the fast ion phase space trajectories overlap, the modes can access much more free energy from the fast ion distribution and grow explosively. This leads to a substantial modification of the fast ion distribution, which in turn excites additional, otherwise stable, modes, leading to an "avalanche" effect [145, 146]. The modelling of fast ion transport in TAE avalanches is underway with the NOVA code and ORBIT code [147].

6.4 Modelling of Fishbones and Sawteeth

Fishbone and sawtooth instabilities share many common features. For example, both have a bursting feature and the toroidal mode number n is equal to 1. Figure 6.18 shows that they also have similar plasma parameters except that the electron temperature in the fishbone shots is higher. The other differences are: (i) the magnetic fluctuation measured by Mirnov coils is generally larger in the sawtooth shots than in the fishbone shots, (ii) the $n = 1$ mode in the fishbone shots has a chirping feature, but not in the sawtooth shots; (iii) relatively strong CAEs exist in the sawtooth shots; (iv) the time scale of sawtooth is generally larger than fisbhones. To understand which factor of the mode the most affects the fast-ion transport and why high energy fast ions first respond, the modelling of fast ion transport by the fishbones with the ORBIT code [148] and NOVA code [149, 150] is underway: first, the radial structure of the fishbone density perturbation measured by 5 fixed-frequency reflectometers is compared to the modeled reflectometer response to eigenmodes found by the NOVA-K ideal stability code. The ideally unstable internal kinks, expected to have structure similar to fishbones, are considered. The best match is used as an approximation for the fishbone structure. Second, the approximate fishbone structure will be used as

an input in the ORBIT guiding-center code to consider the effects of the fishbone on the fast ions. Third, the fast ion distribution before and after the fishbone event will be dumped out from the TRANSP code and ORBIT code. They will be used in the FIDA_NPA simulation code to predict the NPA/SSNPA signals before and after the fishbone event. A comparison of those results with the SSNPA and NPA measurements can hopefully determine whether the mode amplitude is responsible for the observed fast-ion loss in the sawtooth cases.

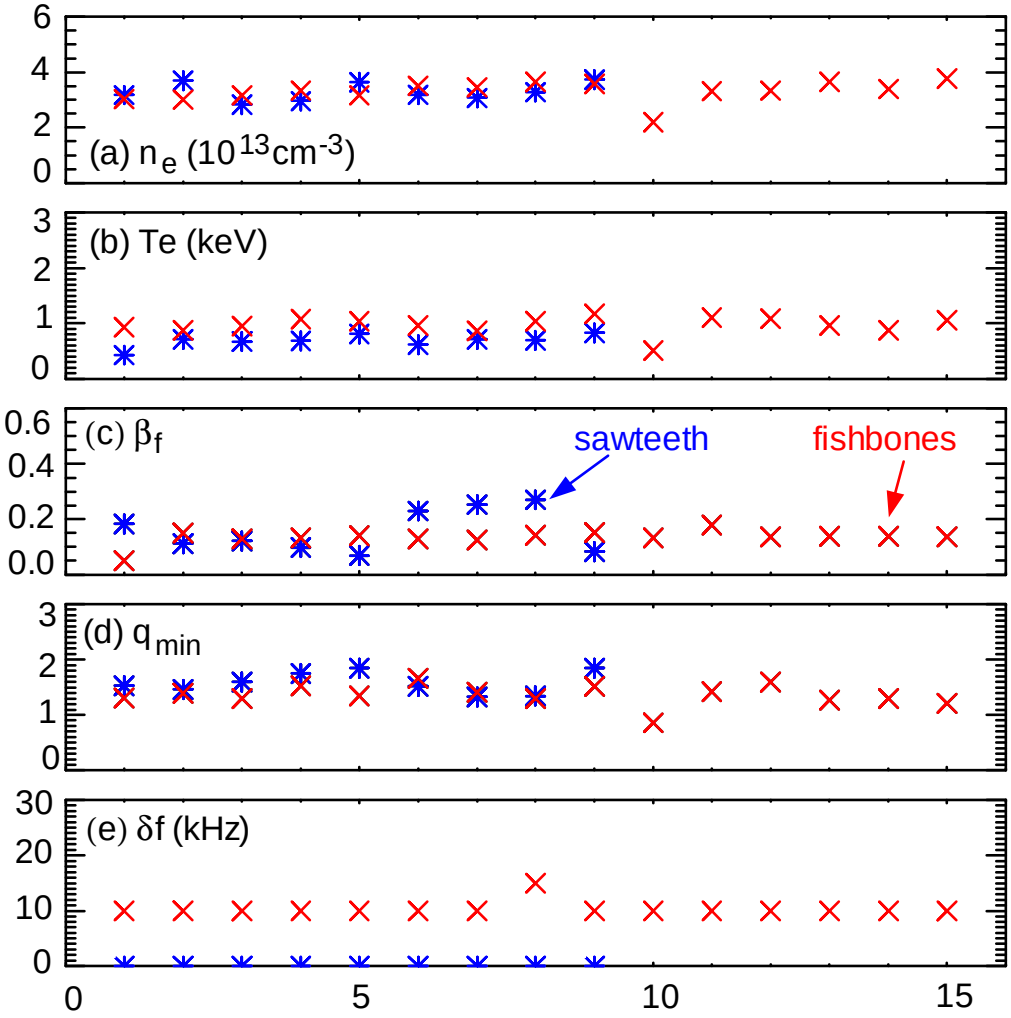

Figure 6.18: Comparison of (a) the central electron density, (b) the central electron temperature, (c) the classically estimated, volume averaged fast ion beta, (d) $q_{\min}$, and (e) the frequency sweep range in the fishbone and sawtooth shots.

6.5 Summary

As shown in Sections 6.3.1 and 6.3.2, the measurements of neutron rate, E||B type NPA and SSNPA suggest that fishbones generally have weak effects on fast ion confinement (less than 5% neutron rate drop), but sawteeth often result in strong (up to 30%) neutron rate drops and fast ion loss. It is also observed that high-energy fast ions respond early than low-energy fast ions. The modelling of fast ion transport during fishbones is ongoing with the ORBIT and NOVA-K codes.

Chapter 7

Conclusions and Future Work

The main objective of this dissertation has been to measure the profiles of accelerated fast ions during combined NBI and HHFW heating and to compare these measurements with the predictions from bounce averaged Fokker-Planck CQL3D code. It addition, the behavior of fast ions during instability bursts such as fishbones and sawteeth is also examined with various fast ion diagnostics and the numerical modelling is underway. In this chapter, we briefly summarize the key results and suggest possible upgrades for the SSNPA diagnostic and interesting areas for future research.

7.1 Summary of Results

Chapter 3 described the newly built SSNPA diagnostic, which consists of four chords with tangency radii of 60, 90, 100 and 120 cm that view across the three co-injection neutral beam lines. Each chord of the SSNPA utilizes a silicon photodiode that is coupled to fast digitizers to measure the energy distribution of charge exchange fast neutral particles. The performance of the SSNPA diagnostic has been improved

with good electromagnetic shielding, fast digitization of raw signals, software-based pulse height analysis and pulse shape discrimination (Sect 3.2.2, 3.2.3, and 3.3.1). The SSNPA diagnostic has achieved an energy resolution of $\sim$ 10 keV and a time resolution of 2 ms (Sect. 3.3.2). The noise of the SSNPA diagnostic is mainly from pulse pile-up and neutron/gamma ray induced noise. (Sect. 3.3.3). The signals of the NPA diagnostics are mainly core-weighted due to active CX reactions with beam neutrals in the intersectional area. However, under certain conditions, the signals from the NPA diagnostics can be edge-weighted due to passive CX reactions with edge neutrals. The NPA diagnostics measure only a small volume in velocity space (Sect. 3.4). The measurements suggest that the SSNPA diagnostic works properly since the temporal evolution of energetic neutral flux obtained with the SSNPA is similar to that obtained with the E||B type NPA, and that fast-ion slowing down time agrees well with the classical theory in quiescent plasmas (Sect. 3.5). Compared with the E||B type NPA, the SSNPA diagnostic has the advantages of compact size, lower equipment cost, and relatively simple design although it has lower count rate and energy resolution.

Chapter 4 mainly presents the development of the FIDA_NPA code, which is used to simulate the NPA/SSNPA active CX signal with a given fast-ion distribution and measured plasma profiles. The neutral flux that can reach the NPA/SSNPA detectors is derived in Sect. 4.4. The FIDA_NPA simulation code correctly treats halo neutrals with the Monte-Carlo method and a random walk model. The simulation suggests that halo neutrals can change the temporal evolution of NPA/SSNPA diagnostics since the ratio of beam neutrals to halo neutrals depends on plasma profiles. But halo neutrals have a minor effect on the NPA/SSNPA energy spectra (Sect. 4.4.2.3). The FIDA_NPA simulation code and the FIDA simulation code share many common modules, since both NPA and FIDA diagnostics rely on charge exchange neutrals. In this thesis, these two codes have been used to predict the NPA/SSNPA and

FIDA signals during quiet plasmas or during HHFW heating.

Chapter 5 shows the measurements of the fast ion radial profile during HHFW heating and comparisons with the CQL3D simulations. With 1.1 MW of HHFW power, the neutron emission rate is about three times larger than in the comparison discharge without HHFW heating (Sect. 5.2.2). The acceleration of fast ions above the beam injection energy is evident on the E||B type NPA, SSNPA array and FIDA diagnostic (Sections 5.2.3 and 5.2.4). The analysis suggests that the accelerated fast ion tail observed by the NPA diagnostic in previous work [113] mainly comes from passive CX reactions at the edge due to the NPA localization in phase space (Sect. 5.3). The spatial profile of the accelerated fast ions measured by the FIDA diagnostic is much broader than in conventional tokamaks because of the multiple resonance layers and large orbits in NSTX (Sect. 5.2.4). The fast-ion distribution function calculated by the CQL3D Fokker-Planck code differs from the measured spatial profile, presumably because the current version of CQL3D uses a zero-banana-width model (Sect. 5.3). These discrepancies indicate that the large Lamor radius and banana width of fast ions in NSTX can significantly affect the fast ion profiles during HHFW heating and these effects should be included for quantitative comparison between measurements and theories.

Chapter 6 shows the different effects of fishbones and sawteeth on the fast ion distribution. It is observed that sawteeth always result in a strong neutron drop. Also, the most outboard chord of the SSNPA shows strong bursts correlated with the sawtooth events. These facts suggest that high energy fast ions are expelled from the plasma. However, pure fishbone events generally have a small effect on the neutron rate (less than 5% neutron rate drop) and the NPA/SSNPA signals. With the conjunctions of bursting CAEs and fishbones, however, the neutron rate drops as much as that in sawteeth. The modelling of fast ion transport due to fishbones is

underway. Hopefully, this can determine whether the mode amplitude is responsible for the observed fast-ion loss in the sawtooth case.

7.2 Suggestions for Future Research

Although the SSNPA diagnostic works properly, it has a time resolution of 2 msec and energy resolution of 10 keV. This is mainly limited by the SNR and the count rate. In terms of hardware, a few improvements and upgrades can be implemented. First, the integration of detectors, preamplifiers and amplifiers should be considered since the signal from the detectors is on the order of a nA. Any EM pickup before the amplifiers will be amplified, which make it difficult to tell real signals from the noise. Second, high quality detectors, charge sensitive preamplifiers and shaping amplifiers are desired. The detectors are required to have low capacitance, low dark current and high radiation hardness. The charge sensitive preamplifiers should have low noise, fast rise time, short decay tail and high energy sensitivity. The shaping amplifiers are the bottle-neck that limits the SSNPA count rate right now. This stage can be removed if preamplifiers with ten times larger gain than the current ones can be built or purchased. Otherwise, shaping amplifiers with differential inputs, low noise, high gain, fast shaping time and high input count rate are needed. Third, cooling of the SSNPA detectors can also be considered since the thermal noise of silicon photodiodes decreases with temperature. Fourth, the energy range of the diagnostic can be extended by using thinner foils. Experimental study is needed to verify the optimum thickness. Fifth, the addition of tangential chords spanning the entire plasma major radius should be considered and one chord should be used to monitor the background noise induced by the neutron or gamma ray. Sixth, the digitizers could be operated at faster frequencies for smoother voltage outputs to

facilitate the detailed pulse height analysis. The pulse height analysis procedures could be optimized to improve the energy resolution and to recover piled-up pulses. Seventh, the pin-hole apertures before the SSNPA detectors could be adjustable inside the vacuum. Additionally, the SSNPA diagnostic could be switched from pulse mode to current mode. The advantage of current mode is that it will get much better SNR and time resolution, but the disadvantage is that it will lose energy resolution.

From an analysis point of view, our self-developed FIDA_NPA simulation code could include the passive charge exchange signals near the plasma edge. This is made possible by mapping a given background neutral density radial profile along the NPA/SSNPA sightlines. Then the charge exchange reactivity with edge neutrals and attenuation factors can be calculated. The CQL3D's applicability to NSTX will improve when it can include the finite Larmor radius effect in its beam package and utilizes time-dependent magnetic equilibria and kinetic profiles. The orbit effects and spatial diffusion could be included in the analysis by using the Monte-Carlo ORBIT-RF code. Hopefully these can help us resolve the discrepancies between the fast-ion profile measurements and the simulations.

Future experiments to measure the accelerated fast ion profile during HHFW heating should investigate other approaches as well. Some slight variations of the techniques presented here can be made. First, modulate the NB source A instead of NB source B or modulate NB source A and B simultaneously. In this way the fast ions are born in the pitch of ~ 0.7, which is closer to the pitch range that can be detected by the E||B NPA and SSNPA diagnostics. Second, during the E||B NPA vertical scan, set its tangency radius to be ~ 60 cm so that it measures charge exchange neutrals in the more perpendicular direction (Fig. 5.14). Thus it may be able to observe the fast ion tail in the active charge exchange signal. Additionally, keep the NB source on when the HHFW is turned off. In this way, we can measure the slowing down of

the accelerated fast ions. These experiments will help us better understand the fast ion behavior during the HHFW heating.

Together with the E||B type NPA, SSNPA and fast-ion loss probe, the newly built FIDA diagnostic can enable us to further our understanding of the fast ion transport due to bursting instabilities including fishbones, sawteeth, TAEs and TAE avalanches. Knowledge of the fast-ion radial distribution will allow detailed quantitative comparison between theory and experiments. Meanwhile, measurements of the mode structure are always helpful for the modelling.

Bibliography

[1] J. Ongena and G. V. Oost, Transactions of Fusion Science and Technology **45**, 3 (2002).

[2] J. Ongena and G. V. Oost, Transactions of Fusion Science and Technology **49**, 3 (2006).

[3] J. A. Angelo, *Nuclear Technology*, Greenwood Publishing Group, 2004.

[4] B. Unterberg and U. Samm, Transactions of Fusion Science and Technology **49**, 415 (2006).

[5] ITER website, http://www.iter.org .

[6] J. Lindl, Phys. Plasmas **2**, 3933 (1995).

[7] S. Pfalzner, *An introduction to inertial confinement fusion*, Taylor and Francis Inc., 2006.

[8] J. D. Lindl, P. Amendt, R. L. Berger, S. G. Glendinning, S. H. Glenzer, S. W. Haan, R. L. Kauffman, O. L. Landen, and L. J. Suter, Phys. Plasmas **11**, 339 (2004).

[9] J. Wesson, *Tokamaks*, The International Series of Monographs on Physics, Oxford University Press, third edition, 2004.

[10] J. D. Lawson, Proc. Phys. Soc. B, **70**, 6 (1957).

[11] E. I. Moses, R. L. McCrory, D. D. Meyerhofer, and C. J. Keane, Optics and Photonics News **20**, 42 (2009).

[12] I. Tamm and A. Sakharov, Proceedings of the Second International Conference on the Peaceful Uses of Atomic Energy **1**, 1 (1961).

[13] C. Braams and P. Stott, *Nuclear Fusion: Half a Century of Magnetic Confinement Fusion Research*, Taylor and Francis Inc., 2001.

[14] International Fusion Research Council (IFRC), Nucl. Fusion **45**, A1 (2005).

[15] Y.-K. M. Peng and D. J. Strickler, Nucl. Fusion **26**, 769 (1986).

[16] R. D. Stambaugh, V. S. Chan, R. L. Miller, and M. J. Schaffer, Fusion Technol. **33**, 1 (1999).

[17] Y.-K. M. Peng, Phys. Plasmas **7**, 1681 (2000).

[18] D. C. Robinson, Plasma Phys. and Contr. Fusion **41**, A143 (1999).

[19] A. Sykes, Nucl. Fusion **39**, 1271 (1999).

[20] M. Ono, S. Kaye, Y.-K. Peng, G. Barnes, W. Blanchard, M. Carter, J. Chrzanowski, L. Dudek, R. Ewig, D. Gates, R. Hatcher, T. Jarboe, S. Jardin, D. Johnson, R. Kaita, M. Kalish, C. Kessel, H. Kugel, R. Maingi, R. Majeski, J. Manickam, B. McCormack, J. Menard, D. Mueller, B. Nelson, B. Nelson, C. Neumeyer, G. Oliaro, F. Paoletti, R. Parsells, E. Perry, N. Pomphrey, S. Ramakrishnan, R. Raman, G. Rewoldt, J. Robinson, A. Roquemore, P. Ryan, S. Sabbagh, D. Swain, E. Synakowski, M. Viola, M. Williams, J. Wilson, and the NSTX Team, Nucl. Fusion **40**, 557 (2000).

[21] S. M. Kaye, M. G. Bell, R. E. Bell, J. Bialek, T. Bigelow, M. Bitter, P. Bonoli, D. Darrow, P. Efthimion, J. Ferron, E. Fredrickson, D. Gates, L. Grisham, J. Hosea, D. Johnson, R. Kaita, S. Kubota, H. Kugel, B. LeBlanc, R. Maingi, J. Manickam, T. K. Mau, R. J. Maqueda, E. Mazzucato, J. Menard, D. Mueller, B. Nelson, N. Nishino, M. Ono, F. Paoletti, S. Paul, Y.-K. M. Peng, C. K. Phillips, R. Raman, P. Ryan, S. A. Sabbagh, M. Schaffer, C. H. Skinner, D. Stutman, D. Swain, E. Synakowski, Y. Takase, J. Wilgen, J. R. Wilson, W. Zhu, S. Zweben, A. Bers, M. Carter, B. Deng, C. Domier, E. Doyle, M. Finkenthal, K. Hill, T. Jarboe, S. Jardin, H. Ji, L. Lao, K. C. Lee, N. Luhmann, R. Majeski, S. Medley, H. Park, T. Peebles, R. I. Pinsker, G. Porter, A. Ram, M. Rensink, T. Rognlien, D. Stotler, B. Stratton, G. Taylor, W. Wampler, G. A. Wurden, X. Q. Xu, L. Zeng, and the NSTX Team, Phys. Plasmas **8**, 1977 (2001).

[22] A. Sykes, R. Akers, L. Appel, E. Arends, P. Carolan, N. Conway, G. Counsell, G. Cunningham, A. Dnestrovskij, Y. Dnestrovskij, A. Field, S. Fielding, M. Gryaznevich, S. Korsholm, E. Laird, R. Martin, M. Nightingale, C. Roach, M. Tournianski, M. Walsh, C. Warrick, H. Wilson, S. You, and MAST Team and NBI Team, Nucl. Fusion **41**, 1423 (2001).

[23] A. Sykes, J.-W. Ahn, R. Akers, E. Arends, P. G. Carolan, G. F. Counsell, S. J. Fielding, M. Gryaznevich, R. Martin, M. Price, C. Roach, V. Shevchenko, M. Tournianski, M. Valovic, M. J. Walsh, H. R. Wilson, and the MAST Team, Phys. Plasmas **8**, 2101 (2001).

[24] S. Kaye, M. Ono, and Y. Peng, Fusion Technol. **36**, 16 (1999).

[25] D. Johnson and the NSTX Team, Plasma Phys. and Contr. Fusion **45**, 1975 (2003).

[26] J. Luxon, Nucl. Fusion **42**, 614 (2002).

[27] Y. Luo, *Fast-Ion D-alphaMeasurements and Simulations in DIII-D*, PhD thesis, University of California, Irvine, 2007.

[28] C. Neumeyer, P. Heitzenroeder, J. Spitzer, J. Chrzanowski, A. Brooks, J. Bialek, H. M. Fan, G. Barnes, M. Viola, B. Nelson, P. Goranson, R. Wilson, E. Fredd, L. Dudek, R. Parsells, M. Kalish, W. Blanchard, R. Kaita, H. Kugel, B. McCormack, S. Ramakrishnan, R. Hatcher, G. Oliaro, E. Perry, T. Egebo, A. V. Halle, M. Williams, and M. Ono, Fusion Engineering and Design **54**, 275 (2001).

[29] W. W. Heidbrink and G. J. Sadler, Nucl. Fusion **34**, 535 (1994).

[30] A. Fasoli, C. Gormenzano, H. Berk, B. Breizman, S. Briguglio, D. Darrow, N. Gorelenkov, W. Heidbrink, A. Jaun, S. Konovalov, R. Nazikian, J.-M. Noterdaeme, S. Sharapov, K. Shinohara, D. Testa, K. Tobita, Y. Todo, G. Vlad, and F. Zonca, Nucl. Fusion **47**, S264 (2007).

[31] W. W. Heidbrink, Phys. Plasmas **15**, 055501 (2008).

[32] D. R. Mikkelsen, R. B. White, R. J. Akers, S. M. Kaye, D. C. McCune, and J. E. Menard, Phys. Plasmas **4**, 3667 (1997).

[33] J. Egedal, M. H. Redi, D. S. Darrow, and S. M. Kaye, Phys. Plasmas **10**, 2372 (2003).

[34] Y. I. Kolesnichenko, R. B. White, and Y. V. Yakovenko, Phys. Plasmas **10**, 1449 (2003).

[35] Y. I. Kolesnichenko, R. B. White, and Y. V. Yakovenko, Phys. Plasmas **9**, 2639 (2002).

[36] E. D. Fredrickson, C. Z. Cheng, D. Darrow, G. Fu, N. N. Gorelenkov, G. Kramer, S. S. Medley, J. Menard, L. Roquemore, D. Stutman, and R. B. White, Physics of Plasmas **10**, 2852 (2003).

[37] N. N. Gorelenkov, E. Belova, H. L. Berk, C. Z. Cheng, E. Fredrickson, W. W. Heidbrink, S. Kaye, and G. J. Kramer, Phys. Plasmas **11**, 2586 (2004).

[38] S. Medley, N. Gorelenkov, R. Andre, R. Bell, D. Darrow, E. Fredrickson, S. Kaye, B. LeBlanc, A. Roquemore, and the NSTX Team, Nucl. Fusion **44**, 1158 (2004).

[39] K. Shinohara, D. S. Darrow, A. L. Roquemore, S. S. Medley, and F. E. Cecil, Rev. Sci. Instrum. **75**, 3640 (2004).

[40] D. Liu, W. W. Heidbrink, D. S. Darrow, A. L. Roquemore, S. S. Medley, and K. Shinohara, Rev. Sci. Instrum. **77**, 10F113 (2006).

[41] T. Stevenson, B. McCormack, G. Loesser, M. Kalish, S. Ramakrishnan, L. Grisham, J. Edwards, M. Cropper, G. Rossi, A. von Halle, and M. Williams, Princeton Plasma Physics Laboratory Report, PPPL-3651 (2002).

[42] J. R. Wilson, R. E. Bell, S. Bernabei, M. Bitter, P. Bonoli, D. Gates, J. Hosea, B. LeBlanc, T. K. Mau, S. Medley, J. Menard, D. Mueller, M. Ono, C. K. Phillips, R. I. Pinsker, R. Raman, A. Rosenberg, P. Ryan, S. Sabbagh, D. Stutman, D. Swain, Y. Takase, J. Wilgen, and the NSTX Team, Phys. Plasmas **10**, 1733 (2003).

[43] M. Ono, Phys. Plasmas **2**, 4075 (1995).

[44] T. L. MUNSAT, *Transient Transport Experiments in the CDX-U Spherical Tours*, PhD thesis, Princeton University, 2001.

[45] B. P. LeBlanc, R. E. Bell, D. W. Johnson, D. E. Hoffman, D. C. Long, and R. W. Palladino, Rev. Sci. Instrum. **74**, 1659 (2003).

[46] D. Johnson, N. Bretz, B. LeBlanc, R. Palladino, D. Long, and R. Parsells, Rev. Sci. Instrum. **70**, 776 (1999).

[47] M. Bell, R. Bell, B. LeBlanc, and S. Medley, Princeton Plasma Physics Laboratory Report, PPPL-3601 (2001).

[48] B. P. LeBlanc, Rev. Sci. Instrum. **79**, 10E737 (2008).

[49] R. Bell, Private communication (2005).

[50] R. Bell, B. LeBlanc, C. Bourdelle, D. Ernst, E. Fredrickson, D. Gates, J. Hosea, D. Johnson, S. Kaye, R. Maingi, S. Medley, J. Menard, D. Mueller, M. Ono, F. Paoletti, M. Peng, S. Sabbagh, D. Stutman, D. Swain, E. Synakowski, and J. Wilson, Princeton Plasma Physics Laboratory Report, PPPL-3591 (2001).

[51] F. M. Levinton and H. Yuh, Rev. Sci. Instrum. **79**, 10F522 (2008).

[52] E. U. Condon and G. H. Shortley, *The Theory of Atomic Spectra*, Cambridge University Press, 1963.

[53] F. M. Levinton, R. J. Fonck, G. M. Gammel, R. Kaita, H. W. Kugel, E. T. Powell, and D. W. Roberts, Phys. Rev. Lett. **63**, 2060 (1989).

[54] S. Sabbagh, S. Kaye, J. Menard, F. Paoletti, M. Bell, R. Bell, J. Bialek, M. Bitter, E. Fredrickson, D. Gates, A. Glasser, H. Kugel, L. Lao, B. LeBlanc, R. Maingi, R. Maqueda, E. Mazzucato, D. Mueller, M. Ono, S. Paul, M. Peng, C. Skinner, D. Stutman, G. Wurden, W. Zhu, and the NSTX Team, Nucl. Fusion **41**, 1601 (2001).

[55] D. Stutman, M. Finkenthal, H. W. Moos, K. B. Fournier, R. Kaita, D. Johnson, and L. Roquemore, Rev. Sci. Instrum. **74**, 1982 (2003).

[56] D. Stutman, M. Finkenthal, V. Soukhanovskii, M. J. May, H. W. Moos, and R. Kaita, Rev. Sci. Instrum. **70**, 572 (1999).

[57] D. S. Darrow, Rev. Sci. Instrum. **79**, 023502 (2008).

[58] S. Medley and A. L. Roquemore, Rev. Sci. Instrum. **69**, 2651 (1998).

[59] S. S. Medley, A. J. H. Donne, R. Kaita, A. I. Kislyakov, M. P. Petrov, and A. L. Roquemore, Rev. Sci. Instrum. **79**, 011101 (2008).

[60] S. S. Medley and A. L. Roquemore, Rev. Sci. Instrum. **75**, 3625 (2004).

[61] W. W. Heidbrink, K. H. Burrell, Y. Luo, N. A. Pablant, and E. Ruskov, Plasma Phys. and Contr. Fusion **46**, 1855 (2004).

[62] M. Podestà, W. W. Heidbrink, R. E. Bell, and R. Feder, Rev. Sci. Instrum. **79**, 10E521 (2008).

[63] W. W. Heidbrink, R. E. Bell, Y. Luo, and W. Solomon, Rev. Sci. Instrum. **77**, 10F120 (2006).

[64] A. Krasilnikov, V. Amosov, and Y. A. Kaschuck, IEEE Trans. Nucl. Sci. , 385 (1998).

[65] A. V. Krasilnikov, S. S. Medley, N. N. Gorelenkov, R. V. Budny, O. V. Ignatyev, Y. A. Kaschuck, M. P. Petrov, and A. L. Roquemore, Rev. Sci. Instrum. **70**, 1107 (1999).

[66] M. Isobe, M. Sasao, S. Iiduka, A. V. Krasilnikov, S. Murakami, T. Mutoh, M. Osakabe, S. Sudo, K. Kawahata, N. Ohyabu, and O. Motojima, Rev. Sci. Instrum. **72**, 611 (2001).

[67] T. Yamamoto, M. Osakabe, M. Isobe, Y. Yoshimura, R. Kumazawa, T. Mutoh, T. Watari, Y. Takeiri, O. Kaneko, C. Takahasi, and K. Matsuoka, Rev. Sci. Instrum. **72** (2001).

[68] A. G. Alekseyev, D. S. Darrow, A. L. Roquemore, S. S. Medley, V. N. Amosov, A. V. Krasilnikov, D. V. Prosvirin, and A. Y. Tsutskikh, Rev. Sci. Instrum. **74**, 1905 (2003).

[69] M. Osakabe, T. Yamamoto, Y. Takeiri, T. Mutoh, E. Asano, K. Ikeda, K. Tsumori, O. Kaneko, K. Kawahata, N. Ohyabu, and O. Motojima, Rev. Sci. Instrum. **72**, 72 (2001).

[70] J. F. Lyon, P. R. Goncharov, S. Murakami, T. Ozaki, D. E. Greenwood, D. A. Spong, and S. Sudo, Rev. Sci. Instrum. **74**, 1873 (2003).

[71] V. Tang, J. Liptac, R. R. Parker, P. T. Bonoli, C. L. Fiore, R. S. Granetz, J. H. Irby, Y. Lin, S. J. Wukitch, J. A. Frenje, R. Leiter, S. Mcduffee, and R. D. Petrasso, Rev. Sci. Instrum. **77**, 083501 (2006).

[72] http://www.ird-inc.com/axuvhigh. html .

[73] TRIM website, http://www.srim.org/ .

[74] Metglas Inc. website, http://www.metglas.com .

[75] EXACQ website, http://www.exacqdaq.com/ .

[76] S. Sabbagh, A. Sontag, J. Bialek, D. Gates, A. Glasser, J. Menard, W. Zhu, M. Bell, R. Bell, A. Bondeson, C. Bush, J. Callen, M. Chu, C. Hegna, S. Kaye, L. Lao, B. LeBlanc, Y. Liu, R. Maingi, D. Mueller, K. Shaing, D. Stutman, K. Tritz, and C. Zhang, Nuclear Fusion **46**, 635 (2006).

[77] T. N. Collaboration, S. Marrone, D. Cano-Ott, N. Colonna, C. Domingo, F. Gramegna, E. M. Gonzalez, F. Gunsing, M. Heil, F. Käppeler, P. F. Mastinu, P. M. Milazzo, T. Papaevangelou, P. Pavlopoulos, R. Plag, R. Reifarth, G. Tagliente, J. L. Tain, and K. Wisshak, Nucl. Instrum. Methods Phys. Res. A **490**, 299 (2002).

[78] P. R. Goncharov, T. Ozaki, S. Sudo, N. Tamura, M. Isobe, T. Group, and L. E. Group, Rev. Sci. Instrum. **75**, 3613 (2004).

[79] W. Guo, S. H. Leeb, and R. P. Gardner, Nucl. Instrum. Methods Phys. Res. A **531**, 520 (2004).

[80] G. F. Knoll, *Radiation Detection and Measurement*, Wiley, New York, 3rd edition, 2000.

[81] U.S. Naval Plasma Laboratory, *NRL Plasma Formulary*, Washington, DC, 2006.

[82] W. W. Heidbrink, J. Kim, and R. J. Groebner, Nucl. Fusion **28**, 1897 (1988).

[83] R. J. Hawryluk, *An Empirical Approach to Tokamak Transport, in Physicsof Plasmas Close to Thermonuclear Conditions*, volume 1, CEC, Brussels, 1980, pp. 19-46.

[84] R. V. Budny, Nucl. Fusion **34**, 1247 (1994).

[85] J. Ongena, M. Evrard, and D. McCune, Trans. Fusion Tech. **33**, 181 (1998).

[86] TRANSP website, http://w3.pppl.gov/transp .

[87] A. Pankin, D. McCune, R. Andre, G. Bateman, and A. Kritz, Comput. Phys. Communications **159**, 157 (2004).

[88] R. W. Harvey and M. G. Mccoy, in *1992 Proc. IAEA Technical Committee Meeting on Advances in Simulation and Modeling of Thermonuclear Plasmas*, Montreal, Quebec, 1992, Vienna: IAEA.

[89] W. W. Heidbrink, K. H. Burrell, Y. Luo, N. A. Pablant, and E. Ruskov, Plasma Phys. Controlled Fusion **46**, 1855 (2004).

[90] Y. Luo, W. W. Heidbrink, E. Ruskov, K. H. Burrell, and W. M. Solomon, Phys. Plasmas **14**, 112503 (2007).

[91] I. H. Hutchinson, *Principles of Plasma Diagnostics*, Cambridge University Press, New York, 1987.

[92] C. F. Barnett, H. T. Hunter, M. I. Kirkpatrick, I. Alvarez, C. Cisneros, and R. A. Phaneuf, *Collisions of H, He, and Li Atoms and Ions with Atoms and Molecules,Technical Report ORNL-6086/V1*, Oak Ridge National Laboratory, 1990.

[93] R. A. Phaneuf, R. K. Janev, and M. S. Pindzola, *Collisions of Carbon and Oxygen Ions with Electrons, H, H2, and He,Technical Report ORNL-6090/V5*, Oak Ridge National Laboratory, 1987.

[94] R. K. Janev, W. D. Langer, K. Evans, and D. E. Post, *Elementary Processes in Hydrogen-Helium Plasmas*, Springer-Verlag, 1987.

[95] A. L. Rosenberg, Ph.D. dissertation, Princeton University (2003).

[96] R. B. White and M. S. Chance, Phys. Fluids **27**, 2455 (1984).

[97] R. Janev, D. Reiter, and U. Samm, Juel Report 4105 (2004), http://www.eirene.de.

[98] T. A. Gianakon, R. J. Fonck, J. D. Callen, R. D. Durst, and J. S. Kim, Rev. Sci. Instrum. **63**, 4931 (1992).

[99] ADAS, http://adas.phys.strath.ac.uk/ .

[100] H. Anderson, M. G. V. Hellermann, R. Hoekstra, L. D. Horton, A. C. Howman, R. W. T. Konig, R. Martin, R. E. Olson, and H. P. Summers, Plasma Phys. Control. Fusion **42**, 781 (2000).

[101] D. F. Finkenthal, *The Measurement of Absolute Helium Ion Density Profies on the DIII-D Tokamak Using Charge Exchange Spectroscopy*, PhD thesis, University of California at Berkeley, 1994.

[102] R. E. Bell, Princeton Plasma Physics Laboratory Report, PPPL-4167 (2006).

[103] V. Tang, *Experimental and Numerical Characterization of Ion-Cyclotron Heated Protons on the Alcator C-Mod Tokamak*, PhD thesis, Massachusetts Institute of Technology, 2006.

[104] H. Kimura, T. Fujii, M. Saigusa, S. Moriyama, K. Hamamatsu, M. Nemoto, and K. Tobita, Plasma Phys. and Contr. Fusion **35**, 845 (1993).

[105] M. Nemoto, Y. Kusama, V. I. Afanassiev, K. Hamamatsu, H. Kimura, T. Fujii, S. Moriyama, and M. Saigusa, Plasma Physics and Controlled Fusion **39**, 1599 (1997).

[106] C. C. Petty, C. B. Forest, R. I. Pinsker, J. S. deGrassie, F. W. Baity, et al., Fast wave current drive in neutral beam heated plasmas on DIII-D, in *Radio Frequency Power in Plasmas (Proc. 12th International Conference (Savannah, 1997))*, p. 225, New York, 1997, AIP.

[107] L.-G. Eriksson, M. J. Mantsinen, F. G. Rimini, F. Nguyen, C. Gormezano, D. F. H. Start, and A. Gondhalekar, Nucl. Fusion **38**, 265 (1998).

[108] R. I. Pinsker, F. W. Baity, S. N. Bernabei, N. Greenough, W. W. Heidbrink, T. K. Mau, C. C. Petty, M. Porkolab, and the DIII-D Team, Experiments on ion cyclotron damping at the deuterium fourth harmonic in DIII-D, in *Radio Frequency Power in Plasmas (Proc. 13th International Conference (Annapolis, 1999))*, p. 144, New York, 1999, AIP.

[109] W. W. Heidbrink, E. Fredrickson, T. K. Mau, C. C. Petty, R. I. Pinsker, M. Porkolab, and B. W. Rice, Nucl. Fusion **39**, 1369 (1999).

[110] C. C. Petty, F. W. Baity, J. S. deGrassie, et al., Plasma Phys. and Contr. Fusion **43**, 1747 (2001).

[111] M. J. Mantsinen, M.-L. Mayoral, V. G. Kiptily, et al., Phys. Rev. Lett. **88**, 105002 (2002).

[112] J.-M. Noterdaeme et al., Nucl. Fusion **43**, 202 (2003).

[113] A. L. Rosenberg, J. E. Menard, J. R. Wilson, S. S. Medley, R. Andre, C. K. Phillips, D. S. Darrow, B. P. LeBlanc, M. H. Redi, N. J. Fisch, N. Team, R. W. Harvey, T. K. Mau, E. F. Jaeger, P. M. Ryan, D. W. Swain, S. A. Sabbagh, and J. Egedal, Phys. Plasmas **11**, 2441 (2004).

[114] W. W. Heidbrink, Y. Luo, K. H. Burrell, R. W. Harvey, R. I. Pinsker, and E. Ruskov, Plasma Phys. and Contr. Fusion **49**, 1457 (2007).

[115] W. Heidbrink, M. Miah, D. Darrow, B. LeBlanc, S. Medley, A. Roquemore, and F. Cecil, Nucl. Fusion **43**, 883 (2003).

[116] G. M. Hammet, *Fast Ion Studies of Ion Cyclotron Heating in PLT Tokamak*, PhD thesis, Princeton University, 1986.

[117] S. S. Medley, Private communication (2008).

[118] R. Kaita, R. Goldston, P. Beiersdorfer, D. Herndon, J. Hosea, D. Hwang, F. Jobes, D. Meyerhofer, and J. Wilson, Nucl. Fusion **23**, 1089 (1983).

[119] R. J. H. et al, Plasma Phys. and Contr. Fusion **33**, 1509 (1991).

[120] V. Kiptily, J. Adams, L. Bertalot, A. Murari, S. Sharapov, V. Yavorskij, B. Alper, R. Barnsley, P. de Vries, C. Gowers, L.-G. Eriksson, P. Lomas, M. Mantsinen, A. Meigs, J.-M. Noterdaeme, F. Orsitto, and J. E. contributors, Nucl. Fusion **45**, L21 (2005).

[121] Y. Luo, W. W. Heidbrink, K. H. Burrell, D. H. Kaplan, and P. Gohil, Rev. Sci. Instrum. **78**, 033505 (2007).

[122] V. S. Chan, S. C. Chiu, and Y. A. Omelchenko, Phys. Plasmas **9**, 501 (2002).

[123] M. Choi, V. Chan, R. Pinsker, C. Petty, S. Chiu, J. Wright, P. Bonoli, and M. Porkolab, Nucl. Fusion **46**, S409 (2006).

[124] K.-L. Wong, Plasma Phys. and Contr. Fusion **41**, R1 (1999).

[125] E. D. Fredrickson, R. E. Bell, D. S. Darrow, G. Y. Fu, N. N. Gorelenkov, B. P. LeBlanc, S. S. Medley, J. E. Menard, H. Park, A. L. Roquemore, W. W. Heidbrink, S. A. Sabbagh, D. Stutman, K. Tritz, N. A. Crocker, S. Kubota, W. Peebles, K. C. Lee, and F. M. Levinton, Phys. Plasmas **13**, 056109 (2006).

[126] K. McGuire, R. Goldston, M. Bell, M. Bitter, K. Bol, K. Brau, D. Buchenauer, T. Crowley, S. Davis, F. Dylla, H. Eubank, H. Fishman, R. Fonck, B. Grek, R. Grimm, R. Hawryluk, H. Hsuan, R. Hulse, R. Izzo, R. Kaita, S. Kaye, H. Kugel, D. Johnson, J. Manickam, D. Manos, D. Mansfield, and E. Mazzucato, Phys. Rev. Lett. **50**, 891 (1983).

[127] R. B. White, R. J. Goldston, K. McGuire, A. H. Boozer, D. A. Monticello, and W. Park, Physics of Fluids **26**, 2958 (1983).

[128] L. Chen, R. B. White, and M. N. Rosenbluth, Phys. Rev. Lett. **52**, 1122 (1984).

[129] B. Coppi and F. Porcelli, Phys. Rev. Lett. **57**, 2272 (1986).

[130] W. W. Heidbrink, K. Bol, D. Buchenauer, R. Fonck, G. Gammel, K. Ida, R. Kaita, S. Kaye, H. Kugel, B. LeBlanc, W. Morris, M. Okabayashi, E. Powell, S. Sesnic, and H. Takahashi, Phys. Rev. Lett. **57**, 835 (1986).

[131] E. Fredrickson, L. Chen, and R. White, Nucl. Fusion **43**, 1258 (2003).

[132] L. Chen, Phys. Plasmas **1**, 1519 (1994).

[133] S. von Goeler, W. Stodiek, and N. Sauthoff, Phys. Rev. Lett. **33**, 1201 (1974).

[134] B. B. Kadomtsev, Sov. J. Plasma Physics **1**, 389 (1976).

[135] J. A. Wesson, Plasma Phys. and Contr. Fusion **28**, 243 (1986).

[136] W. Park, E. D. Fredrickson, A. Janos, J. Manickam, and W. M. Tang, Phys. Rev. Lett. **75**, 1763 (1995).

[137] Y. Nishimura, J. D. Callen, and C. C. Hegna, Phys. Plasmas **6**, 4685 (1999).

[138] Y. I. Kolesnichenko, V. Lutsenko, R. B. White, and Y. Yakovenko, Nucl. Fusion **40**, 1325 (2000).

[139] Y. Kolesnichenko and Y. Yakovenko, Nucl. Fusion **36**, 159 (1996).

[140] Y. Kolesnichenko, V. Lutsenko, Y. Yakovenko, and G. Kamelander, Phys. Plasmas **4**, 2544 (1997).

[141] R. Akers et al., in *Proceedings of the 26th EPS Conference on Controlled Fusion and Plasma Physics*, p. 117, ECA 23J, 1999.

[142] Y. Kolesnichenko, V. Lutsenko, and V. Marchenko, Phys. Rev. Lett. **82**, 3260 (1999).

[143] Y. Kolesnichenko, V. Lutsenko, and V. Marchenko, Nucl. Fusion **40**, 1731 (2000).

[144] Y. I. Kolesnichenko, V. S. Marchenko, and R. B. White, Phys. Plasmas **8**, 3143 (2001).

[145] E. Fredrickson, N. Gorelenkov, R. Bell, J. Menard, A. Roquemore, S. Kubota, N. Crocker, and W. Peebles, Nucl. Fusion **46**, S926 (2006).

[146] H. L. Berk, B. N. Breizman, and M. Pekker, Phys. Plasmas **2**, 3007 (1995).

[147] E. Fredrickson, Bull. Am. Phys. Soc. **53**, 189 (2008).

[148] R. B. White and M. S. Chance, Phys. Fluids **27**, 2455 (1984).

[149] C. Z. Cheng and M. S. Chance, Phys. Fluids **29**, 3695 (1986).

[150] C. Z. Cheng, Phys. Reports **211**, 1 (1992).

Appendices

A Data Acquisition of the SSNPA Array

The output data of the SSNPA diagnostic are sampled by the 12-bit EXACQ CH3160 digitizer boards at 20 MHz. The data acquisition system is controlled by a dedicated Labview program with the control panel shown in Fig. A.1 (The source code is saved in the directory of C:\ssnpa_2008\ssnpa_pc\labview\ssnpa\SSNPA_VI_2009.vi in the local SSNPA PC). A standard TTL signal is used for triggering and the start time is currently set to 10 ms before each shot. The raw data are first saved in the local PC and then uploaded onto the MDSplus tree automatically between shots. Since the SSNPA system picks up huge noise during the NSTX test shots, the power supply of the SSNPA system is remotely turned on after the NSTX test shots and turned off at the end of run day though an AC power controller The noise of the SSNPA system can be monitored with the software "ExacqBench" (C:\Program Files\Exacq\Bench\ExacqBench.exe) provided by the digitizer company.

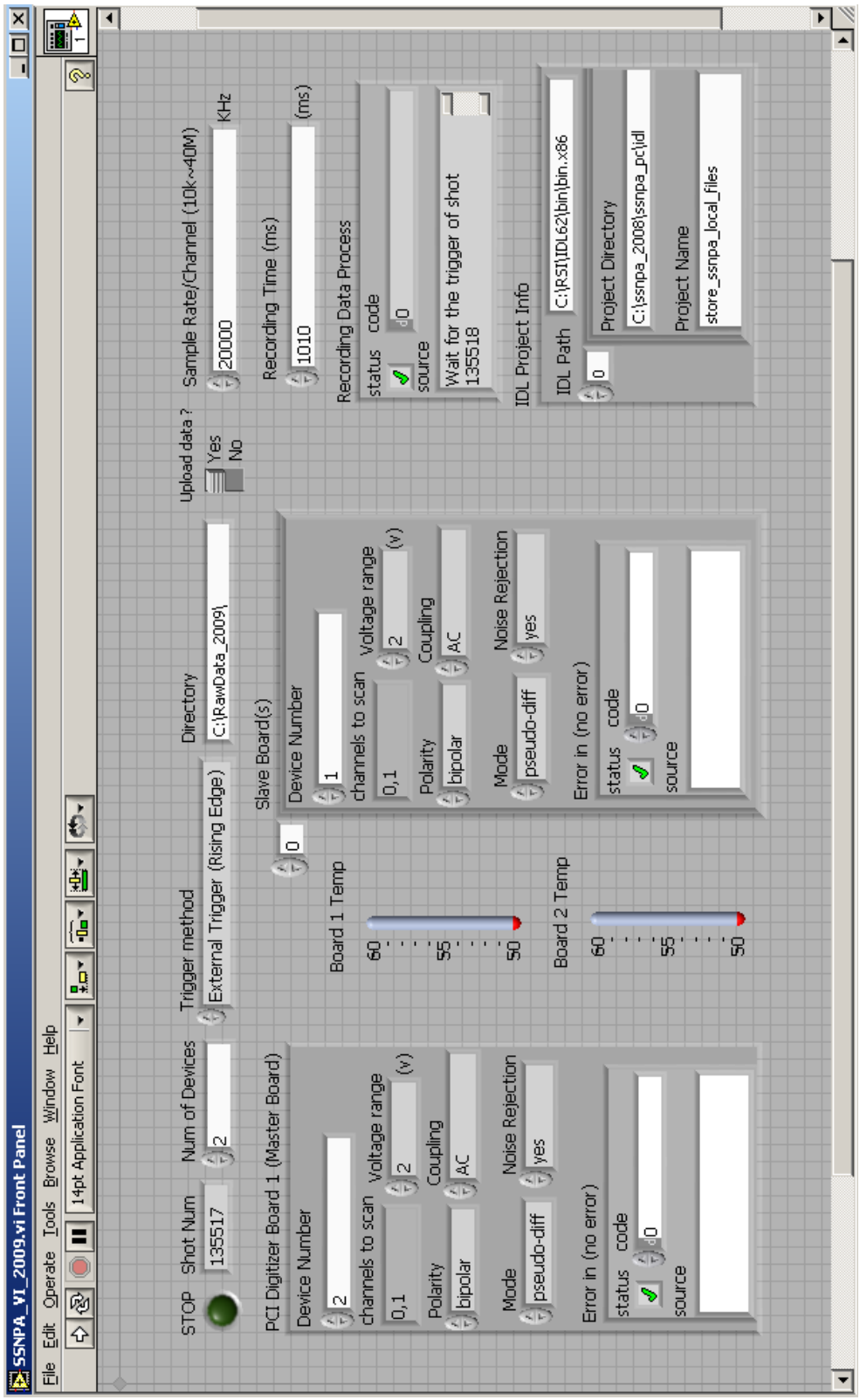

Figure A.1: The Labview control panel for the SSNPA data acquisition system.

B Pulse Height Analysis Routines

The main steps of pulse height analysis are described in Sect. 3.3.1. The main IDL routines for the pulse height analysis are saved in the directory of C:\ssnpa_2008 in the local SSNPA PC and they are:

(1) **get_ssnpa_raw_data.pro** This subroutine reads the SSNPA raw data file including the SSNPA signals, trigger time, time resolution and total sampling points.

(2) **peak_finder.pro** This subroutine smoothes the raw data and find the pulses with the peak magnitude larger than a preset threshold. It also determines the baseline, peak position and peak value, pulse width for each pulse. The pulse height equals the peak value minus the baseline.

(3) **peak_finder_comparison_i.pro, peak_finder_comparison_ii.pro**, and **peak_finder_comparison_iiii.pro**. These subroutines are also peak finder subroutines, but they have more advanced functions. These three subroutines use different methods to search for pulse peaks and positions and the discrepancy between different approaches is less than 5%. For automatic data analysis, the subroutine of peak_finder_comparison_i.pro is used. These subroutines also reject serious pile-up by checking the time length between adjacent overlapping pulses. In addition, the found pulses are normalized to their pulse heights and compared with a model pulse. If the reduced chi-squared is smaller than a specified value (which means the measured pulse shape is very similar to the model pulse), that pulse is accepted as a true signal pulse. Otherwise, the pulse is rejected as EM noise.

(4) **pileup_correction.pro** This routine is used to disentangle the overlapping pulses and determine the pulse height for each pulse. If any pulse width is larger than

a certain maximum value, it is considered a possible pulse pile-up event. In such cases, the first signal is fitted up to the start of the second one. The analytical function obtained from the fitting is subtracted, thus isolating the second pulse, which can then be separately analyzed. This reconstruction requires a minimum fit interval between two pulses in order to obtain stable results for the first pulse.

(5) **pulses_selection.pro** This subroutine is used to select the pulses in certain pulse width range and certain reduced chi-squared range.

(6) **volt_kev.pro** and **kev_volt.pro** These subroutines convert the SSNPA energy axis from volt to keV or from keV to volt based on the SSNPA energy calibration.

(7) **ssnpa_neutral_flux.pro** This subroutine converts the count rate to the NPA neutral flux, as defined in Eq. 4.4.

(8) **ssnpa_plots.pro, plot_rawdata.pro**, **plot_2d3d.pro, ssnpa_contour.pro, plot_time_slice.pro** and **plot_energy_spectrum.pro,** These subroutines are used to plot the SSNPA raw data, temporal evolution, and energy spectrum.

(9) **coarse_data_analysis.pro and fine_data_analysis.pro.** These two subroutines are the two modes of SSNPA analysis programs: coarse data analysis and fine data analysis. The first approach uses the peak finder program, peak_finder.pro, and thus no pulse shape comparison and no pulse pile-up disentanglement. The second approach has all the functions.

(10) **ssnpa_analysis.pro** This subroutine creates an graphical interface for the SSNPA data analysis, as shown in Fig. B.2.

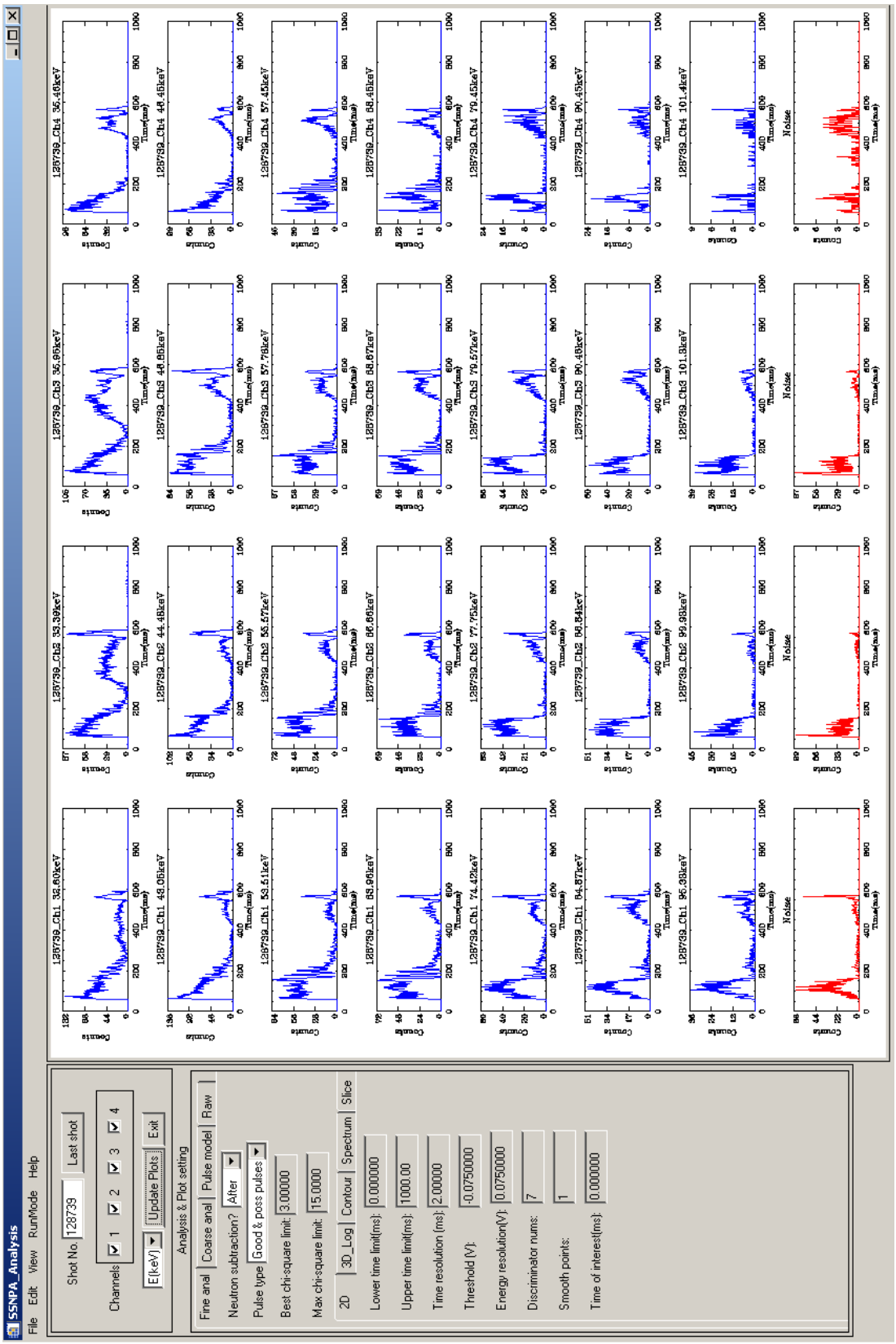

Figure B.2: The graphic interface for the SSNPA data analysis.